OCM 2015

2nd INTERNATIONAL CONFERENCE ON

Optical Characterization of Materials

MARCH 18th – 19th, 2015
KARLSRUHE | GERMANY

KIT Scientific Publishing

Jürgen Beyerer | Fernando Puente León | Thomas Längle (eds.)

OCM 2015

2nd International Conference on Optical Characterization of Materials

March 18th – 19th, 2015
Karlsruhe | Germany

OCM 2015

2nd International Conference on Optical Characterization of Materials

March 18th – 19th, 2015
Karlsruhe | Germany

edited by
Jürgen Beyerer | Fernando Puente León | Thomas Längle

KIT Scientific Publishing

Veranstalter

Fraunhofer Institut of Optronics,
System Technologies and Image Exploitation IOSB
c/o Karlsruhe Center for Material Signatures KCM
Fraunhoferstraße 1, 76131 Karlsruhe

Dieser Tagungsband ist auch als Onlineversion abrufbar unter
http://dx.doi.org/10.5445/KSP/1000044906

Impressum

Karlsruher Institut für Technologie (KIT)
KIT Scientific Publishing
Straße am Forum 2
D-76131 Karlsruhe

www.ksp.kit.edu

Print on Demand 2015

ISBN 978-3-7315-0318-7
DOI 10.5445/KSP/1000044906

Preface

The state of the art in optical characterization of materials is advancing rapidly. New insights into the theoretical foundations of this research field have been gained and exciting practical developments have taken place, both driven by novel applications that are constantly emerging. The big success of the first international conference on Optical Characterization of Materials in 2013 proves the necessity of a platform to present, discuss and evaluate the latest research results in this interdisciplinary domain. Due to that fact, the international conference on Optical Characterization of Materials (OCM) took place the second time in March 2015.

The OCM 2015 was organized by the Karlsruhe Center for Spectral Signatures of Materials (KCM) in cooperation with the German Chapter of the Instrumentation & Measurement Society of IEEE. The Karlsruhe Center for Spectral Signatures of Materials is an association of institutes of Karlsruhe Institute of Technology (KIT) and the business unit Automated Visual Inspection of the Fraunhofer Institute of Optronics, System Technologies and Image Exploitation IOSB.

Despite the conference's young age, the organizing committee has had the pleasure to evaluate a large amount of abstracts. Based on the submissions, we selected 21 papers as talks complemented by 19 poster presentations and several practical demonstrations.

The present book is based on the conference held in Karlsruhe, Germany from March 18–19, 2015. The aim of this conference was to bring together leading researchers in the domain of Characterization of Materials by spectral characteristics from UV (240 nm) to IR (14 µm), multispectral image analysis, X-ray methods, polarimetry, and microscopy. Typical application areas for these techniques cover the fields of, e.g., food industry, recycling of waste materials, detection of contaminated materials, mining, process industry, and raw materials.

The editors would like to thank all of the authors that have contributed to these proceedings as well as the reviewers, who have invested a generous amount of their time to suggest possible improve-

ments of the papers. The help of Henning Schulte and Johannes Meyer in the preparation of this book is greatly appreciated. Last but not least, we thank the organizing committee of the conference, led by Britta Ost, for their effort in organizing this event. The excellent technical facilities and the friendly staff of the Fraunhofer IOSB greatly contributed to the success of the meeting.

March 2015

Jürgen Beyerer
Fernando Puente León
Thomas Längle

General Chairs

Prof. Dr.-Ing. habil. J. Beyerer	Fraunhofer IOSB Karlsruhe
Prof. Dr.-Ing. F. Puente León	Karlsruhe Institute of Technology

Program Chair

apl. Prof. Dr.-Ing. T. Längle	Karlsruhe

Program Committee

Dr. M. Bücking	Schmallenberg
PD Dr. rer. nat. J.-D. Eckhardt	Karlsruhe
Dr.-Ing. R. Gruna	Karlsruhe
Prof. Dr.-Ing. M. Heizmann	Karlsruhe
Prof. Dr.-Ing. O. Kanoun	Chemnitz
Prof. Dr.-Ing. habil. H. Z. Kuyumcu	Berlin
M. Sc. J. Meyer	Karlsruhe
Prof. Dr.-Ing. H. S. Müller	Karlsruhe
Dipl.-Ing. D. Nüßler	Wachtberg
Dr. R. Ostertag	Würzburg
Prof. Dr.-Ing. T. Pretz	Aachen
Dipl.-Inf. M. Richter	Karlsruhe
Prof. Dr. F. Salazar Bloise	Madrid
Dr. H. Schmidt	Kulmbach
Dipl.-Ing. Dipl.-Wirt.-Ing. H. Schulte	Karlsruhe
Prof. Dr. G. Sextl	Würzburg
Dipl.-Ing. M. Taphanel	Karlsruhe
Prof. Dr.-Ing. H. Wotruba	Aachen
Prof. Dr. B. Zagar	Linz

Contents

Spectral Data Processing

Waste Recycling

Mineral Sorting

Industrial Solutions

Non-destructive determination of grape berry sugar concentration using visible/near infrared imaging and possible impact on wine quality

Magali Lafontaine,[1]* Zrinka Bockaj,[2]* Maximilian Freund,[1]
Kai-Uwe Vieth[2] and Christian Negara[2]

[1] Hochschule Geisenheim University,
Von Lade Str. 1, 65366 Geisenheim (Germany)
[2] Fraunhofer IOSB,
Fraunhoferstrasse 1, 76131 Karlsruhe (Germany)
* both authors contributed equally to this work

Abstract Reducing heterogeneity in harvest material may be beneficial for wine quality and this goal may be achieved through advanced berry sorting systems. The general aim is to assess if a relationship could be found between berry sugar concentration and hyperspectral images to determine the possible impact on wine quality. Grapes were picked at different stages of maturity in a one-year time interval and the berries were sorted according to their size and density. Hyperspectral images of the groups were obtained in the vis/NIR wavelength range with a complete spectrum from 400 nm to 2500 nm. Our results showed that vis/NIR images can be used as a tool to improve the segregation of berries from all tested grape varieties based on their sugar content. The PLSR algorithm is trained on all grape varieties together and later validated on each variety separately, proving the possibility of using a general regression model with constant parameters to predict sugar concentrations. Finally, the impact on quality was tested for red wines. Pinot noir berries with higher sugar concentrations presented more color since anthocyanin concentration was higher. Nevertheless, tannin concentration in skins and seeds tended to decrease with increasing sugar concentration. Groups with higher sugar concentration resulted in wines with higher anthocyanin and lower tannin concentration.

1 Introduction

The extension to which variability of quality traits for wine production is encountered in commercial vineyards has been highlighted by the development of new mapping and sorting techniques. In recent years, optical berry sorting machines have been developed permitting to eliminate material other than grape and rotten berries. Advanced berry sorting systems further allow for discrimination between berries of different size and color. This technology would therefore allow producers to create wines of different quality or style from a single production unit in a targeted way. The project "GrapeSort" financed by a German ZIM research project of the BMWI involved two research institutions, Fraunhofer IOSB and Hochschule Geisenheim University with two industrial partners. The aim of this project was to determine suitable parameters correlated with grape and wine composition to be implemented as a quality criterion for improving sorting methods of the fruits [1]. One challenge would be to discriminate the berries according to their ripeness as a high variability, up to 50%, in their sugar concentration can be found. The aim of the study was to determine if a relationship could be found between berry sugar concentration and hyperspectral images of several varieties to implement this methods on a sorting machine. The second step was to assess the possible relevance of sorting berry according to their sugar concentration in relation to wine quality.

2 Berry size and density segregation

While focusing mainly on 3 varieties, in 2013 *Vitis vinifera* L. cv. Pinot noir, Pinot blanc and Riesling, the sortiment was broadend in 2014 with Pinot précoce, Dornfelder, Acolon, Pinot meunier, Lemberger, Trollinger, Müller Thurgau, Pinot gris and Gewürztraminer. Berries collected at different stages of maturity were classified according to their diameter with a sip column and then segregated according to their density in an interval of 5° Oe. All the berries were introduced in the less dense solution, the floating berries were collected, thereafter, the concentration of the solution was increased. The same process was repeated

until all the berry population was sorted. Sorting according to density was successful as density solution concentration was correlated with berry sugar concentration (R^2 = 0.98). For each date, the berries were distributed according to a gaussian bell-shape showing the heterogeneity in sugar concentration up to 50% (Pinot noir 2013 : Figure 1.2A) and it seemed that the variability of the distribution was growing until harvest. Hyperspectral images were captured in the vis/NIR wavelength range with a complete spectrum from 400 nm to 2500 nm on 20-berries subsamples from each density group.

3 Hyperspectral imaging for sugar concentration prediction

The conducted measurements confirm the validity of involving NIR spectroscopy with the primary focus in determining the sugar concentration of grapes. In this paper, we continue the work of [2] and include more grape varieties in the general learning phase. Followed by the application of multivariate data analysis, we investigated the correlation of the prepared hyperspectral images with the laboratory data. At the end, the final validation of the results obtained with the regression analysis will be evaluated and compared for different grape varieties.

3.1 Regression analysis and data preparation

Although the main purpose of determining the sugar concentration is to sort berries into two different groups (with low and high sugar concentration), which generally implies the usage of classification algorithms, we found out that regression algorithms yield better results. Additionally, the possibility of changing the process of automatic berry sorting by only introducing a variable threshold for sugar concentration would significantly simplify the work of the winemaker. The regression problem can be transformed into a two-class classification problem by assigning the label ”high sugar concentration” (class A) or ”low sugar concentration” (class B) according to a defined threshold value, e.g. the median of the ground truth data. Another benefit in contrast to clas-

sification algorithm is that the complete information about the ground truth is taken into account, not only the class affiliation.

Moreover, it is not necessary to retrain the classifier every time when changing the threshold, but only to apply the new threshold value after the regression to define the classes for high and low sugar concentration.

Since the PLSR *(Partial Least Square Regression)* [3] has already been proven as an effective regression algorithm often used with hyperspectral imaging and also in the earlier phases of this project [2], we continued using it for the purpose of this study. PLSR attempts to determine the relationship between a dependent variable (also called *responses*) and one or more independent variables (also called *predictors*) by extracting from the predictor a set of orthogonal factors called latent variables that have the best predictive power.

In our case, the optimal number of latent variables proved to be 20. Moreover, the hyperspectral images of the berries will be used as predictors, and in laboratory measured sugar concentration of the berries as responses. As a result of regression analysis, the general regression model will be obtained as an vector of weights for each of the 99 features of the spectra. Finally, the sugar concentration values can be predicted from original hyperspectral images for each berry using a vector multiplication between a spectrum written as a vector and the computed regression coefficients. It has turned out, that the spectra from the SWIR wavelength range from 1000 nm to 2500 nm are not as useful as the vis/NIR spectra from the wavelength range from 400 nm to 1000 nm to assess the sugar concentration. Therefore the analysis is restricted to the latter.

During the training of the regression algorithm, additional adjustments to the original datasets have been applied, resulting in big improvements of the final results. First of all, the mean spectrum is computed for each berry (object) by averaging all spectra of every pixel of a given berry which also speeds up the whole process by reducing the data which has to be processed.

Furthermore, in this specific case, only the upper range of the vis/NIR wavelength range (708 - 1025 nm), represented by 99 features is extracted and used for regression because the difference in the results when using the whole and half wavelength-band is insignificant. They are even slightly better in the second case. One possible explanation of this phenomena could be that the information contained in the lower

wavelength-band is not important for regression and could probably contain noise.

The dataset on which the regression is performed consists of two different datasets taken in 2013 and 2014 containing 12 different varieties with following properties shown in Table 1.1.

Table 1.1: Properties of each dataset used to train the regressor

Dataset	Dates	Different grape varieties	Number of pixels	Number of objects (berries)	Amount of pixel used
2013	07.10.2013 17.09.2013	3	1,218,687	1,248	100 %
2014	29.08.2014 01.09.2014 12.09.2014 15.09.2014 26.09.2014 30.09.2014	9	1,991,737	1,980	100 %

3.2 Validation and results

To ensure internal validity, the results were computed using one-fold cross-validation.

Further evidence that supports our basic premises about creating the regression model with one combined dataset are shown in Table 1.2. Including a time range of one year and 12 different grape varieties we still gained good results on only one specific grape variety. As a measurement for quality of the regression results, two different metrics will be used: RMSE *(root-mean-square-error)* [3] and PPMC *(Pearson Product Moment Correlation)* [3]. RMSE measures the typical distance of the data to the regression line and will be computed as follows:

$$\mathrm{RMSE} = \sqrt{\frac{1}{n}\sum_{i=1}^{n}(y_i - \hat{y}_i)^2} \tag{1.1}$$

where y_i are the ground truths , $\hat{y}_i$ the predicted values and n the number of features.

The correlation coefficient measures the strength and the direction of a linear relationship between two variables (the ground truths and the predicted values).

Table 1.2: Regression results for each grape variety of dataset 2013 and 2014

Grape varieties	Correlation coefficients	RMSE
Pinot noir 2013	0.829	6.601
Pinot blanc 2013	0.918	5.553
Riesling 2013	0.930	5.855
Gewürztraminer	0.875	4.759
Pinot Meunier	0.868	6.358
Dornfelder	0.830	4.867
Pinot blanc	0.843	5.200
Pinot meunier	0.751	5.122
Acolon	0.832	4.819
Pinot précoce	0.892	5.627
Pinot noir	0.823	5.290
Müller Thurgau	0.823	6.353
Lemberger	0.807	6.260
Trollinger	0.854	4.621

The regression performance of the PLSR algorithm trained with the images of the combined datasets containing all grape varieties taken in 2013 and 2014 was validated on the images of Pinot blanc and Müller Thurgau from 2014 and shown in Figure 1.1. In addition to that, RGB images are also shown, but they differ only marginally and cannot be used in assessing the sugar concentration. These results give a significant insight in the predictive possibilities of our method.

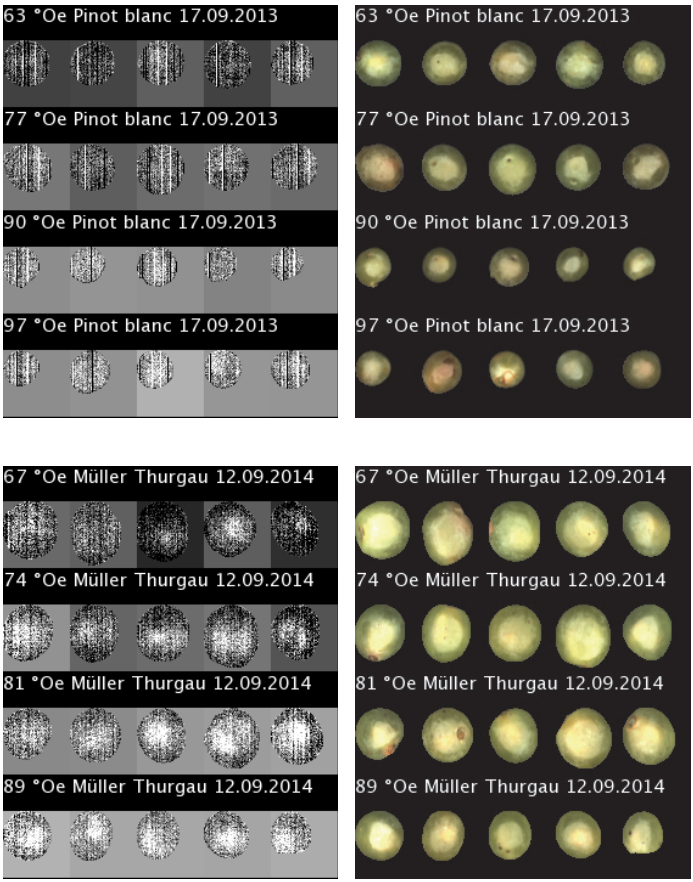

Figure 1.1: Predicted sugar concentration using the PLSR algorithm and RGB images in comparison. The algorithm was trained with 12 different grape varieties with a range of sugar concentrations: 37 - 116 °Oe. The background for grey-value images shows the mean predicted sugar concentration for each berry.

We indeed showed that it would be possible to discriminate the berries according to their sugar concentration by means of NIR spectrometry. The further question to be answered is if it would be relevant

to sort berries according to their sugar concentration. One trial with 100kg Pinot Noir in 2013 [1] showed that the two sorted batches were different in average sugar concentration by 10%. In the trial in 2013 only an RGB camera and an NIR camera with a bandpass filter were used. Therefore, the segregation according to the sugar concentration was not as good as the achievable segregation using NIR spectrometry.

4 Possible impact on wine quality

4.1 Primary compounds

Results of Pinot noir picked on the 06.10.2013 are presented to illustrate the question. Variability in sugar concentration was important as the range of sugar concentration was between 70° Oe and 110° Oe for one single sampling date (Table1.3). With increasing sugar concentration, the total acidity (together with the malic acid concentration) were decreased, while pH increased. The alpha amino acids increased with increasing maturity meaning that an increasing concentration of nitrogen would be available for the yeast during fermentation. All the parameter indicate an increase in quality with increasing sugar concentration.

Table 1.3: Primary compounds analysis of the musts according to the sugar concentration of the different groups. Example for Pinot noir berry population picked on the 06.10.2013.

Sugar content Oe	Amino acids mg/L	Total acidity g/L	Malic acid g/L	pH
70	200	11.10	8.40	2.80
77	201	10.90	8.15	2.90
83	208	9.75	6.72	3.09
90	230	8.97	5.65	3.06
97	256	8.72	5.39	3.18
103	276	8.85	5.66	3.16
110	278	9.12	5.82	3.23

4.2 Secondary compounds

Berry phenolic compounds are crucial to red wine quality as they contribute to red wine color, color stability, structure and mouthfeel. The analysis of phenolics by wet chemistry was proceeded according to [4] for anthocyanins (A) and tannins (T).

Berry anthocyanins contribute to the color of a red wine, their accumulation starts in berry skin after the onset of ripening, veraison and is at maximum around harvest. Anthocyanin concentration and content increased with increasing sugar concentration in berries (Figure 1.2B). This is in accordance with previous work that berries from higher density showed an increase in anthocyanin concentration for several red varieties [5, 6]. Indeed anthocyanin concentration would be strongly correlated to sugar accumulation in berries [7]. Sucrose has been shown to induce anthocyanin production in grape skin [8] what was related to a modulation of the transcription of some key biosynthetic enzymes of the phenylpropanoid pathway [9].

Berry tannins participate mainly to the mouthfeel of a red wine and their accumulation occurs early in grape development, mainly before veraison in both berry skin and seeds. Tannin concentration in seeds and skins was highest in less ripen samples and their concentration in berries decreased with increasing density. But though the decrease in seed tannins seemed established, some studies reported no major changes for tannins of berry skin [10] what may depend on overall ripeness [5, 11]. However, it was pointed out that not only the amount but the extractability of the tannin compounds is changing due to the different interaction of tannins binding with cell wall proteins or polysaccharides.

4.3 Wine analysis

As it would be difficult to predict the actual extraction of phenolics into wine from berry analysis, a method of micro-scale winemaking was developed [12] to produce wine and the method for phenolic extraction was repeatable as the relative standard deviation (RSD) represented around 8%-11% (TP), 5-12% (A) and 8-12% (T).

Wine anthocyanins concentration increased with increasing density (Figure 1.2C). This was already observed for Cabernet sauvignon wine

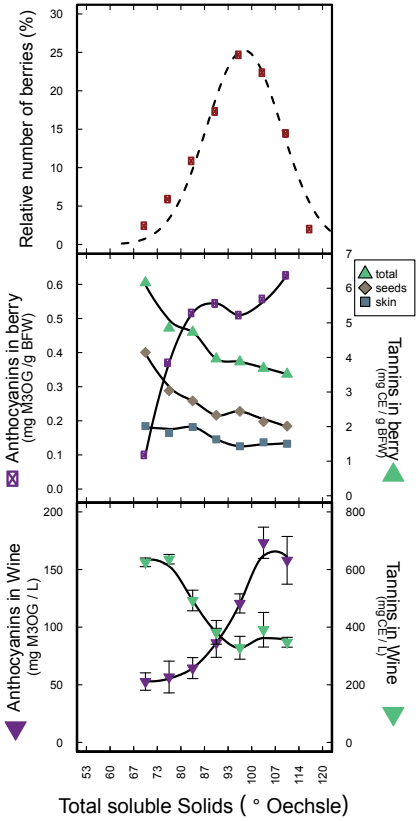

Figure 1.2: Results for Pinot noir bunch samples picked on the 16.10.2013. A: Distribution of the berries according to their density group as ° Oe. B: Berry phenolics compounds as mg per g berry fresh weight according to their density group, Anthocyanins (A) in berry skin, tannins (T) in berry skins and berry seeds together with total tannin concentration. C: Wine phenolics compounds as mg per L according to their density group, Anthocyanins (A) in wines, tannins (T) in wines.

as anthocyanin concentration and color intensity increased with higher density [13]. This may however be due to the higher concentration of

anthocyanins in berry skin or higher ethanol concentration, with higher anthocyanin extraction [13]. A change in extractability of anthocyanins with higher density may also be an explanation as an increase of extractability through grape ripening was observed [14], as a consequence of the cellular wall degradation by pectolytic enzymes, making cell wall pectins permeable to the changes that occur during vinification. Therefore, not only the accumulation of the anthocyanins but also the ease of extraction would be the main factors affecting their extraction into wines [15].

Wine tannins concentration decreased with increasing density. Reports on extraction of tannins are more confusing as for anthocyanins. A significant increase of tannin concentration of the wine with the density of the grapes was previously reported [13]. It was suggested that insufficiently ripened grapes would have a lower extractability of tannins from skins and a higher extractability of tannins from seeds [16] showing a higher contribution of seeds when less ripen [13, 17]. Discrepancies in results may be explained by the berry size, indeed, when sorting berries according to their density and size, wine tannin concentration decreased with increasing maturity [18] but berry size seemed to play larger role.

5 Setting the threshold

We showed that hyperspectral images in the vis/NIR wavelength range can be used for the segregation of berries based on their sugar content. The winemaker could easily transform the regression into the classification by simply giving the threshold value for the sugar concentration to separate berries below and above this threshold. However, deciding about the threshold would be another challenge to be solved depending on the type of wine targeted (Figure 1.3).

6 Conclusion and outputs

We showed that hyperspectral images in the vis/NIR wavelength range can be used as a tool to improve the segregation of berries from all tested grape varieties based on their sugar content. Indeed, discriminating berries according to their sugar concentration would allow to modify

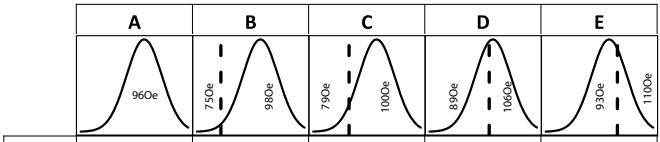

	no sorting	threshold **77°Oe**		threshold **83°Oe**		threshold **90°Oe**		threshold **97°Oe**	
%	100%	2%	98%	19%	81%	61%	39%	83%	17%
TSS (°Oe)	96°Oe	75°Oe	98°Oe	79°Oe	100°Oe	89°Oe	106°Oe	93°Oe	110°Oe
T (mg/L)	398	553	376	472	361	408	373	399	348
A (mg/L)	121	60	127	72	135	113	167	120	158

Figure 1.3: Theoretical wine composition calculated based on the results of Pinot noir (Figure 1.2). Case study depending on the threshold separating the ”low” and ”high” sugar concentration groups: A: no sorting, B: threshold at 77° Oe, C: threshold at 83° Oe, D: threshold at 90° Oe, E: threshold at 97° Oe.

the wine style as an increase in sugar would lead to wines with more color since anthocyanin concentration in berries was higher. Nevertheless, tannin concentration in skins and seeds tended to decrease with increasing sugar concentration leading to wines with decreasing tannin concentration. In further steps, the results of the PLSR algorithm with vis/NIR spectra are used for designing the camera system of the sorting machine.

References

1. M. Lafontaine, M. Freund, K.-U. Vieth, and C. Negara, “Automatic fruit sorting by non-destructive determination of quality parameters using visible/near infrared to improve wine quality: I. Red wine production,” *NIR news*, vol. 24, no. 8, pp. 6–8, 2013.
2. C. Negara, K.-U. Vieth, M. Lafontaine, and M. Freund, “Automatic fruit sorting by non-destructive determination of quality parameters using visible-near infrared to improve wine quality: II. Regression analysis,” *NIR news*, vol. 25, no. 1, pp. 4–6, 2014.
3. W. Kessler, *Multivariate Datenanalyse: für die Pharma-, Bio- und Prozessanalytik*. Wiley-VCH Verlag GmbH and Co. KGaA Weinheim, 2006.
4. J. F. Harbertson, J. A. Kennedy, and D. O. Adams, “Tannin in Skins and

Seeds of Cabernet Sauvignon, Syrah, and Pinot noir Berries during Ripening," *American Journal of Enology and Viticulture*, vol. 53, no. 1, pp. 54–59, 2002.

5. F. Torchio, E. Cagnasso, V. Gerbi, and L. Rolle, "Mechanical properties, phenolic composition and extractability indices of Barbera grapes of different soluble solids contents from several growing areas," *Analytica Chimica Acta*, vol. 660, no. 1-2, pp. 183–9, 2010.
6. S. Río Segade, E. S. Vázquez, and E. D. Losada, "Influence of ripeness grade on accumulation and extractability of grape skin anthocyanins in different cultivars," *Journal of Food Composition and Analysis*, vol. 21, no. 8, pp. 599 – 607, 2008.
7. A. Pirie and M. G. Mullins, "Interrelationships of Sugars, Anthocyanins, Total Phenols and Dry Weight in the Skin of Grape Berries during Ripening," *American Journal of Enology and Viticulture*, vol. 28, no. 4, pp. 204–209, 1977.
8. A. J. G. Pirie and M. G. Mullins, "Changes in anthocyanin and phenolics content of grapevine leaf and fruit tissues treated with sucrose, nitrate and abscisic acid," *Plant Physiology*, vol. 58, pp. 468–472, 1976.
9. M. Ferri, L. Righetti, and A. Tassoni, "Increasing sucrose concentrations promote phenylpropanoid biosynthesis in grapevine cell cultures," *Journal of Plant Physiology*, vol. 168, no. 3, pp. 189–195, 2011.
10. D. Fournand, A. Vicens, L. Sidhoum, J. M. Souquet, M. Moutounet, and V. Cheynier, "Accumulation and Extractability of Grape Skin Tannins and Anthocyanins at Different Advanced Physiological Stages," *Journal of Agricultural and Food Chemistry*, vol. 54, no. 19, pp. 7331–7338, 2006.
11. L. Rolle, F. Torchio, S. Giacosa, S. R. Segade, E. Cagnasso, and V. Gerbi, "Assessment of Physicochemical Differences in Nebbiolo Grape Berries from Different Production Areas and Sorted by Flotation," *American Journal of Enology and Viticulture*, vol. 63, no. 2, pp. 195–204, June 2012.
12. M. Lafontaine, R. Scholz, M. Stoll, and H. R. Schultz, "Anthocyanin concentration in Pinot noir berries and their extraction into wine as affected by rootstock," *Proceedings 17th International Symposium GiESCO*, vol. Asti, Alba CN, Italy 29.08-02.09, 2011.
13. N. Kontoudakis, M. Esteruelas, F. Fort, J. M. Canals, V. D. Freitas, and F. Zamora, "Influence of the heterogeneity of grape phenolic maturity on wine composition and quality," *Food Chemistry*, vol. 124, no. 3, pp. 767 – 774, 2011.
14. N. Saint-Cricq de Gaulejac, N. Vivas, and Y. Glories, "Maturation phénolique des raisins rouges. relation avec la qualité des vins. compara-

ison des cépages merlot et tempranillo," *Progrès Agricole et Viticole*, vol. 115, no. 13-14, pp. 306–318, 1998.

15. I. Romero-Cascales, A. Ortega-Regules, J. M. Lopez-Roca, J. I. Fernandez-Fernandez, and E. Gomez-Plaza, "Differences in Anthocyanin Extractability from Grapes to Wines According to Variety," *American Journal of Enology and Viticulture*, vol. 56, no. 3, pp. 212–219, 2005.
16. C. Peyrot des Gachons and J. A. Kennedy, "Direct Method for Determining Seed and Skin Proanthocyanidin Extraction into Red Wine," *Journal of Agricultural and Food Chemistry*, vol. 51, no. 20, pp. 5877–5881, 2003.
17. J. L. Pastor del Rio and J. A. Kennedy, "Development of Proanthocyanidins in *Vitis vinifera* L. cv. Pinot noir Grapes and Extraction into Wine," *American Journal of Enology and Viticulture*, vol. 57, no. 2, pp. 125–132, 2006.
18. M. Lafontaine, M. Stoll, and H. R. Schultz, "Berry size and maturity affecting phenolic extraction in Pinot Noir wines," in *Proceedings 18th International Symposium GiESCO*, J. Queiroz and A. Carneiro, Eds., vol. 28. Porto (Portugal) 07.07-11.07: Ciência e Técnica Vitivinícola, 2013, pp. 396–400.

Prediction of lamb eating quality using hyperspectral imaging

Tong Qiao, Jinchang Ren, Jaime Zabalza and Stephen Marshall

Centre for excellence in Signal and Image Processing (CeSIP),
Department of Electronic and Electrical Engineering,
University of Strathclyde, Glasgow, UK.
(Corresponding author: jinchang.ren@strath.ac.uk)

Abstract Lamb eating quality is related to 3 factors, which are tenderness, juiciness and flavour. In addition to these factors, the surface colour of lamb could influence the purchase decision of consumers. Objective quality evaluation approaches, like near-infrared spectroscopy (NIRS) and hyperspectral imaging (HSI), have been proved fast and non-destructive in assessing beef quality, compared with conventional methods. However, rare research has been done for lamb samples. Therefore, in this paper the feasibility of HSI for evaluating lamb quality is tested. A total of 80 lamb samples were imaged using a visible range HSI system and the spectral profiles were used for predicting lamb quality related traits. For some traits, noises were removed from HSI spectra by singular spectrum analysis (SSA) for better performance. Support vector machine (SVM) was employed to construct prediction equations. Considering SVM is sensitive to high dimensional data, principal component analysis (PCA) was applied to reduce the dimensionality first. The prediction results suggest that HSI is promising in predicting lamb eating quality.

1 Introduction

Similar to beef production, lamb also plays an important role in UK agriculture, contributing over 10% of total live stock output [1]. Eating quality of lamb is related to many chemical and physical properties. It was found that 3 key factors, which are tenderness, juiciness and flavour, have an influence on the repurchase behaviour of consumers [2]. In addition to those factors, meat surface colour is considered as the most

significant factor determining retail selection of consumers [3]. Usually, evaluation of the above mentioned traits is achieved by measuring some mechanical properties of the meat sample, which can be costly, destructive and time-consuming.

Over the past a few decades, some objective approaches for predicting meat quality traits have been developed. Some examples include ultrasound, near infrared spectroscopy (NIRS), multispectral imaging, hyperspectral imaging (HSI) and various computer vision techniques. Among these approaches, NIRS is the most widely used technique for meat quality evaluation due to its simplicity, rapidity and effectiveness, but one major drawback of this technique is its low spatial resolution for analysing non-homogeneous composition of meat samples [4]. To this end, HSI integrating both spatial and spectral information has emerged, which shows great potential in remote sensing applications [5, 6]. In recent years, some researchers have demonstrated that HSI has some promise for predicting beef quality traits [7]. But to our knowledge, limited research has been conducted using HSI to predict quality traits of lamb samples.

The objective of the paper is to investigate the feasibility of HSI in predicting lamb quality related traits. In this study, ultimate pH was measured as the flavour reference and MIRINZ shear force (SF) was measured as the tenderness reference. Surface colour was measured in CIE (Commision Internationale de l'Eclairage) colour space as L*, a* and b*, where L* is the lightness, a* is redness and b* is yellowness. The prediction equation was constructed by the support vector machine (SVM) on a calibration set and the performance was assessed on the additional validation set. Details will be explained in following sections.

2 Materials and methods

2.1 Lamb sample preparation and image collection

A total of 80 lamb samples were purchased from a commercial abattoir in Scotland. Storing at $3 \pm 2\,^{\circ}\mathrm{C}$ for 7 days after being slaughtered, left lamb loins were removed from packaging. After blooming for 2 minutes [8], HSI samples were collected using a push-broom HSI system (Gilden photonics) with wavelength ranging from 400 to 862.90 nm at a spectral

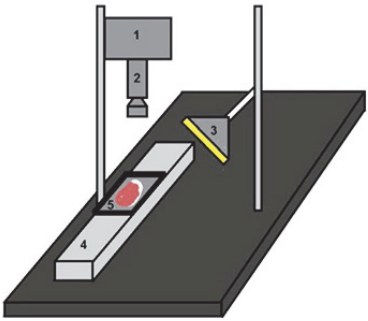

Figure 2.1: Schematic diagram of the HSI system: components 1-5 refer to the CCD camera, spectrograph and lens, halogen lamp, sliding track and scanning tray, respectively.

resolution of about 2.5 nm. Figure 2.1 shows a schematic diagram of the imaging system.

2.2 Measurements of quality related traits

Right after imaging, ultimate pH was determined by probing into the lamb sample derectly using a calibrated Hanna pH meter with a glass electrode (HI 99613). The surface colour was measured in the L*a*b* scale with a Minolta CR-410 colourimeter, where the machine is set to take 3 scans and then average them. Then, each lamb sample was labelled, vacuum packaged and frozen at $-30\,^{\circ}$C to prevent from further ageing. On the night before tenderness measurement, samples were placed in plastic bags and sub-merged in a water bath until reaching an internal temperature of $70\,^{\circ}$C and then chilled in the fridge. On the following day, 10 sub-samples with a 10 mm $\times$ 10 mm cross section were prepared parallel with the muscle fibre axis. All sub-samples were then sheared orthogonal to the fibre axis with a Tenderscot tenderometer (Pentland Precision Engineering Ltd) with a wedge shaped tooth according to the MIRINZ protocol [9]. The peak force was extracted during each shear process and the average value of 10 measurements is considered as the MIRINZ SF. Therefore, there are 5 lamb quality related traits in total for each sample, which are pH, L*, a*, b* and MIRINZ SF.

2.3 HSI data pre-processing

During the imaging process, reflectance of the sample was acquired by the HSI system. But before that, the HSI system has to be calibrated using a white reference image (nearly 100% reflectance) and a dark reference image (0% reflectance), which are 2 extreme illumination conditions. The reason is that the 'dark current' generated from thermal effects of the detectors should be deducted from the produced signal. Thus, the calibration procedures make sure that the sample reflectance is separated from system responses [7]. The following equation shows how the calibrated reflectance is achieved,

$$R = \frac{I-B}{I_0-B}, \tag{2.1}$$

where R is the calibrated reflectance image at one spectral band, I is the raw image at that band, B is the dark reference image and I_0 is the white reference image.

For each hypercube, there are 250 spectral bands acquired, while not all of these bands contain useful information. By removing needless spectral bands, the working wavelength for HSI spectra is 469.47 nm - 862.90 nm.

In order to save computing time, for each lamb sample, a region of interest (ROI) with size of 200 $\times$ 100 pixels was mainly selected from the lean part and then the median reflectance value at each spectral band was calculated to achieve the median reflectance spectrum. This process is illustrated in Figure 2.2. As suggested by other researchers, reflectance spectra (R) should be converted to absorbance (A) by logarithm transformation to linearise the relationship between the concentration of an absorbing compound and the absorption spectrum [10], where the equation is shown below,

$$A = \log_{10}\left(\frac{1}{R}\right) \tag{2.2}$$

As a relatively new technique, singular spectrum analysis (SSA), which is commonly used for time series analysis and forecasting, was applied to HSI absorbance spectra for de-noising. Based on the singular value decomposition, it is able to decompose the original spectrum into a few components, including the 'clean' spectrum, a few oscillations and

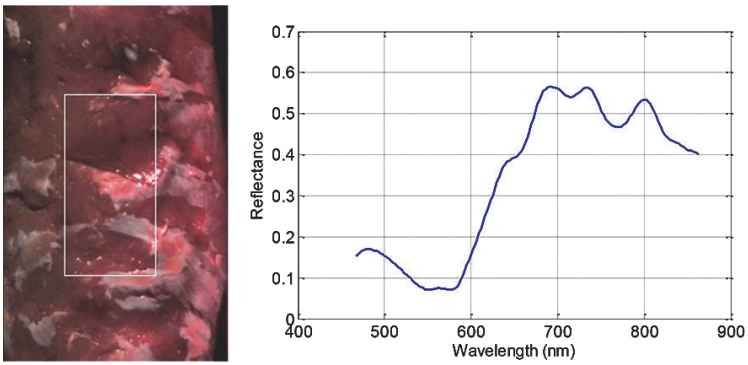

Figure 2.2: HSI median reflectance spectrum extraction. (a) Pseudo colour image of one lamb sample, with ROI marked by the white frame. (b) The median reflectance spectrum of the same sample.

noises. Details of the algorithm can be found in [11]. By reconstructing the spectrum with the first component, subtle noises can be discarded. For the same sample shown in Figure 2.2, the absorbance spectra without SSA and with SSA applied are plotted in Figure 2.3.

2.4 Regression analysis

A variety of statistical regression methods could be applied to construct prediction equations, including multiple linear regression, partial least squares regression (PLSR), principal components regression (PCR) and neural networks [4]. For predicting meat related traits, PLSR is the most common regression approach that researchers choose to build prediction models with NIRS [12–16]. However, PLSR is designed based on the linear algorithm so that the best performance might only be achieved when there is a linear relationship between spectra and quality traits [17], which is not applicable in our study. Therefore, instead of using PLSR, SVM was employed to build regression models. Results in [18] proved that SVM outperforms PLSR for beef quality evaluation using NIRS.

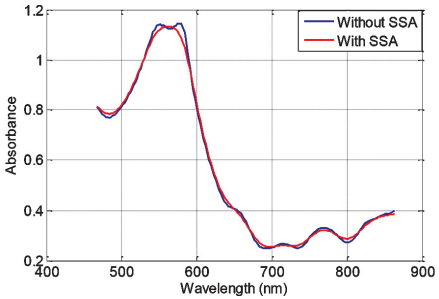

Figure 2.3: HSI absorbance spectrum without SSA applied (blue line) and HSI absorbance spectrum with SSA applied (red line).

The outstanding performance of SVM has been verified in many applications associated with HSI. However, a problem of SVM is that it is sensitive to the curse of dimensionality [19]. As a result, a commonly adopted feature extraction technique, principal component analysis (PCA) [20, 21], is used to reduce the dimensionality of HSI cubes. In this way, only a small amount of features could explain the whole dataset and the rest can be discarded.

With lower dimensional data, SVM could be applied to construct prediction models. For both classification and regression problems, SVM maps the data to a high dimensional feature space using kernel function. Then it is easy to separate the data by a maximal margin hyperplane. As a popular kernel function, the radial basis function (RBF) kernel was chosen. Optimal parameters were tuned using the grid search with 4-fold cross-validation to avoid model over-fitting.

3 Results and conclusion

80 lamb samples were split into the calibration set and the validation set, where prediction models were learnt from the calibration set and verified on the validation set. In this way, the ability of HSI for predicting quality of unknown lamb samples could be tested. In order to split the dataset, each quality trait was sorted in the ascending order. By selecting every 4th sample into the validation set, the rest of data which contain the interleaving 3 samples were allocated to the calibra-

Table 2.1: Summary statistics of all quality traits, including mean, standard deviation (SD) and range, where subscripts cal and val represent the calibration set and the validation set respectively.

Trait	n_{cal}	$Mean_{cal}$	SD_{cal}	$Range_{cal}$	n_{val}	$Mean_{val}$	SD_{val}	$Range_{val}$
pH	60	5.59	0.07	5.46 - 5.90	20	5.61	0.12	5.48 - 6.08
L*	60	41.47	1.83	36.69 - 46.64	20	41.83	2.31	38.74 - 49.63
a*	60	23.28	0.91	20.44 - 25.37	20	23.77	0.83	22.28 - 25.71
b*	60	7.77	0.58	5.89 - 9.15	20	7.85	0.57	7.02 - 9.17
SF	60	5.20	1.36	2.87 - 9.38	20	5.49	1.92	3.43 - 11.99

tion set [22]. This process makes sure that the validation set is a representative of the calibration set, with similar mean, standard deviation (SD) and range. Statistics of each quality trait are shown in Table 12.1. The unit for MIRINZ SF is kilogram force (kgF). The HSI performance for predicting lamb quality is evaluated quantitatively by the coefficient of determination (R^2) and the ratio of performance deviation (RPD). Equations for these metrics are given below:

$$R^2 = 1 - \frac{\sum_{i=1}^{n} (y_i - f_i)^2}{\sum_{i=1}^{n} (y_i - \bar{y})^2}, \tag{2.3}$$

$$RPD = \frac{SD}{RMSE} = \frac{SD}{\sqrt{\frac{\sum_{i=1}^{n} (y_i - f_i)^2}{n}}}, \tag{2.4}$$

where y_i is the original quality trait value, f_i is the predicted value, $\bar{y}$ is the mean of all original trait values, n is the sample number and $RMSE$ is the root-mean-square error in the investigated set. The coefficient of determination ranges from 0 to 1, where 0 represents a poor correlation between the predicted trait values and the reference trait values and 1 standards for a high degree of correlation. The number of principal components was tried from 5 to 50 in a step of 5, and both raw HSI absorbance spectra and SSA-treated absorbance spectra were tested. Combinations of best prediction results are shown in Table 12.2, where A stands for raw absorbance spectra and A + SSA means SSA-treated absorbance spectra.

Table 2.2: Performance for predicting quality traits in lamb using the visible range HSI system.

Trait	Pre-treatment	No. of principal components	R^2_{cal}	$RMSE_{cal}$	R^2_{val}	$RMSE_{val}$	RPD_{val}
pH	A	45	0.54	0.06	0.38	0.11	1.07
L*	A	15	0.83	0.67	0.77	1.34	1.72
a*	A + SSA	40	0.95	0.22	0.48	0.76	1.09
b*	A + SSA	15	0.83	0.34	0.26	0.50	1.13
SF	A + SSA	40	0.82	0.69	0.41	1.52	1.26

As the study is to test the ability of HSI in predicting unknown lamb quality for on-line use, the results of the extra validation set are particularly important. For the prediction of ultimate pH, R^2_{val} is higher than those reported in [1] ($R^2_{cv} = 0.03 - 0.19$). For colour parameters and MIRINZ SF prediction, limited research has been found on lamb. Nevertheless, our results agree with those predicted with beef sample using NIRS [12–16], whose average R^2 values are 0.76 and 0.44 for L* and a*. However, our result of b* is poorer than that of others ($R^2 = 0.57$), which may be due to variation between different samples. Similarly, we compare the MIRINZ SF with Warner-Bratzler SF predicted by others on beef sample. It is found that the average R^2 of their research is 0.30, which is lower than ours ($R^2_{val} = 0.41$).

In conclusion, this paper has demonstrated that HSI could be promising in offering additional information for predicting lamb quality, which might bring beneficial to lamb industries in the future.

4 Acknowledgement

This project is funded by Quality Meat Scotland (QMS) and University of Strathclyde. Authors would like to thank Dr. Cameron Craigie and Scotland's Rural College (SRUC) for helping preparing the data.

References

1. S. Andrés, I. Murray, E. Navajas, A. Fisher, N. Lambe, and L. Bünger, "Prediction of sensory characteristics of lamb meat samples by near infrared reflectance spectroscopy," *Meat Science*, vol. 76, no. 3, pp. 509–516, 2007.
2. L. Jeremiah and D. Phillips, "Evaluation of a probe for predicting beef tenderness," *Meat Science*, vol. 55, no. 4, pp. 493–502, 2000.
3. L. Jeremiah, Z. Carpenter, and G. Smith, "Beef color as related to consumer acceptance and palatability," *Journal of Food Science*, vol. 37, no. 3, pp. 476–479, 1972.
4. M. Prevolnik, M. Candek-Potokar, and D. Skorjanc, "Ability of nir spectroscopy to predict meat chemical composition and quality: a review," *Czech Journal of Animal Science-UZPI (Czech Republic)*, 2004.
5. J. Ren, J. Zabalza, S. Marshall, and J. Zheng, "Effective feature extraction and data reduction in remote sensing using hyperspectral imaging," *Signal Processing Magazine, IEEE*, vol. 31, no. 4, pp. 149–154, July 2014.
6. T. Qiao, J. Ren, M. Sun, J. Zheng, and S. Marshall, "Effective compression of hyperspectral imagery using an improved 3d dct approach for land-cover analysis in remote-sensing applications," *International Journal of Remote Sensing*, vol. 35, no. 20, pp. 7316–7337, 2014.
7. G. K. Naganathan, L. M. Grimes, J. Subbiah, C. R. Calkins, A. Samal, and G. E. Meyer, "Visible/near-infrared hyperspectral imaging for beef tenderness prediction," *Computers and Electronics in Agriculture*, vol. 64, no. 2, pp. 225–233, 2008.
8. S. Shackelford, T. Wheeler, and M. Koohmaraie, "On-line classification of us select beef carcasses for longissimus tenderness using visible and near-infrared reflectance spectroscopy," *Meat Science*, vol. 69, no. 3, pp. 409–415, 2005.
9. A. Frazer, "New zealand tenderness and local meat quality mark programmes," in *Proceedings of the meat quality and technology transfer workshop, 43 rd International congress of meat science and technology, July–August, Auckland, New Zealand*, 1997, pp. 37–51.
10. S. Rust, D. Price, J. Subbiah, G. Kranzler, G. Hilton, D. Vanoverbeke, and J. Morgan, "Predicting beef tenderness using near-infrared spectroscopy," *Journal of Animal Science*, vol. 86, no. 1, pp. 211–219, 2008.
11. J. Zabalza, J. Ren, Z. Wang, S. Marshall, and J. Wang, "Singular spectrum analysis for effective feature extraction in hyperspectral imaging," *Geoscience and Remote Sensing Letters, IEEE*, vol. 11, no. 11, pp. 1886–1890, Nov 2014.

12. S. Andrés, A. Silva, A. L. Soares-Pereira, C. Martins, A. Bruno-Soares, and I. Murray, "The use of visible and near infrared reflectance spectroscopy to predict beef m. longissimus thoracis et lumborum quality attributes," *Meat Science*, vol. 78, no. 3, pp. 217–224, 2008.

13. A. Cecchinato, M. De Marchi, M. Penasa, A. Albera, and G. Bittante, "Near-infrared reflectance spectroscopy predictions as indicator traits in breeding programs for enhanced beef quality," *Journal of Animal Science*, vol. 89, no. 9, pp. 2687–2695, 2011.

14. B. Leroy, S. Lambotte, O. Dotreppe, H. Lecocq, L. Istasse, and A. Clinquart, "Prediction of technological and organoleptic properties of beef longissimus thoracis from near-infrared reflectance and transmission spectra," *Meat Science*, vol. 66, no. 1, pp. 45–54, 2004.

15. N. Prieto, S. Andrés, F. J. Giráldez, A. Mantecón, and P. Lavín, "Ability of near infrared reflectance spectroscopy (nirs) to estimate physical parameters of adult steers (oxen) and young cattle meat samples," *Meat Science*, vol. 79, no. 4, pp. 692–699, 2008.

16. N. Prieto, D. Ross, E. Navajas, G. Nute, R. Richardson, J. Hyslop, G. Simm, and R. Roehe, "On-line application of visible and near infrared reflectance spectroscopy to predict chemical-physical and sensory characteristics of beef quality," *Meat Science*, vol. 83, no. 1, pp. 96–103, 2009.

17. M. Kamruzzaman, G. ElMasry, D. W. Sun, and P. Allen, "Prediction of some quality attributes of lamb meat using near-infrared hyperspectral imaging and multivariate analysis," *Analytica Chimica Acta*, vol. 714, pp. 57–67, 2012.

18. T. Qiao, J. Ren, C. Craigie, J. Zabalza, C. Maltin, and S. Marshall, "Quantitative prediction of beef quality using visnir spectroscopy with large data samples under industry condictions," *Journal of Applied Spectroscopy*, vol. 82, no. 1, January 2015.

19. F. Melgani and L. Bruzzone, "Classification of hyperspectral remote sensing images with support vector machines," *Geoscience and Remote Sensing, IEEE Transactions on*, vol. 42, no. 8, pp. 1778–1790, 2004.

20. J. Zabalza, J. Ren, J. Ren, Z. Liu, and S. Marshall, "Structured covariance principal component analysis for real-time onsite feature extraction and dimensionality reduction in hyperspectral imaging," *Applied Optics*, vol. 53, no. 20, pp. 4440–4449, 2014.

21. J. Zabalza, J. Ren, M. Yang, Y. Zhang, J. Wang, S. Marshall, and J. Han, "Novel folded-pca for improved feature extraction and data reduction with hyperspectral imaging and sar in remote sensing," *ISPRS Journal of Photogrammetry and Remote Sensing*, vol. 93, pp. 112–122, 2014.

22. P. Williams and K. Norris, *Near-infrared technology in the agricultural and food industries*. American Association of Cereal Chemists, Inc., 1987.

Near-infrared optical spectroscopy of sugar-based mixtures – A snapshot to identify issues of influence

Laurent Boulley,[1] Henning Schulte[2] and Jean-François Pierson[1,3]

[1] Mines Nancy Graduate School of Engineering - Université de Lorraine
Campus Artem, 54042 Nancy Cedex, France
[2] Fraunhofer Institute of Optronics, System Technologies and Image Exploitation
Fraunhoferstraße 1, 76131 Karlsruhe, Germany
[3] Institut Jean Lamour (UMR CNRS 7198) - Université de Lorraine
Parc de Saurupt, 54011 Nancy Cedex, France

Abstract Optical spectroscopy is one method used to identify products and ingredients in food industries. This article presents a review of the literature concerning carbohydrates spectra (especially sugar) and compares it to the results that can be obtained with standard hyper spectral imaging (laboratory equipment). The possibility to identify sugar in mixtures is also investigated. The near infrared region is the most accurate to qualitatively detect the presence of sugar. A differentiation between different types of sugar seems not to be possible with the equipment, because of too small differences and the overlap of absorption bands.

1 Introduction

Nowadays the use of spectral signatures is more and more usual in food industries. It is already known how to detect other nutrient families such as proteins [1] or fat [2]. Challenge is the wide application of this technology with a standard measurement equipment. Influences, such as the various reflection of organic products, the needs for a comparable calibration, and the different types of sensors are only some of factors, that need to be taken into account. In the literature, the spectral signatures of products or their ingredients are mostly shown as a function of

their mean and the knowledge about the dispersion of values in measurements becomes more important.

As a snapshot, we did within the laboratory of Fraunhofer IOSB a study, focusing on sugars and carbohydrates. This was undertaken, in order to gather the results already published in the literature and to compare them with those obtained with our own measurements. The aim was to evaluate the possibility of standard optical spectroscopy to detect and characterize especially carbohydrates and sugars. This finding may be a significant advantage for the food-processing industry.

2 Current status of research

Materials and matter interact with the electromagnetic field, atoms can respectively absorb and emit once again photons with the energy $h * \nu$ where h is the Planck's constant and ν is the frequency of the electromagnetic radiation. With the hyper spectroscopy method, cameras take a 2D picture of the sample for each wavelength of the device spectrum that is the "third dimension" of the shot. [3] All the images of this "hyper spectral cube" are then segmented to separate the different parts of the image and analyzed with the software developed at the Fraunhofer Institute IOSB. The reflection spectra obtained in UV, visible or IR areas with a material are specific to this material and constitute its "spectral signature".

The far-infrared area is not here studied, because it can only be evidenced by Fourier transform infrared spectroscopy. In the infrared region, the incident radiation makes the atoms in the molecules rotate and vibrate leading to a rotation-vibration absorption spectra. In the mid-infrared (MIR) region, the stretching and deformation modes give the fundamental absorption bands. In the near-infrared (NIR) range, harmonics, overtones and combinations of fundamental stretching bands are visible. [4, 5] In the visible and the ultraviolet areas, the electronic transitions appear and require much energy from the photons of the incident beam.

Optical spectroscopies bring relevant information about the structure of molecules. NIR spectroscopy is basically chosen instead of visible or ultraviolet spectroscopies, because it gives better results and is very simple of use. This method is rapid, relatively precise, cheap, and non-

destructive. [5, 6] Several studies have already been done on carbohydrates to find the specific absorption peaks of sugars. According to Robert and Cadet, [4] these specific wavelengths are related to the C-H, O-H, C-O and C-C bonds. The region 1100nm-1800nm is linked to the first and second harmonics of the O-H and C-H stretching frequencies, whereas the 1800-2500nm area corresponds to the combination bands of the O-H and C-H stretch. [4, 5] The most accurate wavelengths for monosaccharides are 1457nm (first harmonic O-H stretching), 2062nm (combination of O-H stretching and deformation), 2263nm (O-H and C-C stretching) and 2440nm (C-H and C-C stretching) and for oligo and polysaccharides, they are shifted to 1432nm, 1931nm, 2310nm and 2477nm, as confirmed by the graphs of Henry [7–9].

In the agri-food sector, NIR spectra contain a lot of information about internal and external properties of fruits, such as sugar content, total acidity, pH, soluble solid contents, dry matter, firmness and bruises. [5] NIR spectroscopy is often used to check if fruits or vegetables are green or rotten, to detect surface defects and is also employed to check the sugar concentrations for instance in apples [10, 11], oranges [12, 13], mango [14], kiwifruits [15], sugar beet [16], jujube [17], onion [18], potato tubers [19] but also in fruit juices [20], wine [21] or cakes [22].

Besides, UV spectroscopy requires much more energy so that spectral effects are only detected on gamma-irradiated sugar in water solutions with a peak in the region 260nm-280nm, especially at 267nm for sucrose according to Yordanov, Gancheva and Georgieva and the intensity of the peak is proportional to the gamma-rays absorbed dose. This is due to free radicals created in sugar during irradiation [23–25].

3 Equipment and Methods

For these measurements the spectroscopic equipment of Fraunhofer IOSB was used. A spectral workbench (spectral characterisation with image analysis from UV to NIR, 240 - 2500nm) and a database (including a software for first analysis) were available. This database allowed the study of different parameters of the registered spectra, such as the pixel intensity of the camera, the average value of the sample reflection intensity, the derivative intensity or a filtered intensity versus wavelength. For this study the NIR domain (750nm - 2500nm) has been the

main focus, because of the specific energy reflection within this area. We have also checked that the UV and visible areas did not bring any relevant information. Advantage of the database with its integrated software is the possibility to compare the raw spectra with those out of the database. This way, unknown materials can be investigated and the similarity with the already retained data can be calculated with algorithms with several methods.

The calibration of the devices was made by a 'white plastic reference', which was measured before each experiment. It gave the reference intensity in the calculation of the reflection index. A reflection intensity was then measured after the absorption in the material. If I_0 is the incident reference intensity, I_n the dark current, obtained without any light and I_{sample} the intensity reflected by the sample, the normalized reflection index R is:

$$R = \frac{(I_{\text{sample}} - I_n)}{(I_0 - I_n)} \tag{3.1}$$

The absorption coefficient is then:

$$\alpha = log(\frac{1}{R}) \tag{3.2}$$

On the spectra, absorption matches convexe parts of the reflection curve.

Sugar in mixtures was investigated in the 1050 – 2450nm range. To get rid of the influence of the color, only white materials where used. Commercial powdered sugar was mixed with only one other extra material: commercial flour and gypsum respectively. The different proportions were 0% extra material-100% sugar, 20% extra material-80% sugar, 40% extra material-60% sugar, 60% extra material-40% sugar, 80% extra material-20% sugar, 100% extra material-0% sugar. The influence of sugar in the spectra of more complex mixtures was then examined in commercial candies with edible gelatin and biscuits.

4 Results and Findings

Analysis of results shows that it is possible to detect the presence of carbohydrates in mixtures using NIR spectroscopy. Problems with color

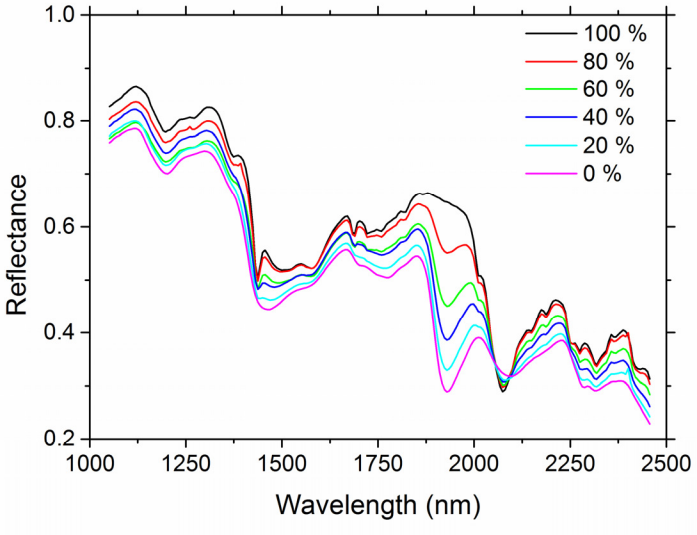

Figure 3.1: Reflectance spectra of sugar - flour mixtures: The percentages given are sugar mass percentages for a constant mass of the sugar-flour mixture.

appear in the visible area and too much energy is required in the ultraviolet one. The results reveal that the relevant wavelengths for sugars depend on the type of bonds, the atoms involved and the geometry (conformation, steric space). The wavelengths can therefore vary in small range from one sugar to another and it is preferable to speak of specific bands. There are mainly two types of influence in measurements with optical spectroscopy, on the one hand from the products and on the other hand from the measurement itself.

Figure 3.1 represents the reflectance spectra for several samples containing a decreasing quantity of sugar and an increasing quantity of flour for a constant total mass. Each one was scanned and the mean value of the reflected light intensity was calculated for each wavelength of the spectra. The graphs reveal that the rise in sugar concentration is linked to an increase in the reflection ratio. More precisely, the spectra obtained indicate that there is a continuous evolution between the

sugar concentrations in the samples and the areas of the concave parts of the curves. The more sugar there is, the more absorption occurs and the bands are really pronounced. The absorption bands characteristic of sugar are located approx. at 1200nm, 1437nm, 2074nm and 2320nm. This result is very close to that of Robert and Cadet [4] and it is really noticeable on the 100% sugar - 0% flour curve. Another trend is that there is a decrease in reflectance when the wavelengths go higher [4, 8].

Besides, the band located at 1930nm that increases with the flour contain is related to water absorption. Then, it can not be taken into account to detect sugar in mixtures. In fact, water absorbs a lot in specific regions, hydrogen bonding creating clusters of water molecules. This phenomenon can hide the carbohydrates bands [26]. Previous studies showed that water molecules without OH group bonded absorbs at 1160nm, those with one OH group with H-bonded absorb at 1200nm, those with two OH with H-bonded absorb at 1250nm and the combination band of water is located in the 1800-2100nm range [27]. In addition, the intensity of water peaks depends also on the external conditions of the surrounding air and on the hygrometry rate.

Figures 3.2 and 3.3 confirm the localization of the carbohydrates peaks. They show similarly to the previous figure the evolution of the reflection ratio for several concentrations in sugar and gypsum and in flour and gypsum respectively.

Convexe parts are visible on the curves in figures 3.2 and 3.3 because of the presence of carbohydrates and water. In the sugar and gypsum mixtures, the bands 1200nm, 1437nm, 2074nm and 2320nm are still fine enough in the samples containing sugar, whereas there is just the influence of water on the curve 0% sugar - 100% gypsum due to the inorganic nature of gypsum. In our experiment, the influence of water appears mainly around 1915nm and the higher its absorption is, the less dissociable the other spectral effects are. In the flour and gypsum mixtures, the sugar bands 1200nm, 1437nm, 2074nm and 2320nm are softened in flour, which contains many other components. Water absorption bands are really visible in gypsum, more than in flour that is dry.

Nevertheless, it is not possible to distinguish various sorts of sugars, for instance make a difference between the saccharose of the powdered sugar and the numerous carbohydrates present in flour. The carbohydrates curves remain global because the precision about the wavelengths is not sharp enough, due to the infrared camera resolution (6nm)

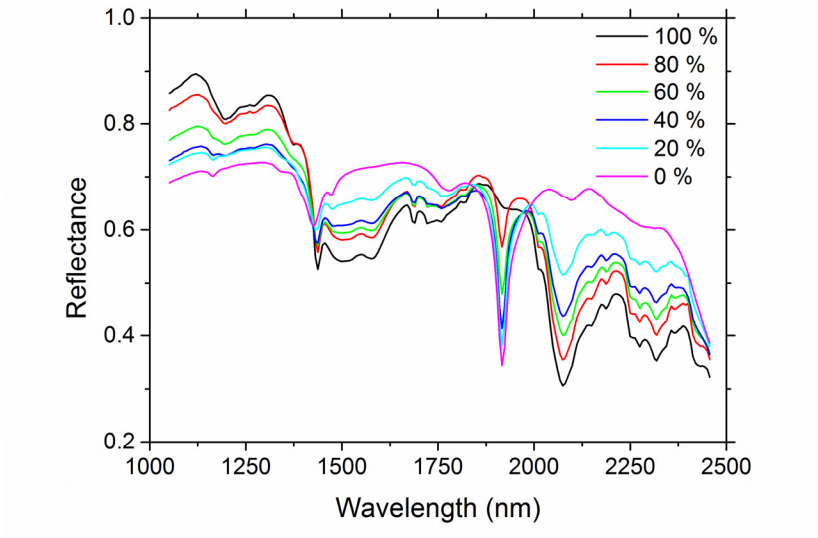

Figure 3.2: Reflectance spectra of sugar - gypsum mixtures: The percentages given are sugar mass percentages for a constant mass of the sugar-gypsum mixture.

and because near-infrared spectroscopy contains much information that is often overlapped in mixtures and complex heterogeneous materials. Moreover, some differences can appear according to the crystalline, liquid or dry form of the sugars [26]. Some variables can also affect the measurements, such as the lightning and light-scattering but also the white balance and the precision of the apparatus itself. Data processing and analysis is therefore required and a second-derivative calculation can give better results and refine the small differences between the spectra [12, 15].

5 Summary

Optical spectroscopy allows to detect the presence of carbohydrates like sugar. But the device used cannot distinguish between the vari-

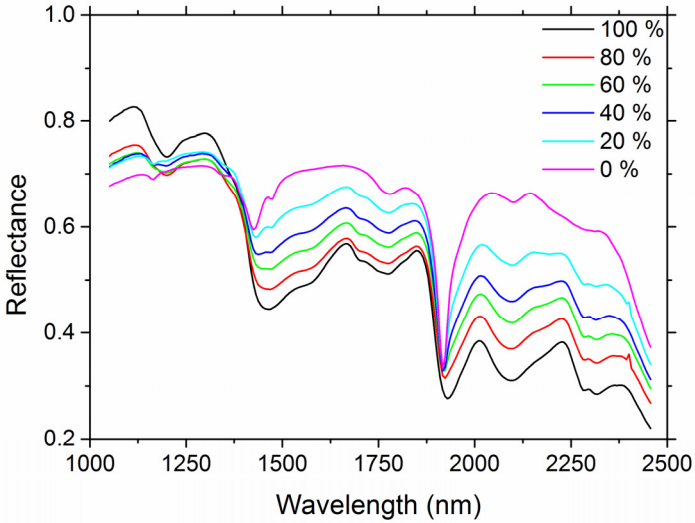

Figure 3.3: Reflectance spectra of flour - gypsum mixtures: The percentages given are flour mass percentages for a constant mass of the flour-gypsum mixture.

ous molecules of sugar, because of too little difference between specific carbohydrates peaks. NIR spectroscopy gives good results about the characteristic absorption bands of sugars, which are 1200nm, 1437nm, 2074nm and 2320nm. The dispersion of experimental values and the resolution of the machine remain an additional challenge. Important is the consideration of absorption due to water around 1915nm. The level of moisture influences directly the dynamics of spectral signatures. The identification of specific signatures of sugars can be very useful for rapid detection in the industrial sector.

References

1. S. Bruun, I. Søndergaard, and S. Jacobsen, "Analysis of protein structures and interactions in complex food by nearinfrared spectroscopy. 1. gluten

powder,," *JOURNAL OF AGRICULTURAL AND FOOD CHEMISTRY*, no. 55, no 18, pp. 7234–7243, 2007.

2. D. L. Pazdernik, A. S. Killam, and J. H. Orf, "Analysis of amino and fatty acid composition in soybean seed, using near infrared reflectance spectroscopy," *Agronomy Journal*, no. vol. 89, no. 4, pp. 679–685, 1997.
3. J. M. Amigo, I. Martí, and A. A. Gowen, "Hyperspectral imaging and chemometrics," in *Data Handling in Science and Technology*, 2013, vol. 28, pp. 343–370.
4. C. Robert and F. Cadet, "Analysis of near-infrared spectra of some carbohydrates," *Applied Spectroscopy Reviews*, vol. 33, no. 3, pp. 253–266, 1998.
5. H. Lin and Y. Ying, "Theory and application of near infrared spectroscopy in assessment of fruit quality: a review," *Sensing and Instrumentation for Food Quality and Safety*, vol. 3, no. 2, pp. 130–141, 2009.
6. J. T. Alander, V. Bochko, B. Martinkauppi, S. Saranwong, and T. Mantere, "A review of optical nondestructive visual and near-infrared methods for food quality and safety," *International Journal of Spectroscopy*, vol. 2013, no. 3, pp. 1–36, 2013.
7. Lester P. KUHN, "Infrared spectra of carbohydrates," *Analytical Chemistry*, vol. 22, no. 2, pp. 276–283, February 1950.
8. R. J. Henry, "Near-infrared reflectance analysis of carbohydrates and its application to the determination of (1→3),(1→4)-β-d-glucan in barley," *Carbohydrate Research*, vol. 141, no. 1, pp. 13–19, 1985.
9. Y. Ying and Y. Liu, "Nondestructive measurement of internal quality in pear using genetic algorithms and ft-nir spectroscopy," *Journal of Food Engineering*, no. vol. 84, no. 2, pp. 206–213, 2008.
10. Y. Ying, Y. Liu, J. Wang, H. Jiang, B. Culshaw, M. A. Marcus, J. P. Dakin, S. D. Crossley, and H. E. Knee, "Non-destructive measurement of sugar content in fuji apple with bifurcated fiber optic sensor," pp. 263–272. [Online]. Available: http://proceedings.spiedigitallibrary.org/proceeding.aspx?articleid=834235
11. E. Bobelyn, A.-S. Serban, M. Nicu, J. Lammertyn, B. M. Nicolaï, and W. Saeys, "Postharvest quality of apple predicted by nir-spectroscopy: Study of the effect of biological variability on spectra and model performance," *Postharvest Biology and Technology*, vol. 55, no. 3, pp. 133–143, 2010.
12. Weijie Li, Pierre Goovaerts, Marc Meurens, "Quantitative analysis of individual sugars and acids in orange juices by nir spec. of dry extract," *Journal of Agricultural and Food Chemistry*, vol. 44, no. 8, pp. 2252–2259, 1996.

13. C. Luo, Xue,, Long, M. Liu, J. Li, and X. Wang, "Nondestructive measurement of sugar content in navel orange based on vis-nir spectroscopy: Ifip international federation for information processing, 4th ifip tc 12 conference, ccta," *Computer and Computing Technologies in Agriculture IV*, vol. Part 1, no. Springer, pp. 467–473, 2011.

14. A. A. Munawar and I. W. Budiastra, "Non destructive inner quality prediction in intact mango with nir spectroscopy."

15. Slaughter, D.C., and C.H. Crisosto, "Nondestructive internal quality assessment of kiwifruit using near-infrared spectroscopy," *Semin. Food Anal.*, no. 3, pp. 131–140, 1998.

16. Y. Roggo, L. Duponchel, and J. Huvenne, "Quality evaluation of sugar beet (beta vulgaris) by near-infrared spectroscopy," *JOURNAL OF AGRICULTURAL AND FOOD CHEMISTRY*, no. vol. 52, no. 5, pp. 1055–1061, 2004.

17. S. Zhang, "Robust model of fresh jujube soluble solids content with near-infrared (nir) spectroscopy," *AFRICAN JOURNAL OF BIOTECHNOLOGY*, vol. 11, no. 32, 2012.

18. D. Vincke, V. Baeten, G. Sinnaeve, P. Dardenne, and Fernández Pierna, Juan Antonio, "Determination of outer skin in dry onions by hyperspectral imaging spectroscopy and chemometrics," *NIR news*, vol. 25, no. 2, p. 9, 2014.

19. J. Y. Chen, H. Zhang, Y. Miao, and M. Asakura, "Nondestructive determination of sugar content in potato tubers using visible and near infrared spectroscopy," *Japan Journal of Food Engineering*, 2010.

20. S. N. Jha and S. Gunasekaran, "Authentication of sweetness of mango juice using fourier transform infrared-attenuated total reflection spectroscopy," *Journal of Food Engineering*, vol. 101, no. 3, pp. 337–342, 2010.

21. Martelo-Vidal, M. J. and M. Vázquez, "Evaluation of ultraviolet, visible, and near infrared spectroscopy for the analysis of wine compounds." *Czech Journal of Food Sciences*, no. 32(1), pp. 37–47, 2014.

22. B. G. Osborne, T. Fearn, and P. G. Randall, "Measurement of fat and sucrose in dry cake mixes by near infrared reflectance spectroscopy," *Journal of Food Technology*, vol. 18, pp. 651–656, 1983.

23. N. D. Yordanov, V. Gancheva, and E. Georgieva, "Epr and uv spectroscopic study of table sugar as a high-dose dosimeter."

24. N. D. Yordanov and E. Georgieva, "Epr and uv spectral study of gamma-irradiated white and burned sugar, fructose and glucose," *Spectrochimica Acta Part A: Molecular and Biomolecular Spectroscopy*, vol. 60, no. 6, pp. 1307–1314, 2004.

25. Y. Karakirova, N. D. Yordanov, H. d. Cooman, H. Vrielinck, and F. Callens, "Dosimetric characteristics of different types of saccharides: An epr and uv spectrometric study," *Radiation Physics and Chemistry*, vol. 79, no. 5, pp. 654–659, 2010.

26. R. Giangiacomo, J. B. Magee, G. S. Birth, and G. G. Dull, "Predicting concentrations of individual sugars in dry mixtures by near-infrared reflectance spectroscopy," *JOURNAL OF FOOD SCIENCE*, vol. 46, 1981. [Online]. Available: http://onlinelibrary.wiley.com/doi/10.1111/j.1365-2621.1981.tb04903.x/pdf

27. R. Giangiacomo, "Study of water–sugar interactions at increasing sugar concentration by nir spectroscopy," *Food Chemistry*, vol. 96, no. 3, pp. 371–379, 2006.

Utilization of spectral signatures of food for daily use

Henning Schulte,[1] Gunnar Brink,[1] Robin Gruna,[1] Reinhard Herzog[1] and Heinrich Grüger[2]

[1] Fraunhofer IOSB, Fraunhoferstr. 1, 76131 Karlsruhe
[2] Fraunhofer IPMS, Maria-Reiche-Str. 2, 01109 Dresden

Abstract The analysis of spectral signatures of materials is an established technology in biochemistry and analytical chemistry. This includes the identification of different materials and some of their ingredients. A common method used is optical spectroscopy. Optical spectroscopy refers to the visible effects caused by the interaction of matter with electromagnetic radiation. Because each element has its own specific energy reflection within different wavelengths, the identification of materials or material families is generally possible. With respect to the availability of sensors, the greatest opportunity for the broad use of this technology is expected in the wavelength of NIR. Given the complexity of reliable identification and verification of spectral signatures of a product, the three aspects that must be minimally considered are as follows: the product itself, the necessary sensors, and the evaluation of the obtained data. Special attention must be paid to the measurement itself, the reflection of the material, and the calibration of the measurement arrangement. There is information available about organic and inorganic products and their spectral reflection within near infrared (NIR). Within our focus of research, existing information related to food is mostly about products and their quality, especially, microbial spoilage, freshness, and ripening. Meat, fruits, and dairy are the most analyzed products in this wavelength region. The quantity of sugar, carbohydrates, and fat is essential for the investigations related to nutrients in a product.

The major trend in the area of sensors (for optical spectroscopic measurements) is the miniaturization and integration of functions, separating out expensive assembly needs. On the other

hand, there is a need for increasing performance. Resolution and wavelength have to match the applied chemometric models with an acceptable signal-to-noise ratio. The availability of new, better, and cheaper spectral sensors will directly influence the market of automated sorting technology. The current focus is on simple and standardized solutions that use sensor technology within the wavelength of visible light. Chinese manufacturers, especially, play an increasingly important role in this development.

To gain all this new scientific knowledge, a broad, sophisticated community of scientists with their institutes is necessary. All of them are connected via a global virtual science network. A key question is an understanding of the primary drivers and the outlook for a future infrastructure. Besides spectral information, one way to gain additional information about products is to combine them, e.g., with volume knowledge.

1 Introduction – Background

There is an increasing desire to identify the chemical composition of different materials stemming from a variety of sources such as industry, consumers, and science. This motivates a broad community of scientists to find simple solutions for such a complex question. Optical spectroscopy might actually be the most promising approach to identify products and provide a higher transparency of their ingredients. A great potential for compact analysis of food and their ingredients lies in optical methods, especially in optical spectroscopy. Based on our analysis of various publications, we can summarize that to acquire complex information, measured data has to be related to other acquired data. For this purpose, a verified database and a calibrated measurement are required. However, given the complexity of secure identification and verification of spectral signatures of products, there are at least three views that must be considered: the actual products, sensors, and the evaluation of required data. Figure 4.1 shows the connection between these fields and the influencing factors.

Products, sensors, and evaluation cannot be analyzed without considering their intrinsic interdependencies and mutual influence on each other. This is described by reflection, calibration, and measurement. Nevertheless, the physical characteristics of products are given. Even

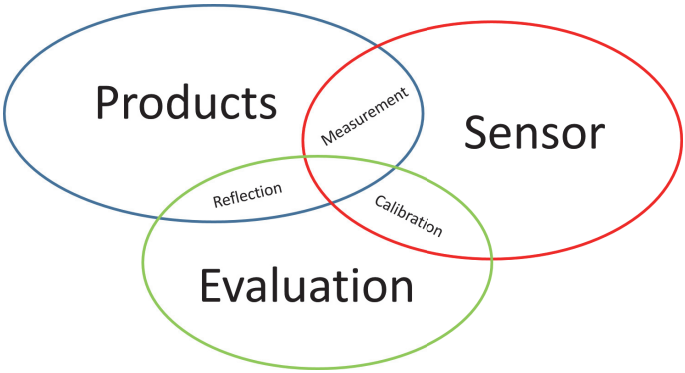

Figure 4.1: Context of Products, Sensor and Evaluation

if lots of scientists do research on this subject, the basis of the results is still the same. As a result, the different measurements are comparable. Currently, there is a single evaluation for each question. This is due to the variances in reflection of products and several challenges in the calibration of measurement.

In general, "spectral analysis" refers to the analysis of the interaction of electromagnetic radiation with a sample by detecting specific changes in the distribution of the intensities ("spectrum") of radiation reflected from the sample. Depending on the sample, this analysis might be performed in a transmission, a reflection, or a transflection setup. Physical effects are well understood. Interaction of optical radiation with solids, fluids, or gases changes the energy state of the respective molecules. The molecules or parts of them can be set into vibration depending on their properties and the properties of the radiation. For analytical purposes, vibrational transitions in the NIR range are useful. The absorption of radiation energy at specific regions or wavelengths allows the specific detection of functional groups in molecules within this range. Due to their characteristic absorption bands, the NIR technique allows the specific determination and quantification of a wide range of organic and inorganic compounds.

2 Application of NIR Spectroscopy

Today near infrared spectroscopy is amongst the most versatile and widely used methods for analytic monitoring of organic products. However, a major challenge for measurements is calibration and validation. This requires a comparison of results, which may be one of the reasons that optical spectroscopy is still not in a broad commercial use.

We note some NIR example applications below. They give an overview of the products and substances that can be monitored. In general, meat and dairy are the most analyzed products for measurements with NIR technology. Within the focus of our research, information is available primarily around products and their quality; especially, microbial spoilage, freshness, and ripening. The quantity of sugar, carbohydrates, and fat is essential for the investigations related to nutrients in a product (see Fig. 4.2).

- Fish: There are many spectral investigations about fish. Salmon is one of the most investigated species. NIR measurement gives information about freshness and quality. In addition, information on fish filet is available, which includes the structure of the filet and the presence of fish bones in it [1–6].

- Meat: Investigations on meat with optical spectroscopy show that the rudiments for the identification of different kinds of meat are available. In addition, there are solutions to distinguish differences in fat, salt, and moisture content. Water and raw proteins can be measured with acceptable reliability. Judging the freshness of meat can be problematic. This is due to of the varying consumption patterns surrounding the different types of meat—hung beef is better than fresh beef, however, elder poultry is not palatable [7,8].

- Dairy: Fat, protein, dry mass, lactose, and solids non-fat (SNF) are routinely measured in milk, cheese, and yogurt samples by Fourier transform infrared spectroscopy (FT-IR). However, these measurements are increasingly transferred to NIR analysis, since only one analytical device is needed when using this technology [9,10].

- Beverages: For beverages, the primary area of interest is around the classification of alcohol content. In addition, information is available on sugar and acid content as well. Furthermore, the quantification of carbohydrates and classification of caffeine content in tea is also investigated [11,12].

- Fruits: In general, NIR measurements are used for analysis of internal bruising, ripening, and quality protection of fruits. In addition, herbicide residue, microbial quality, and verification of origin are also important [13,14].

- Vegetables: Detection of skin-defects, maturity prediction, and sugar content are key areas of investigation. Tomato is the most investigated vegetable; in addition, potatoes and beans are also well investigated, similar to many other plants [15,16].

- Grain: When grains are measured with NIR techniques, the areas of interest are protein in hard red spring wheat, prediction scab, vonistoxin and egosterol in single wheat kernels, general quality, fungicide treatment, classification, and fusarium damage [17,18].

- Nutrients: The identification of nutrients with NIR spectroscopy is a relatively new field of investigation. There is advanced knowledge available on nutrients in milk and meat, especially fat and protein. Fat is measured by NIR techniques in salmon, oil, and meat. Protein is measured in beans, oils, dairy products, and other foods. Minerals and vitamins continue to be a challenge. The measurement of water content with optical spectroscopy is especially troublesome because of the absorption functionality of water [19,20].

3 Global Structure of Scientific Activities

In summary, optical spectroscopy method is important. Given the complexity in finding reliable information and verifying the spectral signatures of products, most scientific activities that use this method are driven by questions around the aspects of product, sensor, or evaluation. On the other hand, the financial aspects have considerable impact.

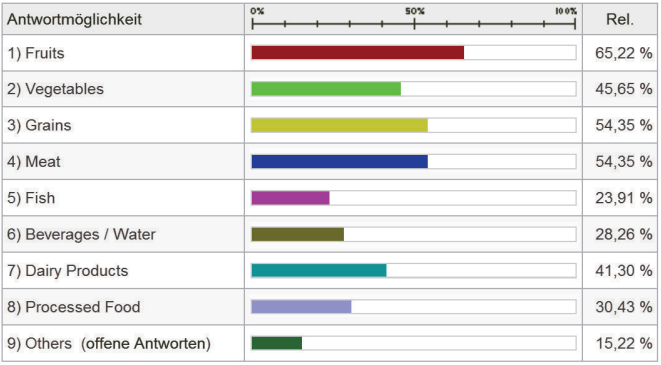

Figure 4.2: The sorts of products Science Institutes work with. Answers out of Online-Survey; 2014 Fraunhofer IOSB.

These are covered from science policy along with the business promotion services of their countries. We see lots of small teams all over the world pushing technical progress in this field. A survey, conducted by Fraunhofer IOSB, showed that most institutes employ less than 10 scientists, who work on the field of spectral food analysis with optical spectroscopy. In addition, all of them are connected due to a virtual science network. Their field of interest is often related to the local influences. For example, there are special government programs or related customers with special questions. In most cases, products are the focus. The question of components is an emerging area of scientific research (Figures 4.3).

- **Europe** – Europe , the challenge is that every region tries to influence their local institutes. Combined with the huge influence of assistance in agriculture by the European Union, this aids individualization of institute's activities. Many scientists have their own specialization even though from an industrial perspective, the problems are solved.
- **USA** - Research in the United States is dominated by the influence of the United States Department of Agriculture (USDA). More than a quarter of all science publications are directly developed with a collaboration with them. The amount of indirect influence

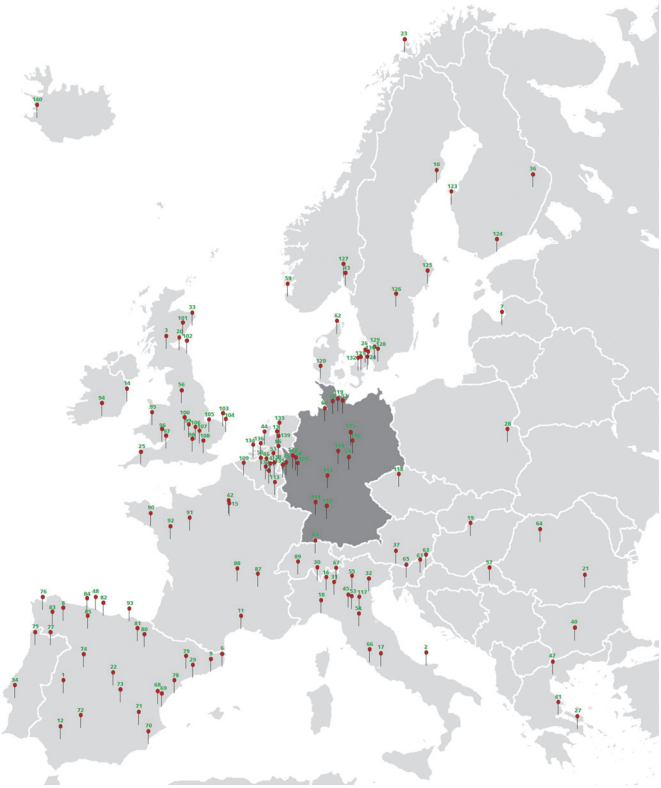

Figure 4.3: Institutes in Europe.

(e.g., by financing programs where USDA is not named in publications) cannot be evaluated.

- **China** – China has seen significant development in the last few years. Starting this century, China's education campaign has resulted in an increasing number of publications, guest students from all over the world, and highly sophisticated industry products. We expect that within a short period of time, many findings in spectral technologies will come from the Chinese science community.

- **Others** - All over the world, there are science activities that use optical spectroscopy for several tasks. This usually relates to questions around local agriculture. However, this might change directly, due to the availability of cheaper sensors or more forward looking infrastructure.

4 Cooperation Between Institutes / Nations

The virtual science network in use with optical spectroscopy is based on several hubs. Publications help link these hubs. First, there is the international education of young people, from guest students to PhD students. The proof of their skills lies in the quality and quantity of their publications. A case study of Fraunhofer IOSB shows that more than a tenth of all publications within the field of optical spectroscopy for food analysis are joint papers written by authors across international boundaries. Another hub is the international conferences, together with the link "publications." There are international conferences held on optical spectroscopy of food nearly every month of the year somewhere in the world. Remote sensing and analysis of other materials have their own conferences for a more complete discussion of that topic. Nevertheless, cultural and language borders still hinder collaboration. For the future, this is a huge challenge and opportunity (see Fig. 4.4).

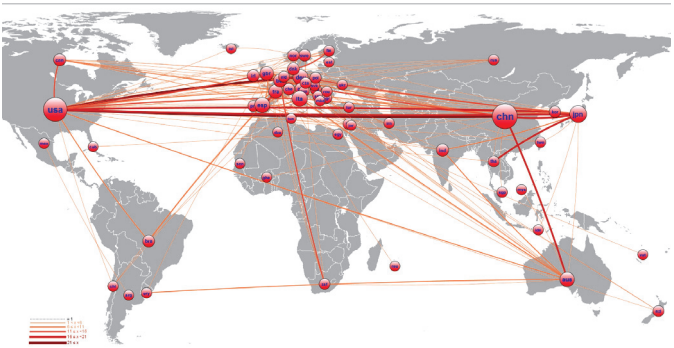

Figure 4.4: Analysis Result out "Web of Science"; 2000-2014 with Threshold 2.

5 Future of Spectral Sensors

Future devices, systems, and applications have to be considered in a chronological order. First, products and applications targeted for the near future timeframe—within the next two years—must be based on existing components. Next for the intermediate timeframe of 3–5 years, new devices will be developed based on existing technologies. Finally, for a farther out timeframe of five years or more, we expect there to be new technologies and principles at play. The most relevant issues for the broad use of optical spectroscopy are price, size, and performance of the spectrometer. In addition, user friendly software and online access to data services must be available. Integration with other components of the host system is useful, for example, by correlation of the spectral data with the evaluation of a regular image from a camera, which is available in almost every mobile system today. Currently, the components in use are primarily photo diode detector arrays. These provide high resolution for reasonable cost in silicon technology. Detectors for use in the NIR region are more expensive, as InGaAs (indium gallium arsenide) or other sophisticated materials are used. Hamamatsu integrated an entrance slit into a detector chip to realize a thumb size spectrometer, with dimensions 27.6 mm $\times$ 13 mm $\times$ 16.8 mm (www.hamamatsu.com), for the UV to VIS region. The use is limited by the sensitivity of the silicon detector. The etch steps used to generate the slit in the chip are not available for the InGaAs material. Other approaches using active MEMS structures can be used to build spectrometers with single detectors to reduce the price and size. Several scanner mirror devices, DLPs from Texas Instruments (www.dlp.com) and MEMS scanning grating devices based on a technology invented and patented by Fraunhofer IPMS [21] are currently available. Spectrometers have been realized (www.hiperscan.com) and announced (SCiO, TellSpec). Currently, the size and price of existing systems is high, and further miniaturization in progress. In the near future, new devices will enable more miniaturized systems for NIR that also have potential for low cost production in high volume [22,23]. A scanning grating chip with integrated slits is used to realize a first prototype of a hybrid integrated spectrometer. The size of the optical bench is approximately 19 mm $\times$ 11 mm $\times$ 10 mm. It measures in the NIR from 950 nm to 1900 nm. DLP based systems can be improved if new light modulators are optimized for spectroscopy in-

stead of projection systems. In addition, progress for fixed grating spectrometer is possible if hybrid chips for optical microstructures and NIR sensitive detector materials can be achieved. Price reduction of InGaAs detectors can enable array detectors with adjusted filters on top for a reasonable cost. Once it becomes possible to tune silicon based detectors for the NIR, the fixed grating approach will get affordable for high volume production. Alternatively, existing detector technologies may be available in a larger area for less cost once production shifts to 6″, 8″, or larger substrates. Furthermore, tunable light sources can open inverse spectroscopy using the generation of tailored light with adjustable spectral properties. Distributed feedback (DFB) semiconductor laser, quantum cascade laser, or tunable incoherent light sources (Patent DE 10 2009 046 831.5) are promising candidates; however, they need technical and commercial development.

Outlook for spectral sensor systems: Depending on user popularity, spectral sensors may develop in the same manner as a digital camera. Once the device becomes standard in mobile systems and platforms, applications and services will grow around it. Food analysis is a major issue. The ideas around this topic go well beyond food and into other kinds of organic matter. Some examples are a "Paint Checker" for preowned car repair detection or counterfeit detection by integration of a hidden marker; for example, fluorescence, into brand logo.

6 Sorting Technology

An optical sorter is a machine that compares objects according to user-defined criteria, recognizes and eliminates flawed and foreign objects from production, and separates products of different grades [1, 2]. Depending on the implemented sensors and the intelligence of the applied sorting algorithm, selection criteria can be chosen amongst color, size, shape, biological properties, and the chemical composition of the sorting objects. In principle, there is a wide variety of applications for optical sorting machines. In the context of steadily increasing requirements on food quality in recent years, optical bulk sorting has become an indispensable technology within the food industry. In addition, optical sorting is gaining increasing importance in the recycling and mining market [24]. Sorting of food products is the most mature, and by far

the largest of the three above mentioned segments (see Fig. 4.5). Based on interviews with experts, we expect that by the year 2018, the food sorting market will have a share of almost 83% of optical sorting [3]. However, due to its advanced level of maturity, market penetration and adoption in the food sector is already relatively high. Consequently, the annual growth average of about 7% is relatively low. As a result of the increase in population and the growing demand among the burgeoning middle class in BRIC countries, the greatest potential for growth can be realized in emerging markets. A further peculiarity about the food sorting market is the fact that the great variety of different foods requires complex and customized sorting solutions [4]. For instance, there are more than 50 different types of nuts. Optical food sorting can determine and select based on properties as different as the content of water, oil, chlorophyll or toxin (e.g., Aflatoxin) present in food. Furthermore, there is a need to measure from the softness in blueberries to the presence of sugar in wine grapes [5–7,25]. Thus, a "one size fits all" solution does not exist. The most traditional area of food sorting is the sorting of grains. Today, approximately 40% of the annual global sales revenues in the food sorting market are generated by sorting seeds and kernels, as well as nuts and dried fruits. Processed fruits and (fresh) vegetables hold a 30% share of sales. Finally, fresh fruits comprise 25% of the revenues, and other commodities take the remaining 5%. With an annual growth rate of 8% and an estimated market share of 14% in 2018, we see the recycling segment as the second largest business in the food sorting market. As a consequence of the global consumption growth and the high costs for manual sorting due to increasing labor costs in emerging markets, the demand for automatic sorting systems continues to grow. Moreover, only a negligibly small proportion of the global municipal solid waste is recycled. Thus, the greatest opportunities for growth are expected in developing countries. Sorting of raw materials is the most recent segment with an estimated market share of 3% by 2018. However, companies in this area expect a growth rate of 15%, which implies that the mining market is also a rapidly growing sector.

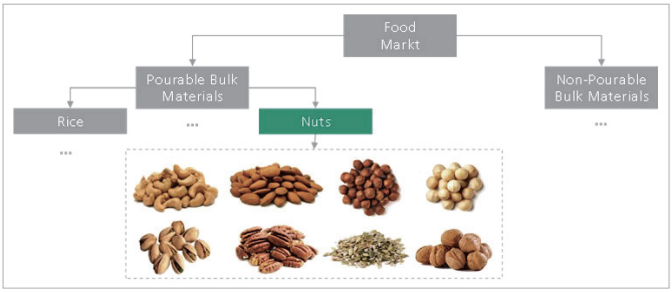

Figure 4.5: Sorting of foods is a diverse field. The transport of goods and the selection criteria vary significantly based on the kinds of goods sorted and require different specialized machinery.

7 Evaluation

In general, molecular spectroscopic methods provide potential solutions to address many food-related questions. The technique is fast and provides real time information via at-, on-, and in-line testing. It is cost-effective, no chemicals or solvents are needed, and generally minor sample preparation is necessary.

The potential factors that have an impact on spectroscopic NIR method performance are as follows:

- Environmental influences (temperature, humidity, vibration, power fluctuations)
- Process related factors (solvation state, lot-to-lot variation, excipient variability, water content)
- Physical factors (polymorphism, particle size or shape)
- Instrumental/computer factors (21 CFR11 compliance, IQ or PQ)
- PV for hardware and software
- Sampling factors (location, temperature, frequency)
- Samples factors (temperature, humidity, homogeneity, age, source, matrix)

- Data pre-processing approach
- User training
- Reference method (technology, validity, robustness)

Given these points, a widespread application with a requirement to satisfy any request is adaptable. A solution can be a customized database in combination with a variety of analytical methods and algorithms that are capable of solving specific questions and general issues. However, some ingredients appear poorly in foods; thus, they have a restricting effect on the measurements. In order to use NIR spectroscopy for quantitative and qualitative chemical analysis, a calibration procedure has to be performed. In addition, NIR spectra have to be obtained for each calibration sample on an NIR instrument. In the next step, the relationship between the NIR spectra and the corresponding reference values of the studied parameter are modeled mathematically. This procedure is referred to as NIR calibration and yields an NIR calibration model for the specific parameters of interest [26]. Finally, the validity of the calibration model is checked using independent samples (see Fig. 4.6).

Application-specific calibration is inevitable for any NIR spectroscopy analysis. Chemometrics provide the mathematical and computational tools to create and develop NIR calibration models by data driven means. These include methods and algorithms from multivariate statistics, pattern recognition, and machine learning [27]. Important methods and key techniques in the chemometric workflow are data preprocessing [28], unsupervised techniques [27], supervised classification, multivariate regression, and model validation [29].

8 ICT Vision

Even the most advanced analytical methods for identification and quality inspections of food and beverages rely on context information. Therefore, we can achieve better analytical quality when the provided context information is precise and complete. Fortunately, in modern food production, a large amount of context information is gathered

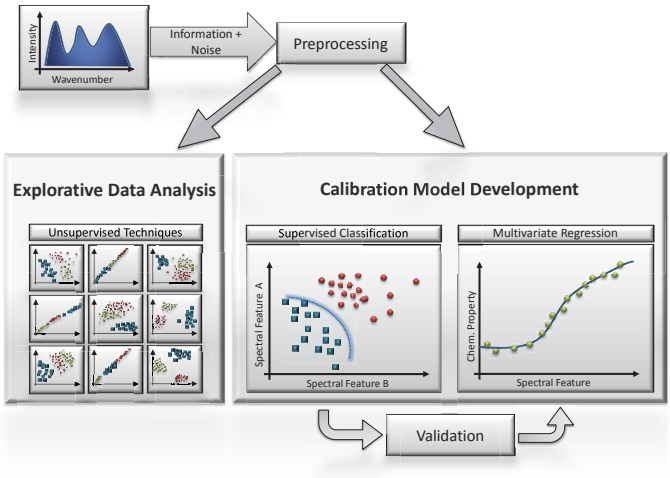

Figure 4.6: Chemometric workflow.

and maintained already. Moreover, with the "Internet of Things"-momentum, we will see an increase in inexpensive and ubiquitous sensors within the production, transportation, and distribution processes. This will also include the final customer and his/her interaction with goods. Information and communication technology (ICT) support for today's complex food supply networks must gather, fuse, combine, exchange, and in general manage many different kinds of data—structural data describing "things" (metadata), observations (sensor data), and data stemming from the business processes themselves (workflow/process data)—in an efficient, transparent, trusted, and quality assuring way (see Fig. 4.7). These are, at the same time, the best sources for complementary context information in order to enable the required analytical capabilities. The current implementations are still a bit stove-piped and there is a need to correlate the information domains. New developments like the open-source middleware OpenIoT provide frameworks to adopt concepts like the "Linked Open Data" into the domain of the internet of things. In the context of spectral signatures and hyper spectral images storage and processing architecture, the existing prototype

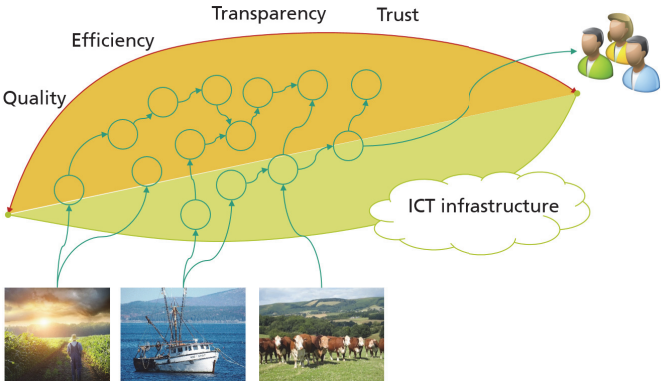

Figure 4.7: Food supply network.

for a hyper spectral database can be considered as a central building block. In order to achieve the ambitious goal of being able to recognize food ingredients and components, other data sources need to be contextualized with the given images. Examples of such data sources are static product-related information (such as barcodes, QR-codes, NFID-codes, etc.), customer-related information (such as personal preferences, calibration settings, etc.), situation/observation related information (such as geo-fencing, scanning history, neighborhood similarity, etc.). The data management system needs to be open and flexible enough for handling all kinds of available context data. The state-of-the-art method to model such heterogeneous data is the use of ontologies. In particular, ontologies provide semantic mechanisms for integrating data coming from heterogeneous and distributed sources (Linked Open Data). Possibly the biggest benefit of using Ontologies is the capability to deal efficiently with the context of information. According to Gartner Predictions for 2015, the context of information will be as influential to mobile consumer services and relationships as search engines are to the web (see Gartner Top End User Prediction for 2010: Coping with the New Balance of Power). Newest developments in semantic stream processing also provide efficient ways for complex processing of data coming from heterogeneous and streaming sources in real-time. Specifically, semantic streaming is still a new discipline but it offers a promising way to

efficiently deal with a huge amount of contextualized semantic data (see "Elastic and scalable processing of Linked Stream Data in the Cloud," Danh Le Phuoc, Hoan Nguyen Mau Quoc, Chan Le Van, and Manfred Hauswirth, in "The 12th International Semantic Web Conference (ISWC 2013)," October 21–25, 2013, Sydney, Australia, 2013.

References

1. J. R. Mathiassen, E. Misimi, M. Bondø, E. Veliyulin, and S. O. Østvik, "Trends in application of imaging technologies to inspection of fish and fish products," *Trends in Food Science & Technology*, vol. 22, no. 6, pp. 257–275, 2011.
2. G. Olafsdottir, P. Nesvadba, and C. Di Natale, "Multisensor for fish quality determination," *Trends in Food Science and Technology*, no. vol. 15, no. 2, pp. 86–93, 2004.
3. I. Sone, R. L. Olsen, A. H. Sivertsen, G. Eilertsen, and K. Heia, "Classification of fresh atlantic salmon (salmo salar l.) fillets stored under different atmospheres by hyperspectral imaging," *Journal of Food Engineering*, vol. 109, no. 3, pp. 482–489, 2012.
4. J.-h. Cheng, J. Qu, D.-W. Sun, and X.-A. Zeng, "Visible/near-infrared hyperspectral imaging prediction of textural firmness of grass carp (ctenopharyngodon idella) as affected by frozen storage," *Food Research International*, vol. 56, pp. 190–198, 2014.
5. H.-J. He, D. Wu, and D.-W. Sun, "Rapid and non-destructive determination of drip loss and ph distribution in farmed atlantic salmon (salmo salar) fillets using visible and near-infrared (vis–nir) hyperspectral imaging," *Food Chemistry*, vol. 156, pp. 394–401, 2014.
6. D. Wu and D.-W. Sun, "Potential of time series-hyperspectral imaging (ts-hsi) for non-invasive determination of microbial spoilage of salmon flesh," *Talanta*, vol. 111, pp. 39–46, 2013.
7. D. F. Barbin, G. Elmasry, D.-W. Sun, and P. Allen, "Non-destructive determination of chemical composition in intact and minced pork using near-infrared hyperspectral imaging," *Food Chemistry*, vol. 138, no. 2-3, pp. 1162–1171, 2013.
8. V. M. Fernández-Cabanás, O. Polvillo, R. Rodríguez-Acuña, B. Botella, and A. Horcada, "Rapid determination of the fatty acid profile in pork dry-cured sausages by nir spectroscopy," *Food Chemistry*, vol. 124, no. 1, pp. 373–378, 2011.

9. A. Melfsen, E. Hartung, and A. Haeussermann, "Accuracy of milk composition analysis with near infrared spectroscopy in diffuse reflection mode," *Biosystems Engineering*, vol. 112, no. 3, pp. 210–217, 2012.
10. X. Fu, M. S. Kim, K. Chao, J. Qin, J. Lim, H. Lee, A. Garrido-Varo, D. Pérez-Marín, and Y. Ying, "Detection of melamine in milk powders based on nir hyperspectral imaging and spectral similarity analyses," *Journal of Food Engineering*, vol. 124, pp. 97–104, 2014.
11. U. Contreras, O. Barbosa-García, J. L. Pichardo-Molina, G. Ramos-Ortíz, J. L. Maldonado, M. A. Meneses-Nava, N. E. Ornelas-Soto, and P. L. López-de Alba, "Screening method for identification of adulterate and fake tequilas by using uv–vis spectroscopy and chemometrics," *Food Research International*, vol. 43, no. 10, pp. 2356–2362, 2010.
12. K. Ilaslan, I. H. Boyaci, and A. Topcu, "Rapid analysis of glucose, fructose and sucrose contents of commercial soft drinks using raman spectroscopy," *Food Control*, vol. 48, pp. 56–61, 2015.
13. B. Seifert, M. Pflanz, and M. Zude, "Spectral shift as advanced index for fruit chlorophyll breakdown," *Food and Bioprocess Technology*, vol. 7, no. 7, pp. 2050–2059, 2014.
14. T. Ignat, S. Lurie, J. Nyasordzi, V. Ostrovsky, H. Egozi, A. Hoffman, H. Friedman, A. Weksler, and Z. Schmilovitch, "Forecast of apple internal quality indices at harvest and during storage by vis-nir spectroscopy," *Food and Bioprocess Technology*, vol. 7, no. 10, pp. 2951–2961, 2014.
15. Peiris, K.H.S., G.G. Dull, R.G. Leffler, and S.J. Kays, "Near-infrared (nir) spectrometric technique for nondestructive determination of soluble solids content in processing tomatoes," *J. Am. Soc. Hortic. Sci.*, no. 123, pp. 1089–1093, 1998.
16. Slaughter, D.C., D. Barrett, and M. Boersig, "Nondestructive determination of soluble solids in tomatoes using near-infrared spectroscopy." *JOURNAL OF FOOD SCIENCE*, no. 61, pp. 695–697, 1996.
17. S. Serranti, D. Cesare, F. Marini, and G. Bonifazi, "Classification of oat and groat kernels using nir hyperspectral imaging," *Talanta*, vol. 103, pp. 276–284, 2013.
18. X. Zhou, Z. Yang, S. A. Haughey, P. Galvin-King, L. Han, and C. T. Elliott, "Classification the geographical origin of corn distillers dried grains with solubles by near infrared reflectance spectroscopy combined with chemometrics: A feasibility study," *Food Chemistry*, 2014. [Online]. Available: http://ac.els-cdn.com/S0308814614014800/1-s2.0-S0308814614014800-main.pdf?_tid=b037aaf6-5446-11e4-a5d9-00000aab0f01\&acdnat=1413362511_f5e5ac132360a579d29d9bee1a2db05a

19. Tarkosova, J., and J. Copikova, "Determination of carbohydrate content in bananas during ripening and storage by near-infrared spectroscopy," *J. Near-infrared Spectrosc.*, no. 8, pp. 21–26, 2000.

20. R. J. Henry, "Near-infrared reflectance analysis of carbohydrates and its application to the determination of (1→3),(1→4)-β-d-glucan in barley," *Carbohydrate Research*, vol. 141, no. 1, pp. 13–19, 1985.

21. F. IPMS, EP 1474665 B1, US 7,034,936 B2, EP 1474666 B1, US 7,027,152 B2.

22. H. Grueger, A. Heberer, F. Zimmer, A. Wolter, H. Schenk, and A. E. Hatheway, "Miniaturized moems spectrometer for nir applications," in *Optics & Photonics 2005*, ser. SPIE Proceedings. SPIE, 2005, pp. 58 770J–58 770J–8.

23. H. Grüger, A. Wolter, T. Schuster, H. Schenk, H. K. Lakner, Y. S. Sidorin, and A. Tervonen, "Performance and applications of a spectrometer with micromachined scanning grating," in *Integrated Optoelectronics Devices*, ser. SPIE Proceedings. SPIE, 2003, pp. 284–291.

24. M. Michelsburg, T.-T. Le, K.-U. Vieth, T. Länlge, G. Struck, and F. Puente León, "From experiments to realizations: Hyperspectral systems," *Sensor Based Sorting*, p. 19.

25. C. Negara, K.-U. Vieth, and S. Gelo, "Quality improvement of wine due to hyperspectral analysis," *Sensor-Based Sorting*, pp. 117–126.

26. D. A. Burns and E. W. Ciurczak, *Handbook of Near-Infrared Analysis*, 0003rd ed. Crc Pr Inc.

27. K. Varmuza and P. Filzmoser, *Introduction to Multivariate Statistical Analysis in Chemometrics*. Crc Pr Inc.

28. F. v. d. B. Åsmund Rinnan, "Review of the most common pre-processing techniques for near-infrared spectra," *TrAC Trends in Analytical Chemistry*, vol. 28, pp. 1201–1222.

29. A. C. Rencher, *Methods of Multivariate Analysis*, 3rd ed. Wiley-Blackwell (an imprint of John Wiley & Sons Ltd).

Near infrared spectroscopy as a tool for in-line control of process and material properties of PLA biopolymer

W. Becker, N. Eisenreich, E. Inone-Kauffmann and W. Eckl

Fraunhofer-Institut für Chemische Technologie, Joseph-von-Fraunhoferstr. 7, 76327 Pfinztal, Germany

Abstract In the field of polymer processing NIR spectroscopy has been increasingly applied for an on-/in-line monitoring mainly at lab scale process development but also for production of high value materials. In this paper the bio-polymer polylactide (PLA) was investigated by NIRS in the range of 1.2 to 2.4 μm in order to identify additives like nanofil® and nano titanium oxide. A twin screw extruder (Haake Polylab PTW 16) was used to extrude polymer pellets mixed with the additives. The optical sensor probes (glass fibers) were placed between screw and nozzle to achieve a good optical throughput and to withstand typical temperature and pressure conditions during the extrusion (up to 220° C and a few 10 MPa). The on-line NIR spectroscopy enabled a real time information which might be used for process control or feeding control on the compound characteristics continuously. The chemometric data evaluation was able to quantify the measured values, especially the content of the additives in the compounds. The established statistical models predicted the actual values with high correlation coefficients (> 0.99). The additives altered viscosity of the melt and mechanical properties (Young´s modulus) of injection moulded test samples of the compound.

1 Introduction

Bioplastics and biocomposites will become decisive and important materials for industrial sectors like e.g. automotive and aircraft applications and consumer products. Demands concerning process and product conditions are challenging tasks and new robust and reliable measurement systems must be utilized. Requirements of product quality

of Bioplastics and Biocomposites request to control effectively compositions and formulations and to run the processes at optimal conditions [1,2]. In-/on-line control method can monitor important parameters directly at the e.g. extruder at real time. Spectroscopy in the wavelength range from ultraviolet, the visible and especially the near and mid-infrared (NIRS and MIRS) is capable of providing in-line molecular information on involved constituents [3, 4]. Application of MIR spectroscopy is limited because of not available fibre optics for the MIR range and is generally more sensitive in handling, the main focus was set on the NIRS for in-/online control, which has gained broad use in industrial processes [3–5]. For polymer processing and recycling NIR spectroscopy is widely used and commercial systems are available [6,7] For polymer processing NIRS supports effectively in-/on-line control if carefully calibrated and statistical data evaluation methods are applied like partial least square regression (PLSR) [8–13]. NIRS measurement techniques are applied to extrusion processes to measure the composition of input feed, compound composition, dispersion conditions or the stability of the process. They detect early e.g. deviations from the target properties, allowing immediate corrections by real time adaptation of process parameters. NIRS is also capable of monitoring additive or moisture content in the melt. In the present work, NIRS is applied to PLA matrix composites containing TiO_2 nanoparticles of about 100 nm to 200 nm diameter and nanofil® to study the monitoring of these additives and to correlate to mechanical properties of test samples. Nanofil® is composed of small nanometer sized clays layered as mineral silicates.

2 Near Infrared (NIR) Spectroscopy

The near infrared spectral region ranges from about 780 nm to about 2500 nm and is dominated by overtone and combination bands. Absorption bands originate mainly form functional groups containing hydrogen like CH, NH and OH. The optical path length for polymers is typically in the range of several millimetres hence measurements can be done in transmission configuration. In the transmission spectra either the absorption bands according to the functional groups can be evaluated for e.g. concentration determination or the stray light can be used for size measurements of e.g. nanoparticles [14]. Additionally, the use

of fibre optics allows long distances between the spectrometer and the probe which is a great advantage in case of difficult or hazardous places or surroundings. Due to the broad absorption bands in the near infrared spectral region the analysis of the spectra i.e. quantification of data via a regression has to be done typically with multivariate regression methods [15,16]. For the measurements a CARL ZEISS diode array spectrometer was used with a spectral range from 950 nm to 2400 nm with a spectral resolution of about 18 nm. Accumulation was five and integration time between 10 ms and 100 ms.

3 Polymer processing Equipment

A twin screw extruder (Haake Polylab PTW 16) was used to extrude fed polymer pellets coated with the additive. The temperature profile of the extruder can be adjusted with up to four temperature zones whereby the extruder length was 40 cm. The extruder was fed by a single screw metering feeder. The polymer granulates and the addtive powders, nano TiO_2 and nanofil®, were weighted and subsequently mixed in a wobble mixer to achieve a good homogenisation of the two materials before the extrusion process whereas the PLA granules became coated in a bath of the particle dusts. The optical sensor probes (glass fibers) were placed between screw and nozzle to achieve a good optical throughput and to withstand temperature and pressure of 300° C and a few 10 MPa. In the probe body a sapphire window and appropriate optics are included. Extruded strands samples were obtained with a Babyplast®) mini-injection moulding machine equipped with a small standard test sample tool. The test samples were analysed by standard mechnical testing to determine Young's modulus, maximum strain and strain at break. 5 samples were 16 composite types, varying additive content, moisture, extruder temperature, screw design, momentum, were manufactured to apply statistical evaluation also to the mechanical properties influenced by the additives and processing parameters

4 Polylactide

Polylactide (PLA) and copolymers of lactic acid can be used on the one hand for medical applications like absorbable suture material and im-

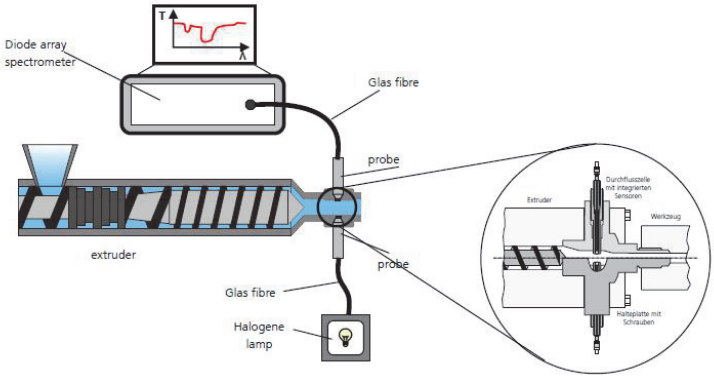

Figure 5.1: Drawing of the extruder equipped with probes for transmission measurement. The probes were installed in an adapter at the extruder die.

plants and on the other hand for biodegradable food packing [17]. For medical applications detailed NIRS investigations were performed in the past [18–20]. Bio-polymers PLA and starch are available commercially, and are suited for engineering biocomposites to be reinforced with natural fibres. In-/online monitoring of important parameters which might influence processing, the formulation itself, natural fibres and additives of the final bio-based materials have to be monitored or even on-/in-line controlled for quality assurance [21, 22]. A NIR spectrum recorded of a PLA raw material powder is shown in Fig.5.2. Main absorption peaks of functional groups in the near infrared spectral range are shown.

5 Effects of nanofil® TiO2 Additives

The additive TiO_2 in PLA was already reported in the PPS23 and showed good correlation on calibration data [21]. In the present work nanofil® content in PLA was varied between 0 to 3 %. Both additives were also mixed and compounded with PLA. As an example for the influence to the spectral behaviour the results of the nanofil® additive are given.

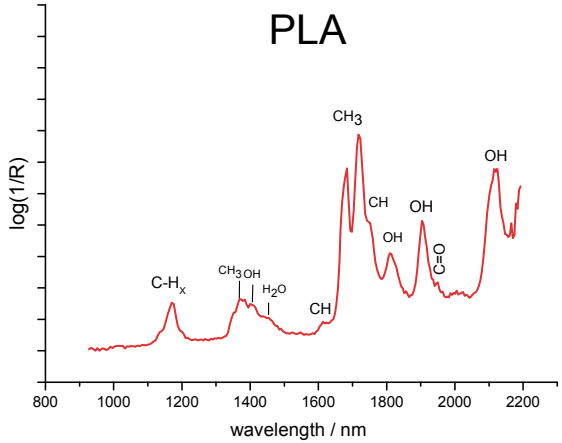

Figure 5.2: NIR spectrum of PLA powder

In Figure 5.3 a SEM picture is given which shows a PLA sample with a TiO_2 / nanofil® mixture. The nanofil® additive shows a well dispersed homogenous structure in the PLA matrix with TiO_2 nano particles spread between the nanofil® component. The nanofil® material is also oriented in different directions and not in clumps indicating that intercalation and exfoliation had happened. This might be because of the extrusion conditions like screw speed, throughput of the material or geometry of the twin screw. The TiO_2 particles can also act like small grinding stones fostering the dispersion process of the nanofil®. This must be verified in subsequent trials.

6 NIR Measurements PLA / nanofil®

PLA was mixed with increasing amount of nanofil® material and extruded. Nanofil® was in the range of 0% (m/m) to 3% (m/m). NIR spectra were measured at the extruder die (Fig.5.1). During extrusion

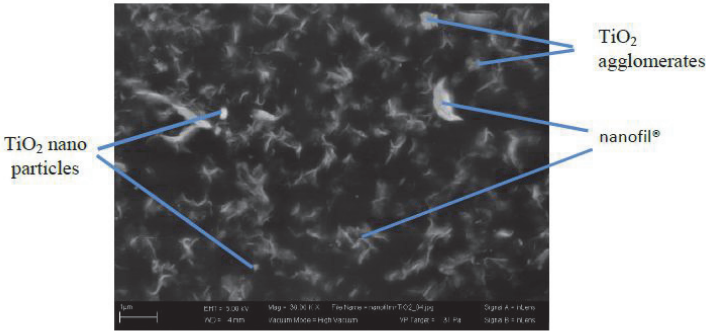

Figure 5.3: SEM picture of a injection moulded test sample of PLA with nano-TiO_2 and nanofil®, ——— 1 μm. Content of nanofil® was 1% (m/m).

the temperature and screw speed were kept constant to ensure a stable process. Hence influences by process conditions are minimized and spectra evaluations give more reliable results. First the intensity of a PLA sample $I(\lambda)_{\mathrm{PLA}}$ was measured in the NIR range and used as reference $I(\lambda)_{\mathrm{PLA}}$ with λ the wavelength. After that PLA samples with increasing nanofil® content were measured giving the intensity $I(\lambda)_{\mathrm{mix}}$. Spectral transmission $T(\lambda)$ was calculated as

$$T(\lambda) = \frac{I(\lambda)_{\mathrm{mix}}}{I(\lambda)_{\mathrm{PLA}}} \tag{5.1}$$

The results of the measurements of selected samples are shown in Figure 5.4. There is a correlation between nanofil® content and transmission. Samples with higher content of nanofil® show a lower transmission over the whole spectral range. Each sample shows increasing transmission from lower to higher wavelengths. This behaviour is caused by light scattering of the nanoclay particles and therefore correlated with the amount of nanoclay. Beside this physical spectral information also chemical information is contained in the spectra. The absorption peak at about 1650 nm to 1680 nm can be assigned to OH and SiO / SiO_2 functional groups. There is also a small peak at 1400 nm which can be assigned to OH functional group [23]. The gap between layers in the

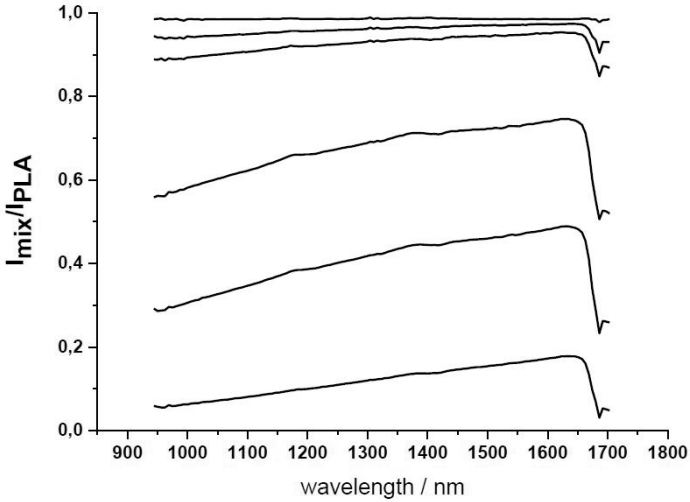

Figure 5.4: NIR spectra of PLA / nanofil® mixture samples. Amount of nanofil® is given in mass percent (m/m%) at each of the spectra.

nanoclays is in the nanometer range. Water can be bound between these layers and can dominating the NIR spectra and influence also mechanical properties of the matrix material. Therefore a control of the nanofil® content is essential for producing polymers with reproducible properties. Transmission spectra were measured and a multivariate prediction (PLSR) model was generated (Figure 5.5). NIR spectra of the composite with additives gave results which led to correlation better than 0.996 indicating the possibility to control their PLA content on processing.

7 Light Scattering

There is light scattering in the PLA / nanofil® caused by the nanoclay composite. Light scattering can be described by Mie theory whereby the presumption is that the particles are non-interacting and spherical [24, 25]. The nanoclays are not spherical and an interaction cannot

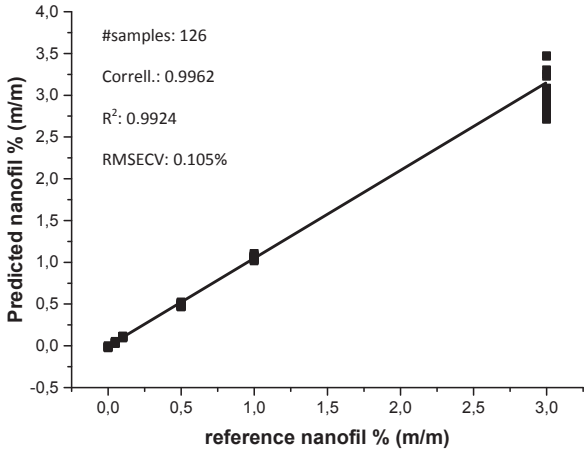

Figure 5.5: PLSR prediction model of the nanofil® content (0 – 3%) in PLA with a correlation better than 0.996. Spectral pre-treatment: vector normalization. Validation method: cross validation

be excluded for higher filling factors. Nevertheless an evaluation based on Mie theory was tried to get information out of the spectral measurements. Light intensity is either decreased by absorption or scattering in the material. The intensity loss through light scattering can be described by:

$$I(\lambda) = I_0(\lambda)\exp(-NC_{\text{sca}}d) \tag{5.2}$$

$I_0(\lambda)$ is the incident intensity, $I(\lambda)$ the intensity of the beam emerging after a distance d, N is the number of scattering particles and C_{sca} the scattering cross section of the particles [14,24]. In case if quotient of particle radius r and wavelength λ is $r/\lambda < 0.8$ the Rayleigh approximation can be used for C_{sca}. For the present evaluation in the wavelength range from about 1000 nm to 2000 nm it was assumed that this approximation

and assumption is valid. Equation (5.2) was transformed to

$$\frac{1}{d}\ln(T(\lambda)) = \tau = \frac{1}{d}\ln\left(\frac{I(\lambda)}{I_0(\lambda)}\right) = -NC_{\text{sca}} \tag{5.3}$$

$$\text{with } \tau = \frac{1}{d}\ln(T(\lambda)) \tag{5.4}$$

τ is called turbitity. The scattering cross section C_{sca} was described in the Rayleigh limit as $C_{\text{sca}} = A/\lambda^n$. The parameter A is a function of particle radius and refractive index of the matrix and the particle and number of particles. For Rayleigh scattering the exponent n is 4. But for increasing particle radius n decreases from 4 to 0 and can be used as an indicator for e.g. particle growth or agglomeration processes [25]. The measurements of Fig. 5.4 were fitted to

$$\frac{1}{d}\ln(T(\lambda)) = \frac{1}{d}\left(\frac{I_{\text{mix}}(\lambda)}{I_{\text{PLA}}(\lambda)}\right) = \frac{A}{\lambda^n} \tag{5.5}$$

Result of the fitting procedure delivers an exponent of the wavelength of about 1.44 for a content of 0.05% of nanofil®. Figure 5.6 shows the plot of the scattering behaviour depending on wavelength. The exponent decreases for increasing content of additive to about 1 for a filling factor of 3% (Fig.5.7). The results of the fitting procedure for all samples are given in Table 5.1.

nanofil® content %	A	n
0.05	1330	1.44
0.1	21424	1.77
0.5	3320	1.25
1	3033	1.14
3	2035	0.95

Table 5.1: Result of the fitting procedure according to equation 3. The n value of sample with 0.1% nanofil® might be caused by agglomeration or incomplete exfoliation.

8 Mechanical Properties

It is well known that nano-particles influence the mechanical properties of composite materials [26, 27]. This is also true for nano TiO_2 and

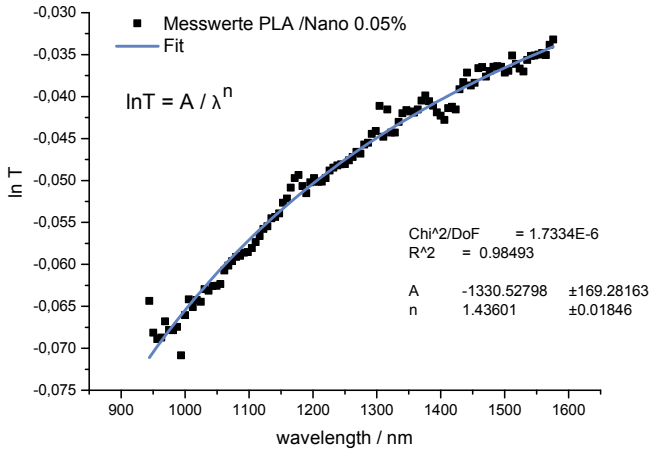

Figure 5.6: Spectral data PLA-0.05% nanofil® with a least squares fit of the scattering relation according to equation (5.5).

nanofil®. The statistical evaluation of the 80 samples of 16 types enabled an analysis of significant influences the additive content, the moisture content, extruder temperature and momentum. Both nano-particles, if present as single additives, increase significantly Young's modulus but decrease maximum strain. However, if both additives are present then the maximum strain increases significantly.

9 Summary

NIR spectroscopy can be used to measure additive content during processing of PLA biopolymer. Transmission spectra can be used to generate multivariate regression models to predict content of nanoclay. Main spectral information is the light scattering of the nanoparticles. Light scattering can also be used to make assertions of state of particle agglomeration and size changes.

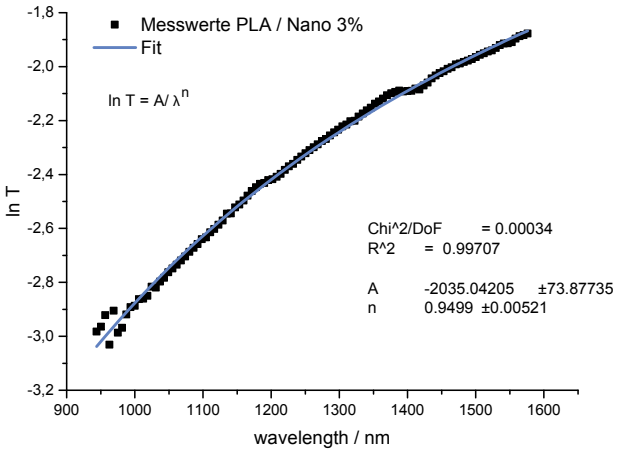

Figure 5.7: Spectral data PLA-3% nanofil® with a least squares fit of the scattering relation according to equation (5.5).

References

1. Bioplastics, "Proceedings of international congress trade show, the industrial applications of bioplastic," York, 2002.
2. D. L. Kaplan, "Biopolymers from renewable resources," 1998.
3. I. Murray and I. e. Cowe, "Making light work: Advances in near infrared spectroscopy," in *Proceedings of the 4th Int. Conf. on NIR Spectroscopy*, 1991.
4. J. Workman, "A review of process near infrared spectroscopy," in *J. Near Infrared Spectroscopy 1*, 1993.
5. U. Eschenauer, O. Henck, M. Hühne, P. Wu, I. Zebger, and H. Siesler, "Process monitoring by spectroscopic methods in the polymer and plastics industry," in *Near infrared technology*, New York, 1992.
6. N. Eisenreich, J. Herz, H. Kull, M. Mayer, and R. T., "Fast on-line identification of plastics by near-infrared spectroscopy for use in recycling processes," in *Antec 96; Plastic racing into the future*, Indianapolis, May 1996.
7. N. Eisenreich and T. Rohe, "Infrared spectroscopy in analysis of plastics

recycling," in *Encyclopedia of Analytical Chemistry Vol.9 John Wiley & Sons Ltd., Chichester, Vol. 9*, UK, 2000.

8. H. Siesler, "Near-infrared spectroscopy of polymers," in *Makromol.Chem. 52*, 1991.
9. D. Fischer, T. Bayer, K. Eichhorn, and M. Otto, "In-line process monitoring on polymer melts by nir-spectroscopy," in *Fresenius J. Anal. Chem. 359*, 1997.
10. M. Hansen and K. A., "in-line monitoring of molten polymers: Near infrared spectroscopy, robust probes, and rapid data analysis," in *Polymer Engineering and Science 34*, 1994.
11. A. Khettry and M. Hansen, "Real-time analysis of ethylene vinyl acetate random copolymers using near infrared spectroscopy during extrusion," in *Polymer Engineering and Science 36*, 1996.
12. T. Rohe, A. Krey, and N. Eisenreich, "In-line monitoring des extrusionsprozesses mit nahinfrarot (nir)-spektroskopie," in *Mit Kunststoffen zu neuen Produkten. Symposium Strategien für die Produktion im 21. Jahrhundert*, FH-ICT Pfinztal, 1997.
13. T. Rohe, W. Becker, A. Krey, H. Nägele, S. Kölle, and N. Eisenreich, "In-line monitoring of polymer extrusion processes by nir spectroscopy," in *J. Near Infrared Spectroscopy, 6*, 1998.
14. V. Guschin, W. Becker, and N. Eisnereich, "Determination of nanoparticle size distribution in media by turbodimetric measurements," in *Chemical Engineering & Technology, 35*, 2012.
15. M. Otto, "Chemometrie," in *Chemometrie*, VCH Weinheim, 1997.
16. H. Martens and T. Naes, "Multivariate calibration," Wiley Chichester, 1989.
17. D. Perrin and J. English, "Polyglycolide and polylactide," in *Handbook of Biodegradable Polymers*, 1997.
18. G. Reich, "Use of dsc and nir spectroscopy to study the hydration, degradation and drug release behavior of pla/plga microparticles and films with free and blocked carboxylic end groups," in *Proceed. Intern. Symp. Control. Rel. Bioact. Mater. 27*, 2000.
19. S. Thosar and R. Forbess, "Determination of copolymer ratios of polylactide-co-glycolide using near-infrared spectroscopy source," in *J. Pharmaceutical and Biomedical Analysis, 20*, 1999.
20. G. Reich and T. Schönbrodt, "Fast and noninvasive near infrared analysis of pla and plga microparticles, films and tablets," in *Proceed. Int. Sypm. Control. Rel. Bioact. Mater., 28*, 2001.

21. E. Inone-Kauffmann and N. Eisenreich, "Biocomp - composites from renewable resources - a european project," in *PPS23 Proceedings*, San Salvador, Brazil, May 2007.

22. W. Becker, E. Inone-Kauffmann, W. Eckl, and N. Eisenreich, "Near infrared spectroscopy for in-line control of biopolymer processing," in *PPS23 Proceedings*, San Salvador, Brazil, May 2007.

23. J. Stone and G. Walrafen, "Overtone vibrations of oh groups in fused silica optical fibres," in *J.Chem.Phys. 76(4)*, 1982.

24. C. Bohren and D. Huffmann, "Absorption and scattering of light by small particles," Wiley-VCH Verlag, 2004.

25. M. Kerker, "The scattering of light and other electromagnetic radiation," Academic Press New York, San Francisco, London, 1969.

26. G. Odegard, T. Clancy, and T. Gated, "Modeling of the mechanical properties of nanoparticle/polymer composites," in *Polymer 46*, 2005.

27. J. Jordan, K. Jacob, R. Tannenbaum, M. Sharaf, and I. Jasiuk, "Experimental trends in polymer nanocomposites—a review," in *Materials Sci. Eng. A, 393*, 2005.

Identification of bio-plastics by NIR-SWIR-Hyperspectral-Imaging

Hollstein, Frank[1]; Wohllebe, Markus[1]; Arnaiz, Sixto[2]; Manjón, David[2]

[1] RTT Steinert GmbH
Hirschfelder Ring 9, 02763 Zittau, Germany
[2] Fundación GAIKER
Parque Tecnológico 202, 48170 Zamudio, Spain

Abstract Bio-plastics are characterized by the highest rate of growth in the plastics industry. In connection with the recycling chain they constitute the so-called "oxo-biodegradation" and drop-in problems. The present study tries to clarify possibilities of automatic recognition and sorting of conventional fossil-based plastics against similar "oxo-biodegradable" plastics and drop-ins by means of NIR-SWIR-Hyperspectral-Imaging (HIS). The spectral structures of the most important plastics (conventional fossil-based plastics and bio-plastics) have been incorporated in a database as references for different plastic types to be subject to identification by NIR-SWIR-HSI. In addition to widespread chemometrical methods (PLS-DA), artificial neural networks (ANN) and support vector machines (SVM) are estimated for classification. For "oxo-biodegradable" plastics it turns out that a decision tree is the most reliable procedure for identification. Different decision trees are passed to an industrial NIR-SWIR-Hyperspectral-Imager for generating chemical images of different plastic mixtures. The mixtures consist of conventional fossil-based plastics and bio-plastics. The aim of the tests was to find bounds for sorting throughput and purity. Results of an industrial sorting trial are finally described.

1 Introduction

Despite there are significant doubts about the environmental sustainability of bio-plastics [1], currently this class of materials has the highest rate of growth in the plastics industry [2–4]. In the context of

the recycling chain they constitute on one hand the so-called "oxo-biodegradation" problems and on the other hand the so-called drop-in problems. The first problem is in connection with the use of oxidation-enhancing additives in the polymer matrix. The second occurs when the chemical structure of a bio-plastics is similar to its pure fossil-based homologous. A mixture of different types of similar plastics within the input stream of a recycling chain can be in some cases useless for reprocessing due to not strict similar physical properties.

The present study attempts to clarify the possibilities of automatic recognition and sorting of bio-plastics, in particular conventional fossil-based plastics against similar "oxo-biodegradable" plastics, by means of NIR-SWIR-Hyperspectral-Imaging. After a brief explanation of bio-plastics material, Hyperspectral-Imaging (HSI) is shortly explained as the state-of-the-art procedure for sensor-based sorting of plastics waste. This involves the three main procedures for extracting useful information from Hyperspectral-Images (PLS-DA (partial last squares discriminant analysis), ANN (artificial neural networks), and SVM (support vector machines)).

Furthermore, the spectral structures of the most important bio-plastics are depicted. Of particular interest are the fingerprints of the chemically similar plastics. The results have been incorporated in a database as references. For classification it turns out that a decision tree is the most reliable procedure for sorting of "oxo-biodegradable" plastics. Different decision trees passed an industrial NIR-SWIR-Hyperspectral-Imager for generating chemical images of different plastic mixtures. The mixtures consist of conventional fossil-based plastics and bio-plastics. The results of an industrial sorting trial are finally described.

2 Bioplastics

The word "bio-plastics" is an expression of leading astray because it primarily suggests just materials that are bio-degradable and therefore supposed environment-friendliness. In the literature the term "bio-plastics" is considered further. It comprises organic materials, in particular organic polymers, that are either bio-based, bio-degradable, or both [5, 6]. A bio-plastics material can be distinguished in one of the follow-

ing three main groups: (1) (partially) bio-based and non-bio-degradable such as bio-PE, bio-PP or bio-PET (so-called ”drop - ins”) as well as technical polymers such as PTT (poly-trimethylene terephthalate) or TPC-ET (thermoplastic co-polyester elastomers), (2) bio-based and bio-degradable such as PLA (polylactic acid), PHA (polyhydroxyalkanoate) or PBS (polybutylensuccinate), and (3) fossil-based (oil, coal, natural gas ...) and bio-degradable such as PBAT (polybutylene adipate-co-terephthalate). For a fully review on present industrial available bio-plastics see [3, 4].

The so-called oxo-biodegradable plastics are a subgroup of bio-plastics. Terms such as ”degradable”, ”biodegradable”, ”oxo-degradable”, ”oxo-biodegradable” are used to promote products made with traditional plastics supplemented with specific additives. The ”oxo-biodegradable” additives are typically incorporated in conventional plastics such as polyethylene (PE), polypropylene (PP), polystyrene (PS), and polyethylene terephthalate (PET). These additives are based on chemical catalysts, containing transition metals such as cobalt, manganese, iron, etc., which cause fragmentation as a result of a chemical oxidation of the plastics’ polymer chains triggered by UV irradiation or heat exposure. In a second phase, the resulting fragments are claimed to eventually undergo biodegradation. But oxo-fragmentable products can hamper recycling of post-consumer plastics. In practice, these plastics are traditional plastics. The only difference is that they incorporate additives which affect their chemical stability. Thus, they are identified and classified according to their chemical structure and finish together with the other plastics waste in the recycling streams. In this way, they bring their degradation additives to the recyclate feedstock. As a consequence the recyclates may be destabilized, which will hinder acceptance and lead to reduced value [7]. As a consequence, some public and private organizations therefore militate against oxo-degradable additives.

Drop-in bio-plastics are bio based or partly bio based non-biodegradable materials such as (partly) bio based PE, PP or PET. Drop-ins seem to feature the same properties and functionalities as their fossil counterparts. It is assumed that the value-added chain only requires some irrelevant adaptations in processing. Use, recycling and recovery follow the same routes as conventional PE, PP or PET products do. But

this must not be the full truth. A mixture of both types can be in few cases useless for reprocessing due to not strict equal physical properties.

3 NIR-SWIR-Hyperspectral-Imaging

3.1 NIR-SWIR spectral range

Due to different views related to the NIR-SWIR spectral range, it is necessary to make some comments in this regard. As a start the term Infrared (IR) refers to the full portion of the electromagnetic spectrum between visible light and microwaves. This large range is generally divided into Near Infrared (NIR, 0.78 - 1.4 µm), Short-Wave Infrared (SWIR, 1.4 – 3.0 µm), Medium-Wave Infrared (MWIR, 3.0 - 8 µm), and Long-Wave Infrared (LWIR, 8 - 15 µm). The classification of infrared spectral ranges was initially based on chemical/physical phenomena like the types of molecular vibrations or the atmospheric windows for the radiation, respectively. Latterly more technical aspects divide up the IR-band based on the response of various semiconductor detectors. The industrially most advanced semiconductor detector materials for NIR-SWIR-detection are InGaAs, ext-InGaAs and HgCdTe, respectively [8–10].

For NIR imaging, $In_xGa_{1-x}As$ is one of the widely used detector materials due to its low dark current. InGaAs thin films typically using an alloy composition of x = 0.53. The spectral response covers at room temperature 0.9 - 1.7 µm. Thus, the 0.9 - 1.7 µm spectral ranges is called NIR-range by most of the detector providers. By increasing the composition to x = 0.82, InGaAs is able to extend its cut-off to 2.6 µm (so called ext-InGaAs). However, the crystal defects due to epitaxy and the decreased shunt resistance, due to a smaller band gap, degrade performance at the longer cut-off wavelengths [11].

An approach to accomplish SWIR imaging under low light level conditions is HgCdTe. $Hg_{1-x}Cd_xTe$ (MCT) is currently the widely used detector materials for SWIR imaging. The ability to tune the cut-on and cut-off wavelengths in SWIR by changing the stoichiometry of the substrate enables application optimizations. The alloy composition x can be fixed to provide an energy band gap equal to the longest wavelength to be measured in the SWIR band [12]. For SWIR imaging mostly a

spectral range from 0.9 – 2.5 µm is chosen. The permission of two different systems (InGaAs and MTC as semiconductor material) based on spectral resolution requirements for the respective application cases.

3.2 Hyperspectral-Imaging

NIR-spectroscopy is currently the most common method for automated sorting of post-consumer plastics. This technique involves irradiating the unsorted (unidentified) plastics with near-infrared waves. When the infrared light reflects off the surface of the plastics, each resin's characteristic infrared absorption band can be measured. These measurements can then be compared directly to known polymer values (correlation analysis) or indirectly by signal transformation and applying of chemometrical procedures to determine the resin type.

NIR-spectroscopy has many advantages. Probably the most significant advantage is the speed of identification. A second advantage is the lack of specimen preparation. Labels or other obstructions like dirt, do not relevant interfere with readings. Another advantage of NIR-based optical systems is that colour does not interfere with proper resin identification. Except for black, the readings are independent of the surface colour.

The special requirements in plastics sorting call for cost-effective, robust NIR spectrometers capable of macroscopic imaging. The best answer to this problem is the application of spectral imaging systems, which are capable of measuring both the spatial and the spectral information in quasi one step. Such devices are called Hyperspectral-Imaging cameras or short Hyperspectral-Imager.

Hyperspectral-Imaging is a combination of spectroscopy with digital image processing. Other than with standard imaging, where only the spatial information plus the three RGB values for each single image pixel are recorded, HSI provides full spectral information (a few hundred values) for each surface pixel over a selected wavelength range.

In instrumentation there are basically three different approaches (**Fig. 6.1**). The first approach is the so called "whiskbroom scanning" (**Fig. 6.1 left**). This sampling method was introduced in the industrial practice of plastics waste sorting in the mid-nineties. A whiskbroom imager scans the sample point-by-point in the x-y-spatial direction and measures a full spectrum of adjacent regions sequentially. The need of using rotating or swinging mirrors to generate a HSI makes such systems mechanically susceptible to faults.

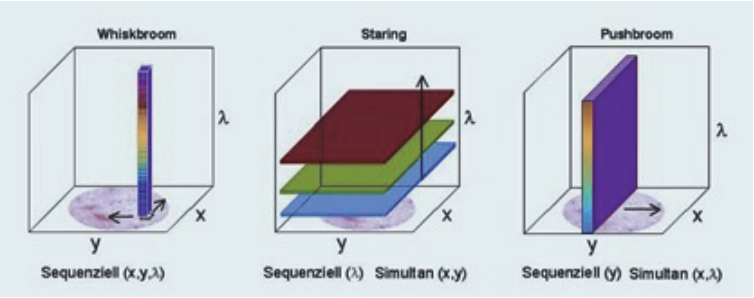

Figure 6.1: Different methods for data acquisition [13]

The second approach is the wavelength scanning method, in remote sensing also called "staring" (**Fig. 6.1 middle**). The sample is kept stationary under the HSI camera and single images are recorded for each different wavelength. The spectral information is provided either by (a) a number of discreet filters, (b) tunable filters or (c) by combination with an imaging Fourier-Transform spectrometer. The images recorded for the different wavelengths are combined in the computer and the spectra calculated. Staring imagers are not been implemented so far for automatic sorting of waste.

The third method, also known as "push-broom scanning" (**Fig. 6.1 right**), requires a relative movement between imager and sample to scan over the surface. Push-broom scanning is currently the state of the art according to advanced plastics waste sorting machines. The spectral imaging system records the spatial information line wise and the spectral information for each pixel along the line by projection of the spectral information along the second axis of a two-dimensional camera chip (focal plane array, FPA). The spectral encoding is provided either by linear

variable filters, by a DMA (digital micro-mirror array) in combination with grating or by dispersive optics forming an imaging spectrograph. A computer combines the slices, derives the second axis and thus reconstructs the full Hyperspectral-Image.

4 Classification Methods

In connection with plastics sorting, classification refers to the assignment of spectral information to a particular source type. Procedures are used that run under the scientific name "chemometrics". The most widespread classification methods used in chemometrics are supervised and unsupervised trainings [14, 15]. The list of such methods is large: linear and quadratic discriminant analysis, partial least squares discriminant analysis (PLS-DA), soft independent modelling of class analogy, hierarchical cluster analysis, k nearest neighbor's and k-means methods to name only the most important. Increasingly also nonlinear methods such as ANN (Artificial Neural Networks, [16, 17]) and SVM (Support Vector Machines, [18]) are used, especially for the so-called Chemical-Imaging. In this paper the performance of PLS-DA, Feed-Forward-ANN and SVM are examined with the main focus on PLS-DA.

4.1 PLS-DA

Partial least squares discriminant analysis (PLS-DA) includes a partial least squares regression of a set Y of binary variables describing the categories of a categorical variable (here types of plastics) on a set X of predictor variables (here wavelength-dependent intensity of NIR reflection) [19]. Partial least squares models are based on principal components (eigenvectors of the covariance matrix) of both the independent data X and the dependent data Y. The central idea is to calculate the principal component scores of the X and the Y data matrix and to set up a regression model between the scores (and not between the original, not rotated data) [20, 21]. This technique is especially suited to deal with a much larger number of predictors than observations and with multicollineality, two of the main problems encountered when analyzing data of NIR reflection spectra (regarding to plastics sorting tasks particular multicollineality).

4.2 FF-ANN

Artificial neural networks (ANN) are a very flexible class of statistical regression techniques. The essential advantage of the application of neural networks is that no explicit assumptions about the functional form of the unknown link need to be made. The most popular ANNs are multi-layer-feed-forward neural networks (FF-ANN) that are trained with a back-propagation learning algorithm [22, 23]. As a drawback of FF-ANN the lack of an exact rule for setting the numbers of neurons and hidden layers for best performance must be mentioned. Also, the computational costs for modelling are extremely high compared to PLS-DA modelling.

4.3 SVM

A Support Vector Machine (SVM) is a set of related supervised learning methods which can be used for classification (and in modified form also for regression). Given a set of training examples, each marked as belonging to one of two categories, an SVM classification training algorithm tries to build a decision model capable of predicting whether a new example falls into one category or the other. If the examples are represented as points in a hyperspace, a linear SVM model can be interpreted as a division of this hyperspace so that the examples belonging to separate categories that are divided by a clear gap that is as wide as possible. New examples are then predicted to belong to a category based on which side of the gap they fall on [24]. A common disadvantage of non-parametric techniques such as SVMs is the lack of transparency of results. SVMs cannot represent scores as a simple parametric function, since (among other things) its dimension may be too high.

5 Application

5.1 Hyperspectral-Imager

For the HSI research a special Hyperspectral-Imager called RTT-HSI 2.2 was employed in push-broom scanning mode. The main system parameters (hereinafter referred to in brackets) are the spectral range (1.2 …

2.2 µm), the full frame pixel counts (320 spatial × 256 spectral, also a reverse arrangement is possible), the digital measuring depth (14 bit) and the frame rate (330 Hz). Under the assumption of a conveyor belt width of 2.00 m and a belt speed of 2.00 m/s follows a resolution of less than 7 × 7 mm² for one surface pixel of an object to be identified on the moving conveyor tape.

5.2 Spectra Library

Identification of spectra is a task similar to pattern recognition. The base is a library of patterns. For the investigations a set of plastic films delivered by the GAIKER co-authors was used. On the one hand, it was a mix of films made of conventional polymers derived from fossil raw materials and on the other hand, it was made of bio-plastics and plastics including oxo-degradable additives (**Fig. 6.2**).

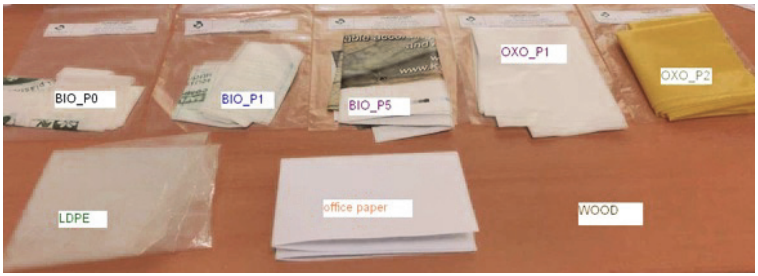

Figure 6.2: Samples to create the spectra library

Fig. 6.3 shows the pattern spectra of bio-plastics regarding to **Tab. 6.1** plus the spectra of LDPE-films, office paper and wood. Office paper and wood were included to illustrate the clear differences against bio-plastics spectra, although they consist likewise of organic material as basic. Also for illustration **Fig. 6.4** contains the pattern spectra of LDPE and OXO_P1 in more detail. OXO_P1 is an oxo-degradable PE-based film that is equivalent to LDPE according to the chemical ground structure.

Table 6.1: Codes for used Bio-plastics

Code	Plastics Type
BIO_P0	Potato starch
BIO_P1	Corn starch
BIO_P5	PLA
OXO_P1	PE (oxo-degradable)
OXO_P2	PE (oxo-biodegradable)

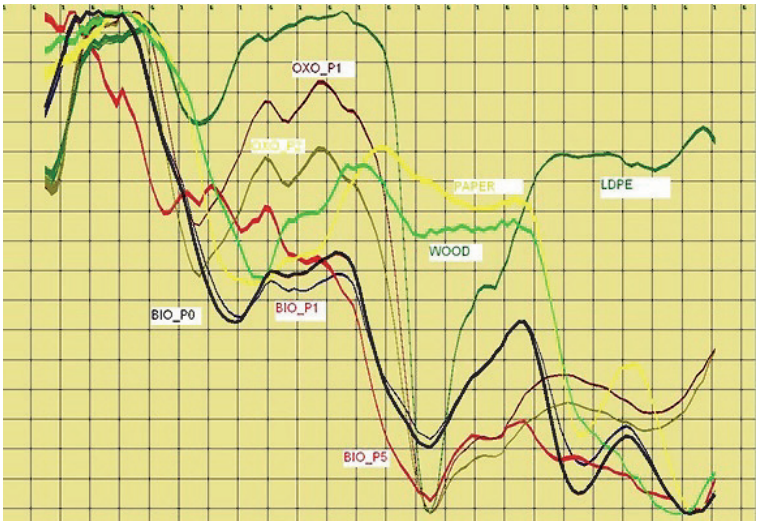

Figure 6.3: Pattern spectra of different bio-plastic films, LDPE films, office paper, and wood; spectral range 1.2 … 2.1 µm, Savitzky-Golay smoothed (window 15, polynomic-order 3), min-max normalized

5.3 Spectra Identification Results

Three questions were target to be answered: (1) are novel bio-plastics distinguishable from the established conventional ones?, (2) is it possible to discover additives for "oxo-biodegradation"?, and (3) are drop-ins recognizable from fossil based similar plastics?

Spectra shown in **Fig. 6.3** can be easily divided into different classes by all of the three classification methods (PLS-DA, FF-ANN, SVM). The

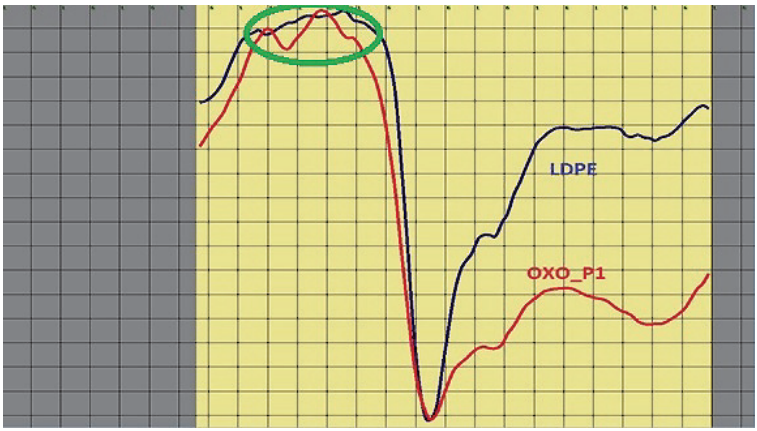

Figure 6.4: Spectra of fossil based PE-films (LDPE) and oxo-degradable PE-films (OXO_P1); min-max normalized regarding ROI (region of interest, yellow background)

differences are so serious that even mixed spectra can be disassembled into so-called endmembers by unconstrained demixing procedures (here not discussed, see [25]).

The codes OXO_P1 and OXO_P2 label two types of "oxo-degradable" and "oxo-biodegradable" PE-films of different providers, respectively. The used incorporated additives are unknown to the authors and there are no references in the delivered data sheets of the films. According to **Fig. 6.3** (OXO_P2) and **Fig. 6.4** (OXO_P1 and LDPE), all of the characteristic bands of PE are well pronounced, but enough differences exist for a classification (**Fig. 6.4, green oval**; this area has been also identified by calculating the VIP (Variable Importance in the Projection, see [26, 27]), here not discussed). To identify the type of spectra by PLS-DA, in the case of OXO_P1, OXO_P2 and LDPE so-called derivative spectra of second order must be generated. This is not necessary when using FF-ANN and SVM as classifiers. But the search for appropriate system parameters for FF-ANN and SVM is very time consuming. Because these parameters are case-specific it should at this point not be subject to any in-depth discussion. However for classification of "oxo-biodegradable" plastics a two-stage algorithm should be used (decision tree), where the second classifier should be either a SVM or an ANN.

To answer the third question, whether drop-ins are recognizable from similar fossil based plastics, the specific case of PET and bio-PET was considered. A conventional PET plastic is made from two components known as mono-ethylene glycol (MEG) and purified terephthalic acid (PTA). MEG makes up for 30 % of the PET weight while the remaining 70 % is made up by PTA. It is possible to replace the fossil-based MEG portions by a bio-based MEG share (bio-MEG). Ethanol from sugar cane and sugar cane by-product-molasses is used as basis of bio-MEG as one of the key plastic ingredients for bio-PET. Aspirations are known to produce also the second base fabric (PTA) from renewable resources, i.e. as a result completely bio-based PET can be produced in the future. In addition there are efforts to develop degradable bio-PET (oxo-bio-PET). Details on the last mentioned procedures are not known from the literature. The procedures are still in the development state.

In the present research the authors tried to explore whether the plastics of ordinary, full fossil based PET bottles and that of so-called PlantBottles^{TM} (brand name of an American soft drink manufacturer) can be distinguished by NIR-SWIR-HSI. As result of extensive series of tests in a laboratory scale is to determine that the products can be assign to the different manufacturers. It is however not been ascertained, whether MEG is fossil-based or has sugar cane as a base. In fact the spectra are more sensitive with regard to different process conditions during plastics production as the origin of the MEG monomers. To elucidate the relationships further investigation are envisaged by exploitation of MWIR and LWIR spectroscopy.

5.4 Sorting Tests

The Hyperspectral-Imager RTT-HSI 2.2 has been used in industrial scale with regard to the separation of different types of plastics including bioplastics. As basic machine a RTT sorter of type UNISORT PR has been used. The input stream was a waste mix of bottles and containers consisting of PET, PP and PLA. The decision for such a composition is therefore justified that PLA bottles will be in future a serious competitor to PET bottles. PET bottles and PLA bottles are hard to distinguish with the naked eye. However within the recycling chain these two plastic types shall not be mixed, because PLA has a significantly lower melting point [28]. Already 0.1 % PLA in a PET recycling process makes the PET recyclate unusable for many end-products.

For the Identification a two-step classification method was used: (1) distinction into classes of conventional plastics by PLS-DA and (2) two-class-grouping by SVM.

After the material is identified pixel by pixel (Chemical-Image), object recognition must be performed based on digital image processing to blow out an item regarding to its waste fraction. The exploited digital image processing is described in [29] and based on a gray scaled image of the HSI. The object reconstruction is then ultimately carried out by means of connected component labelling.

To sum up, the sorting tests have shown that the considered bioplastics can be exact extracted from the input waste stream in a two-stage cognition procedure. The resulting throughput corresponds well with ordinary tasks regarding to automatic plastics waste sorting.

6 Conclusions

Hyperspectral-Imaging is a powerful tool and state of the art in optical characterization of plastics waste. In conjunction with digital image processing and discriminant analysis, the method allows automatic sorting in real time under industrial conditions. In the present work, three questions were target to be answered: (1) are novel bio-plastics distinguishable from the established conventional ones?, (2) is it possible to discover additives for "oxo-biodegradation" in the polymer matrix?, and (3) are drop-ins recognizable from fossil based similar plastics? The first question can be answered fully with Yes. Typically, the NIR spectral range is enough already. With regard to the oxo-degradable plastics (2), the full NIR-SWIR spectral range must be exploited to be able to detect additives, which activate or enhance plastics degradation. For this sorting task a two-stage algorithm of classification should be used (decision tree), where the second classifier should be either a SVM or an ANN. The third question is on the basis of the research results to answer with No. The NIR-SWIR spectra seem more sensitive with regard to different process conditions during plastics production as the origin of the monomers (fossil based or bio-based). To elucidate the relationships further investigation are envisaged by exploitation of MWIR and LWIR spectroscopy.

Acknowledgments

The authors wish to acknowledge the support of the European Commission to the ECO INNOVATION Project FILMSORT (ECO/11/304458/SI2.626548) as frame within this research has been conducted. Some of the results were verified thankworthy by free permission of using the DataLab 3.5 software from H. Lohninger (Vienna, Austria, www.lohninger.com/datalab/) and WEKA 3.7.12 software from University of Waikato (Hamilton, New Zealand, www.cs.waikato.ac.nz/ml/weka/), respectively.

References

1. C. Edwards and G. Parker, "A Life Cycle Assessment of Oxo-biodegradable, Compostable and Conventional Bags," Intertec Expert Services, 2012.
2. A. Detzel, B. Kauertz, and C. Derreza-Greeven, "Study of the Environmental Impacts of Packagings Made of Biodegradable Plastics," in *Report No. 001643/E, Texte Nr. 18/2013*, Umweltbundesamt, Germany, 2013.
3. M. Carus, "Market Study on Bio-based Polymers in the World," in *Proc. 6th Int. Conf. on Ind. Biotechnology and Bio-based Plastics and Composites*, 10 - 12 April 2013, Cologne, Germany.
4. R. P. Babu, K. O'Connor, and R. Seeram, "Current progress on bio-based polymers and their future trends," *Progress in Biomaterials*, vol. 2, no. 11, pp. 1–16, 2013.
5. I. Vroman and L. Taghzert, "Biodegradable polymers," *Materials*, vol. 2, pp. 307–344, 2013.
6. H.-J. Endres and A. Siebert-Raths, in *Engineering Biopolymers, Chapter 1*, ISBN 978-3-446-42403-6, 2011.
7. N. N., "Position paper oxo-biodegradable plastics," *European Bioplastics e.V.*, July 2009.
8. H. Yuan, G. Apgar, J. Kim, J. Laquindanum, V. Nalavade, P. Beer, J. Kimchi, and T. Wong, "FPA Development from InGaAs, InSb, to HgCdTe," *Proc. of SPIE*, vol. 6940, article id. 69403C, 2008.
9. S. Demiguel, "Theoretical analysis and comparison of SWIR active imaging detectors," *Proc. of SPIE*, vol. 7298, article id. 729836, 2009.
10. A. Rogalski, "History of infrared detectors," *OPTO ELECTRONICS REVIEW*, vol. 3, pp. 279–308, 2012.
11. N. K. Dhar, R. Dat, and A. K. Sood, *Advances in Infrared Detector Array Technology, Optoelectronics - Advanced Materials and Devices, S. Pyshkin (Ed.)*, 2013, ISBN 978-953-51-0922-8.
12. L. Duvet, E. Martin, and N. Nelms, "Performance evaluation of MCT arrays developed for SWIR and hyperspectral applications - test bench and preliminary results," *Proc. of SPIE*, vol. 7383, article id. 73834Q, 2009.
13. B. Boldrini, W. Kessler, K. Rebnera, and R. Kessler, "Hyperspectral imaging - a review of best practice, performance and pitfalls for inline and online applications," *J. Near Infrared Spectroscopy*, vol. 20, no. 5, pp. 438–508, 2012.
14. V. N. Vapnik, *The nature of statistical learning theory*, 1995, ISBN 978-1-4757-3264-1.

15. T. Hastie, R. Tibshirani, and J. Friedmann, *The Elements of Statistical Learning*, 2009, ISBN 978-0-387-84858-7.

16. M. K. Alam, S. L. Stanton, and G. A. Hebner, "Near-infrared spectroscopy and neural networks for resin identification," *Spectroscopy*, vol. 9, no. 2, pp. 30–40, 1994.

17. V. G. Maltarollo, K. M. Honório, and A. B. Ferreira da Silva, in *Applications of Artificial Neural Networks in Chemical Problems. In: Artificial Neural Networks - Architectures and Applications, K. Suzuki (Ed.), Chapter 10*, ISBN 978-953-51-0935-8, 2013.

18. O. Ivanciuc, "Applications of Support Vector Machines in Chemistry," *Reviews in Computational Chemistry*, vol. 23, pp. 291–400, 2007.

19. M. Barker and W. Rayens, "Partial last squares for discrimination," *Journal of Chemometrics*, vol. 17, pp. 166–173, 2003.

20. K. G. Jöreskog and H. Wold, "The ML and PLS techniques for modeling with latent variables - historical and competitive aspects," *In K. G. Jöreskog and H. Wold, editors, Systems under indirect observation, Part 1, North-Holland, Amsterdam*, pp. 263–270, 1982.

21. I. S. Helland, "PLS regression and statistical models," *Scandinavian Journal of Statistics*, vol. 17, no. 2, pp. 97–114, 1990.

22. D. E. Rumelhart, G. E. Hinton, and R. J. Williams, "Learning internal representations by error propagation," *In Rumelhart, D. E. and McClelland, J. L., editors, Parallel Distributed Processing: Explorations in the Microstructure of Cognition. Volume 1: Foundations*, pp. 318–362, 1986.

23. R. D. Reed and R. J. Marks II, *Neural Smithing - Supervised Learning in Feedforward Artificial Neural Networks*, 1999, ISBN 0262181908.

24. C. Cortes and V. Vapnik, "Support-Vector Networks," *Machine Learning*, vol. 20, no. 3, pp. 273–297, 1995.

25. C. E. Chein-I, in *Hyperspectral Data Exploitation: Theory and Applications. Chapter 6: Unmixing Hyperspectral Data: Independent and Dependent Component Analysis*, ISBN 978-0471746973, 2007.

26. E. J. S. Wold and M. Cocchi, in *3D QSAR in Drug Design; Theory, Methods and Applications*, ESCOM, Leiden, Holland, pp. 523 - 550, 1993.

27. T. N. Tran, N. L. Afanador, L. M. C. Buydens, and L. Blanchet, "Interpretation of variable importance in Partial Least Squares with Significance Multivariate Correlation (sMC)," *Chemometrics and Intelligent Laboratory Systems*, vol. 138, no. 11, pp. 153–160, 1995.

28. T. Mukherjee and N. Kao, "PLA Based Biopolymer Reinforced with Natural Fibre: A Review," *Journal of Polymers and the Environment*, vol. 19, no. 3, pp. 714–725, 2011.

29. M. Wohllebe, F. Hollstein, R. Steller, and S. Bischoff, "Online-Separation of PET-Bottles by VIS-NIR Spectral Imaging," *Proc. Annual Conference on Image Processing for Automation, Lemgo (Germany)*, 10 Nov. 2011.

Sensitivity and selectivity in optical spectroscopy and imaging: A molecular approach

Rudolf W. Kessler

Steinbeis Technology Transfer Center Process Control and Data Analysis,
Herderstr. 47, 72762 Reutlingen,
Reutlingen University, Process Analysis & Technology, PA&T

Abstract Intelligent manufacturing has attracted enormous interest in recent years. Optical spectroscopy will play a major role in the sensor technology as it provides simultaneously chemical (by absorption) and morphological (by scatter) information. The paper demonstrates, that the sensitivity and selectivity of each individual technology has its limitations due to the structure of the molecule and the quantum mechanical limitations by their interaction with the photons. The absorption and scatter cross sections are defined and discussed in terms of sensitivity and selectivity of the different technologies. These fundamentals cannot be overcome. Furthermore, the suitability and robustness of each technology is pre-determined by the selection of appropriate light illumination sources and the selected detectors. An overview of the different techniques is given.

1 Introduction

Intelligent manufacturing has attracted enormous interest in recent years, not least because of the Process Analytical Technology/Quality by Design platform of the US Food and Drug Administration (FDA) and now also by the German initiative Industry 4.0 [1]. The future of industrial automation will be "arbitrarily modifiable and expandable (flexible), connect arbitrary components of multiple producers (networked), enabling its components to perform tasks related to its context independently (self-organizational) and emphasizes ease of use (user-oriented)". Optical spectroscopy will play a major role in the sensor

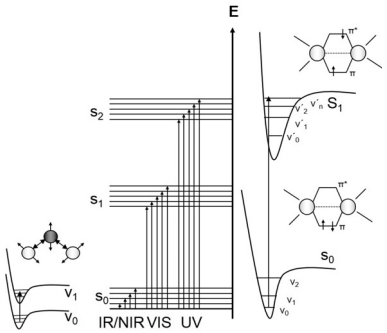

Figure 7.1: Electronic and vibrational transitions in optical molecular spectroscopy [2]

technology as it provides simultaneously chemical (by absorption) and morphological (by scatter) information [1].

Figure 7.1 shows the transitions involved using optical spectroscopy in the ultraviolet-visible range (UV-Vis: ca. 200 – 700nm, electronic transitions), near infrared (NIR: ca. 700 – 2500nm, combination vibrations, 1st, 2nd and 3rd overtones of fundamentals) and mid-infrared range (MIR: 2500nm – 25000nm, fundamental vibrations of valence bonds and fingerprint) [2].

The different ranges need suitable light sources with high intensity for illumination as well as classified detectors with as low as possible dark currents. Raman spectroscopy measures the emission (Raman scatter) from e.g. a virtually excited intermediate state into the vibrational ground state. Fluorescence spectroscopy measures commonly the emission from the first electronic excited state into the ground state (see also Figure 7.2) [2]. In most cases, both technologies use equipment also used in the UV-Vis spectroscopy.

This paper will focus on the optical molecular spectroscopy because the majority of inline applications uses these wavelength ranges. The objective of this paper is to demonstrate, that the sensitivity and selectivity of each individual technology has its limitations due to the structure of the molecule and the quantum mechanical limitations by their interaction with the photons. These fundamentals cannot be overcome.

Furthermore, the suitability and robustness of each technology is predetermined by the selection of appropriate light illumination sources and the selected detectors. Furthermore, system suitability and system testing is an integral part of many analytical procedures as described in the guideline of the international conference on harmonisation of technical requirements for registration of pharmaceuticals for human use (quality: ICHQ2 (R1), Nov. 2005: validation of analytical procedures) [3]. The tests are based on the concept that the equipment, electronics, analytical operations and samples to be analysed constitute an integral system which must be evaluated.

2 Sensitivity

Absorption cross section Sensitivity and selectivity are important features for the use of spectroscopy in sensor applications. "Analytical sensitivity" represents often the smallest amount of substance in a sample that can accurately be measured by a given technology. This is in general the concentration at which the mean response is statistically beyond the noise limits of the signal at zero concentration. In the pharmaceutical industry, specificity is normally used and defined: "Specificity is the ability to assess unequivocally the analyte in the presence of components which may be expected to be present. Typically these might include impurities, degradants, matrix, etc.", [3]. However, the international union of pure and applied chemistry recommends strongly to use only the term sensitivity [4].

The sensitivity of a molecule can be described by the quantum mechanical cross sections which are the effective area that governs the probability of an event of e.g. elastic scattering, or absorption, or emission (e.g. in fluorescence or Raman) of a photon at a specified wavelength with a molecule. The absorption cross section σ is given usually in cm^2/molecule and depend on the individual molecular structure of the compound and the quantum mechanical selection rules. The larger the absorption cross section, the easier it is to photo-excite the molecule. The total cross section is related to the absorbance of the Lambert-Beer's law and is proportional to the concentration of the species (as a number density) and the path length. The extinction or absorbance of the ratation is then the log of the reciprocal of the transmittance [5].

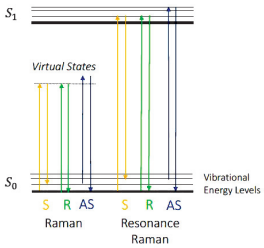

Technology	–log σ_a [cm²/molecule]
Fluorescence	20 - 15
Mid-Infrared	25 - 18
Near-Infrared	28 - 22
Raman	35 - 28
Rayleigh scatter	33 - 24

Figure 7.2: Left: schematics of the Raman scattering (S=Stokes shift, AS=anti-Stokes shift, R: Rayleigh scattering), right: table of absorption cross sections of the different technologies, Remark: figures may be very different for certain molecules

Figure 7.2 depicts the transitions of the Raman Scattering and Rayleigh scattering and shows also some figures of the absorption cross sections of the different technologies [6]. The reader should be aware, that the figure provide just a rough estimation of common data, but the exact figures are molecule dependent and may vary significantly from these data. The figures are in -log σ_a [cm^2/molecule], therefore low numbers show high sensitivity. For the sake of comparison, also the figures of the Rayleigh scattering is shown which can be attributed to a molecular scattering.

Examples of NIR- and MIR absorption spectra Vibrational absorption correspond to changes in the vibrational state of the molecule and are typically found in the infrared region, which is divided into far-, mid- and near-infrared. Ab initio calculations allow to predict the theoretical vibrational states [6]. There are plentiful text books available which can be used to attribute specific peaks to the molecule entity. This is important to relate spectral features in a causal manner to the chemometric models. This feature is also important to get an impression of the selectivity of the analytical method. MIR spectroscopy is a highly sensitive and selective method whereas NIR is not. The advantage of NIR in process analytics is that, due to the low absorption cross section, no sample pre-preparation is needed during the inline measurement. Figure 7.3 shows the NIR spectra of water in transmission with different

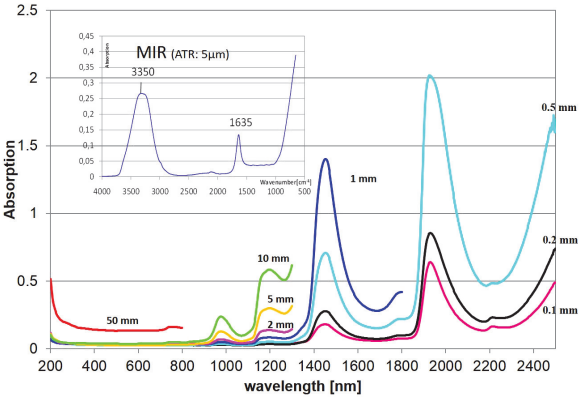

Figure 7.3: NIR spectra of water in transmission with different path lengths. Insert: ATR mid-infrared spectrum of water with a pathlength of app. 5µm [7]

path lengths. Combination bands are reasonable sensitive in the NIR region. The absorbance of the 1st, 2nd and 3rd overtone of the fundamental vibrations are successively at least one order of magnitude lower in their response. The insert shows also the ATR mid-infrared spectrum of water with a pathlength of 5µm only [7].

MIR spectroscopy is ideally suited to detect concentrations down to about the ppm concentration range whereas NIR spectroscopy may be limited to a range of 1%, at most 0.1%. Raman spectroscopy may be limited to about 1%, for specific molecules with a high Raman scattering cross section at a level of 0.1% due to its high selectivity. Fluorescence can be used for the determination of concentrations in the nanogram-range and sometimes even down to a single molecule level.

Example of UV-Vis spectra: Woodward-Fieser rules Electronic absorption corresponds to a change in the electronic state of an atom or molecule and are typically found in the visible and ultraviolet region. The energy associated with the quantum mechanical change primarily determines the frequency of the absorption, but the frequency can be shifted by several types of interactions with the molecule's environment. Absorption of a particular wavelength of light depends in UV-Vis spectroscopy mainly upon the π-electron system of the molecule.

The more the conjugation of the π-electron system within the molecule, the higher the wavelength of light it can absorb. The absorption coefficient μ_a [cm^{-1}] describes a medium containing many chromophores at a concentration described as a volume density ρ_a [cm^{-3}]. The absorption coefficient is essentially the cross-sectional area per unit volume of medium. Experimentally, the units [cm^{-1}] for μ_a are inverse length, such that the product $\mu_a L$ is dimensionless, where L [cm] is the photon's pathlength of travel through the medium.

Robert Burns Woodward and Louis Fieser put down a set of rules which allows one to calculate the wavelength of maximum absorption (λ_{max}) for a molecule empirically [8–10]. Many other authors refined these equations. The following equation (as an example: the Fieser-Kuhn rule) can be used to predict the wavelength of maximum absorption λ_{max} and also maximum absorptivity ϵ_{max}:

calculating λ_{max}

$$\lambda_{max} = 114 + 5M + n(48.0 - 1.7n) - 16.5R_{endo} - 10R_{exo}$$

calculating ϵ_{max} $\epsilon_{max} = (1.74 \times 10^4)n$

λ_{max} is the wavelength of maximum absorption in nm

ϵ_{max} is the maximum absorptivity in [cm^{-1} $mole^{-1}$]

M is the number of alkyl substituents / ring residues in the conjugated system

n is the number of conjugated double bonds

R_{endo} is the number of rings with endocyclic double bonds in the conjugated system

R_{exo} is the number of rings with exocyclic double bonds in the conjugated system.

Figure 7.4 shows an example.

It can be shown, that the properties are directly related to the molecular structure of the chemical entity. Due to the high cross sections, UV-Vis spectroscopy is extraordinary sensitive. However, selectivity is limited as the absorption peaks are clearly related to the number of conjugated double bonds and not to a specific molecule. Maybe in the future the electronic transitions of σ-bonds may be available, however technology must be developed as the absorption is significantly below

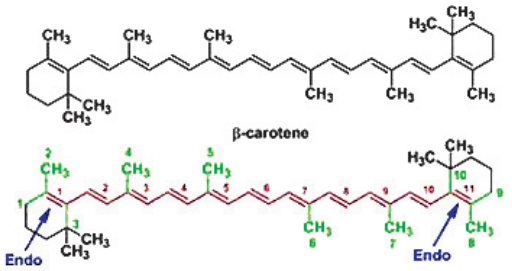

Figure 7.4: Fieser-Kuhn rules to predict the maximum absorption peak and maximum absorptivity of β-carotene (taken from [10])

200nm. Of course, the limit of detection can always be improved at higher signal to noise ratios when better detectors are used and by signal averaging.

Scattering cross section The advantage of optical spectroscopy is that simultaneously the chemical composition (by absorption) as well as the morphology can be measured in a spectrum due to scatter. Scatter perturbs the absorption spectra and is often unwanted and eliminated by chemometric tools. Scattering intensity is a function of the used wavelength and its polarisation and also depends on the angular distribution of the scattered light which in turn is dependent from the size, size distribution and shape of the particle.

As described before, Rayleigh scatter may be associated more to a molecular scatter and is wavelength dependent with $1/\lambda^4$. The scattering cross-section e.g. in the Mie or Fraunhofer regime is a hypothetical area which describes the likelihood of light being scattered by a particle, the scattering center. It is a measure of the strength of the interaction between the scattered particle and one or several scattering centres. Mie theory calculations will yield the efficiency of scattering which relates the cross sectional area of scattering, σ_s [cm^2] to the true geometrical cross-sectional area of the particle, A in [cm^2]. The scattering coefficient μ_s [cm^{-1}] is essentially then the cross-sectional area per scatterer number density ρ_s [cm^{-3}]. Depending on the geometry of the particle

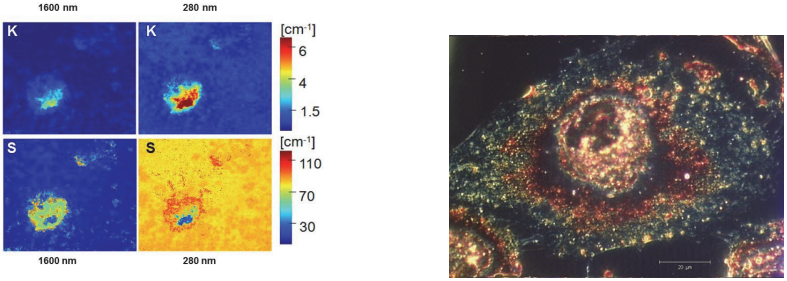

Figure 7.5: Left: Kubelka-Munk calculated scatter (S) and absorption coefficients (K) of an Aspirin particle in microcrystalline cellulose, right: white light scatter intensity of a glioblastoma cell measured in dark field arrangement

and its size, an anisotropy factor g may be integrated to account for forward and backward scattering efficiency [11, 12]. The scatter coefficient increases with shorter wavelengths app. $1/\lambda^n$, with $n = 0.2 \ldots 3$.

Scattering has a diagnostic value e.g. in biomedical sciences. Scattering depends on the ultrastructure of a tissue, e.g. the density of lipid membranes in the cells, the size of nuclei, the presence of collagen fibers, the status of hydration in the tissue, etc. Cells and nuclei are in the range of micrometres, mitochondria and lysosomes are in the range of 100nm to a few microns, membranes or collagen fibrils may be in the range 10nm up to 100nm. Scattering of light by structures on the same size scale as the photon wavelength is described by Mie theory. Scattering of light by structures much smaller than the photon wavelength is called the Rayleigh limit of Mie scattering, or simply Rayleigh scattering.

Using lager particles there is no universal theory to describe scatter. The radiative transfer equation, photon diffusion theory or a more empirical theory like Kubelka-Munk theory is used [1,2]. In any case, more than one measurement is needed to separate the two unknown absorption and scatter. Figure 7.5 shows an example of the scatter of a glioblastoma cell as well as the calculated scatter and absorption coefficients of an Aspirin particle in microcrystalline cellulose [1, 2, 12].

It is important to emphasize, that the scatter coefficient in this example is by a factor of 10 – 100 more sensitive to changes than the absorption coefficient. This means, any change in particle size or particle size distribution will have a significant influence on the spectral signature.

3 Selectivity

As described before although specificity is still used in the pharmaceutical industry, IUPAC recommends strongly to use selectivity to describe its capability to deliver signals that are free from interferences and give "true results" [3,4]. This implies, that if the signal of interferent and analyte can be separated, the sensitivity increases. This is the main reason why Raman spectroscopy can be as sensitive as NIR spectroscopy or even UV-Vis spectroscopy as the peaks of the components can directly be attributed and deconvoluted to the molecular entity, although the Raman cross section may be inferior to NIR and UV-Vis.

One clear definition is the following: "Selectivity of a method refers to the extent to which it can determine particular analyte(s) in a complex mixture without interference from other components in the mixture" [4]. Raman- and MIR-Spectroscopy are very selective spectroscopic methods and in most cases, the spectral features can easily be attributed to the individual molecules and entities. A good example is the selectivity of Raman spectroscopic investigations in aqueous solutions. The Raman signal of water is very weak, thus organic components can be detected without the interference of the water peak. This is not the case with MIR spectroscopy unless the signature lies in the fingerprint region between roughly 1000 – 1500 cm^{-1} (see insert in Figure 7.3). With an increasing photon flux, e.g. using lasers, and increasing path lengths even difficult analytical questions can be solved. UV-Vis and NIR spectroscopy and also fluorescence spectroscopy show broad peaks in solutions or particle mixtures and thus selectivity is significantly reduced. The advantage of UV-Vis and fluorescence spectroscopy is that water is not an interferent.

Using derivative spectroscopy greatly enhances the separation of even small changes in a spectrum with overlapping peaks [13]. Higher order derivative spectroscopy need spectra with a high signal to noise ratio together with a high reproducibility of the spectral signature of the overall system (see robustness below). Due to the technological developments in the silicon semiconductor industry (wavelength range from 170nm up to 1050nm) as well as the high absorption cross sections allow to quantitatively determine the concentration of many-components mixtures with a high precision. Especially in biotechnology, where aqueous systems are common with low concentrations of the compo-

nents, UV-Vis spectroscopy may be favourable upon NIR spectroscopy [7].

Furthermore, chemometric tools like principal component analysis (PCA) or partial least square regression (PLS) together with a pre-treatment of spectra can increase selectivity and sensitivity simultaneously. The responses are then based on interactions usually evaluated in a mathematical domain (chemometrics), giving what has been called "computational selectivity". In fact, selectivity is improved by a higher number of different measurements especially by use of a whole spectrum over a wavelength range instead of single wavelengths and processing the spectral data by chemometric methods with different spectral pre-treatments. The handling of near-infrared spectra in this way is a very good example of this approach.

The combination of several methods may enhance selectivity: multi-modal-sensor technology or multi-modal-spectroscopy [1]. A good example is 2-dimensional fluorescence spectroscopy (Excitation-Emission-Plot) where a mixture of components can spectroscopically be separated due to variations in the emission spectra excited at different wavelengths.

4 Robustness in inline spectroscopy and imaging

According to the ICHQ2 guideline, "robustness of an analytical procedure is a measure of its capacity to remain unaffected by small, but deliberate variations in method parameters and provides an indication of its reliability during normal usage [3]. The evaluation of robustness should be considered during the development phase and depends on the type of procedure under study. It should show the reliability of an analysis with respect to deliberate variations in method parameters. If measurements are susceptible to variations in analytical conditions, the analytical conditions should be suitably controlled or a precautionary statement should be included in the procedure [3]".

As a consequence a series of system suitability parameters must be established to ensure that the validity of the analytical procedure is maintained whenever used. This means that e.g. wavelength drifts, drifts of the intensity and colour temperature of the illuminations source, polarisation changes of the light must be controlled, preferable inline, as well

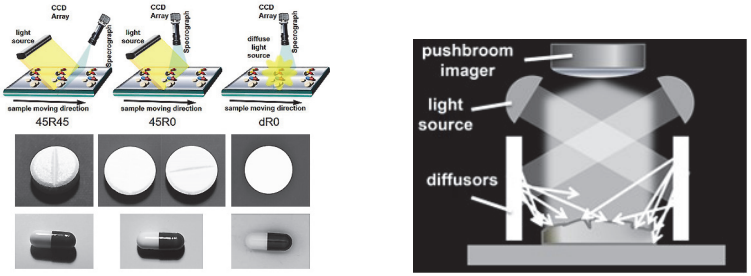

Figure 7.6: Left: example of the different optical set ups realized with an inline pushbroom imaging system and depicts the outline of the results which happen when the different illumination concepts are applied to tablets with a scratch or round shaped tablets with a strong specular reflection. Right: possible inline illumination with an even illumination from all directions

as a robust optical set up including flutter tolerance must be ensured [2]. Figure 7.6 shows an example, how a proper illumination and detection set up can influence the measured information [12].

In diffuse reflection, only scattered photons should be detected and thus all specular reflected photons from the surface of the material should be rejected. The standard setup which is commonly used in practical applications is an illumination at e.g. 45° and detection at 0° (denoted as 45R0). This works fine as long as the macroscopic sample plane is identical to the optical axis of the reflectors. However, specular reflected light can be superposed to diffuse reflected light when micro mirrors are present at the front phase of the sample (e.g. flat microscopic plates inside a lacquer), or a macroscopic curvature of the sample like a round shaped tablet directs the light into the detector. A planar sample like the presented tablet can show at e.g. 45° illumination and detection (45R45) some spots of specular reflection together with a shade. At 45R0 the specular reflections are minimized, but the sample still shows a shadow on the background and some minor shade at the boundaries of the surface.

Please note that if the scratch on the surface is in the direction of illumination (Figure 7.6, 45R0), no or little shade is produced, but in case of a mismatch of the orientation between illumination and the scratch, shades and even specular reflection may be observed. This optical arti-

fact can be eliminated by a proper data pretreatment and analysis, but very often at the expense of robustness of the chemometric model.

With diffuse illumination, no shadow on the surface and on the background material is present: the sample is almost ideally and homogeneously illuminated. If the sample is not planar like the capsule, a specular reflection spot is still present even at diffuse illumination but at a detection at 0° (dR0). The solution in this case may be to illuminate and detect the sample with an integrating sphere. Ideally the sample is therefore illuminated by a perfect Lambertian source and the detector is also integrated into an integrating sphere. A good approximation to a Lambertian illumination can be realized as shown in Figure 7.6, right, with the advantage to use it also for a continuous inline control.

5 Summary

Selectivity and sensitivity are key elements for an analytical chemist. Besides these key elements, many other aspects must also be taken into account to ensure robustness of the inline measurement [1, 2]. If the existing data are objectively classified, for example, from spectroscopic measurements, a direct and causal correlation of the spectral information to the functionality of the material is possible. The spectrum (the "spectral fingerprint" or "process trajectory") represents the entire morphology (due to scattering) and chemistry (due to absorption) of a substrate and can therefore be directly linked to the particular functionality of a product. Table 7.1 tries to summarize some features of the different techniques.

It is important to emphasize, that inline quality control by spectroscopic techniques is a holistic approach. Process chemists, process engineers, chemometricians, and many other technologists must work together where multimodality will be a bedrock supporting the production of smart materials in smart factories [1].

	UV/VIS/ s-NIR	NIR	MIR	Fluorescence	Raman
Selectivity	+	++	+++	++	+++
Sensitivity	+++	+(+)	+++	+++(+)	++(+)
Sampling	+++	+++	+	++	+++
Working in aqueous media	+++	+	+	++	+++
Applicability	+++	++	+	+	+
Process analytical tool	+++	+++	+	+	+++
Light guide glass	+++	+++	(+)	+++	+++
Signal	Absorption	Absorption	Absorption	Emission	Scattering
Samling online/inline	s, l, g	s, l	s, l, g	s, l (g)	s, l, (g)
Techniques	Transmission Reflectance ATR	Transmission Reflectance ATR	ATR (Transmission)	Reflectance Transmission	Reflectance
Relative costs	1	3 - 5	6 - 10	4 - 6	8 - 12

Table 7.1: Summary of properties of optical spectroscopic techniques for inline control (modified from [1] and [2])

References

1. R. W. Kessler, "Perspectives in process analysis," *J. Chemometrics*, vol. 27, pp. 369–378, 2013.
2. R. W. Kessler, Ed., *Prozessanalytik – Strategien und Fallbeispiele aus der industriellen Praxis*. Wiley-VCH Weinheim, 2006.
3. "Guideline of the international conference on harmonisation of technical requirements for registration of pharmaceuticals for human use (quality: Ichq2(r1)," Nov. 2005: validation of analytical procedures.
4. J. Vessmann, R. I. Stefan, J. F. van Staden, K. Danzer, W. Lindner, D. Burns, A. les Fajgelj, and H. Müller, "Selectivity in analytical chemistry," *Pure Appl. Chem.*, vol. 73, pp. 1381–1386, 2001.
5. http://en.wikipedia.org/wiki/Cross_section_(physics), download January 12th, 2015.
6. R. Aroca, *Surface-Enhanced Vibrational Spectroscopy*. John Wiley & Sons Ltd, 2006.
7. A. Kandelbauer, M. Rahe, and R. Kessler, "Process control and quality assurance – industrial perspectives," in *Handbook of Biophotonics, Vol.3: Photonics*

in Pharmaceutics, Bioanalysis and Environmental Research, First Edition, A. C. Juergen Popp, Valery V. Tuchin and S. Heinemann, Eds. Wiley-VCH Verlag GmbH & Co. KGaA, 2012.

8. R. Woodward and R. Burns, "Structure and the absorption spectra of alpha, beta-unsaturated ketones," *J. Am. Chem. Soc.*, vol. 63, no. 4, p. 1123, 1941.
9. L. F. Fieser, M. Fieser, and S. Rajagopalan, "Absorption spectroscopy and the structures of the diosterols," *J. Org. Chem.*, vol. 13, no. 6, pp. 800–6, 1948.
10. A. Mehta, "Ultraviolet-visible (uv-vis) spectroscopy – woodward-fieser rules to calculate wavelength of maximum absorption (lambda-max) of conjugated carbonyl compounds," postet on August 5, 2012 in Analytical Chemistry, Notes, "Ultraviolet-Visible (UV-Vis) Spectroscopy – Fieser-Kuhn Rules to Calculate Wavelength of Maximum Absorption (Lambda-max) of Polyenes (with Sample Problems)", postet on May 23, 2013 in Analytical Chemistry, Notes, download January 2015 from Wikipedia: http://de.wikipedia.org/wiki/Woodward-Fieser-Regeln.
11. L. S. Jacques and S. A. Prahl, "Course in biomedical optics," download January 2015, http://omlc.org/education/index.html.
12. B. Boldrini, W. Kessler, K. Rebner, and R. W. Kessler, "Hyperspectral imaging: a review of best practice, performance and pitfalls for inline and online applications," *Journal of Near Infrared Spectroscopy*, vol. 20, pp. 438–508, 2012.
13. J. Karpinska, "Basic principles and analytical application of derivative spectrophotometry," in *Macro to Nano Spectroscopy*, J. Uddin, Ed. InTech Publisher, 2012.

Towards many-class classification of materials based on their spectral fingerprints

Matthias Richter[1,2] and Jürgen Beyerer[2,1]

[1] Karlsruhe Institute of Technology, Institute for Anthropomatics and Robotics
Adenauerring 4, D-76131 Karlsruhe, Germany
[2] Fraunhofer Institute of Optronics, System Technologies and Image Exploitation (IOSB), Fraunhoferstr. 1, D-76131 Karlsruhe

Abstract Hyperspectral sensors are becoming cheaper and more available to the public. It is reasonable to assume that in the near future they will become more and more ubiquitous. This gives rise to many interesting applications, for example identification of pharmaceutical products and classification of food stuffs. Such applications require a precise models of the underlying classes, but hand-crafting these models is not feasible. In this paper, we propose to instead learn the model from the data using machine learning techniques. We investigate the use of two popular methods: support vector machines and random forest classifiers. In contrast to similar approaches, we restrict ourselves to linear support vector machines. Furthermore, we train the classifiers by solving the primal, instead of dual optimization problem. Our experiments on a large dataset show that the support vector machine approach is superior to random forest in classification accuracy as well as training time.

1 Introduction

Recent developments in consumer electronics have made compact hand-held spectrometers affordable for end-consumers. Products operating in the visible to the near infrared electromagnetic spectrum will most likely be available within this decade and might even be integrated into our smart phones in the not too distant future. This development gives rise to many exiting opportunities from research over retail to

health care. An obvious application is the identification and characterization of materials such as ore, food, and pharmaceutical products. For this the spectral signatures of different materials have to be condensed in some sort of model. Although the properties of many substances are well understood, building this model by collecting and combining expert knowledge is infeasible due to the sheer number of different materials. Moreover, this approach does not scale when more categories are to be included in the model. Instead, it is desirable to automatically infer the model from a given annotated sample of signatures. This way, human interaction is reduced to simply providing measurements and labels (e.g. material classes).

In this paper, we propose to use machine learning techniques to *learn* the model from a large, labeled sample of spectral signatures. Here we only consider classification: Given the spectrum of an unknown object, find the material of that object. We base the methods on our existing spectral material database, which contains hyperspectral images covering the UV, VIS and SWIR spectral bands (see [1] for more details). This dataset poses a number key challenges to the classification system:

- The number of classes is very large and novel classes can be added to the dataset at any time.
- Since the database consists of hyperspectral *images*, the number of spectral signatures per material is very large. In addition, the dataset is imbalanced, meaning that certain materials are represented with more signatures than others.
- The signatures show a high intra-class variance, especially (but not only) in recordings of natural materials.
- The system has to be able to cope with the high dimensionality of the data and the resulting *curse of dimensionality*[3].

Using spectral signatures to classify different materials is not a new idea. Mostly due to historical reasons, a lot of this research is conducted in the area of remote sensing, where one goal is to discriminate different types of land coverage (e.g. urban areas, types of forestry, and healthy

[3] The number of training samples required to estimate reliable models grows exponentially in the dimensionality of the feature space (also known as *Hughes phenomenon*).

vs. diseased crops). Here, specialized image processing and machine learning techniques have been proven useful to both classify coverage as well as extract discriminative features from raw data [2]. As documented in several extensive surveys (e.g. [3, 4]), a large portion of this work is concerned with support vector machines (SVM). This is due to their ability to derive good decision boundaries even with very few samples and large feature spaces, which is typically the case in remote sensing [5]. Recently the attention has turned toward the Random forest (RF) framework (e.g. [6, 7]). One benefit is that RFs can be used to determine spectral bands that are most suitable for classification. This information can later be employed to significantly reduce the amount of the stored data.

In light of this vast body of research and many successful applications, it is a bit surprising that this development is only slowly followed on a finer scale, e.g. in automated visual inspection. This is probably best explained by the relatively high costs of hyperspectral imaging sensors as well as slow data processing. Nonetheless, Lorente et al. reported recent developments in both sensor technology and techniques to analyze the data [8]. They find that the most prevalent methods revolve around classical statistical tools like principal component analysis and partial least squares for dimensionality reduction and linear discriminant analysis and artificial neural networks for classification.

However, all methods presented in [8] as well as the approaches found in remote sensing only deal with with a relatively moderate number of classes. In this paper, we instead ask the question: What machine learning methods are best suited to classify a large number of different classes based on their spectral signatures? For that we compare two promising candidates: support vector machines and random forests.

2 Methods

Given a set $\mathcal{D} = \{(\mathbf{s}_n, y_n)\}|n = 1, \ldots, N\}$ of spectral signatures $\mathbf{s}_n \in \mathbb{R}^D$ and class labels $y_n \in \mathbb{N}$, we search a hypothesis $H(\mathbf{s}) = y$ that maps unknown signatures to the most probable class. We wish the hypothesis to be consistent with $\mathcal{D}$, that is the number of misclassifications $H(\mathbf{s}_i) \neq y_i$ should be small. At the same time it should generalize well and not make too many mistakes on unseen data.

We take the spectral signature $\mathbf{s} = (s_1, \ldots, s_D)^\top$ to be the output of a hyperspectral sensor, meaning that each s_d corresponds to the measured intensity of a certain spectral band. However, we don't pay too much attention to the physical world: Whether $\mathbf{s}$ represents reflectance or transmission or how $\mathbf{s}$ has been processed to ensure comparability (black-/white-balance, normalization, etc.) is not of our concern, as long as these properties are consistent over all measurements.

2.1 Linear Support Vector Machines

As mentioned in Section 1, support vector machines have been very successfully applied to classification of hyperspectral data. A linear SVM is a binary classifier ($y = \pm 1$), that classifies $\mathbf{s}$ according to

$$H(\mathbf{s}) = \operatorname{sgn}(\mathbf{w}^\top \mathbf{s} + b). \tag{8.1}$$

From a geometric perspective $\mathbf{w} \in \mathbb{R}^D$ and $b \in \mathbb{R}$ define a hyperplane in the D-dimensional feature space. Classification into either the positive or negative class amounts to determining whether $\mathbf{s}$ falls "left" or "right" of that hyperplane. In training, $\mathbf{w}$ and b are chosen to best separate the two classes while simultaneously maximizing the *margin*, i.e. the distance $\frac{1}{\|\mathbf{w}\|}$ of the hyperplane to nearest training samples (the *support vectors*). This amounts to solving the unconstrained optimization problem [9]

$$\text{minimize} \quad \|\mathbf{w}\|^2 + C \sum_{n=1}^{N} L(y_n, \mathbf{w}^\top \mathbf{s}_n + b), \tag{8.2}$$

where $L(y, t)$ denotes the *loss* to classify a sample as $\operatorname{sgn}(t)$ when the true class is y. We use $L(y, t) = max(0, 1 - yt)^2$, but other loss functions are possible as well. The parameter C balances the two conflicting training goals: a large value puts more emphasis on class separation, while a small value results in larger margins.

Traditionally equation (8.2) is minimized by solving a dual problem. However, it has been shown that if the number of dimensions D is small in comparison to the number of training samples N, primal optimization is both faster and produces more stable results [9].

There are also extension to nonlinear classification by using kernel functions to implicitly map features into a higher-dimensional space,

where linear separation is possible. However, as the dimensionality of the spectral signatures is already very high and because it can reasonably be assumed that the signatures are normally distributed and therefore linearly separable, we chose to stick with linear SVMs.

Multiclass SVM

Equation (8.1) formalizes SVM as a binary classifier, but the goal is to classify spectral signatures into one of (very) many different classes. A straightforward way to extend SVM to multi-class problems is to train multple classifiers $h_{ij}(\mathbf{s})$ that separate class i from class j – one for each unordered pair of classes. Classes are assigned by majority-vote[4]:

$$H(\mathbf{s}) = \arg\max_y \sum_{i,j} \mathbf{1}[h_{ij}(\mathbf{s}) = y]. \tag{8.3}$$

While simple, this *one-vs-one* scheme has two key advantages over a closed form multi-class SVM formulation: Firstly, when novel classes are introduced only parts of the classifier have to be retrained. Secondly, it allows to exploit prior knowledge in classification: When one knows a list of candidate classes for a given material (e.g. minearals, plastics), only a small number of classifiers has to be evaluated, which decreases computation time as well as the risk of misclassification. This comes at the cost of increased computation effort in training and classification. However, as classification only requires a single dot-product, this is not a major concern.

2.2 Random Forests

Random forests have become popular alternative to SVMs. The training algorithm is relatively simple, yet provides good results out of the box with little to no parameter tweaking. A random forest is an ensemble of decision trees, where each tree h_t is trained separately on a different random subset of the training samples. The nodes k in each tree correspond to thresholds τ_k and features s_k. The restulting binary test $s_k < \tau_k$ divides the training set for $\mathcal{D}_k$ that node into $\mathcal{D}_k^+$ and $\mathcal{D}_k^-$. It is chosen

[4] We abuse notation and write $h_{ij}(\mathbf{s}) = y$ to denote that h_{ij} voted in favor of class y.

to minimize the gini impurities, i.e. with $\mathcal{D}_k^\circ$ denoting either split:

$$I_G(\mathcal{D}_k^\circ) = 1 - \sum_y \left(\frac{\sum_{\mathbf{x}_n \in \mathcal{D}_k^\circ} \mathbf{1}[y_n = y]}{|\mathcal{D}_k^\circ|} \right)^2. \tag{8.4}$$

The training procedure is repeated recursively on the two child nodes until some stopping criterion is met. To encourage diversity in the trees of the ensemble, only a random subset of N_f features (usually $N_f = \lceil \sqrt{D} \rceil$) is considered for each split. After construction, the M_t leaf nodes of the tree correspond to disjoint regions $\mathcal{R}_{tm}$ in the feature space; each region is associated with an estimate of class membership probability

$$\hat{p}_{tm}(y) = \frac{1}{|\mathcal{R}_{tm}|} \sum_{\mathbf{s}_n \in \mathcal{R}_{tm}} \mathbf{1}[y_n = y]. \tag{8.5}$$

The class of a sample is predicted by traversing each tree and averaging the reached probability estimates,

$$H(\mathbf{s}) = \arg\max_y \hat{p}(y|\mathbf{s}), \text{ where} \tag{8.6}$$

$$\hat{p}(y|\mathbf{s}) = \frac{1}{T} \sum_{t=1}^{T} \sum_{m=1}^{M_t} \mathbf{1}[\mathbf{s} \in \mathcal{R}_{tm}] \; \hat{p}_{tm}(y). \tag{8.7}$$

As this procedure only involves thresholds and sums, RFs are very fast classifiers. Training and prediction are also trivial to parallelize by training or traversing each tree in its own thread. Furthermore, each tree can in principle be inspected and the decisions it takes can be understood. However, the main advantage over SVMs is that RFs are inherently multi-class classifiers. Yet in our case this can also be seen as a drawback, as prior knowledge cannot easily be incorporated and the whole classifier has to be retrained when novel classes are introduced.

3 Experiments

We compared the suitability of both methods using two subsets of our hyperspectral database [1]. We constrained our experiments to measurements in the near infrared spectrum; the dimensionality of the spectral signatures was $D = 224$. The first subset contained 13 classes and of

Table 8.1: Overview over the dataset used in this study.

Samples in set A		Additional samples in set B	
Material class	**Samples**	**Material class**	**Samples**
Acolon grapes	37 933	Dornfelder grapes	41 688
Calcite	190 656	Hard candies	20 731
Chalcedony	117 652	Hazelnuts	34 911
Dolomite	300 286	Lemberger grapes	77 388
Ivy leaves	108 859	Milk	123 308
Maple leaves	129 987	Müller-Thurgau	109 695
Magnesite	565 639	Pinot blanc grapes	720 936
Pinot gris grapes	91 389	Pinot meunier grapes	41 315
Pinot noir grapes	688 459	Pinot noir précoce grapes	73 667
Quartz	118 675	Riesling grapes	810 418
Sausage	344 588	Serpentine	421 729
Talc	136 520	Trollinger grapes	189 095
White bread	430 960	Wheat flour	112 132
		White Sugar	139 945

more than 3 000 000 samples. The second subset contained 14 additional materials, resulting in 27 classes and more than 6 000 000 samples in total. Table 8.1 lists the used materials and number of samples for each class. The dataset contains very different (e.g. *Quartz*, *Ivy leaves*), very similar (wine varieties, minearals) and very loosely defined (*Sausage*, *White bread*) materials. It is also heavily imbalanced: *Riesling*, for example, is represented by twenty times more samples than *Acolon*.

We performed stratified 5-fold cross-validation in all experiments. With linear SVM, we set $C = 1$ and did not perform any parameter tuning. With RF, we set the number of trees to $T = 10$ and experimented with different maximum tree depths d as stopping criterion.

With 13 classes, training all 78 SVM classifiers took $42min$ on a $2.6GHz$ 16-core Intel Xeon CPU. This amounts to roughly $30s$ per classifier or $0.2ms$ per training sample. Training a RF with $d = 10$ required $41min$ ($0.9ms$/sample) to complete, while a RF with $d = 20$ increased training time to $52min$. On average, classifying a single sample required $171\mu s$ with one-vs-one SVMs, while with RFs it took only $8\mu s$ resp. $10\mu s$ with $d = 10$ and $d = 20$ respectively.

Classifier performance is summarized in Table 8.2. It can be seen that

Table 8.2: Overview over the results of our experiments.

Dataset	Classifier	Mean F_1	Min F_1
A	SVM	$0.95_{\pm 0.0003}$	$0.79_{\pm 0.001}$
A	RF ($d = 10$)	$0.85_{\pm 0.003}$	$0.59_{\pm 0.025}$
A	RF ($d = 20$)	$0.90_{\pm 0.001}$	$0.49_{\pm 0.007}$
B	SVM	$0.79_{\pm 0.0002}$	$0.28_{\pm 0.002}$
B	RF ($d = 20$)	$0.74_{\pm 0.001}$	$0.03_{\pm 0.003}$
B	RF ($d = 30$)	$0.79_{\pm 0.001}$	$0.16_{\pm 0.005}$
B	RF ($d = 50$)	$0.79_{\pm 0.001}$	$0.22_{\pm 0.005}$

the SVM approach consistently outperforms RFs, but the results suggest that RF can reach similar performance with deeper decision trees. However, deeper trees will also significantly increase the training time.

Figure 8.1 shows confusion matrices for the SVM and RF classifiers in the 13-class experiment. Overall the SVM classifier is relatively consistent; most often confused are the classes 1, 8 and 11 (*Acolon*, *Pinot gris* and *Pinot noir*) as well as the minerals *Quartz*, *Magnesite* and *Chalcedony* (classes 5, 9 and 10). RF is more robust towards the latter, but more susceptible to confuse the wine varieties to the point where *Acolon* and *Pinot gris* are more often classified as *Pinot noir* than the true class. Similar results can be observed in Fig. 8.2: Classification is quite consistent and confusion is concentrated on similar material groups (wine varieties and minerals). Here, too, random forest is more more susceptible to misclassification than one-vs-one SVM.

4 Summary

In this paper, we investigated the suitability of linear support vector machines and random forest classifiers for the task of discriminating a large number of materials using their spectral signatures. While RF supports multi-class classification out of the box, SVM does not. To achieve multi-class classification, multiple linear SVMs were combined to a single classifier in a one-vs-one scheme. Experiments showed that the SVM approach is superior both in classification performance and training time. The former can be attributed to multiple classifier fusion, while the latter is a result of the *primal* (instead of the usual *dual*) for-

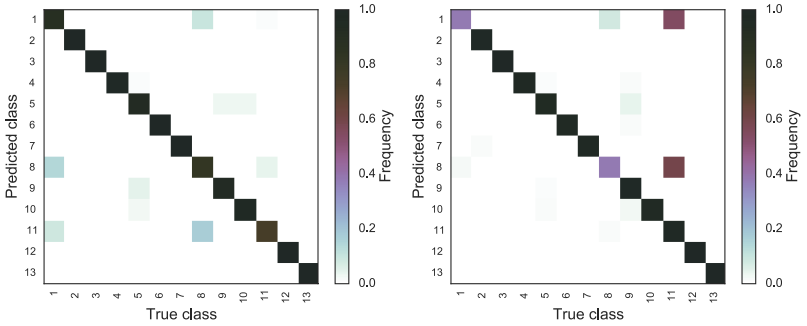

(a) SVM (b) RF ($d = 20$)

Figure 8.1: Selected confusion matrices in the 13-class experiments.

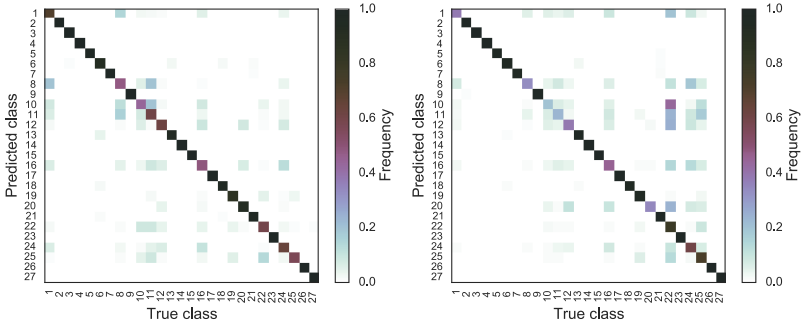

(a) SVM (b) RF ($d = 50$)

Figure 8.2: Confusion matrices in the 27-class experiments.

malization of the training goal. Classification time, on the other hand is significantly slower. However, since it is still performed in the order of a few hundred microseconds, this is not too big of a concern. In light of these results, we suggest to prefer SVM over RFs. This has the additional benefit that prior knowledge about the material class can easily be incorporated in classification.

In the future, we expect to be able to reduce training time and increase classification performance by suitable pre-processing methods (e.g. whitening, dimensionality reduction) and automatic parameter

tuning. Additionally, we would like to explore the potential of the recently proposed extreme learning machines (ELM) [10] as an alternative to support vector machines. Preliminary experiments with ELM have shown promising results in that regard.

References

1. S. Irgenfried and C. Negara, "A framework for storage, visualization and analysis of multispectral data," in *OCM 2013 - Optical Characterization of Materials - conference proceedings*, 2013, pp. 203–214.
2. P. K. Varshney and M. K. Arora, *Advanced image processing techniques for remotely sensed hyperspectral data*. Springer, 2004.
3. A. Plaza, J. A. Benediktsson, J. W. Boardman, J. Brazile, L. Bruzzone, G. Camps-Valls, J. Chanussot, M. Fauvel, P. Gamba, A. Gualtieri *et al.*, "Recent advances in techniques for hyperspectral image processing," *Remote sensing of environment*, vol. 113, pp. S110–S122, 2009.
4. G. Mountrakis, J. Im, and C. Ogole, "Support vector machines in remote sensing: A review," *ISPRS Journal of Photogrammetry and Remote Sensing*, vol. 66, no. 3, pp. 247–259, 2011.
5. F. Melgani and L. Bruzzone, "Classification of hyperspectral remote sensing images with support vector machines," *IEEE Transactions on Geoscience and Remote Sensing*, vol. 42, no. 8, pp. 1778–1790, Aug. 2004.
6. P. O. Gislason, J. A. Benediktsson, and J. R. Sveinsson, "Random forests for land cover classification," *Pattern Recognition Letters*, vol. 27, no. 4, pp. 294–300, 2006.
7. V. Rodriguez-Galiano, B. Ghimire, J. Rogan, M. Chica-Olmo, and J. Rigol-Sanchez, "An assessment of the effectiveness of a random forest classifier for land-cover classification," *ISPRS Journal of Photogrammetry and Remote Sensing*, vol. 67, pp. 93–104, Jan. 2012.
8. D. Lorente, N. Aleixos, J. Gómez-Sanchis, S. Cubero, O. L. García-Navarrete, and J. Blasco, "Recent Advances and Applications of Hyperspectral Imaging for Fruit and Vegetable Quality Assessment," *Food and Bioprocess Technology*, vol. 5, no. 4, pp. 1121–1142, Nov. 2011.
9. O. Chapelle, "Training a support vector machine in the primal," *Neural Computation*, vol. 19, no. 5, pp. 1155–1178, 2007.
10. G.-B. Huang, "An insight into extreme learning machines: random neurons, random features and kernels," *Cognitive Computation*, pp. 1–15, 2014.

NIR spectral imaging for the in-line detection of preservatives in recovered wood

Dirk Mauruschat, Jochen Aderhold, Burkhard Plinke and Peter Meinlschmidt

Fraunhofer Institute for Wood Research (WKI),
Bienroder Weg 54E, D-38108 Braunschweig

Abstract Various contaminants in recovered wood, including wood treated with preservatives, limit its use for the production of particle boards due to technical reasons and, in some countries, national legislation. In order to sort them out from a stream of recovered wood, in-line detection techniques for these contaminants are necessary. The work presented here shows that NIR spectral imaging has the potential to differentiate between various organic and inorganic wood preservatives qualitatively as well as quantitatively.

1 Introduction

Recovered wood becomes more and more important as a raw material for particle board production in Europe. However, the amount of recovered wood used for wood based panels is quite different in the EU countries due to different national legislation. In Germany for example, recovered wood for wood based panels has to be free from thermoplastic and duroplastic polymers, PVC, coatings, foam, wood preservatives and suchlike, which is often not the case in practice. Consequently, the share of recovered wood in particle boards is only 33 % in Germany whereas it amounts to 89 % in Italy [1].

A possible way to increase the use of recovered wood for panel production is to upgrade it by sorting out the contaminants. This requires powerful in-line methods for the fast detection of the above mentioned materials. Among these, wood preservatives are most difficult to detect. In an internal research project of the Fraunhofer Gesellschaft, various methods for the detection of wood preservatives were examined,

including ion mobility spectroscopy, X-ray fluorescence, and near infrared spectral imaging. The latter is particularly interesting for sorting highly contaminated material because it allows not only the detection but also the localization and selective removal of single contaminated particles.

2 State of the Art

The removal of contaminants such as stones, concrete, and metals from recovered wood by physical and mechanical methods using differences in density, electrical conductivity or magnetic properties is state of art. The remaining task is to sort out contaminants which are similar to wood in the above mentioned properties. This is true for plastics and of course for wood treated with preservatives.

A possible way to sort out these remaining contaminants is to adapt commercially available sorting systems for plastics and similar materials (see fig. 9.1). To do this, it is necessary to shred the wood into chips having a size of a few centimetres and to put them on a conveyor belt. On the conveyor belt the chips pass a detection unit where the presence (and, if possible, the position) of a contaminated chip is detected. At the end of the conveyor belt a row of compressed air operated nozzles can be used to selectively remove the contaminants from the wood stream. Many different methods have been successfully applied to the detection of contaminants in recovered wood in the laboratory. Among these, ion mobility spectroscopy (IMS, [2]), X-ray fluorescence (XRF, [3]) and near infrared (NIR) spectroscopy [4] have recently proven their potential to detect organic and inorganic wood preservatives in-line. XRF is particularly suited to detect preservatives containing As, Cu and similar elements. Organic contaminants can be detected at very low concentrations in the mg/kg range by IMS. However, both techniques are not spatially resolving. This means that they can only tell the presence, but not the position of a contaminant. Consequently, one has to sort out not only the contaminant itself but some of the surrounding good material as well. This is not a problem for wood with a low level of contamination. For highly contaminated wood, however, it is necessary to remove only the contaminated chips in order to work efficiently. For such applications, a spatially resolving detection technique is mandatory.

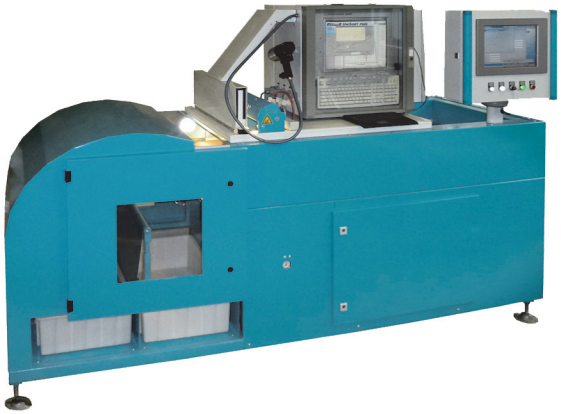

Figure 9.1: Commercially available sorting system for the recycling industry (RTT Steinert)

For NIR spectroscopy, cameras with good spatial and spectral resolution are now available which makes this technique suitable for sorting applications. The advantages of NIR spectroscopy are that the method is contactless, non-destructive, free of radiation hazards, rapid and easy to use. The sample preparation is simple, if needed at all. Therefore in-line measurements are possible, enabling the implementation in an existing sorting system.

A potential challenge for NIR detection of wood preservatives is their often low concentration which can be below 0.1 % - 0.5 % and thus below the limits of detection. NIR is not known as a technique for trace analysis. On the other hand, preservatives are normally applied to the surface of wood pieces, and NIR spectra originate close to the surface. Thus, there is hope to find sufficiently strong signals. Furthermore, inorganic compounds are often difficult to detect in NIR spectra. Consequently, one important aim of the work presented here was to find out if organic and even inorganic wood preservatives can be detected in NIR spectra of recovered wood at sufficiently low concentrations so that an efficient NIR sorting becomes possible.

Sample No.	PCP	Lindane	$CuCO_3$ $Cu(OH)_2$	H_3BO_3	Cu-HDO	Benzalkonium-chloride	Propiconazol	Didecylpolyoxyethyl-ammoniumborate
Holz10B	x	x						
Holz8			x	x	x			
Holz9			x	x		x	x	
Holz1D	x	x	x	x				x

Figure 9.2: Specifications of samples treated with four different mixtures of wood preservatives

3 Experimental

NIR spectra were taken using a SpectralEye RedEye 2.2 system from inno-Spec GmbH (Germany). The system is sensitive in the wavelength range from 1100 nm to 2200 nm, has a transmissive grating and a cooled extended InGaAs detector with 256 x 320 pixels (spectral x spatial) and a frame rate of 330 Hz. Spectral images were acquired using the push-broom imaging principle [5]. Samples were scanned using a black conveyor belt at a speed of 5 m/min. In such a way, a complete spectrum for every pixel of the surface was obtained. The samples were illuminated with four halogen lamps having a power of 250 W each.

In order to increase the signal-to-noise ratio, the recorded spectral images had to be smoothed in the spectral dimension by Savitzky-Golay filtering and in the spatial dimensions by median filtering. Afterwards various chemometric techniques [6] were applied in order to reduce the data, including principal components analysis (PCA) and the PARAFAC algorithm. In some cases, additional data classification by means of Linear Discriminant Analysis (LDA) was necessary.

One surface of a number of pine wood samples with a size of a few centimetres was treated with four different typical mixtures of commercially available wood preservatives. These mixtures consist of several components. Fig. 9.2 shows which components are present in the samples, together with the sample numbers. Samples were arranged on a board as shown in the left part of fig. 9.3 and scanned as described above. The right part of fig. 9.3 shows the spectral image of the samples, averaged in the spectral dimension. The distortion in transport direction is a consequence of the specific conveyor belt speed chosen.

A second set of six pine wood samples was treated with Cu(II) sulfate only, but with various concentrations ranging from less than 1 mg Cu

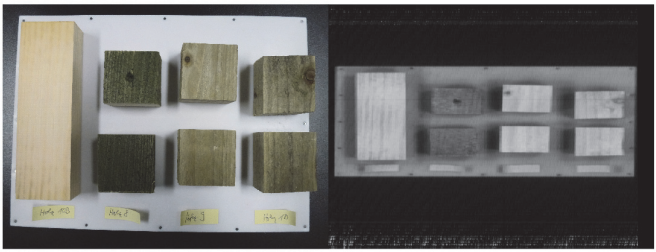

Figure 9.3: Colour photography and spectral image (mean intensity mapped as grey values) of the of samples

per kilogram dry mass (untreated wood) to 25390 mg Cu per kilogram dry mass. The concentrations were measured by wet chemistry.

4 Results

In a first step the spectral image was divided into a training set and a validation set. These sets corresponds to the lower and to the upper half of fig. 9.3, respectively. The training set was then manually segmented into regions of equal chemical composition. Reference spectra were obtained by spatial averaging over these regions. Fig. 9.4 shows the raw spectra of the first set of samples. They have different intensities, but also slightly different structures so that a discrimination of the various samples seems feasible. Especially the intensity and also the intensity variations of sample Holz8 are much smaller than in the other samples. This corresponds to the darker colour of the sample (fig. 9.3) due to the fact that it is the only sample containing Cu-HDO. Additional reference spectra were obtained for the underlying board, for the conveyor belt, and even for the paper labels (fig. 9.3). It is often recommended to get rid of intensity differences and linear trends by taking the first or second derivative of the spectra. However, intensity differences can also be regraded as additional information which helps to differentiate between samples. Furthermore, taking the derivative will amplify noise. Smoothing algorithms such as the Savitzky-Golay algorithm will

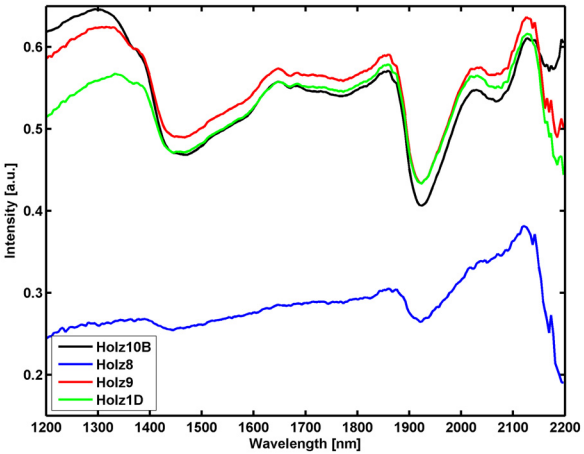

Figure 9.4: Raw spectra of the first set of samples

reduce this effect, but at the expense of loosing spectral information. In the work presented here, we have tried all three options (raw data, first and second derivative) and obtained the best classification results for the raw data. This can be different for samples with a more complex topography and corresponding intensity differences due to shading.

In a next step, all spectra of the chemically homogeneous regions were analysed in order to check if they are close enough to the reference spectra to allow an automatic classification, or if the random variations are too big to make this possible. In order to apply standard classification methods, the typically 248 spectral intensity values for each geometrical pixel have to be condensed into a smaller number of data points. The most important methods for this purpose are the principal components analysis (PCA) and the canonical polyadic decomposition, also known as PARAFAC. Both methods were applied in this work, and a number of four components was chosen for both in order to account for at least 99 % of the data variance. Score plots were generated for every possible combination of components, and those plots were selected which gave the best clustering for spectra which belong together. These are shown in 9.5. It is apparent that the separation of different clusters is more pronounced in the PARAFAC components than in the PCA com-

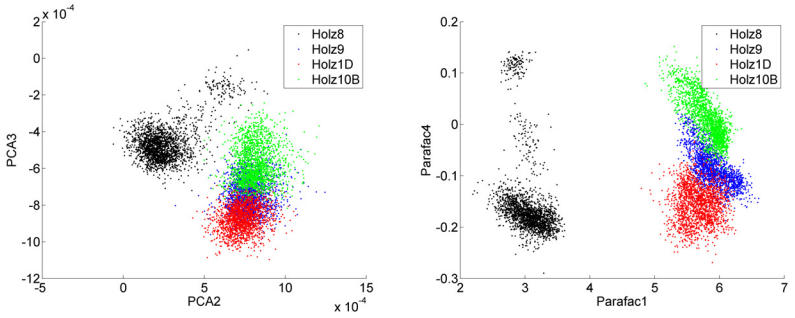

Figure 9.5: Optimum score plots for PCA and PARAFAC, respectively

ponents for these samples. Consequently, the PARAFAC algorithm was chosen for the next steps. This does not mean, however, that PARAFAC is generally superior to PCA. In a last step it was tested if the information obtained from the training set is sufficient to properly classify the complete spectral image (including the validation set). Although a cluster analysis by k-means could be a suitable classification method for this special case, the more general Linear Discriminant Analysis (LDA) was applied. The idea of this method is to compare every single spectrum of the spectral image to each of the seven reference spectra (four samples, board, conveyor belt, and paper labels) and put it into the same class as the reference spectrum it is most similar to. Actually, the PARAFAC components from the last step were chosen as the input for LDA rather than the spectra themselves. Taking the latter as the input gave inferior results, since the number of spectral data points per spatial pixel is too high for this method.

The result of the classification is shown in 9.6. Every spatial pixel is coded with a specific colour given by the class it was classified into. It can be seen that the complete spectral image (including the validation set) is in general classified properly. Some misclassification appears where the samples throw shadows onto the board. It is believed that this problem can be solved by standard methods of image segmentation.

The second set of samples, treated with various concentrations of Cu(II) sulfate, was analysed in the same way. For the reference spectra, a linear regression between the four principal components and the

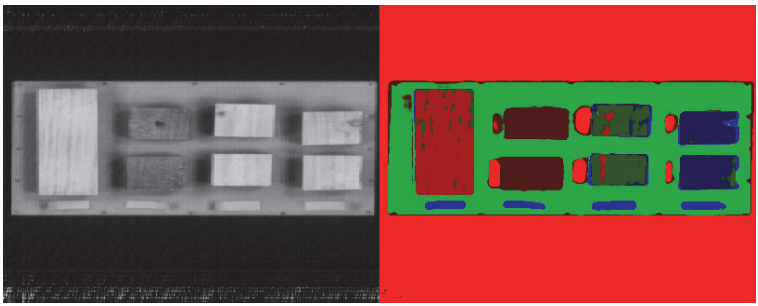

Figure 9.6: Classification result. Each colour corresponds to one class.

Cu concentration was made. The Cu concentrations calculated from the reference spectra using this linear regression are compared to the wet chemically measured Cu concentrations for the six samples in fig. 9.7. The agreement is quite good, with the exception of the highest concentration which is a possible outlier. In the same way, Cu concentrations could be calculated for each spatial pixel using the local spectra. The resulting concentration image is shown in fig. 9.8. Apparently, the characteristic pattern of late wood and early wood of the samples is still visible. It remains to be checked if this is a direct influence of the wood chemistry on the spectra, or if the preservatives diffuses differently into late wood and early wood, respectively.

5 Summary and Conclusion

Pine wood samples treated with various kinds and various concentrations of wood preservatives were characterized by NIR spectral imaging. After proper data processing it was possible to classify the spectra according to the chemical composition at surface. This is true not only for organic preservatives, but also for inorganic preservatives. This is most likely the consequence of a chemical reaction between the inorganic preservative and the wood constituents. In at least the case of Cu(II) sulfate the preservative can be detected quantitatively.

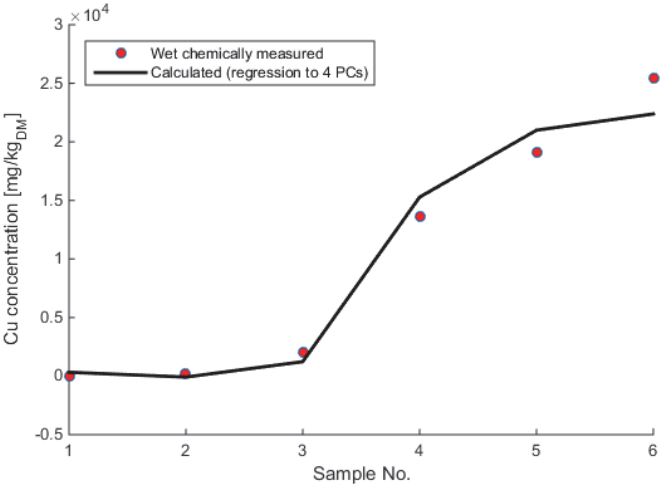

Figure 9.7: Comparison of wet chemically measured and calculated Cu concentrations

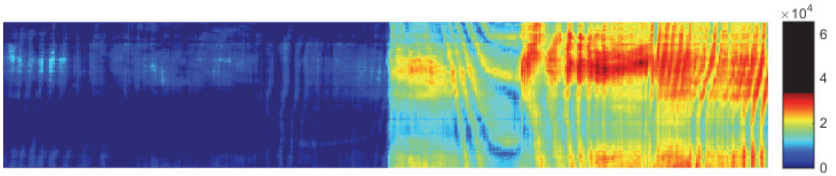

Figure 9.8: Concentration image calculated from the spectral image. Values are in mg Cu per kilogram dry mass.

References

1. "Epf annual report 2013/14," European Panel Federation, Tech. Rep., 2014.
2. D. Mauruschat, A. Schumann, P. Meinlschmidt, J. Gunschera, and T. Salthammer, "Application of gas chromatography-field asymmetric ion mobility spectrometry (gc-faims) for the detection of organic preservatives in wood," *International Journal for Ion Mobility Spectrometry*, vol. 17, no. 1, p. 1, 2014.

3. R. Briesemeister, "Analyzing the suitability of x-ray fluorescence (xrf) devices for detecting foreign material in recovered wood," 2013.
4. M. Asbach, D. Mauruschat, and B. Plinke, "Understanding multi-spectral images of wood particles with matrix factorization," in *OCM 2013-Optical Characterization of Materials-conference proceedings*. KIT Scientific Publishing, 2013, p. 191.
5. R. W. Kessler, *Prozessanalytik: Strategien und Fallbeispiele aus der industriellen Praxis*. John Wiley & Sons, 2012.
6. W. Kessler, *Multivariate Datenanalyse: für die Pharma, Bio-und Prozessanalytik*. John Wiley & Sons, 2007.

Acquisition and storage of multispectral material signatures – Workflow design and implementation

Stephan Irgenfried[1] and Jürgen Hock[2]

[1] Karlsruhe Insitute of Technology
Institute for Anthropomatics and Robotics IAR
Intelligent Process Control and Robotics Lab IPR
Engler-Bunte-Ring 8, 76131 Karlsruhe
[2] Fraunhofer Institute of Optronics,
System Technologies and Image Exploitation
Fraunhoferstr. 1, 76131 Karlsruhe

Abstract This article describes design, hard- and software implementation of devices and a workflow for acquisition, processing, storage and analysis of multispectral material signatures. An approach for a consistent process from measurement to analysis is presented, utilizing standard formats for multi-dimensional image data. Finally applications are demonstrated that make use of the material signatures database.

1 Introduction

The "spectral fingerprint" of materials, which describes, how the material reflects or absorbs incident light at different wavelengths, is of use for many applications in science and industry, e.g. quality inspection, sorting, pharmacy or food freshness checks. All the applications have in common, that they need a base of material signatures data to be used for comparison, classification and analysis. Based on the ideas and the work presented in [1] we describe additional components of the workflow, the implementation of the whole tool chain, the data acquisition and storage infrastructure and the data analysis and access modules.

2 Related Work

In [2] Hüni et. al differentiate between file based spectral libraries and spectral databases which make use of a Database Management System (DBMS). Literature shows, that this assumption is not used consistently. There are spectral libraries with online access as well, e.g. [3]. In the view of Clark et. al [4], an ideal spectral library contains many materials and covers a large wavelength range together with metadata about the measurement. They created the USGS Digital Spectral Library [3]. In [5] Bojinski et. al introduced a change in infrastructure from pure file based libraries to using a relational database for their system called SPECCIO [4]. They describe the advantages of this architecture which have been picked up and extended by our work. Improvements to the SPECCIO database model were published by Hüni and Tuohy in [6]. In the same work they presented a database client software for data acquisition, processing and database access called SpectraProc. Ferwerda et. al implemented a similar architecture in [7], including a web-based interface and sample location view in Google Earth®. Their website [5] was not accessible by Jan. 15th 2015. Some of the page can be accessed using wayback machine [6]. Compared to SPECCIO, SpectraProc and Ferwerda's work, our approach is a hybrid system which uses both, file based storage and a relational database. This is similar to the Common Hyperspectral Image Database Design CHIDB published by Tian et. al in [8]. Other databases accessible via a web-based interface are the ASU Spectral Library[7], founded by Christensen et. al [9] and the ASTER spectral library[8] by Baldridge et. al [3].

3 Workflow

Figure 10.1 shows the components of our workflow, starting with material measurement and ending with data analysis. For the repeatability of the measurements and to get results comparable to measurements

[3] http://speclab.cr.usgs.gov/spectral-lib.html
[4] http://specchio.ch
[5] http://www.hyperspectral.info
[6] http://web.archive.org/web/20140103004905/http://hyperspectral.info/
[7] http://speclib.asu.edu/
[8] http://speclib.jpl.nasa.gov

Figure 10.1: Workflow of the material signature acquisition and storage

taken by other institutions, we developed standard procedures to be executed for every measurement, e.g. white and black balance. With the help of a web-based application, the user is guided through the whole process reducing the risk of incomplete or inconsistent records in the database. To keep flexibility high in the whole process, we split it in several separate modules, which will be described in more detail later.

4 System Components

4.1 Data Acquisition / Material Measurement

Data acquisition is the fundamental part of the introduced workflow for multispectral data analysis and can be characterized by the following general requirements:

- capturing of samples for different kind of solid materials,
- repeatable capturing of broadband material spectra.

Considering these key points, a detailed material spectra analysis can be accomplished. Fulfilling the requirements, Fraunhofer IOSB Karlsruhe developed a data acquisition procedure and special technical infrastructure, shown in figure 10.2.

Several measurement stations are equipped with different kind of spectrometer bundles, to cover the characteristic bandwidth ranges:

- UV 240-400nm
- VIS 400-1000nm
- SWIR 1000-2500nm

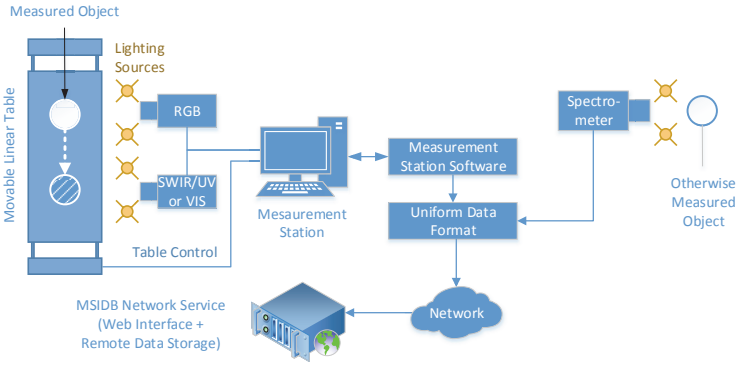

Figure 10.2: MSIDB technical environment infrastructure

The SWIR and UV spectrometer bundle includes a multispectral push broom scanner and an attached RGB scanner respectively. The attached RGB image is commonly used for image registration purposes. Therewith material measurements from different measurement stations can be spatially registered with each outher. The VIS measurement station covers already the RGB color space and requires no additional RGB image. After the data fusion from particular measurement stations a total bandwidth from 240nm up to 2500nm is be reached.

The spectrometer bundles are mounted to the base frame of the measurement station, looking down on a linear movable table. Capturing of the material surface image is achieved by moving the table perpendicular to the line of sight of the cameras in synchronization with the camera clock. That requires fine mechanical characteristics and adjustment options, which can be achieved by using an electromechanical drive.

According to the physical characteristics, different kinds of light sources are installed: halogen lamps for SWIR, deuterium lamps for the UV measurement station. The VIS measurement station contains mixed fluorescent and halogen lamps with an additional Ulbricht sphere diffusor.

The acquisition is accomplished by the measurement station software, which was developed to operate multiple spectrometer devices. Finally,

acquired material measurements are stored localy on the measurement station in the internal uniform data format, to be processed within the next workflow step.

4.2 Measurement Post-Processing

To reduce or preclude the influence of temperature or sensor aging, the base characteristics of the data acquisition devices are captured in separate steps.
As a first step, the dark current of the sensor is recorded with the sensor being protected from incoming light. This step is required to measure the actual dynamic range of the sensor. Together with the white balance step, both steps are also used to identify corrupt or defect pixels in the line sensor of the multispectral camera.
For the white balance, a two-substep approach is used. The white balance reference material Teflon is measured before every material sample to avoid sensor or environment drift between white balance and measurement. The white balance material itself is calibrated in regular intervals by comparing its reflectance properties with those of a SPECTRALON probe to compensate aging or usage caused degradation of white balance quality.
Data from black current and white balance measurements is used to correct the measured material image. The correction step corresponds to the flat-field correction technique described in [1]. Resulting image contains the sensor integration time independent reflectance of the captured material.
Finally, corrupted image pixels will be canceled out in the data. The position of this pixels is known by separate statistical analysis of specific camera sensor properties and is estimated from a large dark current and the white balance image sequence.
The measurement post-processing is being performed automatically during each data upload procedure.

4.3 Data Upload

The data upload procedure is performed through a web-based user interface. Multispectral image data captured by the measurement station

contains one or more objects of the material probe or even objects of different material types.

The images have to be annotated with metadata containing classification information for every pixel in the multispectral image data block. This separate step is performed using a semi-automatic, MATLAB®-based segmentation procedure. The user manually marks sample pixels belonging to the same class of material. Then the system automatically segments objects and background, based on an energy minimization function in the spectral domain.

Together with the corresponding mask file, the images are then uploaded to the database. During this step, the user also adds metadata like project number, environmental conditions or material description to the database record.

Furthermore the uploaded data can be accessed manually by the web-based user interface or from within applications by using the data access interface through the network.

4.4 Database

Database infrastructrue

All acquired measurements are stored in the database together with the measurement metadata. As it contains a large amount of raw and pre-processed files, it is important to ensure fast access to the data, enough storage volume and metadata management flexibility. Therefore the database is splitted into two divisions – the SQL database and the blob storage, as shown in the figure 10.3. The SQL database is used to store the common metadata about projects, material lists, pixel classification annotations and measurement relationships. The binary data of the measurements is stored in the separate blob division. Each measurement blob contains a binary file and corresponding metadata file, which describes the binary file format.

The separation in data storage divisions allows fine-grained utilisation of hardware components, like mixing of solid-state and hard drives. An usefull option for fast and transparent caching of non-persistent data is utilisation of the virtual drive assigned to a physical RAM sector. This technique is commonly used for the internal data preparation routines during the upload. The database server itself utilizes the Intel Xeon®

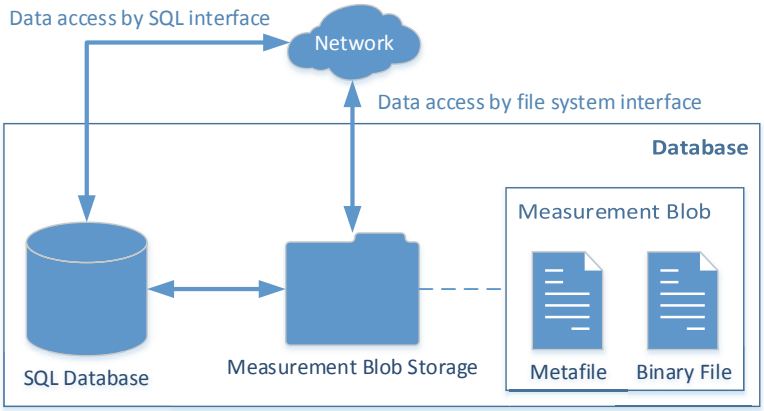

Figure 10.3: Database and data access overview

64-bit multi-core processor architecture. This allows a high degree of computing task parallelization for online data processing and analysis.

Data Model

In the relational database we keep the metadata about the measurements. In addition, project, campaign, devices and user management is implemented. For a maximum of flexibility, it is possible to add arbitrary key-value-pairs of information to each data record. A set of metadata about a measurement consists of

- Material information
  Which material was measured and how was its' status, e.g. grain size, temperature, humidity

- Measurement information
  Where and when did the measurement take place? Which device was used and who operated it? Which files belong to the measurement?

- Campaign information
  To which campaign and project does the measurement belong? Who is allowed to access the data?

A vast amount of metadata is stored to provide detailed information on how a measurement was carried out and which processing steps were applied to the data. We store file results of every processing step in the lorm term storage to provide access, analysis and possible error correction at every step.

4.5 Data Access

The measurement database provides a bi-directional interface to import and export data via network. Depending on the application needs there are two separate data access methods, as shown in figure 10.3.

The high-level data access is provided through the SQL-Server standard connection mechanisms, e.g. SQL-Server, ODBC or ADO. The flexibility of SQL allows to send complex queries from within applications like MATLAB® or programming languages like C#. One of the possible use case scenarios is precise searching of measurements by specific properties, like camera kind or acquisition location in a given time period.

The preprocessing and sharing of the binary blob data over the SQL interface is achieved by the Microsoft SQL CLR [9] technique. This allows custom C# classes to be run inside the SQL database environment. The classes are called from within a regular SQL query, have read-write permissions on the physical hard-drive and return a SQL conform query response. Calls to SQL CLR applications are therefore transparent for the end user. One of the possible use case scenarios is computation of statistical metrics or comparison of different measured images.

The low-level data access is implemented as a file sharing interface. Using this interface requires knowledge of the internally used data format, but also allows additional functionalities like mass data modifications or data sharing via network.

Internally, an ENVI (ENvironment for Visualizing Images)- [10] based data format is used to store measurement blobs, see also figure 10.3.

[9] http://msdn.microsoft.com/en-us/library/ms254498.aspx
[10] http://www.exelisvis.com/docs

Every measurement blob contains a metafile. It stores information on measurement properties, e.g.:

- Image size (height, width, spectral band count)
- Image value type (16bit, 32bit, signed, unsigned, complex)
- Integration or exposure time
- Short description and acquisition timestamp

The metafile allows quick reconstruction of image aquisition conditions, which is essential for measurement data import and export routines.

The binary file contains only the image data, according to the specified binary format. ENVI is a simple data format, which can hold common data types, real and complex values.

This uniform measurement data format rounds up the database access interface and is the basis for the multispectral data processing. On the one hand, it makes it possible to to import measurements from custom spectrometer devices or other databases, as previously shown in figure 10.2. Using custom conversion tools, measurements from external data sources like the ASTER spectral library [4] can be imported into the database. On the other hand due to simplicity and flexibility of the ENVI data format complex data analysis, like spectral filter design or classificator design, can be easily realized in common programming environments.

4.6 Applications

- Visualization of Multispectral Data (ViMuDat)[11]
  This web-based application allows online access to the data in the multispectral database and data analysis. Materials can be searched in the database by name, project, customer, material and measurement properties. Spectral signatures of the materials found can be compared and visualized, several basic statistics algorithms, e.g. normalization and averaging, can be applied on the

[11] http://msidb.iosb.fraunhofer.de/

data. Also the expected spectral signature after applying an optical filter can be previewed, which gives the user a first impression whether different materials can be separated by using their spectral signatures. Figure 10.4 shows the user interface of ViMuDat.

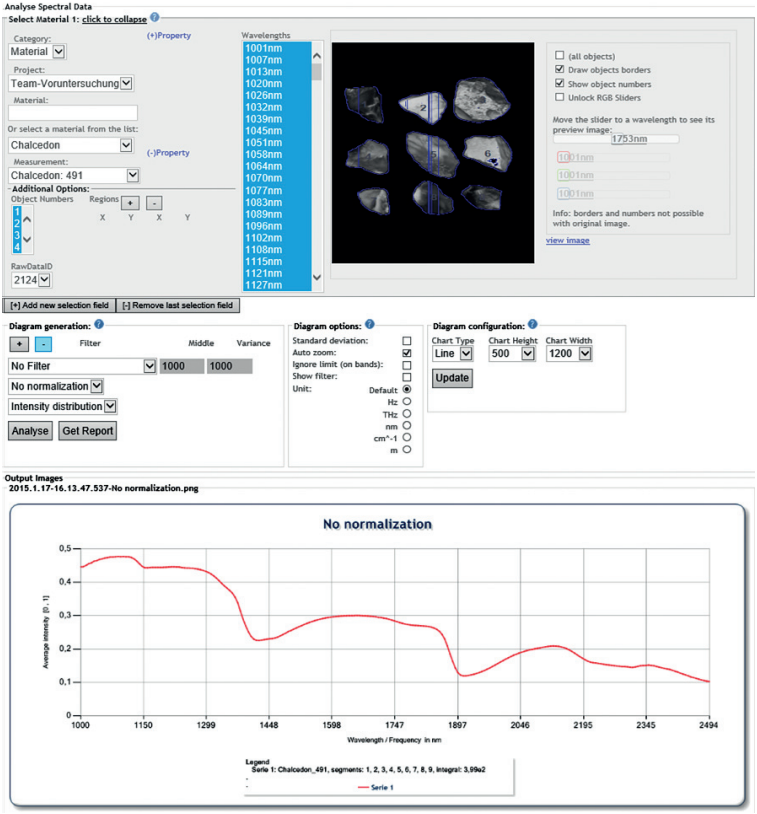

Figure 10.4: Visualization of Multispectral Data (ViMuDat)

The material selection area is located on the left side of the picture. On the right side, the image for the selected wavelength is shown. Page bottom shows the spectral signature of the selected material.

- Spectral Unmixing
  For applications like demonstrated in [10] it is required to have a broad basis of material measurements to improve success rates for material classification using spectral unmixing. Our database supports these applications by providing direct access to the data for bulk queries.

- QueryMe
  Implemented as web- and standalone-applications, QueryMe allows real-time classification of materials, e.g. with a handheld spectrometer, based on classificators trained with the data from our multispectral database.

5 Summary

We presented a detailed view inside our infrastructure for acquisition, processing, long-term storage and analysis of multispectral material signatures. Material samples are measured in a wide spectral range, normalized by using white- and black-balance of the measurement devices, uploaded to the hybrid material signatures database and analyzed using online, web-based analysis or offline tools like ENVI® or MATLAB®. Our online data analysis includes spectral signature view as well as standard mathematical operations and optical filter preview for fast testing on discriminability of materials. User rights management ensures configurable access to data and analysis functions.

6 Outlook

Currently our infrastructure is extended on both ends. Mobile measurement devices are included in the workflow for easy sampling of materials and data upload to the database. Material classification and spectral unmixing are set up to create mobile applications for material identification, especially focused on handheld measurement devices. Our material signature fund is also continuously growing by numerous measurements of food samples, minerals, miscellaneous organic and inorganic materials.

7 Acknowledgements

We especially thank the students that spend a lot of creativity and effort in numerous projects over the last years in setting up and improving this infrastructure and applications as part of the projects *ViMuDat*, *UpToDatE*, *Bring2Light* and *QueryMe*.

References

1. S. Irgenfried and C. Negara, "A framework for storage, visualization and analysis of multispectral data," in *OCM 2013 - Optical Characterization of Materials - conference proceedings*, J. Beyerer, F. Puente León, and T. Längle, Eds. Karlsruhe: KIT Scientific Publishing, 2013, pp. 203–214.
2. A. Hüni, J. Nieke, J. Schopfer, M. Kneubühler, and K. I. Itten, "The spectral database specchio for improved long-term usability and data sharing," *Computers & Geosciences*, vol. 35, no. 3, pp. 557–565, 2009.
3. A. Baldridge, S. Hook, C. Grove, and G. Rivera, "The aster spectral library version 2.0," *Remote Sensing of Environment*, vol. 113, no. 4, pp. 711–715, 2009.
4. R. N. Clark, G. A. Swayze, A. J. Gallagher, T. V. V. King, and Calvinm W. M., "The u. s. geological survey, digital spectral library: Version 1: 0.2 to 3.0 microns: U.s. geological survey open file report 93- 592," 1993. [Online]. Available: http://speclab.cr.usgs.gov/spectral.lib04/clark1993/spectral_lib.html#Abs
5. S. Bojinski, M. Schaepman, D. Schläpfer, and K. Itten, "Specchio: a web-accessible database for the administration and storage of heterogeneous spectral data," *ISPRS Journal of Photogrammetry and Remote Sensing*, vol. 57, no. 3, pp. 204–211, 2002.
6. A. Hüni and M. Tuohy, "Spectroradiometer data structuring, pre-processing and analysis – an it based approach," *Spacial Sciene*, vol. 52, no. 2, pp. 93–102, 2006.
7. J. G. Ferwerda, S. D. Jones, and P.-J. Du, "A web-based open-source database for the distribution of hyperspectral signatures," in *Geoinformatics 2006: Geospatial Information Technology*, ser. Proceedings of SPIE, H. Wu and Q. Zhu, Eds. Seattle, WA and USA: SPIE, 2006, vol. 6421. [Online]. Available: http://proceedings.spiedigitallibrary.org/proceeding.aspx?articleid=1295832

8. L. Tian, N. Liao, and A. Chai, "Common hyperspectral image database design," in *SPIE Proceedings Vol 7513*, ser. SPIE Proceedings, SPIE, Ed., 2009, vol. 7513, pp. 75 132Y–75 132Y–9. [Online]. Available: http%3A//proceedings.spiedigitallibrary.org/proceeding.aspx?articleid=774930
9. P. R. Christensen, J. L. Bandfield, V. E. Hamilton, D. A. Howard, M. D. Lane, J. L. Piatek, S. W. Ruff, and W. L. Stefanov, "A thermal emission spectral library of rock-forming minerals," *Journal of Geophysical Research*, vol. 105, no. E4, p. 9735, 2000.
10. M. Michelsburg and F. Puente Leon, "Spectral and spatial unmixing for material recognition in sorting plants," in *OCM 2013 - Optical Characterization of Materials - conference proceedings*, J. Beyerer, F. Puente León, and T. Längle, Eds. Karlsruhe: KIT Scientific Publishing, 2013, pp. 179–190.

From measurement to material – Preparing hyperspectral signatures for classification

Jennifer Walocha[1] and Matthias Richter[1,2]

[1] Karlsruhe Institute of Technology, Institute for Anthropomatics and Robotics
Adenauerring 4, D-76131 Karlsruhe, Germany
[2] Fraunhofer Institute of Optronics, System Technologies and Image Exploitation (IOSB), Fraunhoferstr. 1, D-76131 Karlsruhe

Abstract Due to the possibility of classifying unknown materials fast and accurately the industries interest in spectroscopy is growing. However, reliable classification is a matter of suitable preprocessing. Existing solutions found in the literature are often very specific a particular combination of materials. In this paper we present a method to preprocesses hyperspectral data in order to enables general classification of many materials. The system is divided into five modules: selection, transformation, reduction, decorrelation and classification. We demonstrate our method in a demonstrator system that is available as both web- and standalone application.

1 Introduction

Classification of materials is prevalent in industry, especially in the field of quality assurance, but also finds application in other areas, e.g., in mining and food safety. Here the difficulty is to classify fast and accurately on the basis of the provided measurement.

Due to the continuing progress in sensor technology, companies are now able to afford improved optical sensors which generate images with increasing quality. Previously high-priced hyperspectral sensors, primarily used in remote sensing and meteorology, gradually replace conventional RGB- and multispectral cameras. The data from these systems is used to obtain highly detailed measurements.

However, raw or incorrectly processed measurements may prevent meaningful analysis of the data. Furthermore, statistical analysis and

machine learning techniques may become slow when the data is not properly processed. Normalization of the measurements is also needed to ensure that data from different sources (e.g. different camera sensors) is comparable.

In this paper, we propose a procedure to preprocess hyperspectral data in order to achieve comparability and to improve speed and accuracy of the subsequent classification stage. We measure great importance towards the possibility of classifying numerous spectral signatures from different materials corresponding to a very large number of classes. We demonstrate our methods with our software *QueryMe*.

In the following, we give a short overview of common procedures for classifying hyperspectral images and compare them to our method. In Section 2, we describe our method and the different steps taken in order to process the measurements. Acquisition and storage of hyperspectral signatures and our software *QueryMe* are briefly outlined in Section 3. Finally, we summarize our results and give an outlook towards further research in Section 4.

1.1 Related work

Several procedures for classifying hyperspectral images can be found in the scientific literature. However, most of these methods are only concerned with a very specific application scenario. For instance, Serranti et al. developed a hyperspectral imaging system utilizing the near infrared spectrum to detect polyolefin, polyethylene and polypropylene in building and construction waste [1]. In addition to the classification of a particular substance, objects are often compared with respect to specific quality criteria, for example, to measure the ripeness or health of fruits and vegetables, like tomatoes [2] and mushrooms [3]. In many applications only a small subset of problem-specific wavelengths is selected. For instance, Elmasry et al. employed partial least squares regression and stepwise discrimination analysis to select three discriminative wavelengths with the goal to detect developing bruises on McIntosh apples [4]. Liu et al. processed hyperspectral images with a Gabor filter bank to assess the quality of pork meat [5]. Using this technique, they achieved perfect classification in their experiments.

All these methods are engineered to very specific needs. However, in this paper we consider a much larger problem domain: classification

of many (order of hundreds) materials. Therefore, such methods will likely not provide the expected classification performance.

1.2 Contributions

In this paper, we present a system to enable general classification of hyperspectral data without regard to a specific problem domain. In our analysis, we found it beneficial to divide the process into separate functional blocks, each with a dedicated task: selection, transformation, reduction, decorrelation and classification. We analyzed these components and give recommendations for concrete methods that we find most useful. Moreover, with *QueryMe* we provide a prototypical implementation of our methods. The software is implemented as a library; we provide access to the functionality in form of both a web- and and a stand-alone application.

2 Methods

The methods proposed in this paper are applicable to different types of measurements. The only requirement is that all measurements represent the same type of information, e.g. all measurements represent

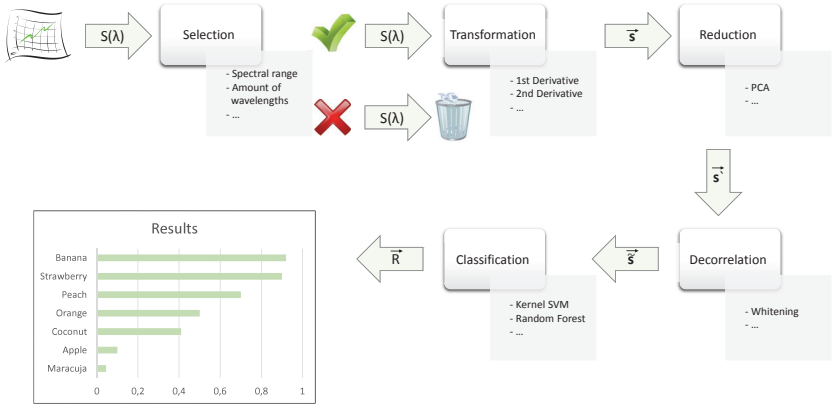

Figure 11.1: Overview of the preprocessing and classification steps.

absorbance-spectra or all measurements represent reflection spectra. Furthermore, we assume that the data is normalized to a common baseline. That is the influence of the sensor, lighting, etc. are removed from the measurements (see also Sec. 3).

We define a spectrum to be a mapping

$$\mathcal{S} : \mathbb{R}_+ \to [0,1] \lambda \mapsto \mathcal{S}(\lambda) = I, \tag{11.1}$$

where λ denotes a wavelength and $\mathcal{S}(\lambda) = I$ denotes the measured normalized intensity at that wavelength. In practice, a measurement is defined only on certain sampling points λ_i, $i = 1, \ldots, N$ within an interval (or support) $\mathcal{D} = [\lambda_{\text{low}}, \lambda_{\text{high}}]$. We simply perform linear interpolation between the sampling points λ_i. Sometimes the sensor may contain dead or defective pixels that do not provide usable measurements. To handle these cases augment the definition of $\mathcal{S}$ and assign a special value $\mathcal{S}(\lambda) = \perp$.

As seen in Figure 11.1, we identified four major preprocessing steps a measurement has to pass before entering the classification (or learning) stage. The first step, selection, either accepts a measurement to further processing or drops it if it is not suitable for classification. If accepted, a measurement undergoes a transformation stage where discriminative regions in the spectrum are accentuated and a feature vector is derived. This is followed by a feature reduction, where the dimensionality of the feature vector is reduced and redundant information is removed. Finally, the feature vectors are decorrelated to reduce runtime and increase classification performance of certain machine learning algorithms. Each step is explained in more detail in the following.

2.1 Selection

The selection stage determines whether to accept or deny an unknown spectrum. In the learning phase, this is to ensure that all training data is valid. Here a spectrum is only accepted if the spectrum's support matches or exceeds a user-definable range that the classifier should be trained on. Spectra that are defined over a larger support are truncated to match the desired range (see Fig. 11.2(a)).

In classification, it ensures that the classifier is able to correctly classify the measurement. Here it is verified that the classifier was learned

using spectra that have the same or smaller support than $\mathcal{S}(\lambda)$. If the support is smaller, the spectrum is truncated to the range requested by the classifier (see Fig. 11.2(b)).

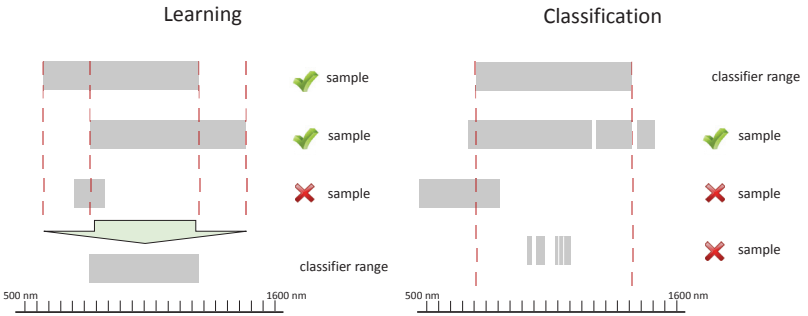

Figure 11.2: Selection of spectra based on the support.

In both cases, only spectra that contain no invalid values, i.e. only spectra with $\mathcal{S}(\lambda) \neq \perp$ for all $\lambda \in \mathcal{D}$, are allowed. Other "sanity checks" are also possible, e.g., whether the measurement contains a minimum number of sample points or if the maximum intensity of the spectrum exceeds a threshold.

2.2 Transformation

To accentuate the discriminative parts in a spectrum, it is processed by function $\mathcal{T}(\mathcal{S}(\lambda)) = \mathcal{S}'(\lambda)$, where $\mathcal{T}$ is an arbitrary transformation.

In our case, we chose the first derivative

$$\mathcal{T}(\mathcal{S}(\lambda)) = \frac{d\mathcal{S}}{d\lambda}(\lambda) \tag{11.2}$$

to emphasize sudden changes in the spectral signature. The drawback is that this also increases the influence of additive noise and therefore decreases the signal to noise ratio. Other possible transformations include power-normalization $\mathcal{T}(I) = \mathrm{sgn} I|I|^{\alpha}$ or normalization by mean and standard deviation over the intensities, $\mathcal{T}(I) = (I - \bar{I})/s_{\mathcal{I}}$. After normalization, the spectrum is sampled into a feature vector

$\mathbf{s} = (s_1, \ldots, s_K)^\top$ of size K. Each entry $s_k = \mathcal{S}'(\lambda_k)$ corresponds to a value of the transformed spectrum, where the sample points λ_k are evenly spaced over the support.

2.3 Reduction

In the reduction step, the dimensionality of the feature vector is reduced and redundant information is eliminated resulting in a lower-dimensional feature vector $\mathcal{R}(\mathbf{s}) = \mathbf{s}' \in \mathbb{R}^D$, with $D < K$. Common choices for $\mathcal{R}$ include principal component analysis, partial least squares regression or feature selection methods.

2.4 Decorrelation

Finally, the feature vector $\mathbf{s}'$ is decorrelated through whitening, $\tilde{\mathbf{s}} = W\mathbf{s}'$, where W is the whitening matrix. This is done in order to speed up the subsequent machine learning algorithms and increase the performance of certain classification methods. If the machine learning algorithm is not sensitive to correlated features, this step may be skipped.

2.5 Classification

Using the processed features, we train one kernel SVM (RBF-kernel) for each material in a one-vs-all scheme. In classification, this allows to reduce the number of evaluated classifiers by exploiting hierarchical structures in the database (see [6]): The user may select certain groups of materials that the unknown material likely belongs to, thereby reducing the possibilities for misclassification.

3 Implementation

In this section, we detail the implementation of our methods explained in Section 2. Prior to this, we summarize our procedure of acquisition and normalization as well as the storage of hyperspectral images.

3.1 Acquisition

A general solution for the classification problem bears the difficulty not only to classify different kinds of materials but also to classify measurements acquired by various sensors in many places. For this reason measurements are normalized to a common reference frame and stored in our hierarchical database of hyperspectral material signatures in order to be available at all times. As a first step, the measurements need to be normalized to a common reference "white" to remove the influence of lighting and varying dynamic range of the different sensors. Moreover, dark current in the sensors manifests as noise, which also has to be removed from the measurements. To achieve both, we follow the approach by Irgenfried and Negara [6], which we briefly outline in the following.

Each time before a measurement is acquired, a mean dark current spectrum $D(\lambda)$ is determined by taking a measurement with a closed shutter. Then, the spectrum of a white thin teflon tile is measured to obtain a reference white spectrum $W(\lambda)$. Finally, the raw measurement $I_{\text{raw}}(\lambda)$ is recorded and the final, normalized measurement is computed according to

$$I(\lambda) = \frac{I_{\text{raw}}(\lambda) - D(\lambda)}{W(\lambda) - D(\lambda)}. \tag{11.3}$$

Afterwards, the foreground of the image is separated from the background in a semi-automatic segmentation step. Finally, the resulting meta-data is imported into the relational database while the measurements, segmentation and registration files are kept in compact binary data files and are accessed through a common data access layer. This composition allows high performance with a huge amount of data stored. Moreover, as mentioned in Section 2, the measurements are organized into material groups which is used to restrict the number of classifiers to evaluate in the classification stage.

3.2 QueryMe

QueryMe implements our methods mentioned in Section 2 in a pipeline model (see Fig. 11.3). A separate pipeline is created for the training

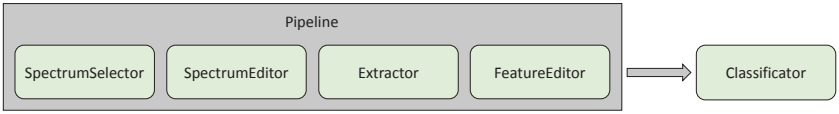

Figure 11.3: Overview of the processing pipeline used for both learning and classification.

and classifying phases. In both pipelines each processing step is implemented in a modular fashion and can be be exchanged or even entirely omitted. The modules are named *SpectrumSelector*, *SpectrumEditor*, *Extractor*, *FeatureEditor* and *Classificator* and correspond to the processing steps detailed in Section 2. The system allows to introduce further modules at will, e.g. to normalize measurements from different sources. Moreover, the algorithms of those modules are exchangeable so that the whole system is not rigid and different kinds of mathematical methods may be applied. This is most useful in the final module, *Classificator*, as the optimal solution for this module is not known at the present. The entire pipeline can be serialized and saved in a single so that a user may swap several, specialized pipelines depending on the tasks.

4 Conclusion

In this paper, we presented a procedure to preprocess hyperspectral measurements in order to facilitate classification of different materials. Moreover, we implemented our method as a demonstration system that is available as web- or standalone application.

However, there is still room for improvement. Once learned, a classifier can not be updated and must therefore be trained from scratch when the database is updated. Recent developments in online-learning methods offer solutions to that aspect.

We would also like to investigate which preprocessing steps are most suited in the context of classification with hyperspectral datasets, especially with regard to the reduction step.

Finally, it would be interesting to adapt the existing method to support not only classification of materials, but also chemometric regression techniques, to e.g. grade ripeness of fruits, and spectral unmixing, to discover the composition of unknown objects.

References

1. S. Serranti, A. Gargiulo, and G. Bonifazi, "Classification of polyolefins from building and construction waste using nir hyperspectral imaging system," *Resources, Conservation and Recycling*, vol. 61, pp. 52–58, 2012.
2. G. Polder, G. W. A. M. van der Heijden, I. T. Young, "Hyperspectral image analysis for measuring ripeness of tomatoes." in *2000 ASAE Annual International Meeting*, ASAE, Ed., vol. 003089, 2000.
3. M. Taghizadeh, A. A. Gowen, and C. P. O'Donnell, "The potential of visible-near infrared hyperspectral imaging to discriminate between casing soil, enzymatic browning and undamaged tissue on mushroom (agaricus bisporus) surfaces," *Computers and Electronics in Agriculture*, vol. 77, no. 1, pp. 74–80, 2011.
4. G. Elmasry, N. Wang, C. Vigneault, J. Qiao, and A. ElSayed, "Early detection of apple bruises on different background colors using hyperspectral imaging," *LWT - Food Science and Technology*, vol. 41, no. 2, pp. 337–345, 2008.
5. L. Liu, M. O. Ngadi, S. O. Prasher, and C. Gariépy, "Categorization of pork quality using gabor filter-based hyperspectral imaging technology," *Journal of Food Engineering*, vol. 99, no. 3, pp. 284–293, 2010.
6. S. Irgenfried and C. Negara, "A framework for storage, visualization and analysis of multispectral data," in *OCM 2013 - Optical Charcterization of Materials*, 2013, pp. 203–214.

Hyperspectral imaging applied to end-of-life (EOL) concrete recycling

Giuseppe Bonifazi, Roberta Palmieri and Silvia Serranti

Sapienza – Universitá di Roma
Dipartimento di Ingegneria Chimica Materiali Ambiente
Via Eudossiana, 18 00184 Rome, Italy

Abstract The recovery of materials from Demolition Waste (DW) is a significant target of the recycling industry and it is important to know which materials are present in order to set up efficient sorting and/or quality control actions. The implementation of an automatic recognition system of recovered products from End-Of-Life (EOL) concrete materials can be an useful way to maximize DW conversion into secondary raw materials. In this paper a new approach, based on **H***yper***S***pectral* **I***maging* (HSI) sensors, is investigated in order to develop suitable and low cost strategies finalized to the preliminary detection and characterization of materials constituting DW flow stream. The described HSI quality control approach is based on the utilization of a device working in the near infrared range (1000-1700 nm). Acquired hyperspectral images were analyzed. Different chemometric methods were applied. Results showed that it is possible to recognize DW materials and to distinguish the recycled aggregates from the investigated contaminants (brick, gypsum, plastic, wood and foam).

1 Introduction

The huge amount of generated Construction and Demolition Waste (CDW) constitutes a serious problem. Eurostat estimated a total production of 970 million tons/year, representing an average value of almost 2.0 ton/ per capita only in Europe. This estimation is lower than the reality because this type of waste is often illegally dumped [1]. On the other hand, during the last century, the use of global materials increased eight-fold with almost 60 billion tons currently used per year.

It has been forecast that the demand for these materials will double by 2050. CDW recycling is of fundamental importance because it allows to have "new materials" to use but also because it reduces environmental pressure, preventing the increase of land use for waste disposal and also avoiding the exploitation of non-renewable raw materials. Environmental impacts linked with the non-renewable raw materials extraction include extensive deforestation, soil loss, air and water reserves pollution. In this context, the benefits of effective CDW recycling are evident. The construction sector addressed significant efforts to find methods to re-use the high volumes of CDW generated each year. A practical solution can be to produce recycled aggregates from End-Of-Life (EOL) concrete as a replacement for natural aggregates. In this way, adopting recycling strategies to the EOL concrete, the improvement of environment condition and the secondary raw materials collection can be achieved at the same time [2]. In order to obtain marketable recycled aggregates , pollutants, such as brick, plastic, wood, gypsum, etc., usually present into a Demolition Waste (DW) stream, must be absent or under the limits required by the market. Therefore, the realization of an automatic system able to identify DW materials is desirable in order to make easier their conversion into useful secondary raw materials. Therefore the possibility to develop efficient, reliable and low cost sensing technologies able to perform detection/control actions during all recycling steps has to be explored.

Main aim of this study was the DW stream classification by optical sensors in order to identify concrete aggregates and unwanted contaminants (i.e. brick, wood, plastic, gypsum and foam). The developed classification method is based on the utilization of HyperSpectral Imaging (HSI) sensing devices acting in the NIR range (1000-1700 nm). An integrated hardware and software architecture constitutes the HSI system: it allows to digitally capture and handle spectra, as they result along a pre-defined alignment on a surface sample properly energized [3], [4]. Hyperspectral sensor produces a 3D dataset, the "hypercube", characterized by two spatial and one spectral dimensions. In the hyperspectral images, the wavelength bands are typically in an equally spaced sequence, so a full spectrum is obtained for each pixel that can be analyzed giving spectral information about samples [5]. Samples spectral behavior is linked to their physical-chemical features according to the different investigated wavelengths and it can be used for a rapid materials recognition/classification.

2 Materials and methods

2.1 Samples

Strukton company (NL) provided samples representative of some contaminants of concrete collected after the demolition of a building in Groningen (NL). More in detail, samples are particles of wood, plastic, gypsum, brick and foam. The investigated concrete aggregates came from the same demolition waste, but after Advanced Dry Recovery (ADR) processing in TUDelft (Delft, NL) [6]. This study was thus carried in order to define the best classification strategy for identification of aggregates and pollutant materials. In order to reach this goal, HSI model classification was performed using two experimental set-up, as described in the following.

Experimental set-up 1: the training sample set. Particles of brick (2 particles), aggregates (3 particles), wood (1 particle), gypsum (3 particles), foam (3 particles) and plastic (4 particles), arranged in 7 lines, were acquired generating a training image sample set used to build the classification model (Figure 12.1) [7].

Experimental set-up 2: validation sample set. Twelve random particles were arranged in three separated parallel lines, obtaining 4 different material

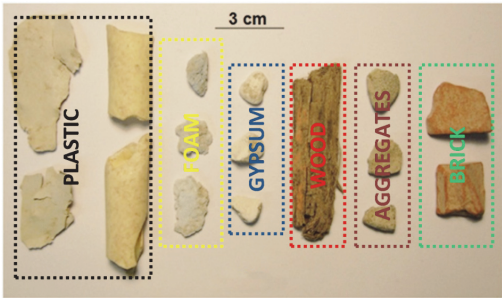

Figure 12.1: Digital image representative of the training sample set (Experimental set up 1).

particles for each row and a validation sample set was thus acquired (Figure 12.2). This second acquisition was carried out in order to validate the classification model developed through the training sample set.

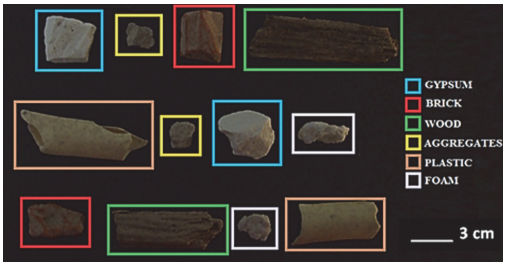

Figure 12.2: Digital image representative of the validation sample set (Experimental set up 2). Each material, belonging to the same class, is identified by a frame of the same color.

2.2 The hyperspectral imaging (HSI) system

Hyperspectral images were acquired adopting a specifically designed platform by DV srl (Padova, Italy) located at the Laboratory for Particles and Particulate Solids Characterization (Latina, Italy) of the Department of Chemical Materials and Environment Engineering (Sapienza -

University of Rome, Rome, Italy). The adopted platform is able to perform both static and dynamic analysis, indeed it is equipped with a conveyor belt (width=26 cm and length=160 cm) with adjustable speed to simulate the behavior of material flow-stream in a real industrial plant. Moreover the system consists of a NIR Spectral Camera™(Specim, Finland) equipped with an ImSpector N17E™imaging spectrograph working with a spectral sampling/pixel of 2.6 nm, coupled with a Te-cooled InGaAs photodiode array sensor. The device works as a push-broom type line scan camera allowing the acquisition of spectral information for each pixel in the line. In order to provide the required energy for the process, a diffuse light cylinder containing five halogen lamps producing a continuous spectrum signal optimized for spectra acquisition in the NIR wavelength range (1000-1700 nm) is present.

A PC unit equipped with a specifically developed software (Spectral Scanner™v.2.3), allowing to acquire, collect and manage the spectra, controls the HSI system. Hyperspectral data were acquired in the 880-1720 nm wavelength range, with a spectral resolution of 7 nm, for a total of 121 wavelengths. The width of the images was 320 pixels and the number of frames was variable according to the length of the image to acquire. A calibration, obtained recording two reference images (one for black and one for white) was carried out preliminarily. Black image (**B**) was acquired in order to remove the dark current effect of the camera sensor covering the camera lens with its cap. The white image (**W**) was acquired adopting a standard white ceramic tile under the same condition of the raw image. Corrected hyperspectral image (**I**) was obtained applying the following equation to the original sample image **S**:

$$\mathbf{I} = \frac{\mathbf{S}-\mathbf{B}}{\mathbf{W}-\mathbf{B}} \cdot 100$$

3 Spectral data analysis

The PLS_Toolbox (Version 7.8, Eigenvector Research, Inc., Wenarchee, USA) running under Matlab®(Version 7.5, The Mathworks, Inc., Natick, Massachusetts, USA) environment was used in order to analyze hyperspectral images. After a preliminary pre-processing procedure, chemometric techniques were applied. Principal Components Analysis

(PCA) was used in order to explore the data, to define classes and to evaluate the best algorithms for successive classification models, while for classification purpose Partial Least-Squares Discriminant Analysis (PLS-DA) was adopted.

3.1 Spectra pre-processing and exploratory analysis

In order to remove effects due to the background noise, at the beginning and at the end of the acquisition range, the raw spectra were cut: spectral variables were thus reduced from 121 to 93 obtaining a new investigated wavelength interval (1006 to 1650 nm).

To highlight samples spectral differences and to reduce the impact of possible external sources of variability, hyperspectral data were preprocessed adopting a combination of three algorithms was applied: Mean Centering (MC), Detrend and Standard Normal Variate (SNV). MC is one of the most common pre-processing methods calculating the mean of each column and subtracting this from the column: each row of the mean-centered data includes only how that row differs from the average sample in the original data matrix. Detrend algorithm removes constant, linear, or curved offset; while SNV is a weighted normalization adopted to solve scaling or gain effects due to path length effects, scattering effects (depending on the physical nature of the material and the particle size), source or detector variations, or other general instrumental sensitivity effects [8]. After preprocessing, Principal Component Analysis (PCA) was applied as exploratory data analysis [9]. PCA projects the samples into a low dimensional subspace, whose axes (the principal components, PCs) point in the direction of maximal variance, compressing the data. Looking at the distribution of samples into the PCs space, it is possible to interpret differences and similarities among them: the more they are grouped, the more they have similar spectral features. Furthermore, PCA highlights the presence of trends among samples, giving preliminary information about distribution of different specimen on an image [10].

3.2 Partial Least-Square Discriminant Analysis

Partial Least-Square Discriminant Analysis (PLSDA) was adopted in order to build a predictive model able to classify aggregates and pollu-

tants. This technique is a supervised classification method as requires a prior data knowledge [11] and it is a linear method based on the use of partial least squares regression. Starting from samples with known classes, a discriminant function is built to be used to classify new unknown samples, made of the same material of the known ones. PLS-DA builds a subspace of latent variables (LVs), which are liner combinations of the original variables, and it looks for the LVs with a maximum covariance. It is necessary to evaluate the optimal dimension of the LVs subspace in order to perform the best classification model as possible [12]. The PLS-DA model allows to assign to each unknown sample (in this case, pixel) only one of the available defined classes, according to the similarity among spectra. Prediction maps are PLS-DA results: each class is defined by a different colour.

4 Results

The spectra of the different materials, collected in the NIR range, provides chemical information about their composition, being spectral signatures absorption bands strictly related to C-H, O-H and N-H overtones.

4.1 Explorative analysis and class setting

The explorative analysis was carried out after spectra preprocessing applying Mean Center, Detrend and SNV algorithms.

The sample set corresponding to the *Experimental set up 1* was analyzed by PCA: the majority of the variance was captured by the first two PCs, where PC1 and PC2 explained 58.43% and 25.03% of the variance, respectively.

The six classes were clearly identified on the PCA score plot because samples, in fact, are clustered into six different groups (Figure 12.3). Therefore the training dataset was easily created by removing some border cluster points “different” from all other spectra of the same category and by setting class of the remaining pixels.

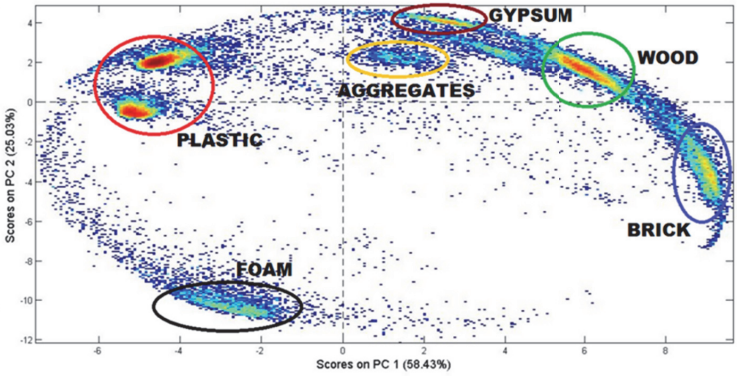

Figure 12.3: PCA score plot after preprocessing: all the classes are identified.

4.2 PLS-DA classification

In order to classify the sample set corresponding to the *Experimental set up 2*, a PLS-DA method was applied.

The number of latent variables was chosen based on the minimum classification error in the venetian blind cross-validation and it was 5 LVs and the obtained values of Sensitivity and Specificity are shown in the Table 12.1. These parameters are the model efficiency indicators: the more the values are close to one, the better the modelling.

Table 12.1: Sensitivity and Specificity for the PLS-DA model built for the classification purpose.

Applied algorithms in the PLS-DA model	**Class**	**Sensitivity**		**Specificity**	
		Calibration	*Cross Validation*	*Calibration*	*Cross Validation*
Detrend, SNV, Mean Center	Aggregates	0.997	0.997	0.002	0.002
	Brick	0.988	0.988	0.996	0.996
	Gypsum	0.982	0.981	0.999	0.999
	Plastic	1.000	1.000	1.000	1.000
	Wood	0.985	0.985	0.939	0.939
	Foam	1.000	1.000	1.000	1.000

The Sensitivity, true positive rate, estimates the model ability to avoid false negatives (i.e. number of samples of a given type correctly classified as that type). The Specificity is the estimation of the model ability to avoid false positives (the number of samples not of a given type correctly classified as not of that type).

Sensitivity and Specificity are very close to 1, except for the Specificity of aggregates: there are many false positive, probably due to dirtiness on the particles surface. Indeed, these materials were not washed, so some pixels, corresponding to pollutant, can have a similar spectra of aggregates distorting the classification result. Furthermore there are some light scattering problems due to the "rough" and heterogeneous particles surface that can contribute to the presence of errors and/or misclassifications.

In order to verify its classification ability, the built model was applied to the image corresponding to the *Experimental set up 2*. The results, in form of prediction maps, are reported in Figure 12.4a. The built model gives a good classification even if some sporadic misclassifications occur, but it is easy to indentify the predominance of a single class on each object. Therefore it is possible to impose a constraint on the maximum percentage of pixels assigned to each object in the image: the class with the major number of pixels on an object is assigned to the entire object, to reach this goal the percentage of pixels belonging to each class for every object in the image was measured.

In Figure 12.4b are reported the labels for the particles of the *Experimental set up 2* used to build the Table 12.2, showing the percentages of pixels belonging to each class for every particle.

A new classification was obtained after the imposition of the constraint rules about the maximum percentage of assigned pixels to a specific class (Figure 12.5).

5 Conclusions

The possibility to develop an efficient recovery and reuse of concrete materials, considered as secondary raw materials, represents one of the main targets in the DW sector. The achievement of this goal can contribute to decrease the steady supplies of good quality natural aggregates but in the same time it can secure large supplies of concrete ag-

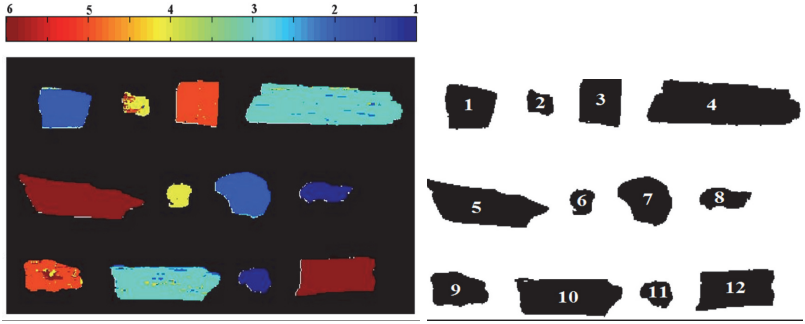

Figure 12.4: Experimental set up 2: (a) prediction maps obtained as result of PLS-DA classification model where classes are: foam (1), gypsum (2), wood (3), aggregates (4), brick (5) and plastic (6); (b) labels corresponding to each classified particles.

Table 12.2: Percentage of pixels belonging to each class (i.e. foam, gypsum, wood, aggregates, brick and plastic) in every particle of the Experimental set up 2.

	Particles											
Materials (%)	1	2	3	4	5	6	7	8	9	10	11	12
Foam	0	0	0	0	0	0	0	100	0	0	100	0
Gypsum	97.31	0.74	0	2.82	0	0.25	98.35	0	0.16	6.63	0	0
Wood	0.85	0.25	0	95.7	0	0.5	1.65	0	0	90.23	0	0
Aggregates	1.84	71.51	0.53	1.51	0	98.75	0	0	4.76	3.02	0	0
Brick	0	14.1	99.3	0	0	0	0	0	82.71	0.12	0	0
Plastic	0	13.4	0.13	0	100	0.5	0	0	12.37	0	0	100

gregates to the construction industry and moreover it can reduce the environmental constraints linked to the DW wastes disposal, especially in urban regions. Several benefits can be thus reached: i) the reduction of new non-renewable resources exploitation and of the costs linked to transport and energy production, ii) the possibility to utilize materials that otherwise should be lost (i.e. land filled), iii) the land preservation in respect of future urban development and, finally, iv) the reduction of the impact, on the environment, of new exploitation activities of

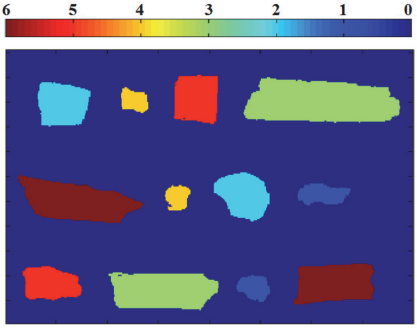

Figure 12.5: New classification, as resulting from Experimental set up 2, after the application of the constraint rules about the maximum percentage of assigned pixels to each class: background (0); foam (1); gypsum (2); wood (3); aggregates (4); brick (5); plastic (6).

non-renewable resources. Starting from these premises the possibility to identify a suitable sensor technology for quality measurement and control of recycled streams along the entire chain, from demolition to "new" concrete and/or mortar production, able to recognize and characterize recycled aggregates, as well as the presence of contaminants can represent an important starting point to develop, implement and set up on-line control strategies to apply before and after demolition actions. In this study a procedure based on HyperSpectral Imaging in the NIR region was thus developed in order to identify different materials in a DW stream: five kind of contaminants (i.e. brick, plastic, gypsum, wood and foam) and recycled aggregates. Analysis were carried out adopting chemometric methods: PCA for the exploratory analysis and PLS-DA for the classification purpose. Obtained results showed that the classification was good and sporadic misclassifications are probably due to light scattering, samples heterogeneity and presence of impurities. In order to improve the classification, a logic defining the maximum percentage of assigned pixels to each class for every particle was implemented: only one class was thus attributed to each object in the image to be predicted. The proposed HSI based approach is not-expensive, fast and reliable. For all these reasons it can be profitably utilized to set up on-line strategies finalized to improve recycling processes efficiency,

reducing costs and improving the "final quality" of the recovered products.

Acknowledgments

This study is funded by the European Commission in the framework of the FP7 Collaborative project "Advanced Technologies for the Production of Cement and Clean Aggregates from Construction and Demolition Waste (C2CA)". Grant Agreement No 265189.

References

1. F. Pacheco-Torgal, "Introduction of construction and demolition waste (cdw)," in *Handbook of recycled concrete and demolition waste*. Woodhead Publishing Limited, Cambridge, 2013.
2. F. Martín-Morales, M. Zamorano, I. Valverde-Palacios, G. Cuenca-Moyano, and Z. Sánchez-Roldán, "Quality control of recycled aggregates (ras) from construction and demolition waste (cdw)," in *Handbook of recycled concrete and demolition waste*. Woodhead Publishing Limited, Cambridge, 2013.
3. T. Hyvarinen, E. Herrala, and A. Dall'Ava, "Direct sight imaging spectrograph: a unique add-on component brings spectral imaging to industrial applications," in *Proc. SPIE Electronic Imaging, vol 3302*, San Jose, CA, USA, January 1998.
4. P. Geladi, H. Grahn, and J. Burger, "Multivariate images, hyperspectral imaging: background and equipment," in *Techniques and Applications of Hyperspectral Image Analysis*. Jhon Wiley & Sons, West Sussex, England, 2007.
5. P. Geladi, J. Burger, and T. Lestander, "Hyperspectral imaging: calibration problems and solutions," in *Chemometrics and Intelligent Laboratory Systems, vol.72*, 2004.
6. W. de Vries, P. Rem, and S. Berkhout, "Adr: a new method for dry classification," in *Proc. of the ISWA International Conference*, Lisbon, Portugal, 2009.
7. R. Palmieri, G. Bonifazi, and S. Serranti, "Automatic detection and classification of eol-concrete and resulting recovered products by hyperspectral imaging," in *Proc. SPIE Advanced Environmental, Chemical, and Biological Sensing Technologies XI, vol 9106*, Baltimore, Maryland, USA, 2013.
8. B. Wise, N. Gallagher, R. Bro, J. Shavar, W. Winding, and R. Koch, "Pls toolbox user manual." Eigenvector Research Inc., 2005.

9. S. Wold, K. Esbensen, and P. Geladi, "Principal component analysis," in *Chemometrics and Intelligent Laboratory Systems, vol.2*, 1987.

10. J. Amigo, I. Marti, and A. Gowen, "Hyperspectral imaging and chemometrics: a perfect combination for the analysis of food structure, composition and quality," in *Data Handling in Science and Technology, Vol.28*. Federico Marini (Ed.), Amsterdam: The Netherlands, 2013.

11. M. Barker and W. Rayens, "Partial least squares for discrimination," in *Journal of Chemometrics, Vol.17*, 2003.

12. D. Ballabio and V. Consonni, "Classification tools in chemistry. part 1: linear models. pls-da," in *Analytical Methods, Vol.5*, 2003.

Significant characteristics in VIS- and IR-spectrum of construction and demolition waste for high-precision supervised classification

Katharina Anding,[1] Petr Kuritcyn,[1] Elske Linß[2] and S. M. Latyev[3]

[1] Ilmenau University of Technology, Faculty of Mechanical Engineering, Department of Quality Assurance and Industrial Image Processing, Gustav-Kirchhoff-Platz 2,98693 Ilmenau
[2] Bauhaus-University of Weimar, Faculty Civil Engineering, Geschwister-Scholl-Straße 8, 99423 Weimar
[3] National Research University of Information Technologies, Mechanics and Optics; Faculty of Photonics and Optical Information Technology, Department of Computer Photonics and Videomatics, Kronverkskiy av. 49, 197101 St.Petersburg

Abstract This paper discusses the possibility of automatic classifying of construction and demolition waste (CDW) by using methods of spectral analysis and supervised classifiers. The classification performances in colour images shown, that we have to use additional spectral information to solve the recognition task in a satisfactory manner. Therefore, investigations in visible (VIS) and infrared (IR) spectrum were done for analysing significant characteristics in spectrum, which are useful for automatic classification of C&D aggregates.

1 Introduction

Construction and demolition waste (CDW) are with around 53 million tons per year one of the biggest waste flow in Germany [1]. Certainly, the rate of the recyclable amount depends on the composition and heterogeneity of the material. For recycled masonry aggregates and recycled mixed aggregates, the lowest recycling rates are found because of the high heterogeneity and the mineral admixtures. Therefore, the

reuse of these materials is very difficult. As in other sectors of recycling, for example the glass or plastic recycling, the sensor-based sorting has been becoming more interesting in the recycling of building materials and sorting of minerals in the last years.

The application of automatic sensor sorting in the areas of mining and recycling is successful in Europe and will increase in the following years. The benefits are the increase of the end product value and the cost reduction of downstream handling steps in the processing [2].

The results of object recognition in colour images [3], [4] shown, that we have to use other added spectral information to solve the recognition task in a satisfactory manner. Therefore, investigations in VIS and IR spectrum were done for analysing significant characteristics in spectrum, which are useful for classification the C&D aggregates.

We used two different spectrometers for analysing the CDW classes, the VIS spectrometer Ocean Optics USB2000+ with a detector range of 200 to 1100 nm and the Polytec PSS 2120 with an InGaAs detector and a range of 1100 to 2100 nm. In our classification routine we used supervised machine learning classifiers on the basis of PCA-processed feature vectors.

The investigations were done on new, not used building materials, which were crushed for obtaining homogeneous recyclates. The investigations were done on particles of a particle size of 8/16 mm. Several spectral attributes were found, which have discriminatory power to classify the chosen materials.

2 Analysis of VIS Spectrum of Several CDW Classes

First investigations of the specific VIS spectrums are shown in Figure 13.1 (left side). We used a light source, which shows a stable emitted lightning till 720 nm. The wavelength range from 420 to 470 nm are not useful because of the low signal-to-noise ratio in this range.

In the spectrum range of 470-720 nm some materials show significant features, for example the classes of brick show significant characteristics in VIS for identifying in context of the classes of concrete. Other materials are similar in first derivation like concrete, gypsum, aerated concrete etc. And also phenotypic very similar classes like sand-lime brick and aerated concrete. The separation on the basis of the VIS spectra was

tested by a classifier on a small dataset. By using random forest classifier, the recognition rate reached the value of 72.4%. It needs the use of other wavelength ranges (like IR spectrum information) for auspicious results.

3 Analysis of IR Spectrum of several CDW classes

Within a research project at the Bauhaus University Weimar were carried out studies on the spectral characteristics of building materials forming pure minerals in cooperation with the firm LLA Instruments GmbH [2]. Many pure minerals have spectral features (absorption bands) in the near infrared wavelength range between 1100-2500 nm. The characters appearing in construction materials are minerals, especially the mineral classes carbonates, silicates (including layered silicates), and sulfates (especially gypsum products) and oxides (e.g. hematite) assigned. In further investigations a bigger amount of samples (nearly 1100 samples out of the 9 superordinated classes: lightweight concrete, concrete, aerated concrete, sand-lime brick, dense and porous brick, gypsum, asphalt and granite) was used by capturing and analysing their IR spectrum. Figure 1 (right side) [4] shows that the class specific characteristics in IR are more useful for classification between the different classes as in VIS (see Figure 13.1 (left side)). Figure 13.1 (right side) shows a good distinction of some of the defined categories of building materials in the IR-spectrum. The mineral composition of normal concrete and lightweight concrete varies depending on the used aggregates. However, the mineral calcite is detectible by near infrared at 1911 nm. Aerated concrete can be seen very well based on the formed tobermorite phase in the IR spectrum. During the steam curing in the autoclave of aerated concrete tobermorite formed between 30 and 40 percent by mass. The spectrum of the aerated concrete show adsorption bands at 1430 and 1920 nm and additional a less intensive band at 1680 nm.

All sulphates like gypsum, plasters and plasterboard show high characteristic absorption bands at 1440, 1750 and 1930 nm, which is very good detectable. There is a small shifting about 10 to 15 nm in the spectrum of gypsum and plasterboard, which can be used for the differentiation of these materials. The examined sand-lime bricks consist is also

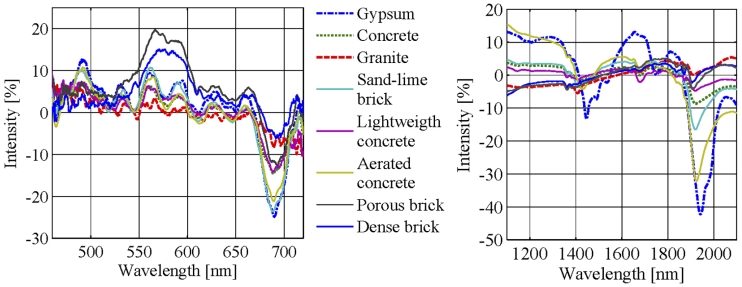

Figure 13.1: First derivation of VIS (left) and averaged and centered IR spectrums (right) of several CDW classes.

detectable by the mineral tobermorite. As a vapour cured product the sand-lime brick also contains the mineral tobermorite. The characteristic absorption bands are at 1410, 1680 and 1920 nm. The bricks are very variable in its mineralogical composition depending on the used clay for the production. The peak in the spectrum is at 1900 nm and is different from the concrete peak at 1911 nm, which is the feature for differentiation. From the recycling point of view a brick with a minimal bulk density of 2.0 g/cm³ can also be used for the production of recycling concrete so that a separation is desirable.

After analysing the IR spectrums, a feature selection by principal component analysis was done. Figure 13.2 shows the recognition rates by using 1 up to 10 principal components. The first 10 principal components with highest information content were used for the application of a supervised classifier for differentiation between the given classes. For the use of the first three principal components the highest information content (cumulative variance) of 98.4% was reached. The classification with the classifier random forest resulted in a recognition rate of 88.9% by using the first three principal components. The application of the first 10 principal components instead of the 501 dimensional wavelength-specific information accelerated the classification time significantly without producing a loss of information. A total recognition rate of 98.3% was achieved by using the first 10 principal components (cumulative variance = 99.995%) and of 91.5% by using only the first 5 components (cumulative variance = 99.95%) and by using a 10-fold

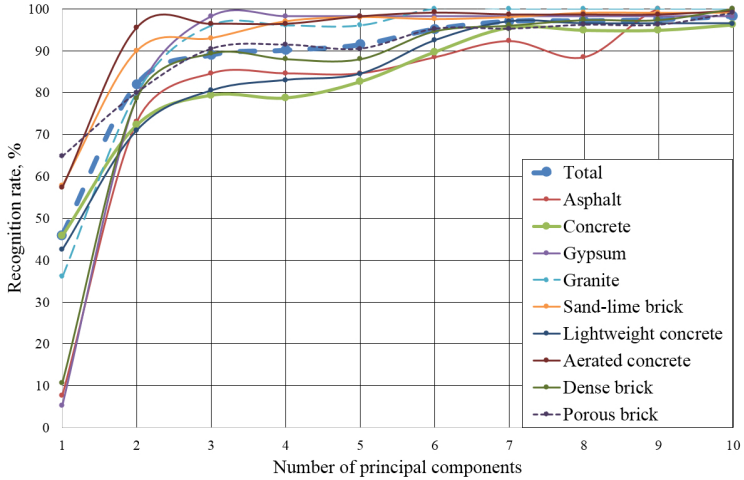

Figure 13.2: Total and single recognition rates by using the first 10 principal components.

cross validation. The achieved individual recognition rates are 100% for asphalt, 96.1% for concrete, 98.2% for gypsum, 100.0% for granite, 99% for sand-lime brick, 96.5% for lightweight concrete, 99.5% for aerated concrete, 100% for dense brick and 99% for porous brick by using the first 10 principal components. The most false classifications appear between the classes lightweight concrete and concrete. To get a recognition rate of higher than 90% for the main class concrete, it is possible to use more than 6 principal components for training the classifier. In the result the application of the PCA provides good performances with a low computational effort.

An alternative method for feature selection is the InfoGain filter. The results of the analysis are shown in figure 13.3. This method shows not so good results, because the reduction of the total number of wavelengths had no significant influence. The total recognition rate amounts to 87.25%, if all 498 wavelengths were used in the classification. For a decreased number of best wavelengths, between 250 and 300, the recognition rate increases minimally up to 88.1%. If only 50 of best wavelengths were used, the recognition rate decreases again to a value of

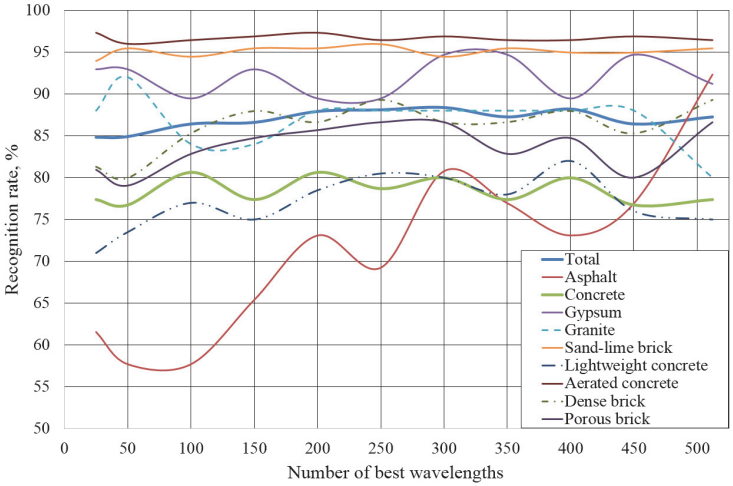

Figure 13.3: Performance of random forest on selected wavelengths from IR spectrums of CDW by InfoGain filter

84.91%. Therefore, we can conclude that InfoGain does not bring any significant improvement. That means no comparable efficiency for less calculation effort.

In addition to PCA and filter methods for feature selection, a wrapper method for feature selection was tested. This method use a classifier for feature selection. This method has an advantage in a direct integrating of the classifier into the selection process, which leads to the increase of the recognition rate, but a given disadvantage is the higher calculator effort. The classifier random forest was used for feature selection. After calculating with the 11 best wavelengths a recognition rate of 87.9% could reached by using the classifier random forest and 92.5% by using the Nu-SVM classifier. The direct comparison of different feature selection methods shows that the best performances have wrapper method and PCA (see figure 13.4). Wrapper method improved the total recognition rate, compared to standards datasets by 5%. The PCA still shows better results – here the increase is 4% for 5 principal components and 10% for 10 principal components.

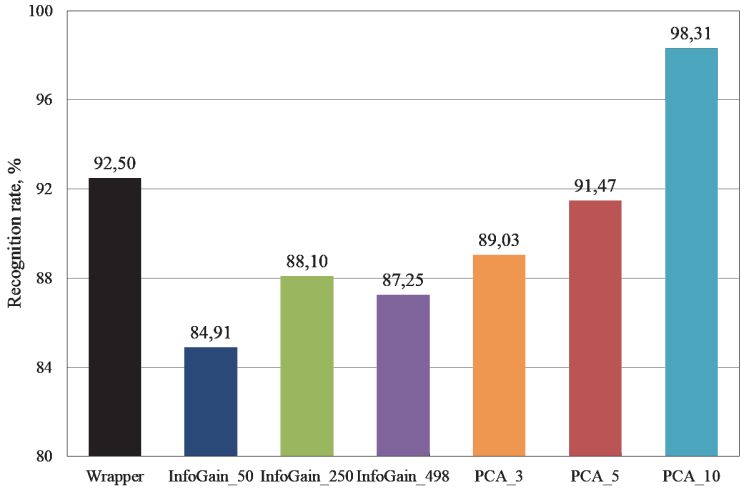

Figure 13.4: Comparison of classification performance by several feature selection methods

4 Summary

The first investigations in the VIS spectrum range showed that some materials show significant spectrum characteristics for identifying (e.g. brick). Other materials show only differences in intensity like concrete, gypsum, aerated concrete. Classes with similar chemical substances (lightweight concrete and concrete) showed very similar spectral characteristics without significant differences in intensity. The achieved recognition rate by using classifier random forest on the VIS spectrum is 72.4%. This causes the necessity for additional using of colour image information and other spectral information.

The first investigations in the IR spectrum range showed that concrete and brick in the infrared spectrum are well distinguishable in principle. Gypsum as impurity in the C&D waste is very well detectable by IR. Aerated concrete and sand lime brick can also be very well recognized by IR sensors. Lightweight and normal concretes and dense and porous brick show a little amount of false classifications in the IR spectrum. A total recognition rate of 98.3% was achieved by using the

first 10 principal components of the IR spectrum and of 90.8% by using the first 5 principal components of the IR spectrum. InfoGain filter showed insufficient results and small improvement of total recognition rate. An opposite to InfoGain, the wrapper method showed a good performance with a total recognition rate of 92.5% by using Nu-SVM classifier on selected 11 best wavelengths. Therefore, the best way for solving the analysing task is to complete the IR information by information of the colour image analysis and to use supervised classifiers of machine learning.

Further investigations are planned for combining feature vectors of colour image analysis and IR spectrum analysis.

References

1. "Mineral construction waste – monitoring 2010," Kreislaufwirtschaft Bau, Berlin, 2013.
2. "Nir-sorting of cdw. final report of aif scientific project. aif-kf 2155712," Bauhaus-University Weimar, 2013.
3. K. Anding, E. Linß, H. Träger, M. Rückwardt, and A. Göpfert, "Optical identification of construction and demolition waste by using image processing and machine learning methods," in *14th Joint Int. IMEKO Symp.*, Jena, Germany, 2011.
4. P. Kuritcyn, K. Anding, E. Linß, and S. M. Latyev, "Increasing the safety in recycling of construction and demolition waste by using supervised machine learning," in *IMEKO Joint Symposium 2014 TC1 - TC7 - TC13*, Madeira, Funchal, September 2014.

Quality of open air, single-shot LIBS spectra from waste particles

Han Xia and M. C. M. Bakker

Delft University of Technology, Faculty of Civil Engineering and Geosciences, Resources and Recycling group, Stevinweg 1, 2628 CN Delft

Abstract This work investigates the ability of LIBS to produce quality spectra from small particles of concrete demolition waste with single-shot spectra in open air. The $2-8\,mm$ materials are rounded river gravel, green glass shards and plastic flakes. Considered are focal length, air, moisture, laser energy and laser angle of incidence. The research methodology is an experimental study using the observation depth and spectral abundance as quality indicators. The relation between ablation volume, breakdown threshold, signal strength and observation depth is captured in a simplified model to provide a better understanding of the dependence of the spectra on the laser incidence angle and material positioning in the laser beam. A $100\,mm$ lens provided a compromise between spectral abundance, level of air interference and achievable observation depth. The study indicates LIBS can yield good quality data, even in cases of up to $3\,mm$ surface roughness. Surface moisture did raise the percentage of bad spectra from an average 4 % to 18 %, but overall LIBS is still capable of providing quality data under challenging conditions.

1 Introduction

Laser-induced break down spectroscopy (LIBS) receives much attention from industry as a potential quality inspection technology [1]. Here, LIBS is under development for the inspection of particulate demolished concrete ($2-32\,mm$) to ensure that the quality is suitable for recycling into new concrete. To that end LIBS must detect the number and type of quality degrading pollutants per ton, such as glass and plastic particles. In addition, inspection must take place while the material is in bulk

transport on a conveyor belt, i.e. the inspection may not interrupt the recycling process. These and additional environmental challenges (e.g. moisture, dust) posed to LIBS in an envisioned application must first be investigated under controlled conditions in the lab. Rounded river gravel is used to represent the concrete aggregates and shredded shards of glass and plastic flakes represent the pollutants. All materials are in the smallest range $2-8\,mm$ that represents the highest challenge to LIBS.

LIBS is a plasma emission spectroscopic technique where the spectrum is representative for the elemental composition of the material and also highly characteristic for the material type in case of fingerprinting. LIBS employs high power laser pulses that exceed the material breakdown threshold of the material under inspection, typically in the range $10^9-10^{14}\,W/cm^2$ [2]. The direct laser heat vaporizes a tiny amount of material into a hot plasma with electron density $10^{16}-10^{19}\,cm^{-3}$ and gas temperature of $10^3-10^5\,K$ [3, 4]. After the laser shot the plasma keeps radiating and cools down until it delivers the elemental information as the atomic/ionic emission spectrum, where the photon energies correspond with the possible and specific electron transitions between atomic or ionic energy levels.

Particulate waste materials are complicated in shape, size and material composition, while the average environmental conditions in a recycling setting can be rather harsh. Both factors negatively affect the quality of the LIBS data and have to be understood and counteracted. Anomalous spectra arise as a result of off-target optical focusing, angled particle orientation, or poor surface conditions such as dust, a thick oxide layer or moisture. A solution could be to use two lasers or one with a higher shot rate to compensate for the loss of spectra, but this would render the LIBS inspection inefficient and considerably more expensive. It is therefore of paramount importance to investigate conditions and counter measures that can minimize the chance of anomalous spectra.

The objective of this work is to determine the conditions under which LIBS may still produce good quality spectra with single-shot spectra in open air. In detail, the influences of the open air, surface moisture, focal length, laser energy, and laser angle of incidence are taken into account. The research methodology is an experimental study employing the observation depth, which is the maximum distance range in which the target material spectrum can still be detected, and the spectral abundance, which is the number of identifiable emission lines.

2 Experimental

2.1 Setup and sample preparation

The beam from a diode pumped Q-switched Nd:YAG 1064 nm laser (6.9 ns, $11-18\,mJ$, max. 100 Hz) is directed downwards and focused on the sample surface. The incoming plasma emissions are guided antiparallel to a spectrometer working at $250-820\,nm$ range. The triggering of the laser unit and possible delayed spectrometer is performed by an external double pulse generator (Agilent 33500 series). The minimum integration time is set to 1 ms. Samples were mounted on a $2D$ motorized stage which height could be varied in steps of 0.5 mm. Three fused silica plano-convex lenses are available with focal lengths of 35 mm, 50 mm and 100 mm. This optical setup is relative robust and allows for the variations in plasma position and the possible plasma shielding effects from nearby particles. More details of the setup may be found in [5]. A polypropylene plate of 1 mm thick was shredded to flakes in the sieve size range $2-8\,mm$. Green glass bottles (varying thickness $1-3\,mm$) were smashed to produce shards in this range. Rounded river gravel was acquired from a concrete manufacturer and sieved to $2-8\,mm$. For the moist material tests the materials are wetted and left on a sieve until the free water has seeped out. Specifically for the observation height tests and laser angle tests the more flat particles were selected to minimize edge and surface curving effects.

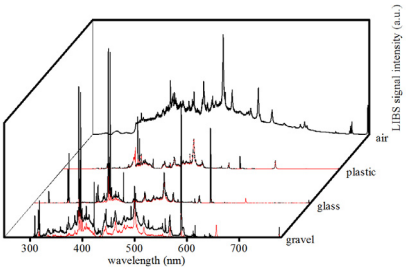

Figure 14.1: Averaged spectra from air and dry and moist (red dotted line) plastic, glass and gravel.

3 Results and discussion

As a reference Fig. 14.1 shows the averaged spectrum (10 shots at 11 mJ/shot) for a particle of plastic, glass and gravel, using the 35 mm focusing lens. The spectra for the moist material are shown in red. Note that the 10 shots are taken in different positions on the particle. These quality spectra are quite distinguishing in the three materials. The presence of moisture reduces the elemental intensity from the material and increases it for hydrogen ($H\alpha$), while the air emissions remain relatively constant. The air spectrum shows quite a few unresolvable emission/absorption bands that may add to the noise. Due to transparency of the green glass the emission lines of Si are rather weak. It is noted that gravel is rather heterogeneous in composition and therefore also its spectrum is subject to quite some variations.

To eliminate the undesired open air emission lines they must be classified w.r.t. to the targeted materials. To this end, a thousand spectra in air (i.e. without target material) were recorded and all emission lines that occur in more than 500 of them are identified as air emission lines. Fig. 14.2 (a) shows the abundance of the spectra in terms of the numbers of identified material and air emission lines using three focusing lenses. With increasing focal length, the material emission lines decrease while the air emissions remain relatively constant. To compare the spectrum quality for wet and dry materials we use some thousand particles of each type of material. Each type is put in a bucket which is manually

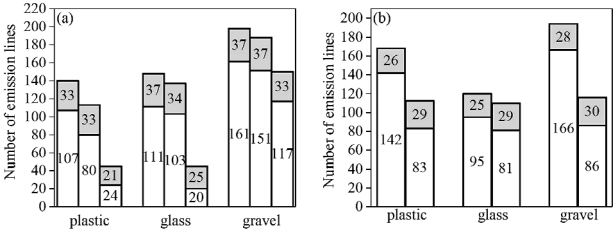

Figure 14.2: Number of emission lines from plastic, glass, gravel (white bars) and air (grey bar tops). Each material subgroup from left to right is related to (a) using 35, 50 and 100 mm lenses at 1 Hz diode frequency and (b) the dry and moist material at 100 Hz diode frequency, respectively.

moved/shaken continuously in horizontal directions as well as up and down (towards and away from the laser focus) while the laser acquires the spectra. In this fashion many different particles will be sampled. After elimination of the miss-shots a total of 5000 spectra are acquired for both dry and moist materials. The abundance of the spectra in terms of the number of identified air emission lines and material related emission lines are shown in Fig. 14.2 (b) for the dry and moist materials. It is noted that the shot rate was set to 100 Hz (18 mJ/shot). The output laser energy varies to some degree depending on the shot rate, optical oscillator, working temperature and diode pumping efficiency. Compared to the corresponding case in Fig. 14.2 (a) (dry case and 100 mm lens) considerably more emission lines are present from plastic and glass, but also for gravel it has increased. The abundance for air remained practically the same as for the lower laser energy setting, which indicates that using the highest energy is quite favourable. The abundance in the presence of surface moisture is lower, which may be attributed to a partial absorption of the laser energy.

This is due to the increase in Rayleigh length (cf. Fig. 14.3 (a)) with focal length and decrease of the laser waist radius increases (cf. Fig. 14.3 (b)) by which the power density decreases. Furthermore, the solid angle for plasma emission collection also decreases, and therefore the overall signal to noise ratio. The latter effect increases with the breakdown threshold of the material in question. A longer Rayleigh

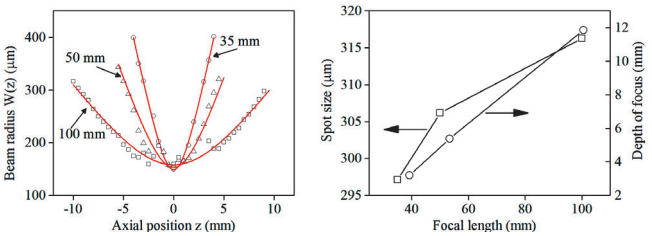

Figure 14.3: Laser profile for burn paper using three focal lengths. (a) Beam waist radius in axial direction; (b) Spot size (squares) and depth of focus (circles).

length facilitates the LIBS observation depth and should be determined in a compromise between focal length and spectral abundance.

The actual laser beam profile causing the ablation spot in a material is notoriously difficult to determine. However, it does play a crucial role in the whole process from material ablation to photon collection. To get a reasonable estimate, we determine the maximum laser beam profile using $0.5\,mm$ thick burn paper, as it has a lower breakdown threshold than the target materials. The profile is determined from the burn hole diameter produced at different distances w.r.t. to the laser focus. Three focal lengths are tested and the holes are analyzed using microscopy image analysis. The Gaussian beam model which beam radius is given by:

$$W(z) = W_0 \cdot \sqrt{1 + (z/z_0)^2}\,, \tag{1}$$

where W_0 is the beam waist radius with spot size is $2W_0$, z_0 is the Rayleigh length with depth of focus $2z_0$. W_0 and z_0 are fitted for the burn paper in Fig. 14.3. The formula mostly used to calculate the (diffraction limited) spot size predicts $150\,\mu m$ for the $100\,mm$ lens, which proves to be a factor 2 smaller than the measured spot size. A probable cause is that the plasma disturbs/scatters the laser beam, resulting in a significantly larger spot. To a lesser but still measurable degree, also spherical and chromatic aberrations of refractive components like lenses result in a larger spot size.

Next task is to determine the observation depth (OD) from which the material dependent breakdown threshold can be estimated. Here we

define the observation threshold where material emissions disappear, by which it give an upper limit. The OD is determined as the average from multiple emission lines as shown in Table 14.1.

The air influence is noticeable in both the N and H lines in plastic, causing a larger OD than the average OD for carbon species. For glass and gravel, the OD for air is comparable with the OD for the material emission lines. Outside the range set by the material OD the air spectra dominate and degrade the quality of the spectrum. More abundant spectra can be acquired with 35 mm and 50 mm lenses, but the OD prove smaller. All subsequent tests will therefore be conducted with the 100 mm lens.

The influence of the laser incidence angle (LIA) is investigated in Table 14.2 for different species. Most emission lines are little sensitive to the LIA with the exception of those near the UV, such as Mg 279 nm and Si 288 nm. The OD identifies the preferable emission lines that carry robust information. The complex shapes of glass and gravel particles may have influenced the measured OD in Table 14.2, by which the average OD is more reliable. Using the average OD from Table 14.2 in Eq.(1), the breakdown thresholds are calculated as 1.6, 1.5 and 1.0 W/cm^2 for plastic, glass and gravel, respectively.

There is no observable monotonic trend in the dependence on LIA, as also reported in [6], and not even a common trend between the different materials. Main issue is that even for relatively large LIA there may still be sufficient signal strength, which is mandatory for application of LIBS to small granular materials. To better understand the dependence of the spectral amplitude and observation depth on the LIA (θ) we use a simplified model where the average spectrum is assumed directly proportional to the ablation hole volume $V_h = A_h \cdot z_h$ where A_h and z_h are the ablated surface $\pi \cdot W(z)^2/cos(\theta)$ and depth of the hole, respectively. The latter parameters may be estimated using the Beer-Lambert absorption law for fluence $F_b = F_{avg} \cdot exp\left(-\alpha \cdot z_h\right)$, where the initial average fluence is defined as $F_{avg} = E_p/(A_h \cdot \tau_p)$ (E_p: pulse energy, τ_p: pulse width). Finally, the hole volume is described by:

$$V = \frac{A_h}{\alpha} \cdot ln\left(\frac{F_{avg}}{F_B}\right). \tag{2}$$

The following discussion is restricted to plastic since those flat flakes offer the most reliable experimental LIA and sample distance dependence.

Table 14.1: Average OD [mm] of emission lines using a 35, 50 and 100 *mm* lens.

	air	wavelength [mm]	OD [mm]		
			35 mm	50 mm	100 mm
plastic		386, 387, 388 (CN), 516 (C_2)	2.8	3.5	5.3
	Nitrogen	463, 500, 504, 568 ($N\ II$)	3.5	3.8	7.8
	Water	656 (H_α)	3.5	4.0	6.5
	Oxygen	777 ($O\ I$)	2.0	2.5	-
glass		279 ($Mg\ II$), 393&397 ($Ca\ I$) 589 ($Na\ I$)	3.0	3.8	7.8
	Nitrogen	463, 500, 504, 568 ($N\ II$)	3.3	4.5	6.0
	Water	656 (H_α)	3.0	4.0	-
	Oxygen	777 ($O\ I$)	3.0	3.5	0.5
gravel		279 ($Mg\ II$), 288, 385 & 390 ($Si\ I$) 634 ($Si\ II$), 393, 397, 422, 445, 616, 644 & 646 ($Ca\ I$), 309 ($Al\ I$), 455 & 493 ($Ba\ II$)	4.3	4.5	12.0
	Nitrogen	463, 500, 504, 568 ($N\ II$)	4.3	5.5	13.0
	Water	656 (H_α)	4.0	5.5	5.5
	Oxygen	777 ($O\ I$)	4.0	6.0	9.5

Table 14.2: OD [mm] for different laser incidence angles (LIA) and emission lines (100 *mm* lens).

	plastic		glass			gravel		
LIA[°]	CN 388	Ca 397	Na 589	Mg 279	Ca 318	Na 589	Al 309	Si 288
0	7.5	7.5	10.0	9.0	10.0	16.5	15.0	7.0
15	7.0	6.0	10.0	9.0	10.0	18.0	17.5	9.5
30	7.0	7.0	8.0	7.0	8.0	17.5	15.5	5.0
45	6.5	6.5	10.0	6.5	8.0	16.5	15.5	4.0
60	6.0	6.5	7.5	6.0	7.0	15.0	13.5	3.0

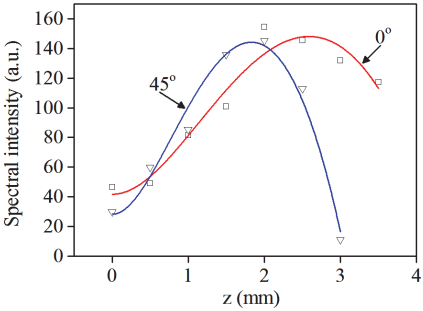

Figure 14.4: Experimental average intensities for plastic for 0 and 45 deg LIA as a function of plastic surface distance from the laser focus (z=0). The corresponding model fitted intensities are shown as continuous curves.

We explain how the signal strength depends on the position of the material in the laser beam. Fig. 14.4 shows the data points for the spectral intensity of plastic in the OD range for which the laser focus is on and below the flake surface. It also shows predicted curves for these two selected cases using the beam fitted with Eq.(1) and the fluence-ablation hole model in Eq.(2). The OD and maximum signal become smaller with larger laser angle, and the signal strength indeed increases with increased hole size (i.e. larger z and thus larger focus). More striking is that for the maximum signal the flake surface must be kept a few millimetres above the laser focus. It is noted that in reality the maximum signal may also be influenced by the laser angle through a dependency on the electric field polarization [7].

4 Summary

We investigated various factors that may affect the quality of LIBS spectra while inspecting small particles of gravel, glass and plastic using single-shot spectra in open air. The quality is inferred using the observation depth and spectral abundance. A long focal length lens of 100 mm provided a compromise between spectral abundance, air interference and achievable optical depth. The optical depth varied between

3-18 mm as the laser incidence angle varied from $0^\circ - 60^\circ$. The actual value depends on the material type (i.e. the matrix) and the particular emission line under consideration. Nevertheless, the results indicate that in case for a surface roughness of up to 3 mm the inspection may still yield quality spectra. By fitting the experimentally determined laser beam profile, the breakdown thresholds are calculated as 1.6, 1.5 and 1.0 GW/cm^2 for plastic, glass and gravel, respectively. Based on the observation depth a threshold value can be determined to identify the anomalous spectra. For dry and moist materials the percentage of bad spectra is on average 4 % and 18 %, respectively. Moreover, the observation depth and abundance indicators provide a method to identify the reliable wavelengths that are suitable for either chemometric methods or classification algorithms.

References

1. R. Noll, C. Fricke-Begemann, M. Brunk, S. Connemann, C. Meinhardt, M. Scharun, V. Sturm, J. Makowe, and C. Gehlen, "Laser-induced breakdown spectroscopy expands into industrial applications," *Spectrochimica Acta Part B: Atomic Spectroscopy*, 2014.
2. D. Cremers and L. Radziemski, *Handbook of Laser-Induced Breakdown Spectroscopy*. New York, USA: Wiley, 2006.
3. J. Cowpe, R. Pilkington, J. Astin, and A. Hill, "The effect of ambient pressure on laser-induced silicon plasma temperature , density and morphology," *Journal of Physics D: Applied Physics*, 2009.
4. M. Baig, A. Qamar, M. Fareed, and A. R. Anwar-Ul-Haq, M., "Spatial diagnostics of the laser induced lithium fluoride plasma," *Physics of Plasmas*, 2012.
5. H. Xia and M. Bakker, "Reliable classification of moving waste materials with libs in concrete recycling," *Talanta*, 2014.
6. R. A. Multari, L. E. Foster, D. A. Cremers, and M. J. Ferris, "Effect of sampling geometry on elemental emissions in laser-induced breakdown spectroscopy," *Applied Spectroscopy*, 1996.
7. V. P. Ageev, S. Burdin, I. Goncharov, Y. N. Goncharov, V. I. Konov, Y. A. Skvortsov, V. N. Tokarev, and N. Chapliev, "Energy thresholds for air-breakdown plasma formation on the surfaces of solid targets under the action of tea CO_2 laser pulses," *Soviet Journal of Quantum Electronics*, 1983.

Sensor-based sorting of mineral construction and demolition wastes by near-infrared

Elske Linß,[1] Horst-Michael Ludwig,[1] Mirko Landmann,[2]
Andrea Karrasch[3] and Ferdinand Kaiser[4]

[1] Bauhaus-Universität Weimar, F. A. Finger Institute of Building Materials Science, Coudraystraße 7, 99423 Weimar, Germany
[2] IAB Institut für Angewandte Bauforschung Weimar gGmbH, Über der Nonnenwiese 1, 99428 Weimar, Germany
[3] LLA Instruments GmbH, Justus-von-Liebig-Straße 9-11, 12489 Berlin, Germany
[4] S+S Separation and Sorting Technology GmbH, Regener Straße 130, 94513 Schönberg, Germany

Abstract Near-infrared based sorting is one possibility to turn recycled mixture of mineral construction and demolition wastes (CDW) into usable materials and has been investigated in a German research and innovation project. The target was to find suitable optical attributes for the identification of aggregates from construction and demolition wastes. The interdependencies between features from the spectrum analysis and the mineralogical composition of unused building materials were analyzed. Within the presented research project was constructed in cooperation with two German companies a sorting system, which allows sorting of mineral construction and demolition waste in industrial scale.

1 Introduction

Construction and Demolition Waste (CDW) is the biggest waste flow in Germany with an amount of 53.1 million tons CDW in the year 2010. Regarding the application of C&DW aggregates, it can be concluded that, independently of the recycling rate, most of them are used in road pavements and earth works, not really substituting the natural aggregate applications. Only a very small amount of recycled aggregates (only 1 wt.-

% in the year 2008) flows back in the production of recycled concrete. CDW from building constructions are heterogeneous mixtures, containing clay brick, mineral bounded building materials (concrete, sand-lime brick, autoclaved aerated concrete, lightweight concrete), mortars, plasters, insulation materials, wood, plastics, etc. In future, as a consequence of modern masonry construction, an increased volume of complex material composites and wider material diversity in mineral construction and demolition waste can be expected. To enable the reuse of recycled aggregates in the production, such material composites must be separated into unmixed material fractions. Main focus is the separation of gypsum attachments and composite particles, which are unavoidable through mechanical crushing. Not only old concrete can be recycled, also other recycled materials like clay or sand-lime bricks can be reused as feedstock in the production, thus closing the cycle. In this case, the heterogeneous C&DW must be turned into homogeneous, recycled material fractions. Otherwise, a cost-intensive landfilling cannot be avoided. The heterogeneity of C&DW aggregates prevents the profitable reuse. Therefore it is necessary to develope appropriate sorting processes. Sensor-based single particle sorting devices are the most promising techniques to sort efficiently usable material fractions and to remove impurities from the recyclable fractions.

2 Sorting of mineral construction and demolition wastes by hyperspectral near-infrared imaging

Figure 15.1 shows the principle of the detection of the reflective of the electromagnetic radiation in near infrared range, which has been applied in the research project. The reflected spectrum is measured by a hyperspectral camera KUSTA2.2MSI from LLA Instruments GmbH allowing the recognition of mineral particles. The spectrograph scans the particles that move on a conveyor. It is possible to scan particles with a minimal particle size of up to 4 mm. The software allows a chemometric evaluation of the spectral information. For this, a statistical method called PLS (Partial Least Squares Regression) is used. The signals from the software control the air pulses, which remove “bad” material from the ”good” fraction.

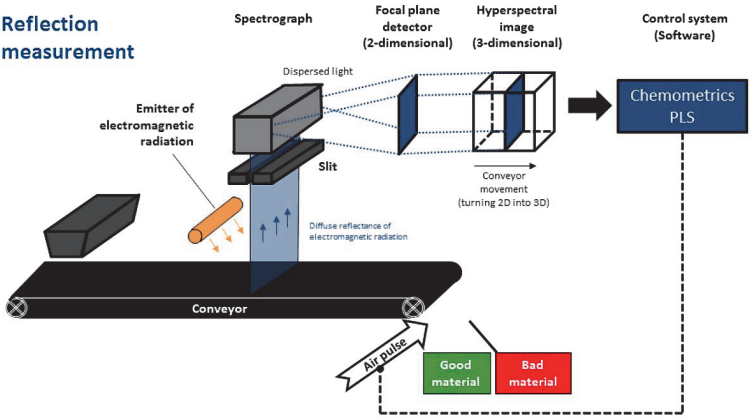

Figure 15.1: Principle of the identification by near-infrared technology [1]

3 Experimental and Results

3.1 Samples for the identification of different components of construction and demolition wastes

In a first step near infrared spectra of different unused building materials were taken and analyzed by chemometric methods for data analysis and classification. The interdependencies between features from the spectrum analysis and the mineralogical composition will be analyzed for the following material classes - conrete, lightweight concrete, autoclaved aerated concrete, clay brick, sand-lime brick, natural aggregates, gypsum, plastics and wood. From each building material class, about ten varieties (sub classes) were investigated regarding their mineralogical composition and their typical near-infrared spectrum. The target was to find suitable optical features for the identification of C&DW aggregates. In Figure 15.2 an overview is given about the evaluated samples and their bulk density. All Particles had a particle size of 8/16 mm. In a second step spectra of real recycled materials were added to the database.

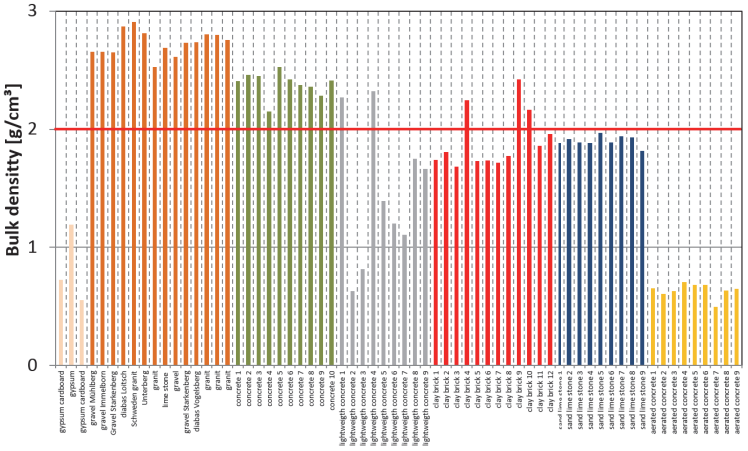

Figure 15.2: Overview of the bulk density of all analyzed unused building materials (grain size 8/16 mm)

3.2 Measurements and Results

A lot of pure minerals have characteristic absorption bands in the near-infrared wavelength range between 1100 – 2500 nm. According to the near-infrared active absorptions, the minerals can be divided into the following groups - Hydrous minerals, Minerals with characteristic hydroxide and Carbonate minerals. The hydroxide groups show absorption bands in the wavelength range from 1350 to 1430 nm which are mineral-specific and therefore ideal for evaluation purposes. The different binding states in the crystal lattice causes small differences in the absorption wavelengths of different hydroxile groups. The wavelength can vary in the range of only a few nanometers, but is sufficient for the identification. The unprocessed spectra are characterized by broad absorption bands in particular in the wavelength range between 1350 - 1450 nm and 1800 - 2100 nm, which are composed of the superposition of the absorption of different minerals and water. In preliminary experiments, building materials forming minerals were measured in pure form with the laboratory spectrometer uniSPEC2.2S and archived. The minerals occurring in construction materials are in particular assigned to the mineral classes: carbonates, silicates (including

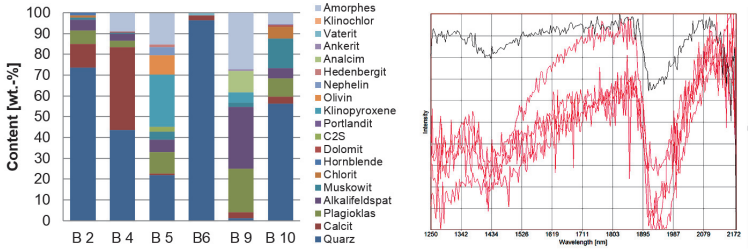

Figure 15.3: Mineralogical composition (left) and spectra (right) of some concrete samples

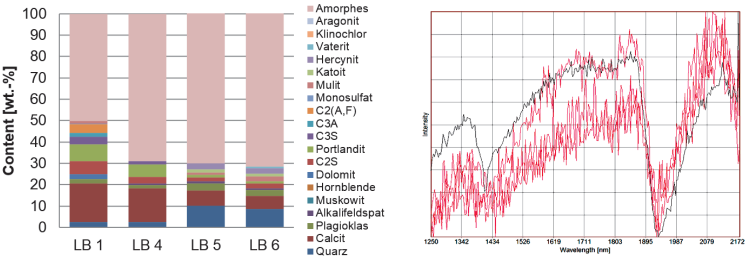

Figure 15.4: Mineralogical composition (left) and spectra (right) of some lightweight concrete samples

layered silicates), sulfates (especially gypsum products) and oxides (e.g. hematite) [2]. Furthermore, at the Bauhaus-University Weimar, the mineralogical composition of selected samples was determined. The X-ray diffractometry was carried out on powdered samples. For this purpose, the material was ground to < 63 µm respectively in the disc mill. The preparation for X-ray diffraction was carried out by front-side preparation ("frontloading"). The measurements were performed with a Siemens D5000 diffractometer. The qualitative phase analysis was performed using Diffrac Plus EVA, Bruker AXS, against the PDF-2 database (NIST) and the ICSD database (FIZ Karlsruhe). In Figures 15.3 to 15.8, the mineralogical compositions and single scan NIR spectra for concrete, lightweight concrete, aerated concrete, clay bricks, sand lime bricks and gypsum are shown separately. The single scan NIR spectra were recorded with a NIR hyperspectra imaging camera

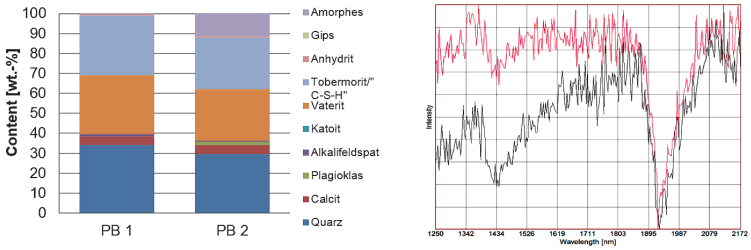

Figure 15.5: Mineralogical composition (left) and spectra (right) of some aerated concrete samples

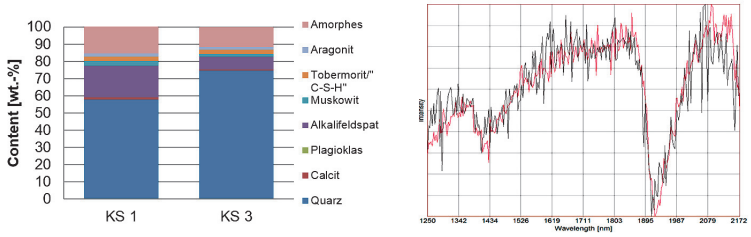

Figure 15.6: Mineralogical composition (left) and spectra (right) of some sand lime brick samples

KUSTA2.2MSI at a belt speed of 2 m/s and a repetition rate of 270 Hz. The mineralogical composition of the concrete is very different, depending on the aggregate (Figure 15.3 left). A differentiation in different types of concrete by NIR is therefore not possible. However, the mineral calcite is detectable and suitable for detection by means of infrared (Figure 15.3 right). Figure 15.4 shows the mineralogical composition and the spectra of the investigated lightweight concrete. Again, the mineral phase composition varies depending on the aggregate used. Also, the X-ray amorphous content is very high. The lightweight aggregates used in lightweight concrete such as expanded glass or expanded clay show in the infrared spectrum no significant bands. A differentiation between normal and lightweight concrete is not possible. Autoclaved aerated concrete can be identified very well on the basis of the tobermorite phase, which was formed during the steam curing in an

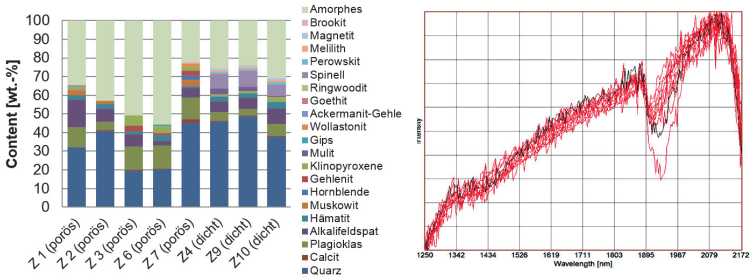

Figure 15.7: Mineralogical composition (left) and spectra (right) of some clay brick samples (porous and dense)

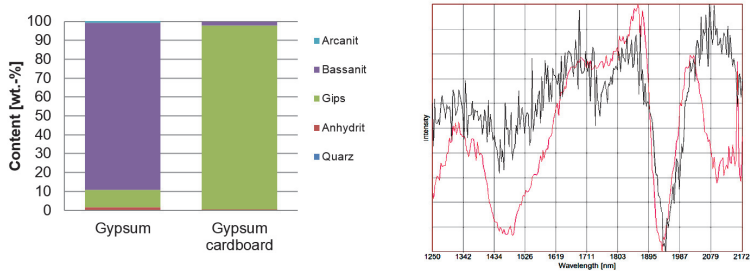

Figure 15.8: Mineralogical composition (left) and spectra (right) of some gypsum samples

autoclave (Figure 15.5). The tobermorite content in aerated concrete is between 30 and 40 wt.-%. The characteristic peak in the spectrum of tobermorit is located at 1426 nm and 1920 nm, as shown in Figure 15.5 right. The investigated sand-lime bricks consist mainly of quartz, which is undetectable in the near infrared spectrum. The calcite content is low. As steam cured material sand lime brick also contains tobermorite, but in smaller quantities (Figure 15.6). The investigated bricks are very inhomogeneous, as shown in Figure 15.7. Depending on the clay used for their preparation, the composition varies in a wide range. The bricks show a typical spectrum, so that it can be identified. But it is not possible to distinguish bricks with lower and higher density by differences in the spectrum. To distinguish the different quality of bricks the evaluation

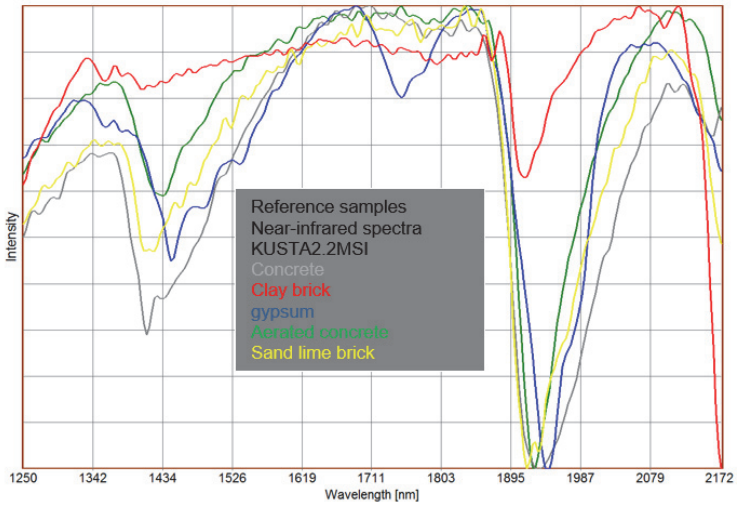

Figure 15.9: Comparison of the spectra of the investigated materials, shown as 2nd derivation of the Intensity

of different features and feature vectors in the visible spectrum is very well suited as found in previous studies of LINSZ and ANDING [3]. In Figure 15.8 the mineralogical compositions of the investigated gypsum are shown. The bands for gypsum and bassanite also referred to as hemihydrate – are very noticeable in the near-infrared spectrum and can be used for identification.
Figure 15.9 compares the object average spectra for representative materials of each type investigated.

3.3 Development of a Prototype

In cooperation with the companies S+S Separation and Sorting Technology GmbH and LLA Instruments GmbH, a sorting system has been developed, which allows the sorting of mineral construction and demolition wastes under real conditions (Figure 15.10). The hyper spectral camera offers a much higher spatial resolution at a very high refresh rate (possible measurement frequency of up to 270 Hz) due to the used

Figure 15.10: Near-infrared sensor based sorting machine for CDW

2D sensor array. Therefore, even small particles can be detected and sorted. By means of the demonstrator, the performance limits are being tested.

3.4 Algorithm for the separation of different material combinations

The procedure for the creation of the sorting file is as following: Before NIR sorting of different building materials is possible, the chemometrical identification have to be developed. For this purpose, a sufficient number of spectra for each material class must be recorded. Spectra containing artifacts or exhibiting a low signal to noise ratio must be removed from the learnset. The learnset includes both spectra of unused building materials and spectra of recycling materials. In the learnset, the identified material groups must be included as different types. The learnset is then utilized for a PLS (Partial Least Squares Regression)analysis. The PLS is a statistical chemometric method for data evaluation based on principal component analysis. The results of the principal component analysis - the score vectors are used for the classification of unknown material. The calculated score vectors can be visualized by a so called scores plot in 2-D or 3-D. The 3-D Scores plot for the separation of gypsum from concrete and also of gypsum from sand lime brick are shown in Figure 15.11.

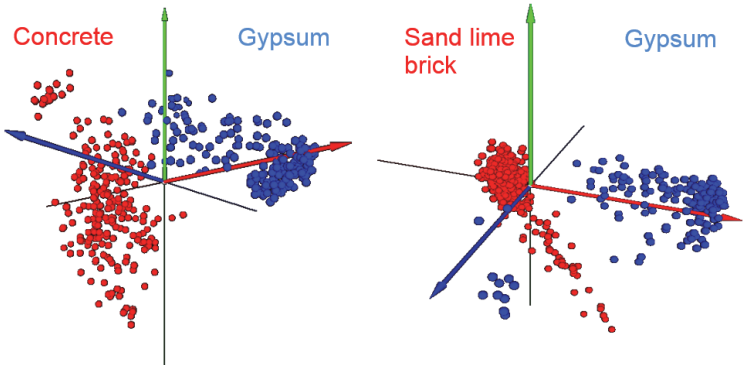

Figure 15.11: PLS Scores Plot for the system gypsum/concrete (left) and gypsum/lightweight concrete (right) (Software "KustaSpec", LLA Instruments GmbH, Germany)

4 Summary

The results can be summarized as follow:

- In principle, concrete and brick are well distinguishable in the infrared spectrum.
- Autoclaved aerated concrete and sand lime brick can also be very well recognized by near-infrared sensors.
- Lightweight and normal concrete cannot be distinguished in the near-infrared spectrum.
- Gypsum as impurity in the waste stream is very well detectable by near-infrared.
- A distinction between dense and porous clay bricks is not possible at the present state of knowledge by means of near-infrared.
- Clay brick material is not always recognizable. To explain the reasons, more research is needed.

Within the presented research project, an optical sorting method based on hyperspectral near-infrared sensors and the necessary recognition software is developed.

References

1. *Landmann,M.; Müller, A.; Ulsen, C.; Karrasch, A.; Linß, E.: Chemical-mineralogical sorting of mineral construction and demolition wastes for a better recovery. Presentation, 1st Int. Conf. on Minerals in the Circular Economy, Espoo, Finland, 28.11.2014*, 2014.
2. *Linß, E. and Karrasch, A.: NIR-Sortierung von Bauschutt: Abschlussbericht zum AiF-Forschungsprojekt AIF-KF 2155712. Bauhaus-Universität Weimar, Weimar, 2013*, 2013.
3. *Linß, E.; Anding, K.; Schnellert, T.; Ludwig, H.-M.: Identification of Construction and Demolition Waste by Using Image Processing in the Visual and Near-infrared Spectrum, and Machine Learning Methods. Proceedings of the 18. iBausil, Weimar, 12.-15.09.2012*, 2012.

Application of near-infrared (NIR) spectroscopy to sensor based sorting of an epithermal Au-Ag ore

M. Dalm,[1] M. W. N. Buxton[1] and F. J. A. van Ruitenbeek[2]

[1] Resource Engineering, Faculty of Civil Engineering and Geosciences, Delft University of Technology,
P.O. Box 5048, 2600 GA, Delft, The Netherlands
[2] Department of Earth Systems Analysis, Faculty of Geo-Information Science and Earth Observation (ITC), University of Twente,
P.O. Box 6, 7500 AA, Enschede, The Netherlands

Abstract Test work was performed with near-infrared (NIR) spectroscopy on 94 ore samples from a South-American Au-Ag mine. The aim of the test work was to investigate if alteration minerals can be detected with the NIR sensor that can be used as indicators of ore value. Partial least squares discriminant analysis (PLS-DA) was applied to the spectral data to make classification models that use the measured NIR spectra to distinguish samples with certain Au, S or C grades. This showed that detection of mineralogy with NIR spectroscopy can be used to discriminate on i) ore particles with low Au and Ag grades ii) ore particles with high carbon contents iii) ore particles with high sulphide contents.

1 Introduction

Sensor based sorting represents all applications where singular particles are mechanically separated on certain physical properties after determining these properties by a sensor. It can be incorporated as a pre-concentration step in ore processing operations to eliminate subeconomic ore material prior to conventional processing. This has potential to reduce the costs of processing mined materials [1–6]. Sensor types that are currently used with sensor based sorting include optical,

near-infrared, X-ray transmission, X-ray fluorescence and electromagnetic sensors [7, 8]. None of these sensors have been proven to be able to directly detect the Au content of epithermal Au ores.

Near-infrared (NIR) sensors used in sensor based sorting record the intensity of NIR radiation that is reflected from a solid material as a function of wavelength. NIR radiation is electromagnetic radiation, or light, with wavelengths ranging from 700 nm to 1 mm. Certain solid materials produce intense absorption of radiation around specific wavelengths in this region. This is caused by electronic molecular processes (crystal field effects, charge transfer, colour centres, conduction band transitions) and/or molecule bond vibrations [9, 10]. Identification of minerals is often possible by analysing the locations, shapes and relative intensities of all absorption features in the NIR spectrum of an ore particle. Not all minerals can be identified with NIR spectroscopy. It is restricted to minerals containing elements or molecule bonds that produce diagnostic absorptions. Minerals that that produce diagnostic absorptions are referred to as NIR active minerals.

Test work was performed to investigate the applicability of an NIR sensor to characterise epithermal Au-Ag ores on their economic value. The NIR sensor was selected because NIR spectroscopy has been proven to be a valuable tool in mapping the distribution of alteration minerals at epithermal ore deposits [11]. Deposition of Au and Ag at these deposits is related to the formation of specific alteration minerals [12–14]. It is therefore possible that the detection of alteration mineralogy with an NIR sensor can be used for predicting the economic value of the ore.

2 Hydrothermal alteration at epithermal ore deposits

Epithermal Au-Ag deposits are formed by hydrothermal activity that is driven by a magmatic intrusion occurring at several kilometres below the Earth's surface. Hydrothermal activity is the movement of hot aqueous (hydrothermal) fluids through the Earth's crust and interaction between these fluids and the rocks through which they pass. The hydrothermal fluids responsible for epithermal deposit formation originate from the magma and are released due to cooling of the magmatic intrusion [15]. Au, Ag and other elements are dissolved within these fluids as ions or complex ions. After release from the magma, the hy-

drothermal fluids flow towards the surface due to the relatively high pressure and temperature. The ascending magmatic fluids may subsequently mix with meteoric fluids which changes the fluid chemistry and temperature.

Epithermal Au-Ag deposits form at depths up to 1500 m below the surface and temperatures < 300 °C. Sharp pressure and temperature gradients in this environment results in boiling of the hydrothermal fluids, which changes fluid composition and forces Au and Ag to precipitate [13, 15]. The hydrothermal fluids that introduce Au and Ag in epithermal deposits also introduce, remove and/or redistribute other pre-existing components of the host rock. This is referred to as hydrothermal alteration [15]. Hydrothermal alteration results in the formation of alteration minerals. The type of alteration minerals that are formed depends on the pressure and temperature of the hydrothermal fluids and on the composition of both the hydrothermal fluids and the host rock [15]. Because precipitation of Au and Ag also depends on hydrothermal fluid properties, it is related to the formation of specific alteration minerals [12–14].

3 Sorting objectives of the test work

Test work was performed to investigate the applicability of an NIR sensor to characterise epithermal Au-Ag ores on their economic value. The economic value of the ore samples that were used for the testwork mainly depends on the Au grade. Ag is mined as a by-product and higher Ag grades increase ore value. Relatively high concentrations of carbonaceous materials or sulphide minerals on the other hand decrease ore value because these lower the recovery of Au and Ag during ore processing. The objectives of the testwork were therefore to investigate if an NIR sensor can be used to distinguish i) ore particles with low Au and Ag grades, ii) ore particles with high carbon contents, iii) ore particles with high sulphide contents.

4 Methods – Test work approach

The test work included NIR spectroscopic measurements on 94 samples that originate from a South-American mine. This mine exploits a high-

sulphidation epithermal Au-Ag deposit. Each sample is a rock particle of about 5-15 cm in diameter. The sample set consists of 80 samples that were collected from the ore zone of the deposit and 14 samples that were collected from an unmineralised zone. These different zones are defined by the geological deposit model that is used by the mine. The subsets were selected at random from two locations that were about 250 m apart.

7 NIR reflection spectra were measured on each sample with an ASD Fieldspec3 portable spectroradiometer. This device records reflected NIR radiation at wavelengths ranging from 350 to 2500 nm. For analysis of the measured NIR spectra, this wavelength range was subdivided into two regions. This was done because two different types of absorption processes take place in these regions. At wavelengths ranging from 350 to 1300 nm the measured NIR spectra are dominated by charge transfer absorptions of the Fe-ion (Fe2+ and Fe3+). These absorptions therefore allow determination of Fe-bearing mineralogy. This wavelength region will be referred to as the visible (VIS) region of the NIR spectra. At wavelengths ranging from 1300 to 2500 nm the measured NIR spectra are dominated by absorptions from molecule bond vibrations. These absorptions allow determination of hydrothermal alteration mineralogy. This wavelength region will be referred to as the short wave infrared (SWIR) region of the NIR spectra.

The NIR active mineralogy was determined from each measured NIR spectrum by comparing the spectra with reference spectra from the GMEX spectral interpretation field manual [16] and the USGS spectral library [17]. X-ray diffraction (XRD) was performed on a subset of 36 samples to validate the determined NIR active mineralogy. Selection of this subset was based on a classification of samples on the NIR spectra. Fire assay was performed on the samples in the subset to determine their Au and Ag grades. Carbon and sulphur contents of samples were determined by using a LECO analyser [18].

5 Methods – Classification with Partial Least Squares Discriminant Analysis (PLS-DA)

A classification model known as partial least squares discriminant analysis (PLS-DA) was applied to investigate the potential of using the NIR

spectral data to distinguish between pre-defined groups of samples. PLS-DA is based on partial least squares (PLS) regression [19]. This is a method that is used for calibrating a multivariate linear prediction model [20,21]. PLS regression hereby allows investigating the possibilities of predicting a set of response variables from a large set of predictor variables. A detailed description of PLS regression is presented by Wold et al. [21] and Abdi [22].

The difference between PLS-DA and PLS regression is that instead of predicting one or more dependent variables, PLS-DA is used to predict a certain class analogy. This is performed by simply calibrating a PLS regression model in which the set of response variables is replaced by a dummy matrix with assigned class memberships [19]. The advantage of PLS-DA over most other classification models is that PLS-DA does not only relate the predictor data to class membership, it also models the common structure between these datasets. This is achieved by finding a set of latent variables (LVs) that describe maximum covariance between the predictor and class data [21,22]. By using the LVs, the model is able to handle numerous and collinear predictor variables [21]. This was considered an advantage for making classification models based on the NIR spectral data, since this type data can be correlated and noisy.

PLS-DA was performed on individual NIR spectral measurements. 7 measured spectra on each individual sample were used for this. To calibrate the PLS-DA models, the spectra were assigned to the class that the sample belongs to. Only two different classes were used in each PLS-DA model. Definition of the classes was based on the sorting objectives stated in section 3. The PLS-DA model predicts a response for each measured spectrum. Responses for samples were calculated by averaging the responses that resulted for the individual measurements. By applying a threshold to these averaged responses, classification of samples was performed. Apart from the responses, PLS-DA also calculates loadings and scores. The loadings contain information on the wavelength regions that are important for classification into the classes [21,22]. The scores describe the relationship between these loadings and the measured spectra.

PLS-DA was applied to the VIS region (400 – 1300 nm) and the SWIR region (1300 – 2500 nm) of the NIR spectra separately. The spectra on the SWIR region were hull quotient corrected before applying the PLS-DA. This type of correction removes the overall reflection of the NIR spec-

tra, so that only the absorption features that are produced by molecule bond vibrations remain [10]. This is necessary to ensure that the model only uses the features that relate to mineralogy to perform the classification. The spectra on the VIS region were not corrected. This was not needed because the charge transfer absorptions that occur in this region dominate the overall reflection of the spectrum.

When using PLS-DA, it is important to select the optimal number of LVs that are used by the model. A higher number of LVs increase the accuracy of the model on data used for calibration, but the predictive power on other data may be decreased due to 'overfitting' [21, 22]. To select the optimal number of LVs, only 75 percent of the samples were used for model calibration. The remaining samples were used to validate the resulting classifications. The error rate of classification versus the number of LVs was calculated for 100 randomly chosen calibration and validation subsets. The number of LVs at which the lowest average error rate resulted for the validation subset was selected for creating the PLS-DA classification model.

The PLS-DA was performed with algorithms from the classification toolbox for Matlab from the Milano Chemometrics and QSAR Research Group [23]. Before applying the PLS-DA the data was mean-centered.

6 Results – Mineralogy determined with NIR spectroscopy

Figure 1 presents an overview of measured NIR spectra of all the different minerals that were determined on the samples with NIR spectroscopy. The minerals determined from the VIS region of the NIR spectra are presented separately of those from the SWIR region. Almost all spectra in figure 1 match those of single minerals [16,17]. Only the SWIR spectra of diaspore and dickite are mixed with other minerals. The spectrum of diaspore in figure 1 shows additional features by pyrophyllite around 1400 and 2170 nm. The presented spectrum of dickite is actually dominated by broad water absorptions that occur around 1400 and 1940 nm. Dickite was determined from the small absorption features that occur at 1380, 1415, 2175 and 2205 nm. The spectrum of water that is presented in figure 1 is likely produced by small fluid inclusions in quartz. The occurrence of quartz with fluid inclusions is common at ep-

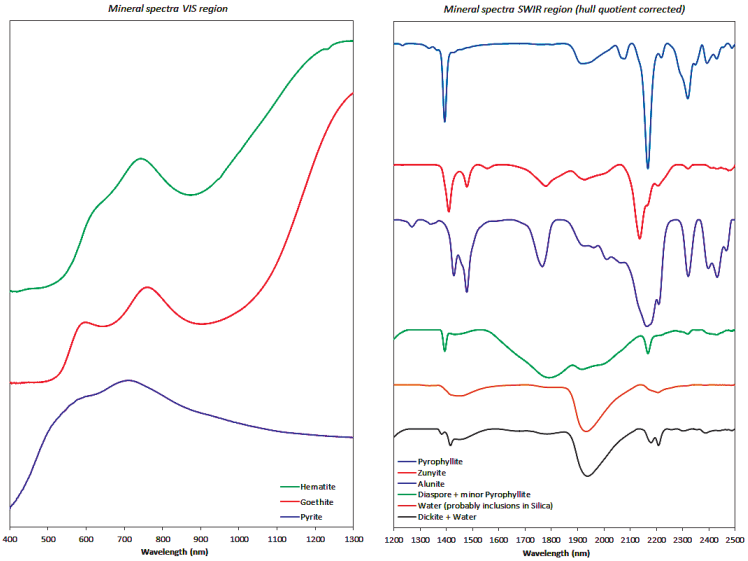

Figure 16.1: Measured NIR spectra of identified minerals

ithermal deposits [13] and was validated by XRD. It was made sure that all samples were dry while taking the measurements.

The SWIR region of the measured NIR spectra often contains absorptions by 2 or 3 different minerals. The VIS region on the other hand only shows a dominant mineralogy because all the characteristic mineral absorptions overlap. A fraction of the measured VIS spectra also had no characteristic shape at all, indicating an absence of significant amounts of Fe-bearing minerals. In total, 22 different combinations of NIR active mineral assemblages were determined from the samples. Minerals that were most often identified include pyrophyllite, quartz (water spectrum), hematite and goethite. Diaspore and zunyite were often determined from mixed spectra with pyrophyllite. Dickite always occurred together with quartz.

Apart from the spectra in figure 1, also spectra with a very low reflection over the entire VIS and SWIR spectral ranges were measured. It resulted that these spectra are representative for the carbonaceous ore

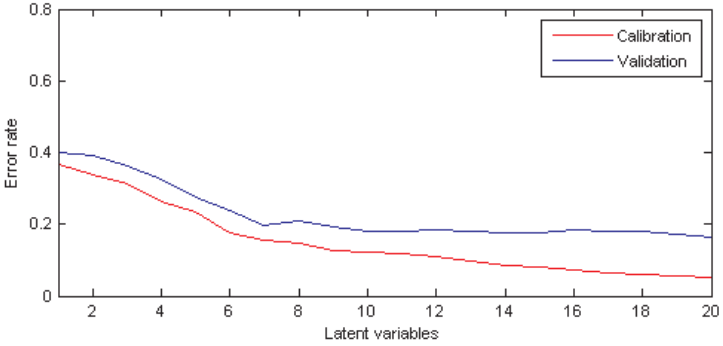

Figure 16.2: Error Rate vs. nr of Latent Variables in PLS-DA

materials. The low reflection of carbonaceous samples is also observed visually from their dark black colour.

XRD validated the occurrence of almost all minerals that were identified with NIR spectroscopy. The only mineral that was not validated by XRD is dickite. However, it is possible that the weight fraction of dickite in the samples is below the limit of detection of XRD. The NIR spectra from which dickite was identified also showed only weak absorption features of this mineral, indicating relatively low concentrations.

7 Results – Classification model for sorting on Au

Different PLS-DA classification models have been produced to classify the samples on the sorting objectives stated in section 3. This section presents an overview of the results from a PLS-DA model that was aimed at distinguishing samples with Au grades < 0.20 ppm. Processing of ore samples below this grade is not profitable. The classification was performed on the SWIR region of the spectra.

The first step in the PLS-DA classification was to select the optimal nr of LVs that are used by the model. This was performed by calculating the error rate of classification versus the number of LVs for 100 randomly chosen calibration and validation subsets. Figure 2 presents

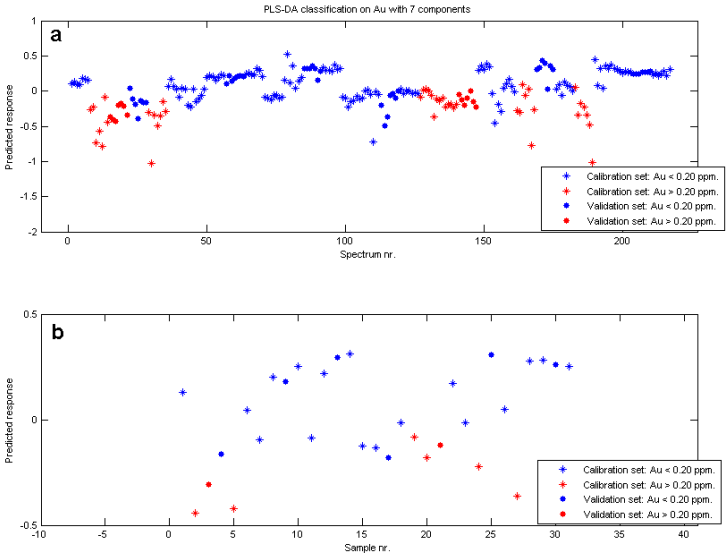

Figure 16.3: Predicted responses from PLS-DA

the average of these classifications. This figure shows that there is no significant decrease in the error rate of the validation subset when more than 7 LVs are used. 7 LVs were therefore selected for performing the PLS-DA classification.

Figure 3a presents the responses that the PLS-DA model calculated for each measured SWIR spectrum. The different colours in this figure refer to the different classes on which the model was calibrated. The calibration of the model is performed in such a way that the difference between the predicted responses of the two classes is maximised. Figure 3b shows the sample responses, which were calculated by averaging the responses of the SWIR spectra that were measured on each sample. The stars and dots in figure 3a and 3b refer to samples that were used for calibration and validation of the model. The figures show that for each class the responses of the validation subset fall within the range of responses of the calibration subset. The classification results are therefore consistent for samples that were not included during model calibration.

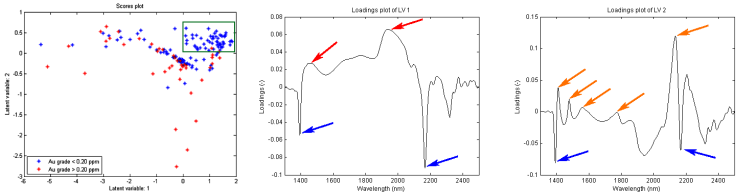

Figure 16.4: Scores and Loadings from PLS-DA

Using different calibration and validation subsets produced similar results.

Figure 3b shows that there is overlap between the predicted responses of the two classes. However, it also shows that calculated responses $>$ -0.05 only result on samples with low Au grades. By applying a threshold to the responses it is therefore possible to distinguish a group of samples that all have Au grades < 0.20 ppm. To investigate which SWIR spectral features allow identification of these samples, the scores and loadings of the model were analysed.

Figure 4 presents the scores and loadings for the first two LVs that are used by the PLS-DA model. The green rectangle indicates a region on the score plot where only measurements on low grade samples result. The first loadings plot shows that these measurements can be distinguished on the basis of absorption features relating either to water (red arrows) or pyrophyllite (blue arrows). The second loadings plot shows that the distinction between spectra is also based on the occurrence of either pyrophyllite (blue arrows) or zunyite (orange arrows). The scores of the low grade samples in the green rectangle are positive on both the 1st and 2nd LV. This relates to NIR spectra that are represented by absorption features in the negative direction of the loadings of both LVs. It results that low grade samples can be identified from the occurrence of spectral features relating to pyrophyllite and absence of features relating to water (quartz) and zunyite. Investigation of scores and loadings of other LVs of the model also showed that features relating to diaspore are characteristic for the low grade samples. These results were confirmed by visual interpretation of the spectra and the determinations of mineralogy that resulted from XRD.

Table 1: Geochemistry of samples with pyrophyllite & no zunyite (Class 1) and other samples (Class 2)

Averages before classification		Averages Class 1 (45 %)		Averages Class 2 (55 %)	
Au (ppm)	0.261	Au (ppm)	0.086	Au (ppm)	0.405
Ag (ppm)	1.594	Ag (ppm)	0.000	Ag (ppm)	2.906
As (%)	0.007	As (%)	0.002	As (%)	0.011
C (%)	0.002	C (%)	0.000	C (%)	0.004
S (%)	0.758	S (%)	0.721	S (%)	0.788

Table 2: Geochemistry of samples with carbon (Class 2) and other samples (Class 1)

Averages before classification		Averages Class 1 (86 %)		Averages Class 2 (14 %)	
C (%)	0.722	C (%)	0.002	C (%)	5.186
Au (ppm)	0.239	Au (ppm)	0.261	Au (ppm)	0.104
Ag (ppm)	1.644	Ag (ppm)	1.594	Ag (ppm)	1.960
As (%)	0.007	As (%)	0.007	As (%)	0.006
S (%)	0.938	S (%)	0.758	S (%)	2.052

Table 3: Geochemistry of samples with pyrite (Class 2) and other samples (Class 1)

Averages before classification		Averages Class 1 (71 %)		Averages Class 2 (29 %)	
Au (ppm)	0.261	Au (ppm)	0.313	Au (ppm)	0.132
Ag (ppm)	1.594	Ag (ppm)	2.245	Ag (ppm)	0.000
As (%)	0.007	As (%)	0.009	As (%)	0.001
C (%)	0.002	C (%)	0.003	C (%)	0.000
S (%)	0.758	S (%)	0.190	S (%)	2.147

Figure 16.5: Sample classification based on mineralogy detectable with NIR spectroscopy

8 Results – Overview of classification results

The previous section presented an example of how PLS-DA was used to identify certain minerals from the SWIR spectra that are characteristic for samples with Au grades < 0.20 ppm. The same method was applied to other Au grades and the carbon and sulphur content of samples. Also the VIS region of the measured spectra was investigated by using the same approach. Based on the information that this provided, certain assemblages of NIR active minerals could be defined that only occur on samples with Au, C or S grades within a certain range. Figure 5 presents the results of three classifications that were based on distinguishing samples that contain these mineral assemblages. PLS-DA modelling showed it was possible to make this distinction on the basis of NIR spectral data.

The classification result in table 1 is based on distinguishing samples that contain pyrophyllite while zunyite is absent. The table shows

significant differences between the average Au and Ag grades of both sample groups. The maximum Au and Ag grades of group 1 are furthermore 0.19 and 0.00 ppm. It results that the NIR sensor can be used to distinguish a fraction of the sub-economic ore samples. However, it should be noted that it is unknown how well these samples represent the entire ore deposit.

The classification result in table 2 is based on distinguishing samples with a low overall reflection. The samples that contain carbon generally absorb most of the NIR radiation which is also visible from their dark black colour. Classifying the NIR spectra on the average reflection therefore allows distinguishing carbonaceous ore samples.

The classification result in table 3 is based on distinguishing samples of which the VIS spectra are characteristic for pyrite. VIS spectra of samples in group 1 either showed Fe-oxide minerals or no diagnostic mineral absorptions. By distinguishing samples containing NIR active pyrite, significant differences between the average sulphur content of both sample groups results.

9 Conclusions

The following conclusions were drawn from the testwork

- It is possible to use NIR spectroscopy to distinguish ore samples with low Au and Ag grades. This is based on specific alteration mineral assemblages detectable from the SWIR region of the NIR spectra (1300 – 2500 nm).
- The average NIR reflection of samples can be used to distinguish samples with relatively high C contents. This distinction can also be made visually because carbonaceous samples have a dark black colour.
- It is possible to use NIR spectroscopy to distinguish between samples with high and low S contents. This is based on detecting either Fe-oxide or Fe-sulphide minerals from the VIS region of the NIR spectra (350 – 1300 nm).
- PLS-DA is an effective technique to investigate classification possibilities based on NIR spectroscopic data.

References

1. J. Salter and N. Wyatt, "Sorting in the minerals industry: past, present and future," in *Minerals Engineering, 4*, 1991.
2. R. Sivamohan and E. Forssberg, "Electronic sorting and other preconcentration methods," in *Minerals Engineering, 4*, 1991.
3. H. Wotruba and F. Riedel, "Ore preconcentration with sensor based sorting," in *Aufbereitungs technik,46(5)*, 2001.
4. M. Dalm, M. Buxton, J. van Ruitenbeek, and J. Voncken, "Application of near-infrared spectroscopy to sensor based sorting of a porphyry copper ore," in *Minerals Engineering 58*, 2014.
5. M. Buxton and J. Benndorf, "The use of sensor derived data in optimization along the mine-value-chain," in *International congress of the ISM*, Clausthal-Zellerfeld, 2013a.
6. ——, "The use of sensor derived data in real time mine optimization: A preliminary overview and assessment of techno-economic significance," in *Proceedings of the 2013 SME Annual Meeting*, 2013b.
7. H. Harbeck and H. Kroog, "New developments in sensor based sorting," in *Aufbereitungstechnik, 49(5)*, 2008.
8. J. Bergmann, "Sensor based sorting," in *Industrial Minerals*, July 2011.
9. G. Hunt, "Spectral signatures of particulate minerals in the visible and near infrared," in *Geophysics 42(3)*, 1977.
10. R. Clarck, "Spectroscopy of rocks and minerals and principles of spectroscopy," in *Manual of remote sensing, remote sensing for the earth sciences, vol. 3*, 1999.
11. A. Thompson, P. Hauff, and A. Robitaille, "Alteration mapping in exploration: application of short-wave infrared (swir) spectroscopy," in *Society of Economic Geologists Newsletter, 39*, 1999.
12. N. White and J. Hedenquist, "Epithermal gold deposits: styles, characteristics and exploration," in *Society of Economic Geologists Newsletter, 23*, 1995.
13. S. Simmons, N. White, and D. John, "Geological characteristics of epithermal precious and base metal deposits," in *Economic geology, 100th anniversary volume*, 2005.
14. R. Sillitoe, "Epithermal models: genetic types, geometrical controls and shallow features," in *Mineral deposit modelling*, 1993.
15. F. Pirajno, "Hydrothermal mineral deposits, principles and fundamental concepts for the exploration geologist," 1992.

16. AusSpec, "G-mex spectral interpretation field manual," AusSpec International ltd., 2008.
17. R. Clark, G. Swayze, R. Wise, E. Livo, T. Hoefen, R. Kokaly, and S. Sutley, "Usgs spectral library splib06a: U.s. geological survey, digital data series 321," [online] http://speclab.cr.usgs.gov/spectral-lib.html, 2007.
18. LECO, "Leco carbon/sulphur analyzers," [online] http://www.leco.com/products/analytical-sciences/carbon-sulfur-analyzers, 2015.
19. M. Sjostrom and S. Wold, "Pls discriminant plots," in *Pattern recognition in practice II*, 1986.
20. T. Naes and H. Martens, "Multivariate calibration ii. chemometric methods," in *Trends in analytical chemistry, 3(10)*, 1984.
21. S. Wold, M. Sjostrom, and L. Eriksson, "Pls-regression: a basic tool of chemometrics," in *Chemometrics and intelligent laboratory systems,58*, 2001.
22. H. Abdi, "Partial least squares regression and projection on latent structure regression (pls regression)," in *Wiley interdisciplinary reviews: computational statistics, 2(1)*, 2010.
23. D. Ballabio, "Classification toolbox," [online] http://michem.disat.unimib.it/chm/download/softwares.htm, 2013.

Applicability of hyperspectral fluorescence imaging to mineral sorting

Sebastian Bauer, Dominic Mann and Fernando Puente León

Karlsruhe Institute of Technology, Institute of Industrial Information Technology, Hertzstraße 16, 76187 Karlsruhe, Germany

Abstract Hyperspectral fluorescence images of mineral samples have been acquired. Their spatial and spectral structure is analyzed and the samples are classified. Mineral samples from the same deposit may show large spectral differences, while samples from different deposits can appear quite similar. These analyses are a good start into the research of using mineral fluorescence as sorting technique, but more effort has to be taken to come to satisfying classification results.

1 Introduction

There are quite a few techniques for mineral sorting, e.g., X-ray fluorescence and laser-induced breakdown spectroscopy (LIBS) [1, 2]. Most of them suffer from drawbacks like high cost or difficulties in handling, such as X-rays. In this article, the applicability of hyperspectral fluorescence imaging as alternative mineral discrimination technique is investigated. Fluorescence is the short-lived form of luminescence, which is the emission of light after optical excitation. Due to energy loss, the wavelength of the radiation emitted by the sample is longer than the excitation wavelength (so-called Stoke's shift) [3]. A small portion of chemical impurities (e.g., rare earth ions), the luminescent centers, also called activators, are responsible for the emission of fluorescence photons, and small amounts of other impurities such as Fe^{2+}, Co^{2+} and Ni^{2+}, the so-called quenchers, drastically reduce the intensity of the fluorescence [4]. Due to the fact that small amounts of impurities determine not only the intensity, but also the fluorescence color, specimens of the same mineral kind but of different locales can vary greatly in fluorescence intensity and color [5].

Hyperspectral fluorescence imaging has been used for determinining the state and constituents of food such as corn and apples [3,6,7], but to the best of our knowledge not yet been applied to mineral sorting. Kim et al. [8] describe a system for the hyperspectral analysis of fluorescence and reflectance combined with 3D analysis. Although they also examine minerals with their system, their main focus is on investigations of biological and fine arts issues such as the visual appearance and perception of birds. They do not consider the different fluorescence spectra of minerals for sorting applications. Fluorescence studies of minerals have been reported by Hofer et al. [9], however, they only measured point spectra. In this article, in contrast, we will describe hyperspectral fluorescence images. By acquiring hyperspectral images, it is possible to investigate space-resolved spectra of the samples and analyze the spatial variance of the investigated sample. The space-resolved acquisition of fluorescence spectra bears the potential of providing reliable means of mineral discrimination because more information, i.e., more spectra and the spatial relationship between them, can be analyzed. Therefore, e.g., smaller surface areas with and without skin can be analyzed.

2 Experimental setup

We already presented the first results of hyperspectral fluorescence imaging of a small set of mineral samples [10] as well as feasible image reconstruction techniques [11]. We now contribute an analysis of a larger sample number of more different mineral types and point out the spatial characteristics of the fluorescence radiation. Additionally, the spectra were recorded at a higher spectral resolution, i.e., 4 nm instead of 17 nm. We still use the same setup: Within a closed box, the samples are illuminated by a tunable monochromatic light source with a 300 W xenon arc lamp of which spectrum the interesting part is cut out by a 300 mm Czerny-Turner monochromator. The resulting light is directed to the sample by a high-reflectance aluminum mirror with about 85 % reflectance across the spectral range from 250 to 800 nm. The light emitted by the sample is filtered by an acousto-optical tunable filter (AOTF, Gooch&Housego HSi-300). This is a filter which transmits a certain wavelength at a selected bandwidth. Both wavelength and bandwidth can be adjusted almost arbitrarily between 450 and 800 nm,

while the smallest possible bandwidth is 1.5 nm. Such a filter allows for fast and flexible wavelength selection. The light that passed the filter is acquired by an Andor iXon$_3$ 897 EMCCD (electron multiplying charge-coupled device) with 512 $\times$ 512 pixels. In this type of camera, the photo electrons are multiplied electrically in an on-chip multiplication register before readout. For this reason, there is a higher signal level before the read noise is added. Although some noise is added during the multiplication process, the total SNR increases. Even the registration of single photons is possible when appropriate settings are used. Cooling the chip down to about −85 °C almost completely eliminates the dark current and allows for long exposure time spans, as the only relevant noise component is the time-independent read noise.

We chose excitation wavelengths from 260 to 360 nm in steps of 20 nm. The light source was running continuously. The spectral resolution of the acquired images is 4 nm with a bandwidth of 3.9 nm, resulting in a total of 86 pictures of the scene at wavelengths from 450 to 790 nm. In contrast to [10], the exposure time has been adjusted to take care of the varying spectral intensity of the light source such that regardless of the wavelength, the same number of photons is delivered to the samples. This results in exposure times per single image ranging from 24 to 112.8 s. A total of 33 minerals of 6 different mineral types originating from different natural mineral deposits was analyzed, see Table 17.1.

Table 17.1: Used minerals.

type	magnesite	talc	dolomite	granite	chlorite	quartz
number of samples	13	8	5	2	3	2

3 Fluorescence analysis

No pre-processing of the minerals such as cutting etc. was performed. All samples had a dust-free surface. The samples were split up into three scenes as the illumination spot was not big enough for all samples. A complete hyperspectral image of each scene was acquired. Each band's image was then filtered by the Hessian Schatten norm regularization method [12]. To correct for the spatially inhomogeneous illu-

mination, the spatial fluorescence intensity of white paper was measured. Each fluorescence image of the samples was divided by these corresponding spatial intensity values. The pixel spectra were corrected by taking the spectral sensitivity/transmission of the lens, the AOTF, the camera window and the EMCCD sensor into account. The numbers were taken from the supplied data sheets. There are, however, unknown correction factors that could not be figured out yet. They could be due to inaccurate parameter values automatically used by the software during the sweep.

Figure 17.1 shows the image of one scene acquired at 526 nm using 320 nm excitation wavelength. This image clearly shows the intensity differences of the fluorescence of the samples at the considered wavelength. After applying the image filtering, the sample contours can be seen better. Note that the two white magnesite samples (lower left corner) are the brightest, while there is quite a large intensity difference between them. Talc (last three samples in the top row and first four in the middle row) shows the second brightest fluorescence in this scene, even stronger than the yellow magnesite samples (last two samples in the middle row). Granite (two samples in the upper left corner) fluoresces at a very low intensity. It is mentionable that just like with the two white magnesites, there is an intensity difference between the two granite samples. The three chlorite samples in the lower right corner show almost no fluorescence.

As not all spectra can be presented here, the average spectra of each magnesite sample at 360 nm excitation wavelength are shown in Fig. 17.2. It can be seen that samples from different origins have different fluorescence spectra.

The acquired spectra cannot be compared to literature fluorescence spectra due to two reasons: Firstly, the previously mentioned unknown spectral correction factors, and secondly, the fluorescence spectra depend on the natural mineral deposits the samples are taken from. Because of the fact that all spectra were recorded with the same setup, however, they can be compared amongst each other.

Since hyperspectral fluorescence images of minerals have not been analyzed in the English literature before, it is very interesting to take a look at the spatial differences of the emitted fluorescence spectra. As can be seen in Fig. 17.1 and Fig. 17.2, respectively, the fluorescence intensity at a considered wavelength includes very discriminative information

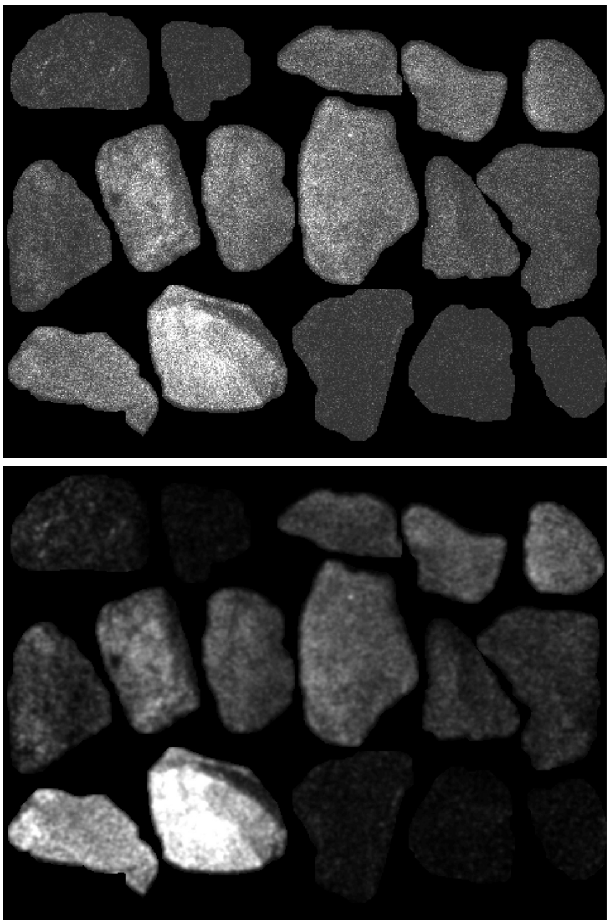

Figure 17.1: Top: Raw image of one scene at 526 nm using an excitation wavelength of 320 nm. Bottom: filtered and intensity corrected image. The background parts have been masked. Both images share the same grayscale: pixel values of 0 are shown in black, 500 in white. The samples in the top row are from left to right granite (two samples) and talc (three samples). The second row includes four samples of talc with pyrite and two yellow magnesite samples, while the last row consists of two samples of white magnesite and three chlorite samples.

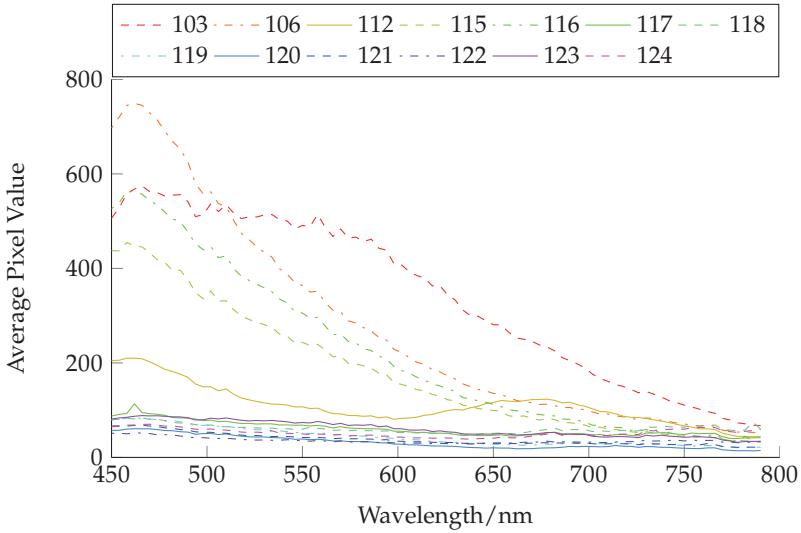

Figure 17.2: Mean spectra of the magnesite samples.

about the present minerals. Therefore, it should be investigated if the sample geometry has an impact on the measured intensity. Figure 17.3 displays two images of one magnesite. The shading used in the left image (fluorescence image at 360 nm excitation wavelength), however, is not a physical one: The color of each pixel shows the intensity of the corresponding pixel spectrum. It is interesting to note that although no change in mineral composition can be seen in the color image, there is a high illumination intensity at the breaking edge.

Figure 17.4 shows a similar picture of a dolomite sample. The green circle marks an edge with an angle of almost 90° which is relatively hard to distinguish from the adjacent surfaces, although the light comes from the viewing direction. Especially in the region highlighted in red, there is no difference between the two surfaces. The light spot on the left comes from some crust on the mineral surface which could be mortar or naturally grown. As the sample had a paper sticker attached to it, there is another white spot in the lower part of the image. From these two examples, it can be stated that the geometry can, but must not nec-

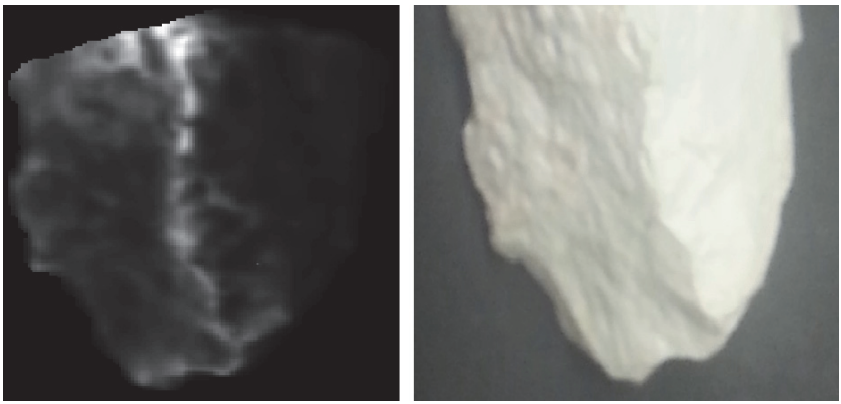

Figure 17.3: The pixel colors in the left picture show the sum of all spectral values of the considered pixels (i.e., the integral of the pixel spectrum). White indicates the highest spectral sum, while black indicates the lowest. The upper corner of the image has been cut off due to low illumination intensity. The right image is an RGB image of the same sample.

essarily have an impact on the fluorescence intensity. This fact should be considered in future sorting machines.

4 Classification and results

We already presented the classification results of a small sample [10,11], but we only used 21 wavelengths instead of 86. Due to the fact that just a small sample was considered, the classificators were trained with pixels from the same samples that were to be classified. As in the present study, hyperspectral images of more samples were acquired, we now are able to give the classification results of all minerals with at least two pieces from the same origin. Minerals of the same sort from the same origin form one class such that there are five magnesite classes and five other classes each formed by a different mineral type. We used the pixels of one mineral out of each class as training data and all other minerals from all classes as test data. This results in ten classes and one mineral of each class was selected as training sample. All other minerals from these classes were used as test data and had to be classified

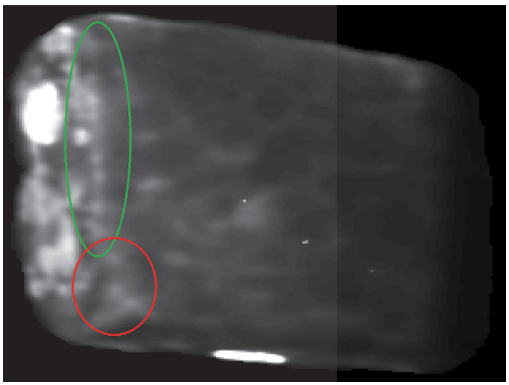

Figure 17.4: Intensity image of a dolomite sample at 360 nm excitation wavelength.

into one of the ten classes. We used three different types of classifiers: linear discriminant analysis (LDA), the k-nearest neighbors algorithm (KNN, 5 neighbors) and the spectral angle mapper (SAM) [11, 13]. The SAM classifier is invariant against illumination differences. This is due to the fact that it interprets a spectrum as a vector in the N-dimensional space with N being the number of spectral bands. It compares each pixel spectrum with one reference spectrum of each class by calculating the spectral angle between two vectors, i.e., one reference spectrum and the respective test spectrum. By the calculation of the angle, a distance measure independent of the spectrum intensity is introduced due to the fact that the spectra are divided by their norm. The reference spectra of each class are the mean spectra of the respective training samples. The training samples are not considered in the object classification rate (an object is classified as one class if most of its pixels are classified into this class). The resulting 16 minerals are classified as given in Table 17.2. All classifiers show rather low classification rates, but one should keep in mind that 10 different classes consisting of only 6 different minerals have been considered. If magnesite samples are classified incorrectly, they mostly are classified into the wrong magnesite class. This underlines that there are large spectral fluorescence differences between samples of the same type, but from different deposits. On the other hand, a

sample of a certain deposit can be more similar to another sample from a different deposit than to one sample from the same deposit. Interestingly, the SAM classifier which neglects differences in the pixel intensity does also not perform well at all illumination wavelengths.

Table 17.2: Classification results.

Excitation	LDA	KNN	SAM
260	0.56	0.75	0.63
280	0.50	0.69	0.69
300	0.38	0.50	0.75
320	0.44	0.31	0.50
340	0.44	0.31	0.25
360	0.44	0.38	0.25

5 Summary

Hyperspectral fluorescence images of 33 minerals from 6 different types have been acquired and their spectral and spatial information has been analyzed. State of the art classifiers have been applied to the pixel spectra and showed classification results that should be improved by more sophisticated classifiers. For further work improving the classification results, it would be useful to take the intensity differences due to object geometry and illumination into account. The intrinsic advantage of hyperspectral images, i.e., the knowledge of the space-dependent spectra, should also be used for improving the classification results, as texture information (see Fig. 17.1) can also be included into the classification process. Due to the high variability in the spectra from different samples, even more samples should be investigated.

References

1. H. Wotruba and H. Harbeck, "Sensor-based sorting," *Ullmann's encyclopedia of industrial chemistry*, Wiley-VCH, 2010.
2. M. Gaft, L. Nagli, Y. Groisman, and A. Barishnikov, "Industrial online raw

materials analyzer based on laser-induced breakdown spectroscopy," *Applied spectroscopy*, vol. 68, no. 9, pp. 1004–1015, 2014.

3. M. Kim, Y. Chen, P. Mehl *et al.*, "Hyperspectral reflectance and fluorescence imaging system for food quality and safety," *Transactions – American Society of Agricultural Engineers*, vol. 44, no. 3, pp. 721–730, 2001.
4. M. Gaft, R. Reisfeld, and G. Panczer, *Modern luminescence spectroscopy of minerals and materials*. Springer, 2005.
5. The fluorescent mineral society: Fluorescent minerals. [Online]. Available: http://uvminerals.org/fms/minerals
6. H. K. Noh, Y. Peng, and R. Lu, "Integration of hyperspectral reflectance and fluorescence imaging for assessing apple maturity," *Transactions of the ASABE*, vol. 50, no. 3, pp. 963–971, 2007.
7. H. Yao, Z. Hruska, R. L. Brown, and T. E. Cleveland, "Hyperspectral bright greenish-yellow fluorescence (BGYF) imaging of aflatoxin contaminated corn kernels," in *Optics East 2006*. International Society for Optics and Photonics, 2006, pp. 63 810B–63 810B.
8. M. H. Kim, T. A. Harvey, D. S. Kittle, H. Rushmeier, J. Dorsey, R. O. Prum, and D. J. Brady, "3D imaging spectroscopy for measuring hyperspectral patterns on solid objects," *ACM Transactions on Graphics (TOG)*, vol. 31, no. 4, p. 38, 2012.
9. I. Hofer, R. Huber, G. Weingrill, and K. Gatterer, "Luminescence- and reflection spectroscopy for automatic classification of various minerals," in *OCM 2013-Optical Characterization of Materials-conference proceedings*. KIT Scientific Publishing, 2013, p. 227.
10. S. Bauer and F. Puente León, "Industrielle Sortierung von Mineralen anhand von hyperspektralen Fluoreszenzaufnahmen – Potenzialbewertung," in *Forum Bildverarbeitung 2014*, F. Puente León and M. Heizmann, Eds. Karlsruhe: KIT Scientific Publishing, 2014, pp. 215–226.
11. ——, "Gewinnung und Verarbeitung hyperspektraler Fluoreszenzbilder zur optischen Mineralklassifikation," *tm - Technisches Messen*, vol. 82, no. 1, 2015.
12. S. Lefkimmiatis, A. Bourquard, and M. Unser, "Hessian-based norm regularization for image restoration with biomedical applications," *Image Processing, IEEE Transactions on*, vol. 21, no. 3, pp. 983–995, 2012.
13. F. Kruse, A. Lefkoff, J. Boardman, K. Heidebrecht, A. Shapiro, P. Barloon, and A. Goetz, "The spectral image processing system (SIPS) – interactive visualization and analysis of imaging spectrometer data," *Remote sensing of environment*, vol. 44, no. 2, pp. 145–163, 1993.

Visible and infrared reflectance spectroscopy for characterization of iron impurities in calcined kaolin clays

Adriana Guatame-Garcia and Mike Buxton

Delft University of Technology,
Stevinweg 1, 2628 CN Delft, The Netherlands

Abstract Visible (VIS) and Short Wavelength Infrared (SWIR) Reflectance Spectroscopy are used to determine the presence of iron impurities on calcined kaolin. For industrial applications, primary kaolin is calcined by roasting at temperatures of greater than 1100 °C. The presence of iron impurities in the primary kaolin affects the optical properties of the processed calcined clay. Spectral analysis in the VIS and SWIR ranges allows the analysis of iron phases in kaolin. In the kaolin calcination sequence, features in the VIS range change as a consequence of the variations in iron oxidation. Some of these variations are related to iron released in the breakdown of the kaolinite crystal lattice, which is identified by the changes in the SWIR features. The spectral characterization of the calcination of kaolin contributes to the understanding of these processes. Its application would enable more precise control of calcined kaolin properties and help to optimise the calcination process.

1 Introduction

For industrial applications, primary kaolin is calcined by roasting at temperatures of greater than 1100 °C. The resulting calcined kaolin clays are widely used in the manufacture of pigments and coatings. For such applications the key parameters determining calcined product quality are colour and brightness. The latter is used as the industrial standard for measuring the optical properties of papers [1], and therefore it is of maximum importance in kaolin processing. Brightness is defined by

the norm ISO 2470 as a mathematical function having an effective wavelength of 457 nm and a bandwidth of 44 nm [2]. The presence of iron impurities in the primary kaolin prior to calcination affects visual colour and brightness in the processed calcined clay.

Kaolin is mainly composed of kaolinite; ancillary minerals such as feldspars, micas, oxides and hydroxides are also commonly present. Most of these minerals host iron either within the crystal lattice or as a surface element. Special interest in iron impurities in kaolin and calcined kaolin arises from its influence on the colour and brightness of the clay products [3]. Nevertheless, the close coexistence of the minerals in the kaolin clays hinders the evaluation on the nature of the iron [4].

The thermal treatment of kaolin aims to transform kaolinite into metakaolin. In this process, kaolin minerals are dehydrated and dehydroxylated, leading to modifications in the crystal lattice. During the transformation iron is released and oxidized. This residual iron in the form of hematite acts as a chromophore giving a yellow/pink shade to the calcined clay [5].

Usually X-ray diffraction (XRD) and X-ray Fluorescence (XRF) are used as preferred techniques for kaolin mineral and chemical characterization, respectively. However, they are sometimes constrained by parameters such as particle size or require extensive preparatory work. In the mineral processing industry there is a growing interest in real-time or near real-time techniques that can be easily implemented in a production environment. In this context, Visible and Infrared Reflectance Spectroscopy has the potential to be an adequate technique for characterisation of calcined kaolin processing. This technique is well known for requiring simple or no sample preparation and for the availability of instruments that can be used in situ and provide real time data.

The spectral features that describe the transformation of kaolinite into metakaolin have been identified in the short and mid infrared ranges by using FTIR spectroscopy [6, 7]. The breakdown of M-OH bonds (M=metal), especially those related to Al-containing phases are the main features in the kaolinite-metakaolin spectra. Distortions in the kaolinite crystal lattice due to impurities can be recognized in the spectral profile, for example, in cases where Fe replaces Al in the kaolinite structure [8–10]. In addition, iron in kaolin ancillary minerals such as goethite and hematite, and its influence on the optical properties of the kaolin industrial products have been mainly researched in the visible range of

the spectrum using diffuse reflectance spectroscopy [11].

In this study, Visible (VIS) and Short Wavelength Infrared (SWIR) Reflectance Spectroscopy are used to characterize the behaviour and influence of iron in three different calcined kaolin samples. Discrimination between kaolinite structural iron and other iron bearing minerals is done by identification of the main spectral features. These are compared at different calcination temperatures in order to determine how the iron impurities are affecting the kaolinite-metakaolin transformation process.

2 Materials and Methods

Three kaolin samples with different iron content were prepared for spectral analysis. They were named Feed 1, Feed 2 and Feed 3 and represent low, medium and high Fe content, respectively. These samples were calcined at various temperatures using a muffle furnace. They were calcined at temperatures from 500 to 1200°C at 100°C intervals. Each feed was split into 6 subsamples and placed in the calciner and heated from ambient to the specified temperature at a rate of 15°C per minute. The resulting powders were measured for ISO brightness, XRD and XRF. The XRF measurements for Fe_2O_3 are indicated in Figure 18.1.

Visible and short wavelength infrared spectra were collected with an ASD FieldSpec spectrometer, using the contact probe and the internal light source. Measurements were completed over compacted powders with a flat surface for oriented kaolinite crystals. Analyses of the resulting spectra were undertaken using the Hyperspectral Python software, always over convex hull removed spectra (CR).

3 Spectral identification of Fe in Kaolin

3.1 VNIR spectrum: Fe compounds in kaolin

Spectral features typical of iron compounds in the visible and near infrared (VNIR) are present near 430, 520 and 870-960 nm (Figure 18.2). These absorptions are characteristic of Fe^{3+} present in hematite. The wavelength position and depth of these features varies in relation to the initial feed composition and calcination temperature. However, they are

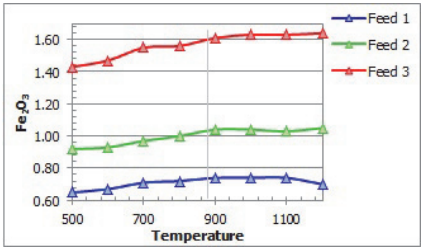

Figure 18.1: Fe_2O_3 content measured by XRF. Vertical line before 900°C represents a point where the iron oxide increasing rate decreases

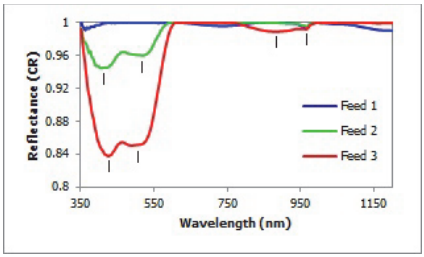

Figure 18.2: Main spectral features detected in the VNIR spectra. Absorptions at 430, 520 and 870 nm are due to Fe oxides. The small feature at 966 nm belongs to kaolinite

more clearly present along the calcination sequence in Feed 3. Absorptions nearby 670 nm, as an indicator of Fe^{3+} in goethite, are not detected in any of the samples. In Feeds 1 and 2 a broad absorption at 740 nm and a sharp one 966 nm are present in the lowest temperatures (Figure 18.2), and might belong to kaolinite instead of hematite. The intensity of the 870 absorption in Feed 3 would mask these kaolinite features.

Features in the visible range are used to explain the brightness and colour variations in the samples. Hematite absorptions in this range affect the reflectivity ratio, measured as the ratio of the reflectance values at 450 and 600 nm in not continuum removed spectra [12], which is likely related to the ISO brightness standard (Figure 18.3). Therefore, hematite content can be taken as the main parameter that affects the visible characteristics of the samples.

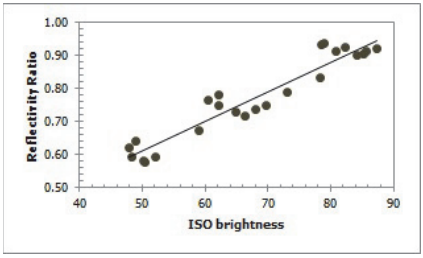

Figure 18.3: Correlation between Reflectivity Ratio and ISO brightness as mean for describing the optical properties of the samples

3.2 SWIR spectrum: Kaolinite structure

The SWIR spectra of the 3 feeds at the lowest temperature are very similar. As expected, the characteristic kaolinite features dominate the spectral profile with only small differences in some of the absorptions (Figure 18.4). Well-developed features that characterize the strength of OH bonds, as well as the Kaolinite Crystallinity Index (KX) demonstrates that kaolinite in these samples has highly ordered structure. However, these same parameters suggest that kaolinite in Feed 1 has a higher order of crystallinity than Feed 2 and Feed 3.

Studies developed by [8] indicate that Fe^{3+} – Al^{3+} substitution in kaolinite causes an absorption band at 2240nm. Nevertheless, this absorption is not clear in any of the feeds. Absorptions due to Fe replacement within the kaolinite structure are not evident in this part of the spectra.

4 Kaolin calcination and spectral changes

Calcination of kaolin affects the entire spectral profile, demonstrating that the thermal treatment affects both the optical and physical parameters of the calcined clay. As remarked previously, features in the VNIR spectra are mainly related to iron hosted in kaolin ancillary minerals, whereas features in the SWIR range are closely related to the kaolinite crystal structure.

Kaolinite, as the main kaolin component, dominates the processes oc-

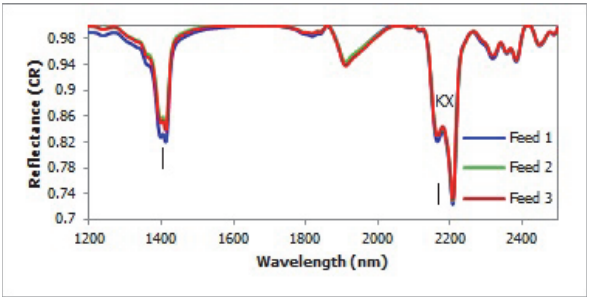

Figure 18.4: Characteristic kaolinite absorptions in the SWIR spectra. The doublet at 2200 nm is diagnostic for kaolinite identification and is used to measure the Kaolinite Crystallinity Index (KX)

curring during calcination. The main process is driven by the kaolinite – metakaolin transformation, and therefore affects the OH-related features measured in the SWIR range. The dehydroxylation process can be illustrated by the flattening of the 1400 and 2200 absorptions with increasing temperature (Figure 18.5). The transformation of these features is similar for the three feeds, although there are subtle differences at specific calcination stages. From 500 to 700°C OH features are weakened, but they still preserve the characteristic kaolinite doublets. Spectra at 800°C represent the most distinctive differences for the 3 feeds. The KX, calculated for the whole calcination sequence, shows that Feed 3 has a faster dehydroxylation rate, whereas Feed 2 to seems to have a more stable structure than Feed 1 (Figure 18.6). After 900°C none of the kaolinite distinctive features are recognized, although weak OH absorptions are still present. After this point, the most prominent feature occurs at 1900nm, which corresponds to the water feature (Figure 18.5).

Changes in the VNIR spectra along the calcination sequence differ between feed types due to the compositional differences. However, as shown in Figure 18.7, some points are comparable. At lower temperatures, hematite features are clearly dominant in Feed 2 and 3. They are always deeper in Feed 3. They are absent in Feed 1. Instead in Feed 1 most of this part of the spectrum is dominated by kaolinite, with some small features. Up to 700°C the maximum absorption in Feeds 2 and 3 is at 430nm. Above 800°C this absorption weakens and the 520nm fea-

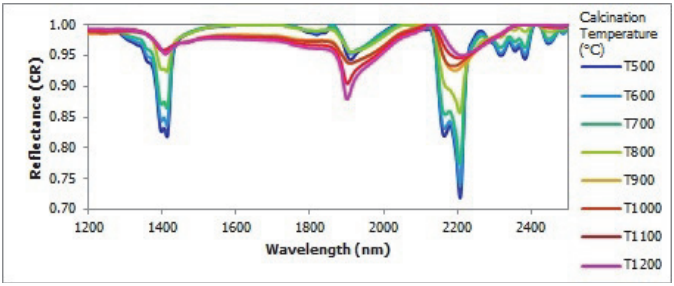

Figure 18.5: Changes in the SWIR spectra due to dehydroxylation with increasing the calcination temperature. OH-related features at 1400, 2200 and 2250-2400 nm become shallower and smoother at higher temperatures

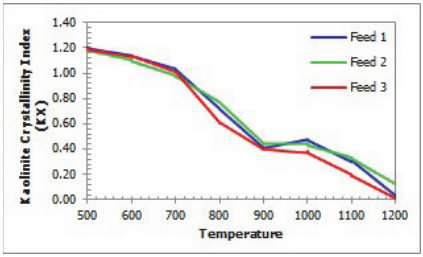

Figure 18.6: Variations in kaolinite crystallinity along the calcination sequence, as a measure of dehydroxylation degree

ture is the deepest one. It disappears in Feed 2 at 1000°C and in Feed 3 at 1100°C. After 800°C the 520nm absorption becomes the most relevant absorption, not only for Feeds 2 and 3, but also for Feed 1, where an incipient Fe-feature appears and remains present until 1100°C. At this temperature the same feature is also weaker for the other feeds. In contrast, the broad feature nearby 870nm gets deeper along the whole sequence for Feeds 2 and 3. This feature is not present in Feed 1. At 1200°C a goethite absorption feature is apparently present in Feed 3.

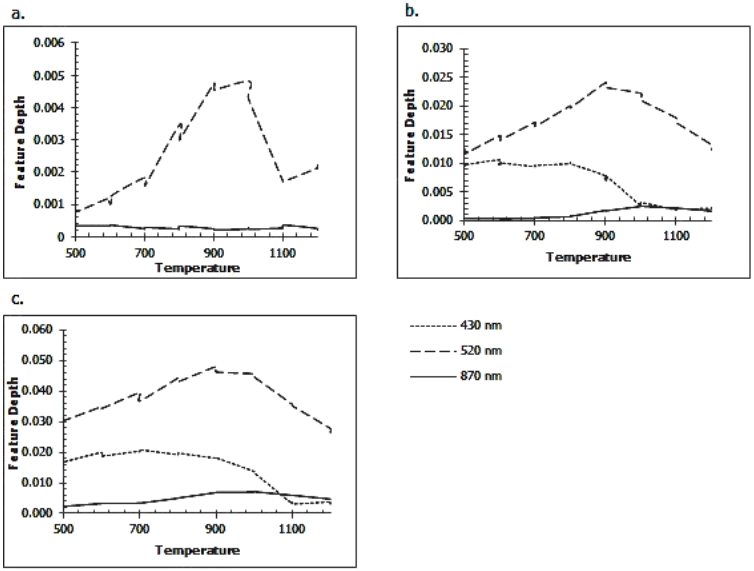

Figure 18.7: Variations in the VNIR absorptions along de calcination sequence, represented as the depth of the feature at a given wavelength. **a. Feed 1, b. Feed 2, c. Feed 3**. The 430nm feature becomes shallower until almost vanishing at higher temperatures. No data is shown for Feed 1 since feature is not present. The 520 nm absorption reaches its maximum depth at 900°C in all the feed types. Broad absorption in the 870 nm region gets deeper with increasing temperature, although its intensity is very low in relation to the other features. This feature is not developed in Feed 1

5 Discussion

Kaolinite-metakaolin transformation

The transformation of kaolinite into metakaolin is clearly recorded in the variations of the SWIR spectral profile. As the lowest temperature measured is 500°C it is assumed that dehydration has taken place already. Therefore the main process occurring is dehydroxylation. The flattening of the spectral features at 1400 and 2200nm, representing OH bonds and Al-OH stretching respectively, indicates that the attractive forces among atoms weaken when temperature increases. This leads

to distortions in the kaolinite crystal structure. It becomes an amorphous compound referred to as metakaolin. This stage is reached between 800°C and 900°C for the given set of samples. However, the rate of this process is not the same for the three different kaolinites. With Fe^{3+} replacing Al^{3+} in the kaolinite octahedral spaces, the crystal lattice becomes more unstable, and therefore prone to quicker dehydroxylation. It is expected that high iron content and low crystallinity values in the samples correspond to a larger amounts of structural Fe. This is true for Feed 3, which initially has the lowest KX values, and becomes dehydroxylated more rapidly than the other feeds (Figure 18.4). However, this situation is not that clear for Feeds 1 and 2. Even though initially Feed 2 is less crystalline than Feed 1, its dehydroxylation rate is slower. This might indicate that the distortions in its crystal lattice are not necessarily caused only by Fe replacement, but also by other factors that do not destabilize the structure to the same extent as Fe does. It might also be possible that the crystallinity measurement has been affected by factors such as mineral mixtures. XRD analysis revealed the presence of muscovite in these samples. Nevertheless, due to the invariability on the wavelength position of the Al-OH feature (2207nm) it was assumed that the influence of muscovite in the kaolinite spectra is very small. Despite the fact that muscovite might also host iron in its structure, it reacts similarly to kaolinite. Therefore, it does not have any significant impact on the Fe-related observations.

Even though the absorptions bands that represent Fe^{3+} –Al^{3+} replacement in kaolinite were not identified, other factors suggest the presence of structural iron in the analysed samples. The 800-900°C temperature window, where it is considered that metakaolin formation is taking place, coincides with the peak of energy absorption of iron in the VNIR range. Similarly, the iron content as measured by XRF increases up to 800°C and becomes less variable after this temperature (Figure 18.1). It is interpreted that during dehydroxylation iron has been released from the kaolinite structure. In oxidizing conditions it reacts to formFe_2O_3, and therefore hematite absorptions are enhanced. A decrease in the intensity of these absorptions at the highest temperatures might be explained by particle size effects, as it will be further explained, or by reincorporation of Fe in the structure during the next step of the calcination sequence that results in mullite crystallization. However, the shape of the spectral features at high temperatures suggests that recrystalliza-

tion has not yet taken place. Spectral features in the Mid Infrared range (MIR) may give more complete information about the possible crystallization of mullite. Moreover, the fundamental absorptions in that part of the spectrum should exhibit clearer absorption bands related to structural iron in kaolinite. This could therefore validate the observations herein presented.

Influence of Fe in the calcined kaolin optical properties

In the VNIR range the spectral features are caused by electronic processes, generated in this case by the iron content. Its presence in calcined kaolin clays has a remarkable influence on the optical properties. This influence is conditioned by the amount and the source of iron in the samples. In Feeds 2 and 3 it is clear that most of the initial iron content is derived from hematite as an ancillary mineral, whereas in Feed 1 it might come only from structural iron.

As for the SWIR spectra, features in the VNIR are affected by the calcination process. Higher calcination temperatures increase the energy of the Fe ions, intensifying the ferric charge transfer transitions from 500 to 800°C [12] in feeds 2 and 3. Because of this, features at 430 and 520 nm deepen, which is therefore shown in the colour/brightness of the samples. From 900-to 1200°C reflectivity is mostly driven by the particle size. Small particles interfere with charge transfer and ease energy scattering, resulting in weaker absorptions and increased brightness. In contrast, crystal field effects get stronger at the highest temperature, but because of the wavelength position of its feature, they do not have any effect on the visual colour of the samples.

As previously mentioned, Feed 1 initially does not show Fe-related features at low temperatures. A charge transfer absorption at 507nm appears at 800°C, as a consequence of the release of Fe from the kaolinite structure and its subsequent oxidation. This feature persists until 1000°C after which it vanishes due to particle size effects. It is possible that the enhancement of the 520nm feature in Feeds 2 and 3 at 800°C is reinforced by the increase in hematite amount that comes from structural iron, likewise in Feed 1. However, it is not possible to estimate the magnitude of this contribution.

6 Conclusions

Visible and Infrared reflectance spectroscopy has been shown to be a valuable technique for characterization of calcined kaolin clays. The focus of this study has been on the iron impurities hosted in the kaolinite structure as well as in ancillary minerals. The dehydroxylation process that drives the transformation of kaolinite into metakaolin is illustrated by the smoothening of the characteristic kaolinite spectral features in the SWIR range. In this process, 800-900°C is taken as the temperature range where the largest changes occur in the kaolinite structure. At this temperature iron is released from kaolinite as a consequence of the crystal lattice breakdown. The amount of hosted iron would speed up the dehydroxylation rate.

Spectral features characteristic of iron contained in ancillary minerals are present in the VNIR range. Iron is present as hematite. In Fe-rich samples hematite occurs naturally, whereas in iron - poor samples hematite is derived from iron released from kaolinite. The presence of iron oxides affects the optical properties of the calcined clay up to 800°C. Until this point, the increasing temperature enhances iron absorptions, controlling the shading of the samples. In addition, Fe enrichment from kaolinite contributes to intensify these features. At the highest temperatures the optical properties are influenced mostly by particle size.

Acknowledgments

This work was facilitated by Imerys Minerals Ltd and the STOICISM research project. It has been supported by the European Commission under the 7th Framework Programme through the grant number 310645.

References

1. J. A. Bristow, “What is iso brightness?” *Tappi Journal*, vol. 77, no. 5, pp. 174–178, 1994.
2. ISO, “Paper, board and pulps - measurement of diffuse blue reflectance factor -,” p. 21, 2009.
3. W. B. Jepson, *Structural iron in kaolinites and in associated ancillary minerals*, 1988, ch. 15, pp. 467–536.

4. P. A. Schroeder and R. J. Pruett, "Fe ordering in kaolinite: Insights from 29si and 27al mas nmr spectroscopy," *American Mineralogist*, vol. 81, no. 1-2, pp. 26–38, 1996.
5. S. Chandrasekhar and S. Ramaswamy, "Influence of mineral impurities on the properties of kaolin and its thermally treated products," *Applied Clay Science*, vol. 21, no. 3-4, pp. 133–142, 2002.
6. H. J. Percival and J. F. Duncan, "Interpretation of the kaolinite-mullite reaction sequence from infrared absorption spectra," *Journal of the American Ceramic Society*, vol. 57, no. 2, pp. 57–61, 1974.
7. R. L. Frost and A. M. Vassallo, "The dehydroxylation of the kaolinite clay minerals using infrared emission spectroscopy," *Clays and Clay Minerals*, vol. 44, no. 5, pp. 635–651, 1996.
8. T. Delineau, T. Allard, J. P. Muller, O. Barres, J. Yvon, and J. M. Cases, "Ftir reflectance vs. epr studies of structural iron in kaolinites," *Clays and Clay Minerals*, vol. 42, no. 3, pp. 308–320, 1994.
9. R. L. Frost, "Hydroxyl deformation in kaolins," *Clays and Clay Minerals*, vol. 46, no. 3, pp. 280–289, 1998.
10. S. Petit, J. Madejová, A. Decarreau, and F. Martin, "Characterization of octahedral substitutions in kaolinites using near infrared spectroscopy," *Clays and Clay Minerals*, vol. 47, no. 1, pp. 103–108, 1999.
11. I. G. Gonçalves, C. O. Petter, and J. L. Machado, "Quantification of hematite and goethite concentrations in kaolin using diffuse reflectance spectroscopy: A new approach to kubelka-munk theory," *Clays and Clay Minerals*, vol. 60, no. 5, pp. 473–483, 2012.
12. R. V. Morris, H. V. Lauer Jr, C. A. Lawson, E. K. Gibson Jr, G. A. Nace, and C. Stewart, "Spectral and other physicochemical properties of submicron powders of hematite (alpha -fe2o3), maghemite (gamma - fe2o3), magnetite (fe3o4), goethite (alpha - feooh) and lepidocrocite (gamma -feooh)," *Journal of Geophysical Research*, vol. 90, no. B4, pp. 3126–3144, 1985.

High frequency line cameras for sorting applications

Dirk Nüßler, Paul Warok and Nils Pohl

Fraunhofer FHR
e-mail: {dirk.nuessler,paul.warok,nils.pohl}@fhr.fraunhofer.de

Abstract The increasing number of multilayer structures in sorting applications or the detection and analysis of internal areas in products demands a cheap, safe and fast imaging technology. States of the art are x-ray systems especially for the inspection of food and heat flux thermography for the analysis of invisible defects under the surface. Inspection systems based on these technologies offer many advantages like the transmission through conducting materials, good resolution etc. Unfortunately they share a disadvantage. Based on the detector lines inside these camera systems or the time constant for the heat flux the maximum belt speed is limited. High frequency sensors offer the possibility to measure the transmission through non conducting materials without this hard limitation in speed.

Index Terms—THz imaging, millimeter wave radar, high speed inspection

1 Introduction

High frequency sensors allows a view inside the most non-conducting materials and products. With a typical wavelength between 10 cm and 1 mm the resolution is limited by the chosen frequency range. In the longer wavelength region the transmission through wet materials like fruits or complete walls is possible, but the resolution is very poor. In the higher frequency range the systems reaches a sophisticated resolution but the attenuation through water inside the products rises. The dynamic range of a high frequency system can be limited by many factors. E.g. an A/D converter can decrease the dynamic range despite the dynamic range of the system is much higher. Line cameras can be

realized in transmission and reflection configuration and are separated in continuous wave (cw) systems and systems which offer a range resolution. System with a range resolution uses most times a frequency-modulated or pulsed signal. For the system approach a stepped frequency method (SFM) was chosen because it offers the best tradeoff between a low power sensor and high resolution concept. For the realization of a line camera modern radar technology offers a wide spectrum of several frequencies which can be used. System designs from the lower microwave region up to the THz region are possible. From a more economic point of view the best compromise between costs and resolution can be realized in mm-wave band between 30 GHz and 300 GHz. In the frequency range above 2 THz solid state materials have characteristic absorption lines which can be identified by a recognition algorithm. Without absorption lines a standard finger print analysis is not possible. The change of the dielectric properties over the frequency range is another approach to visualize the differences in the materials (Figure 19.1). As long as the number of different plastics is very low it's rather straight forward to identify materials through simple look-up tables. Real materials show a large diversity due to additives like flame retardants, plasticizers, UV resistance and aging effects. Therefor more versatile classification methods are recommended. In a first approach, methods based on Gaussian Mixture Models (GMM) and a Universal Background Model (UBM) were used. Using the Hilbert envelope of various band-filters, the amplitude and the time-position of the signal peak was extracted as features for a GMM-UBM system.

Photonic THz spectrometers offer the possibility to sweep over a large frequency range in a few milliseconds. Unfortunately, these systems are expensive and to slow for line arrays in a production line with a typical belt speed of 3 m/s. THz Systems based on cheap frequency multipliers are faster but they are working with a smaller frequency range. They could be used for industrial issues if the range is sufficient. Publications in the last years demonstrate the possibility to separate different plastics through their frequency response in the lower THz region [1]. These systems offer the possibility to measure the dielectric properties of non-conducting materials. The change of the properties over the frequency range allows the identification and classification of black plastics (Figure 19.2). To choose the optimum frequency range, the selected machine learning algorithms were trained with test data sets. In a second step a

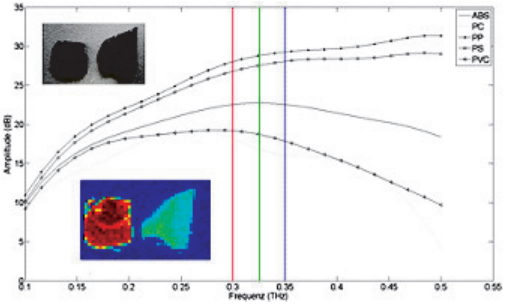

Figure 19.1: Measured results of two different pieces of plastic. In the image the differences between the three frequencies (300 GHz, 325 GHz, 350 GHz) are colorized.

blind test was performed. The lowest frequency range with sufficient results was the W-Band from 75 GHz up to 110 GHz. With a limited number of classes, test sets and a first prototype algorithm a probability between 85% and 90% for identification were realized. Based on these results a decision was made to realize a first test system in the lower THz region [2]. The mm-wave band offers a sufficient resolution for most applications and allows the realization of radar pixels on a printed circuit board (PCB) or on a silicon germanium (SiGe) chip. For the first realization step a sorting application was chosen. In recycling applications sorting machines for plastic uses hyperspectral cameras which measure only the attenuation of the reflected signal. These optical sensors are not able to sort black plastics, due to the reflected light from the black surfaces is too low for a stable detection process.

2 System Concept

To cover the whole width of a conveyor belt a great number of channels is necessary. To reduce costs system concepts with a limited bandwidth are preferred. The main disadvantage of systems with a small bandwidth is the poor range resolution. For a reliable parameter reconstruction algorithm the accurate height information is an important criterion. To compensate this disadvantage the high frequency line camera is combined with an optical height measurement system like a light section

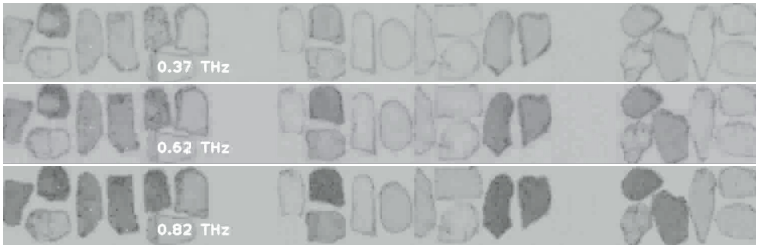

Figure 19.2: Measured attenuation for pieces of plastic for different frequencies in the lower THz region.

sensor or time-of-flight camera (ToF camera). The combination of these two technologies offers a cheap, fast and efficient system concept. The main challenge is the development of cheap high frequency channels in the frequency range above 75 GHz. Modern SiGe technologies seem to be well-suited for the development of line cameras for sorting applications. Their higher yield particularly for more complex chips with a higher number of transistors and the lower price makes this technology attractive. To design a system either focusing lens systems or open waveguide antennas as soon as dielectric tip antennas could be used. Depending on the cost, the resolution and the mechanical integration, open waveguide antennas and dielectric tips offers the best alternative for transmitting and receiving antennas above and under the belt. For a 300 mm width of the conveyor band a minimum number of 31 T/R modules are needed for a pixel width of 10 mm. Resulting in an aperture height for the transmitting antennas of 40 mm above the conveyor band. The transmitter channels are mounted above the band-conveyor. The receiver channels and the digital back-ends are installed under the conveyor belt. To minimize the number of active channels a switch matrix can be used to change one transmit/receive channel between different antenna positions. For the first prototype, a 90 GHz radar module is chosen (Figure 19.3). The system based on a 30 GHz radar module. Due to the tripled operation frequency a radar system with 12 GHz bandwidth from 84 GHz up to 96 GHz is realized. Based on the velocity of the conveyor belt with 3 m/s an update rate of 1 ms per channel is necessary.

Figure 19.3: Block with 4 transmitting channels.

The radar system can be used in different measurement modes like frequency modulated continuous wave FMCW, continuous wave CW or SFM. The frequency generation is based on a direct digital synthesizer (DDS). For the frequency reference a temperature stabilized quartz oscillator with high phase stability was chosen. The system concept demands a precision phase control across the frequency band. The controlling unit of the system is based on a FPGA. Each module of eight channels will be controlled by one Spartan 6 FPGA (DDS, ADC, etc.). A Master Unit with a Virtex FPGA (Virtex 6 Xilinx) combines the measured data and sends them via a Content Addressable Memory (CAM) interface to a Signal Processing Unit (SPU) which provides the measured results. Based on the limited space, the system is build up in a multilayer block structure. Power supply, digital-backend and the eight front-end channels are realized on separated layers (Figure 19.4-19.6).
The antennas mounted in the system are dielectric waveguides with their tips cut in an appropriate angle [3]. The outer dimensions correspond to the inner dimensions of classical waveguides. In the design a rectangular waveguide for the W-Band (frequency range from 75 GHz

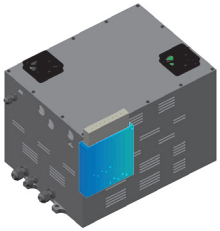

Figure 19.4: Complete receiver block

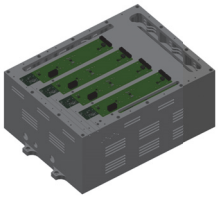

Figure 19.5: One of the two high frequency layer with 4 channels

to 110 GHz) was used with the dimensions 2.54 mm to 1.27 mm. Angle and length of the tips determine the gain of the waveguides, similar to horn-antennas (Figure 19.7). The advantage of this kind of antenna is the flexibility of the waveguide. As the wave is guided mostly outside the waveguides, the antennas are placed very carefully to avoid any contact with other parts of the measurement system. To protect the dielectric tips are covered with a Styrofoam radom.

For a waveguide junction a minimum space of 10 mm up to 20 mm is required. Test measurements and simulations have shown, that a minimum distance of two wavelengths between neighboring dielectric waveguides is necessary to reduce coupling effects. Based on this space requirements it is possible to arrange the antenna elements side by side. For future arrays smaller measurement distance are necessary. For theses arrays the coupling effects between the antenna elements can no longer be ignored. To solve this problem the antenna elements are build-

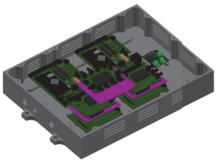

Figure 19.6: Digital backend layer

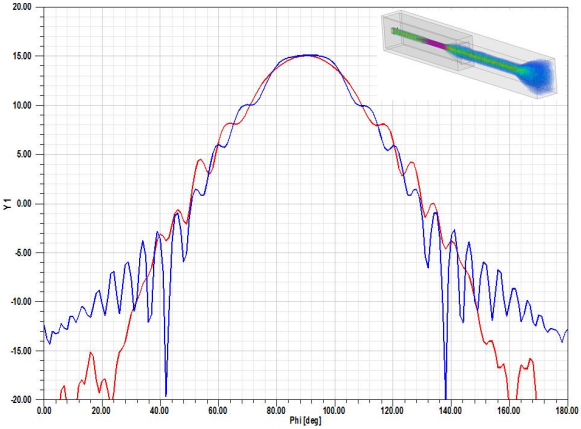

Figure 19.7: Antenna characteristic of the dielectric tips for the E- and the H-plane.

up in four independently lines. Through the different lines the spacing between neighbored antenna elements can be increased.

3 Outlook and summary

The combination of optical sensors with a THz line array in the lower THz frequency range seems to be a promising approach to sort black plastics. To realize the high requirement for a 100% recycling cycle a sophisticated signal processing is needed. The first measurements show

a high accuracy. Under consideration that a non-optimized software algorithm was used the results show a high potential for future developments and are a good basis for the development of a high frequency line array for sorting applications.

References

1. Yun-Sik Jin, Geun-Ju Kim, Seok-Gy Jeo, "Terahertz dielectric properties of polymers," in *Journal of the Korean Physical Society*, 2006.
2. K. Hein, D. Stein, M. Stadtschnitzer, M. Demming, J. Küls, "Classification of polymers using gmm-ubm on high-frequency data," in *Sensor-Based Sorting*, 2014.
3. J. Weinzierl *et al.*, "Simulation and measurement of dielectric antennas at 150ghz," in *Proceedings of the 29th European Microwave Conference*, 1999.

Micro sensor for determination of thin layer thickness and refractive index

Martin Schädel, Dennis Mitrenga, Philip Schmitt, Andreas T. Winzer and Olaf Brodersen

CiS Forschungsinstitut für Mikrosensorik und Photovoltaik GmbH, Konrad-Zuse-Str. 14, 99099 Erfurt, Germany

Abstract We present a microoptical sensor solution for measuring thicknesses and refractive indices of thin layers by measuring changes in polarization of two laser beams under inclined angle of incidence. The compact architecture does not require any moving or rotating components and allows for low-maintenance and robust operation. The measured polarized reflection is modelled by Transfer Matrix method and Levenberg-Marquard fit algorithms in order to obtain the target sample characteristics. Single layer samples of SiO_2, SiO_xN_y and SiN_x on Silicon substrate were analyzed. For several different single layer systems the deviations of layer thicknesses and refractive indices are below 3% as compared to independent reference measurements.

1 Introduction

The characterization of sample surfaces and thin coating layers by measuring changes in light polarization is a rather old discipline. The fundamental relations of light polarization, material properties and sample architecture can be described by Maxwell and Fresnel equations. Today many elaborated measuring techniques base upon these fundamentals, for example spectral or laser ellipsometry or reflectometry [1]. In order to obtain universally applicable and high precision instruments, the complexity of these setups is rather high. Most of the common instruments using rotating optical components (e.g. polarizers), monochromators or CCD elements [2], causing rather large setups with high alignment effort. On the other hand the increasing degree of automation in

production processes requires monitoring and control of product properties in a rather small parameter range. For this scenario high precision laboratory instruments are often overdimensioned. Here small, robust and fast measuring heads are often sufficient and allow for easy integration into production lines and price-conscious monitoring units.

We present a compact sensor that measures the polarized reflection for two wavelengths and operates without any moving or rotating components. The device can be used to determine the optical properties (refractive index) and film thickness of thin surface layers.

We start with a brief description of the theoretical background, including the Transfer-Matrix-Method for multi-layer thin film coatings. This method is used to model the experimental data by Levenberg-Marquardt fit routines. The device architecture and working principle is described in the third section. Experimental results are dicussed and compared with independently analyzed reference samples in section four, followed by a summary and outlook.

2 Theoretical Background

The consideration of Maxwells equation at an interface of two isotropic materials leads to Snell's law and Fresnel equations for the description of electric fields amplitudes and phases [3]. The impact of the interface can be written in form of a matrix [2]:

$$\begin{pmatrix} \underline{E}_{m,i} \\ \underline{E}_{m,r} \end{pmatrix} = \frac{1}{\underline{t}_m} \begin{pmatrix} 1 & \underline{r}_m \\ \underline{r}_m & 1 \end{pmatrix} \begin{pmatrix} \underline{E}_{m,t} \\ \underline{E}_{m,b} \end{pmatrix} = I_m \begin{pmatrix} \underline{E}_{m,t} \\ \underline{E}_{m,b} \end{pmatrix} \tag{20.1}$$

where the $\underline{E}$ are the complex electric fields at the interface m of the incoming (index i), reflected (index r), transmitted (index t) and back reflected light of subsequent interfaces in the layer stack (index b). t_m and r_m are the Fresnel coefficients for transmission and reflection, respectively. Both are functions of the refractive indices at the interface and thus in general depend on wavelength. I_m is called the interface matrix of interface m. For isotropic materials, the parallel and perpendicular fractions of light can be treated independently. Thus I_m is obtained for both cases by using the corresponding Fresnel equations.

The passage of a layer with thickness d_m has impact on the amplitude and phase of the electric field and can also be written in form of a matrix

[2]:

$$\begin{pmatrix} \underline{E}_{m,t} \\ \underline{E}_{m,b} \end{pmatrix} = \begin{pmatrix} e^{i\underline{\beta}_m d_m} & 0 \\ 0 & e^{-i\underline{\beta}_m d_m} \end{pmatrix} \begin{pmatrix} \underline{E}_{m+1,i} \\ \underline{E}_{m+1,r} \end{pmatrix} = L_m \begin{pmatrix} \underline{E}_{m+1,i} \\ \underline{E}_{m+1,r} \end{pmatrix} \tag{20.2}$$

with:

$$\underline{\beta}_m = \frac{2\pi}{\lambda} \underline{N}_m \cos \underline{\phi}_m \quad , \tag{20.3}$$

the layer thickness d_m and the complex refractive index $\underline{N}_m = n_m + ik_m$, wherein n_m is the refractive index and k_m is the extinction coefficient of layer m. Both material properties depend on the wavelength λ. L_m is called the layer matrix of layer m and $\underline{\phi}_m$ is the complex angle of light propagation within the layer m, calculated by Snell's law.

Using the previous equations a layer system with M layers can be written as [2]:

$$\begin{aligned} \begin{pmatrix} \underline{E}_\mathrm{i} \\ \underline{E}_\mathrm{r} \end{pmatrix} &= I_1 L_1 I_2 L_2 \ldots I_M L_M I_{M+1} \begin{pmatrix} \underline{E}_\mathrm{t} \\ 0 \end{pmatrix} \\ &= \prod_{m=1}^{M} (I_m L_m)\, I_{M+1} \begin{pmatrix} \underline{E}_\mathrm{t} \\ 0 \end{pmatrix} \\ &= P \begin{pmatrix} \underline{E}_\mathrm{t} \\ 0 \end{pmatrix} = \begin{pmatrix} P_{11} & P_{12} \\ P_{21} & P_{22} \end{pmatrix} \begin{pmatrix} \underline{E}_\mathrm{t} \\ 0 \end{pmatrix} \quad . \end{aligned} \tag{20.4}$$

P is the transfer matrix of the stacked layer system. The equation can be used to calculate the total external reflected ($\underline{E}_\mathrm{r}$) and transmitted ($\underline{E}_\mathrm{t}$) electric fields for a given $\underline{E}_\mathrm{i}$. In order to express coefficients for reflected light intensities, the real part of the Poynting vector is used and leads to:

$$R = \frac{S_\mathrm{r}}{S_\mathrm{i}} = \frac{|\underline{E}_\mathrm{r}|^2}{|\underline{E}_\mathrm{i}|^2} = \frac{|P_{21}|^2}{|P_{11}|^2}, \tag{20.5}$$

where S_r and S_i are the light intensities (in Wm^{-2}) of the reflected and incidence light, respectively. Eq. 20.5 can be used to calculate the parallel and perpendicular reflection for different wavelengths by changing λ in Eq.20.3 and using the corresponding Fresnel coefficients in Eq.20.1 for each layer in the system.

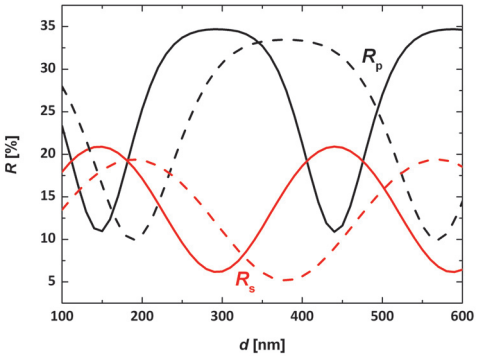

Figure 20.1: Simulated reflectance of a SiO_2 film ($n(660\,\text{nm}) = 1.4563$; $n(850\,\text{nm}) = 1.4525$) on Silicon substrate using a wavelength of 660 nm (solid) and 850 nm (dashed) with parallel (black) and perpendicular (red) polarization

With the previous equations the reflection coefficients of parallel and perpendicular light intensity can be calculated for any (isotropic) layer system. In reverse the equations can be used to find unknown sample properties by fitting the layer properties on experimental data of R_p and R_s. A common fitting routine (for example often applied in fitting spectral ellipsometry data) is the Levenberg-Marquard routine, that combines the Gradient Method and the Hesse Matrix Method in order to find the best agreement of experimental and modelled data in a multi parameter space [4]. For our software we used the figure of merit (FOM) as a measure for the model agreement with experimental data, as it takes into account the individual uncertainties of the measured values [5].

Using a single wavelength allows for two measurable values and thus for modelling up to two independent sample attributes, for example d and n of a transparent surface layer on top of a known substrate. However using only one wavelength has two mayor limitations: first the results of R_p and R_s are periodic in the parameter space, and second the sensitivity on the tested parameter might be very low, depending on the actual sample architecture.

These limitations are illustrated in Fig.20.1 for the example of a SiO_2 film with unknown layer thickness on a silicon substrate. Consider a single wavelength (for example the sold lines in Fig.20.1 for 660 nm) a periodic change in both R_p and R_s with layer thickness is obvious, showing several possible results of d for the same values of R_p and R_s. Thus no unique fit result for the unknown layer thickness is obtained with a single wavelength (unless the sample attribute is already well known and only a small parameter range is allowed in the fit). The second limitation of low parameter sensitivity is obvious in the area of local extrema, where the slopes of R_p and R_s are very small. In this area large changes in d causes only small changes of the measurable reflection. As the measured values will have uncertainties, the modelled parameter will have a rather large uncertainty in this region as well.

In order to overcome these disadvantages, a second wavelength can be applied. As illustrated in Fig.20.1 the additional information allows for unique fit results and increases the model sensitivity on the tested parameter, because at least one of the measured values shows a steep slope in the parameter space.

3 Sensor Architecture

The previous considerations made clear that the sensor requires more than a single wavelength setup. In order to obtain high sensitivity and unique fit results additional information is required, for example by muliple angles of incidence or a second wavelength. We decided for the latter. A schematic of the setup is shown in Fig.20.2 together with a photography of a first demonstrator setup of the optical subunit of the sensor. This unit is controlled by demonstrator electronics and placed in a 3D-printed housing with three adjustable feet for tilt alignment, as shown in Fig.20.3. The components are described in detail in the following sections.

3.1 Micro Optical Laser Source Unit

We chose a wafer based approach in order to achieve a high degree of miniaturization and a technology suitable for a large number of pieces. A low cost - high precision solution is the polymer-on-glass (POG) tech-

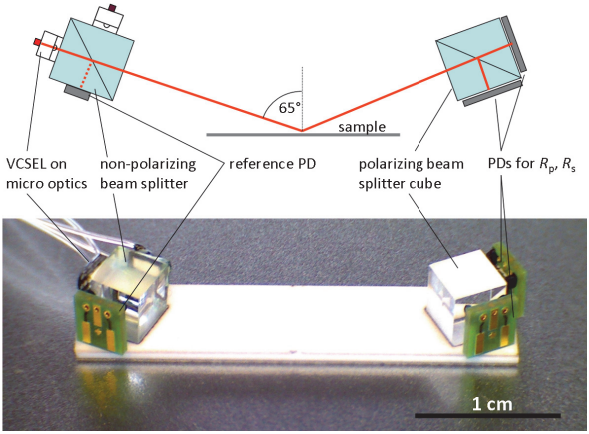

Figure 20.2: Schematic illustration and photography of a populated ceramic holder, including a two-wavelength laser source cube on the left, and a polarization detector cube on the right.

nology, see for instance [6]. Supported by optical simulations a 1100 x 700 x 640 µm³ micro optic was designed. The optics includes a glass wafer with a polymer lens and a polymer spacer at the front, and a lithographically structured thin film metal contact at the back side. The metal acts as an aperture as well as the front contact of the VCSEL (vertical cavity surface emitting laser). The 240 x 240 µm² VCSEL chips were soldered "face down" onto the metal side of the optics wafer. The apertures of the VCSEL chips and those of the optics wafer were aligned to each other. After that, the micro optics were tested for laser beam quality and subsequently diced into individual units. The micro optic laser source achieves spot sizes below 300 µm at the measurement distance.

Two laser units were used for the sensor. Each equipped with single mode VCSEL chip of 670 nm and 850 nm wavelength, respectively. They were mounted on the two entrance sides of a 50:50 beam splitter. Active 5-axis alignment was used together with an on-axis beam profiling camera and a rotating polarizing filter. This ensured the same optical axis and the target orientation of the linearly polarized laser light for both laser units. Since they showed a high degree of linear polarization ($>$ 98%) no additional polarizer is required within the sensor device.

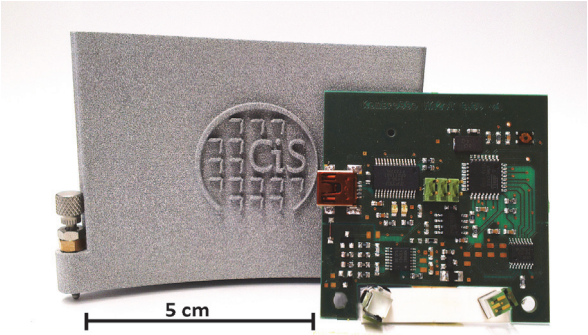

Figure 20.3: Photography of the demonstrator electronics equipped with the optical unit infront of the 3D printed housing.

On the second exit face of the beam splitter cube, a monitor photodiode was mounted. Its signal is used for monitoring and controlling the light intensity of the VCSELs.

3.2 Detector Unit

Two photo detectors were mounted on a second polarizing beam splitter cube (dielectric filter system, degree of polarization $>$ 10000:1 for both wavelengths $\pm$10 nm). As beam misalignment might be a topic in the later application of the sensor, two monolithic double photodiodes are applied. The detector for the parallel polarized part is tilted by 90° against the detector for the perpendicular component. The effect of this arrangement equals a classical 4-quadrant diode and allows for determination of errors in effective angle of incidence and possible light losses. For the application of the sensor in an automated measuring unit, this information can be used for readjustment of the sensor or the sample.

The source and detector units must be aligned according to the target angle of incidence on the sample's surface. As a good compromise between achievable accuracy in sensor alignment and sensitivity on sample attributes, we chose an angle of incidence of 65°. The source and

detector units are mounted on a ceramic holder in order to reduce mechanical stress for example due to temperature or moisture exposure. The ceramics were laser cut and exhibit edge guides for easier alignment of the source and detector beam splitter cubes. The alignment was performed with active source and detector units adjusted by a fixed reference mirror within the assembly tool and controlled by a beam profiling camera on the optical axis. A photography of the optical unit of a first sensor prototype is shown in Fig.20.2 together with a schematic of the setup.

Finally the populated ceramic holder was attached on an electronic board placed in a 3D printed sensor housing.

3.3 Electronics and Software

For the demonstrator a read out and driving circuit was designed and realized in a 5×5 cm² board. The circuit contains a micro controller, an AD-Converter and a DA-Converter to operate the VCSELs with constant current and to read out the amplified and AD converted (16 bit) signals of the photo detectors. The measurement procedure includes a dark measurement (to account for residual ambient light), a measurement with the red and the infrared VCSEL. Several measurements are performed, the mean value is corrected by the dark measurement and transferred to a PC via serial USB connection. The total procedure takes only 50 ms that allows for fast applications like scanning a sample surface or tracking the properties of a moving sample beneath the sensor head.

Measurement and data acquisition is triggered by a PC with a LabView software. The transfer matrix fitting routines are implemented and results of the fit parameters are reported together with confidence intervals and the correlation matrix.

4 Experimental Results

A set of reference samples with different dielectric layers on silicon substrates were fabricated by plasma enhanced chemical vapour deposition (PECVD). We choose SiO_2, SiO_xN_y and SiN_x in three different layer thicknesses each in order to obtain coatings with different refractive in-

dices. The $2 \times 2\,\mathrm{cm}^2$ samples were analyzed in independent external laboratories by spectroscopic ellipsometry and reflectometry. The mean values of n and d of five measuring positions were used as reference for testing the new sensor.

The following results are obtained by a laboratory set up of the sensor. As electronic development is still in progress, a multi channel data acquisition module (NI 9215) was used instead of the sensor specific electronics described in the previous section. Each value is obtained by the average of five measured signals and their corresponding standard deviation. Measurements in the dark and on a blank Silicon sample were performed in order to calibrate light intensities. In combination with the measurements of the sample, R_p and R_s and their corresponding uncertainties are obtained for two wavelengths (670 nm and 850 nm). n and d are then modelled by Transfer-Matrix and Levenberg-Marquardt-Fitting routines.

In Fig. 20.4 the results for the reference samples are illustrated as a function of externally measured reference values. The obtained results with the new sensor are in good agreement with the reference values. The deviation is below 3% for all n and d except for the 200 nm SiN_x layer thickness, which is about 5%.

In addition experiments with two layer systems were performed. Accuracy and model sensitivity for the buried layer decreases significantly as compared to a single layer system. In case of well known attributes of the buried layer, the surface layer of the stack can be characterized with only small increase in deviation and confidence interval (deviation typically below 5%). Similar limitations can be observed for example with professional laser ellipsometers on double layer systems.

5 Summary

We presented the concept and the first results of a miniaturized sensor for reflective polarimetry. The device works with two single mode VCSELs (670 and 850 nm) in a micro optical unit with beam diameters below 300 µm. The lasers are combined by a beam splitter cube and a monitor photo diode in order to obtain a stabilized two-colour laser source unit. The reflected light is detected under an angle of incidence of 65° by a polarization beam splitter cube equipped with photo detec-

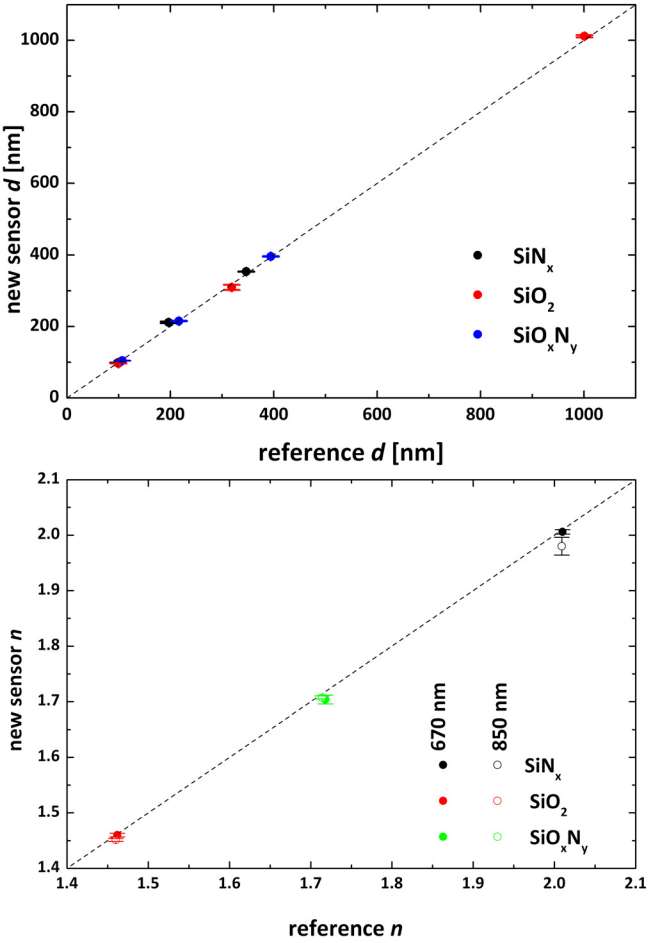

Figure 20.4: Experimental results as a function of externally measured reference values for layer thickness d and refractive index n for different dielectric layers and two wavelengths, indicated in the plots. Error bars indicate the confidence intervals of modelled results of the new sensor device.

tors. The sensor demonstrator is driven by an electronic unit, including AD conversion and serial communiaction with a PC. However the

electronic development is still in progress. A self-developed software is used to model the thickness and the refractive indices of a thin surface layer. As compared to external references a laboratory setup obtained typical deviations below 3% of layer thickness and refractive indices for SiO_2, SiO_xN_y and SiN_x layers with thicknesses in the range of 100 to 1000 nm. Further improvement of the results is expected by application of the final electronics.

Acknowledgment

The development is financially supported by the German Federal Ministry of Economic Affairs and Energy (BMWi), program INNO-KOM-Ost (projects MF130023 and MF130021).

References

1. H. Tomkins and W. McGahan, *Spectroscopic Ellipsometry and Reflectometry*. John Wiley and Sons, Inc., 1999, ch. Appendix, pp. 222–224.
2. R. Azzam and N. Bashara, *Ellipsometry and Polarized Light*. North-Holland, Amsterdam, 1977.
3. J. Jackson, *Klassische Elektrodynamik*. Walter de Gruyter, 2002.
4. W. Press, S. Teukolsky, W. Vetterling, and B. Flannery, *Numerical Recipes in C++: The Art of Scientific Computing*, ser. 2nd edition. Cambridge University Press, 2002.
5. H. Tompkins and E. Irene, *Handbook of Ellipsometry*. 1. Auflage Springer, Berlin, 2006.
6. P. Dannberg, F. Wippermann, A. Brückner, A. Matthes, P. Schreiber, and A. Bräuer, "Wafer-level hybrid integration of complex micro-optical modules," *Micromachines*, vol. 5, no. 2, pp. 325–340, 2014. [Online]. Available: http://www.mdpi.com/2072-666X/5/2/325

Protecting the food supply chain from farm to fork: Utilizing SERS and portable Raman spectroscopy

Maja Sourdaine,[1] Derek Guenther,[1] Cleo Harvey,[1] Yvette Mattley,[2] Adrian Guckian[1] and Oliver Lischtschenko[1]

[1] OceanOptics BV, Geograaf 24, 6921 EW Duiven, the Netherlands
[2] OceanOptics Inc., 830 Douglas Avenue, Dunedin, FL 34698, USA

Abstract Ensuring food safety in various steps along the entire food value chain is crucial to prevent undesired and harmful substances entering the food humans consume. Pesticides and antifungal agents used during growth, processing or along the logistic chain from the field to the consumer can be toxic causing a range of symptoms from stomach pain to the death of the consumer even at trace levels of concentrations. To prevent dangerous additives and contaminants entering the food chain governmental restrictions on a large number of hazardous components have been put into place and are tightly monitored. For a large number of tests complex and sophisticated equipment is required along with time consuming sample preparation steps, not permitting instantaneous sampling of the specimen at the point of measurement or in a timely manner. In order to become a commercially applicable technique, the complexity of the sample preparation and the analysis routine needs to be simplified without losing performance in terms of identification and quantification of the dangerous contaminants. Raman spectroscopy is a technology to allow for quick and rigid analysis of materials without a large amount of sample preparation. The use of surface enhancement of the Raman signal by means of gold or silver nanoparticles would allow for taking this measurement to the field with high accuracy for even small concentrations. The high cost and poor reproducibility of commercially available substrates has so far limited the successful application of SERS measurements along the food value chain. The use of an affordable handheld Raman instrument with mass-producible SERS substrates will be

described in the frame of the contribution with respect to requirements imposed at various stages along the food value chain.

1 Introduction

It is well known that the toxic effect of consuming contaminated food producst can range from the unpleasant but mild digestive problems, up to and including death, depending on the toxin. In order to prevent dangerous substances to enter the food chain a large number of regulations have been introduced [1]. These regulations are overseen and enforced by numerous national and international agencies protecting consumers worldwide. Despite all these efforts, food contaminants can still end up in human or animal food causing significant health scares and economic consequences. The reliable and quick identification of even small amounts of food contaminants, down to trace levels, with high specificity and sensitivity is critical to ensuring the safety of the food chain and ultimately the quality of life for humans and animals alike. With a complex value chain and a high degree of specialization along the modern food value chain, plenty of possibilities arise for dangerous substances to enter the food chain either by accident or sometimes maliciously. The places of contamination vary from storage facilities of seeds, over fields plants grow on, respective upbringing facilities and slaughterhouses in case of livestock or basins for fish via the processing and logistics chain down to the storage and display in the store. Just as the place of contamination can be varied, so can the contamination itself be different. Additives like antibiotics to water or food fed to livestock or fish, fertilizers, fungicides, growth hormones and pesticides used on fields and in storage or even chemical contamination in processing plants can lead to contamination of food. In this paper, we describe how the novel combination of printed silver nanoparticle based SERS (Surface Enhanced Raman Spectroscopy) substrates and state of the art (portable) Raman instrumentation can be used to detect important contaminants such as melamine, fungicides and antibiotics at down to trace levels. The paper will address the design and manufacturing of the novel printed silver nanoparticle SERS substrates as well as present results of measurements of three typical contaminants. All measurements account for the need for quick and efficient point-of-need diagnostics

using portable setups to be used in the field or close to the production lines. The unique combination of silver SERS substrates with available Raster Orbital Scanning (ROS) schemes allows for significant increase in performance of the already powerful ROS setup. Employing silver-based substrates instead of gold increases the sensitivity for the above mentioned applications.

2 Raman Spectroscopy

Raman spectroscopy gives access to the chemical bonding structure of the compound to be identified by means of excitation of the substance using lasers and observing the relaxation of the excited species. The emitted radiation shows peaks that are characteristic for the emitting species like a fingerprint. Major drawback of Raman spectroscopy is the low cross-section for spontaneous Raman scattering, [2] making sound identification of the material of interest challenging, especially for low concentrations. To enhance the amount of scattered light, so called surface enhancement Raman scattering or SERS can be performed. The effect was discovered in 1977 when the compound of interest has been placed on a roughened noble metal surface [3–5]. Today, nanoparticles made from gold or silver are most often used as SERS materials. Sensitivity down to single molecule level has been achieved for specific cases. Amplification factors can range from single digits to several orders of magnitude [6, 7]. With recent advances in laser and detector technologies lowering the costs as well as dramatically reducing the size of the required instrumentation, Raman spectroscopy has become more accessible for use in applications that have traditionally be inaccessible.

3 Experimental Setup

All SERS substrates presented in this paper were mass-printed using the Ocean Optics printable SERS Substrate technology. A novel printing technique and production scheme of the nanoparticles allows a much increased shelf life of the silver SERS substrates by controlling the oxidization of the silver nanoparticles. Slowing down the oxidization of the silver particles allows producing and storing substrates in larger quantities compared to what has been possible up to this point, entering time

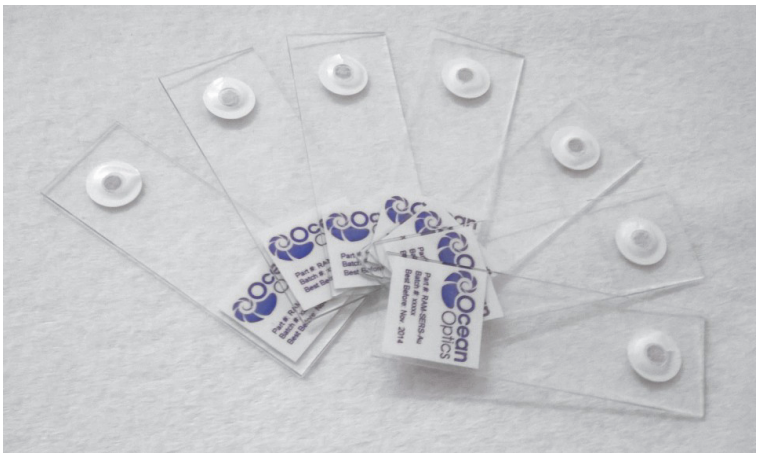

Figure 21.1: OceanOptics printed SERS substrates mounted on microscope slides.

frames that are up to this point only available for gold-based SERS substrates. The measurements have been carried out by drop-casting about 10µl of the analyte of interest, suspended in different solvents onto the printed SERS substrates mounted to conventional microscope slides as can be seen in Figure 21.1.

The samples have then been measured with either the OceanOptics IDRaman Reader using ROS or with a modular fiber coupled Raman system based on a QEPRO spectrometer configured for the use with a 785nm laser. The data was acquired using the OceanView spectroscopy software package. The setups are shown in Figure 21.2 and 21.3, respectively.

Using the IDRaman Reader or IDRaman Mini instruments with ROS schemes allow sweeping a tightly focused laser beam over the surface area to be interrogated, increasing the probability of hitting a SERS-active hotspot (localized region of Raman signal enhancement) on the SERS substrate. ROS results in a higher sensitivity compared to conventional Raman setups as well as a much reduced local heat deposition in the substrate, reducing thermal damage caused by the exposure of the sample to the power density of a tightly focused probing laser

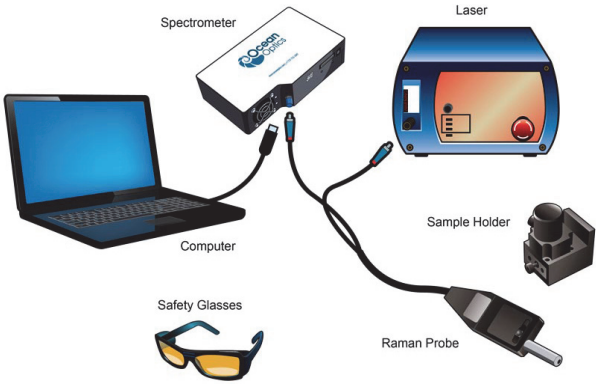

Figure 21.2: Modular fiber coupled Raman setup with OceanOptics QEPRO spectrometer, 785nm laser and fiber optic Raman probe.

beam. The raster orbital scanning scheme is schematically shown in Figure 21.4.

4 Melamine

Melamine has not traditionally been a substance that was tested for in the food industry. The Menu Food Pet Food recall of 2007 changed that when melamine had been added to pet food as non-protein-nitrogen to suggest a higher protein content than actually present. The short comings of not testing for melamine in food became even more obvious when in 2008 6 infants died as a consequence of being fed with melamine stretched milk powder. In 2010, the World Health Organisation (WHO) published the limits for a number of components in foodstuff in the codex alimentarius [8]. For melamine in foodstuff, a maximum value of 2,5mg/kg for general foodstuff and animal food and 1mg/kg for infant foods like milk powder may not be exceeded [9]. The detection at ppm level is thus needed.

Melamine can be detected using SERS at the required levels. The measurements shown have been acquired with a fiber coupled Ramam setup using an OceanOptics QEPRO spectrometer, a fiber coupled 785nm laser and a fiber optic Raman probe. The laser was set to yield

Figure 21.3: OceanOptics IDRaman Reader integrated Raman system with raster orbital scanning capability.

60mW of laser power at the sample. The spectrometer was set for an exposure time of 5s. Using the new mass printed silver-based SERS substrates, sub ppm levels of melamine have been detected successfully with good signal to noise ratio as is shown in Figure 21.5 or with greater detail in Figure 21.6.

To examine batch to batch reproducibility of the Ag-based substrates, several batches from different prints as well as from different nanoparticle synthesis have been tested at 10ppm level with the Ocean Optics 785nm-IDRaman Reader using raster orbital scanning. The power at the sample was set to 62mW and an exposure time of 1s has been used. As can be seen from Figure 21.7, the substrates are very reproducible.

5 Antibiotics

Enrofloxacin is a synthetic broadband antibacterial agent. It is effective against several bacteria including E. coli, Enterobacter, Salmonella and even methicillin-resistant strains of Staphylococcus . It has been used in poultry up to 2005 and is still used in aqua cultures to control bacteria levels. Enrofloxacin can cause bacteria to develop antibiotics resistant strains. Enrofloxacin is not labelled for use in food-producing animals for the United States of America and Canada according to the FAO [10]. According to the FAO, the quantification limit of the analytical meth-

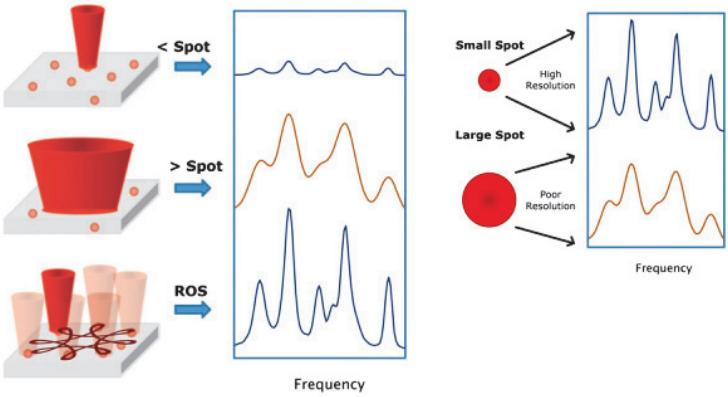

Figure 21.4: Raster orbital scanning schematically.

ods is 10 µg/kg for enrofloxacin in tissue and 5 µg/kg in milk. As a test for feasibility a rather high concentrated sample of enrofloxacin in water has been tested with the IDRaman Reader with raster orbital scanning. At long integration times of 40s the signature is clearly visible as is shown in Figure 21.8 , but a more efficient background subtraction mechanism is needed to reach the signal to noise ratio of the analytical limit. Nevertheless, the absolute count rates achieved with the silver substrates and the detector signal to noise are acceptable.

6 Fungicides

Two different fungicides have been studied in this work – malachite green and thiram. Malachite Green (MG) is an effective fungicide and is also used for parasite control. Malachite green is soluble in water as well as ethanol and attaches well to fat inside the body. MG has half-life times in the order of 45 days for salmon and carp and its use can thus be proven even months after fish have been exposed to MG. In several non-EU countries MG it is used in aquacultures to control fungi and parasites, while in the EU the use of MG for food producing animals is not allowed. The in consequence the European limit is 0 µg/kg for foodstuff. Typical detection limits of MG need to be off the order of

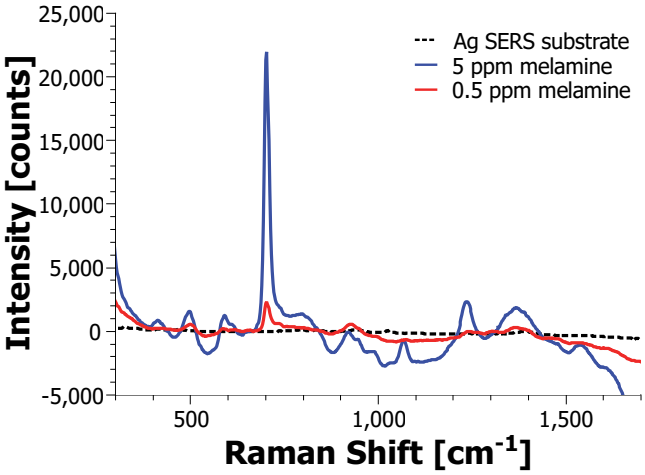

Figure 21.5: Melamine SERS spectra at concentrations of 0.5 and 5 ppm.

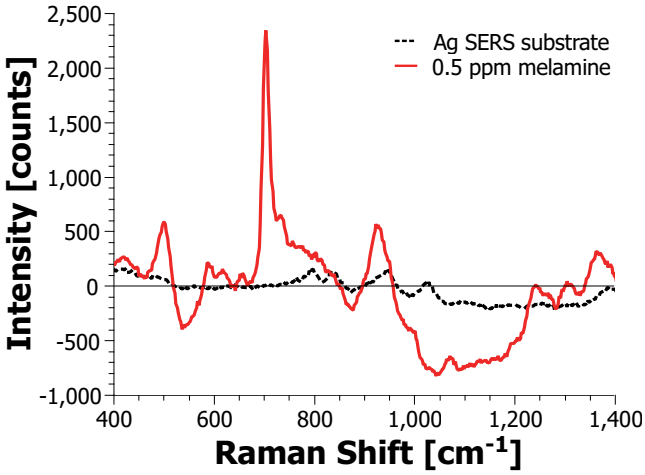

Figure 21.6: Close up of the Melamine SERS spectrum at a concentration of 0.5 ppm.

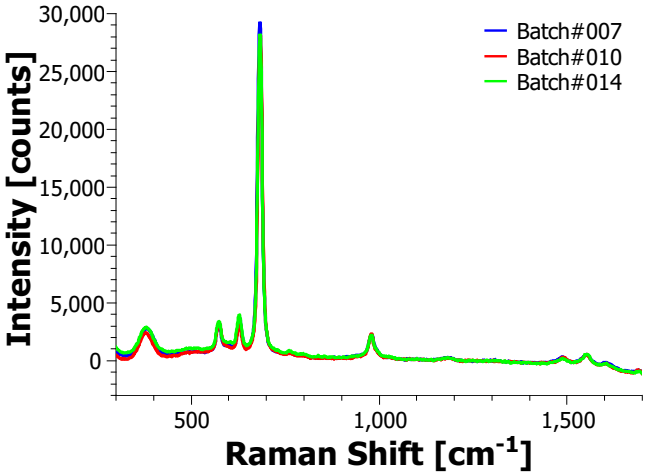

Figure 21.7: SERS spectra for different manufacturing batches at a melamine concentration of 10ppm, measured with IDRaman Reader 785nm and ROS enabled, $P_{785} = 62$ mW, $t_{exp} = 1$ s.

ppb to be acceptable. As with Enrofloxacin, the sensitivity of the silver-based substrates give promising result by almost reaching that value as is displayed in Figure 21.9.

In contrast to malachite green, thiram is a commonly used substance in agriculture. Thiram is used as a broadband fungicide, ectoparasiticide as well as animal repellant. Thiram attaches efficiently to soil particles and remained relatively immobile in clay or high organic matter soils. The half life time for thiram in soil is about 2 weeks. Thiram is nitrousamine precursor contaminating foodstuff. As in the case of melamine, adding Thriam to foodstuff suggests increased values for protein, when conducting traditional protein determination testing. While it is used for protecting young plants in the field and for impregnation of seeds and seedlings widely, its direct addition to meat is not allowed in Germany and the UK, but allowed in other EU countries as well as in the US. In these countries a limit of 200ppm may not be exceeded when added to fresh meat. [11] The SERS spectrum of Thiram solved in acetone is shown in Figure 21.10.

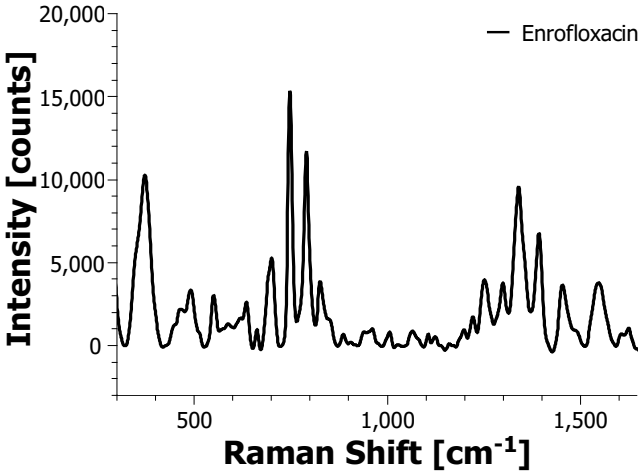

Figure 21.8: SERS spectrum of Enrofloxacin solved in water measured with the IDRaman Reader using ROS at a concentration of 10^{-4} M, $P_{785} = 62$ mW, $t_{exp} = 40$ s.

7 Summary

In this paper, a newly developed mass-printable silver nanoparticle based substrate for surface enhancement of Raman scattering has been introduced. It was demonstrated that the combination of these novel silver SERS substrates with Ocean Optics existing portable Raman instrumentation, ranging from modular fiber coupled systems to integrated Raman readers, is sensitive enough to meet the detection limits of for substances relevant to the food chain security. Results for melamine, antibiotics and antifungals have been shown in combination with the newly developed printed silver SERS substrates.

References

1. K. Matthews, *Practical Food Safety: Contemporary Issues and Future Directions*, R. Bhat and V. E. Gomez-Lopez, Eds. Wiley-Blackwell, 2014.

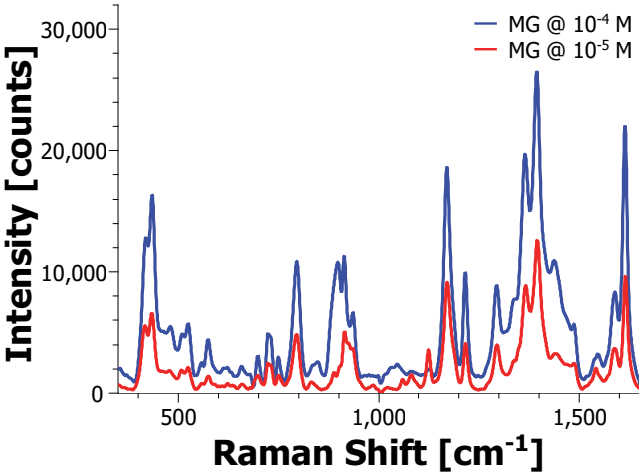

Figure 21.9: Malachite green solved in ethanol measured with the IDRaman Reader using ROS at concentrations of 10^{-4}&10^{-5} M, $P_{785} = 80$ mW, $t_{exp} = 10$ s.

2. D. Gardiner, *Practical Raman Spectroscopy*, D. Gardiner and P. R. Graves, Eds. Springer-Verlag, Berlin, 1989.
3. D. L. Jeanmarie and R. P. Van Duyne, "Surface raman electrospectrochemistry - part 1. heterocyclic, aromatic and alipathic amines adsorbed on the anodized silver electrode," *J. Electroanal. Chem. 84*, pp. 1–20, 1977.
4. M. Fleischmann, P. Hendra, and A. McQuillan, "Raman spectra of pyridine adsorbed at a silver electrode," *Chem. Phys. Lett.*, vol. 26, no. 2, pp. 163–166, 1974.
5. R. A. Alvarez-Puebla, D. S. Dos Santos Jr, and R. F. Aroca, "Surface-enhanced raman scattering for ultrasensitive chemical analysis of 1 and 2-naphthalenethiols," *Analyst*, vol. 129, pp. 1251–1256, 2004. [Online]. Available: http://dx.doi.org/10.1039/B410488A
6. W. E. Doering and S. Nie, "Single-molecule and single-nanoparticle sers: Examining the roles of surface active sites and chemical enhancement," *The Journal of Physical Chemistry B*, vol. 106, no. 2, pp. 311–317, 2002. [Online]. Available: http://dx.doi.org/10.1021/jp011730b
7. K. Kneipp and H. Kneipp, "Single molecule raman scattering," *Appl. Spectrosc.*, vol. 60, no. 12, pp. 322A–334A, Dec 2006. [Online]. Available: http://as.osa.org/abstract.cfm?URI=as-60-12-322A

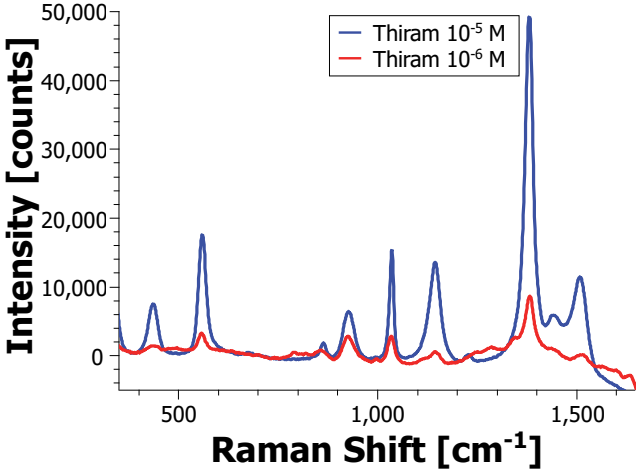

Figure 21.10: Thiram solved in acetone measured with the IDRaman Reader using ROS at concentrations of 10^{-5}&10^{-6} M, $P_{785} = 80$ mW, $t_{exp} = 20$ s.

8. (2015) Codex alimentarius. electronically. Food and Agricultural Organisation of the United Nations. Viale delle Terme di Caracalla, 00153 Rome, Italy. [Online]. Available: http://www.codexalimentarius.org

9. WHO, "Toxicological and health aspects of melamine and cyanuric acid report of a who expert meeting in collaboration with fao, supported by health canada," World Health Organization, Report, 2009, iSBN 978 92 4 159795 1.

10. J. F. E. C. on Food Additives, Ed., *Residue Evaluation of Certain Vetenary Drugs*, ser. FAO JECFA Monographs (6), FOOD AND AGRICULTURE ORGANIZATION OF THE UNITED NATIONS. Viale delle Terme di Caracalla, 00153 Rome, Italy: FAO Communication Division, 2009. [Online]. Available: http://www.fao.org/docrep/011/i0659e/i0659e00.htm

11. J. De Vries, *Food Safety and Toxicity*, J. De Vries, Ed. CRC Press, 1996, p. 71.

Hyperspectral imaging as process analysis technology for inline applications – Laboratory precision meets high sampling accuracy

Matthias Kerschhaggl

EVK DI Kerschhaggl GmbH
Josef Krainer Strasse 35, A-8074 Raaba

Abstract Hyperspectral Imaging (HSI) has found its way into modern production lines as yet another camera technology that combines the means of spectroscopy with computer vision. However, while its imaging capabilities with its increased amount of processed data are already subject to state of the art sorting machines used for product integrity checks and foreign body removal, the potential of doing real-time spectroscopy and quantitative chemical analysis of product streams has up to now not fully been harnessed for the production line. Respective industries still rely solely on highly precise but statistically limited, laboratory based, slow and invasive methods while HSI offers the data needed to perform real-time and statistically representative product sampling as add on. In this regard the potential of HSI as process analysis technology (PAT) will be outlined in this article presenting a first industrial field application based on the HELIOS near infrared hyperspectral imaging camera. Results from this up to now first commercialized application of this kind in the potato industry, i.e. an inline dry matter detection for potatoes, will be discussed.

1 Introduction

Modern factories and production lines consist of a variety of different process steps covered by fully automated machines comprising high-tech sensor units and electronic equipment. These artificial organs of an integrated factory body nowadays produce enormous amounts of data

most of which are only analyzed from a very local point of view with respect to the process location (i.e. data from one machine is used mainly for process control of this particular unit). On the other hand many inline process parameters with rapidly changing states on timescales of minutes at different locations in the product stream are still monitored by means of invasive, laboratory based analysis technologies suffering from low sampling rates (e.g. every 30 min) and limited (not representative) statistics (number of samples orders of magnitudes below the number of product items to be controlled). Recently more and more of these classical methods are combined with more rapid at- and inline process analysis technologies (PAT) with access to high data statistics and almost no latencies in the control and regulation cycle. Both of these developments are subject to a combined trend towards intelligent (in the machine learning sense), interconnected and self-regulating production sites where inline monitoring (and process control) machines (such as e.g. sorting machines) generate real time data at different points of the production flow. These are combined and analyzed (e.g. via multivariate data analysis) and ultimately used for process control at various process locations. Concerning inline PAT one has to keep in mind that it is not simply the goal to imitate and replace the high precision equipment of a well introduced laboratory method with its various advantages [1]. The actual objective is to add to a solid and high precision laboratory quality control the benefits of an inline technology that monitors the product stream all the time. Such it generates lots of representative data over the whole product stream thus harnessing the power of statistical analysis by which (expected) random statistical fluctuations and non-representative outliers can be averaged out. Such effects will subsequently not propagate into a meaningful mean measurement value. On the other hand real systematic deviations on shorter time scales can be observed and reacted at swiftly since statistical parameters such as target value variance or overall distributions are very sensitive to such changes which will not be marginalized. Thus it is crucial that a precise laboratory reference method is used to (re-)calibrate the inline device whose added value is the enhanced accuracy of the quality control via statistical representative expectation values being insensitive to Gaussian noise. With the help of PAT the different processes in a factory can be fine-tuned in order to arrive at the most cost effective production parameters such as energy, water and input of raw material.

In the following the inline application of quantitative dry matter detection in potatoes and French fries, respectively, by means of a HELIOS near infrared (NIR) hyperspectral imaging camera (EVK GmbH, Raaba/Austria [2]) is presented exemplary for the potential of HSI-PAT. Similar applications such as the quantitative anaysis of active pharmaceutical ingredients (API), metal oxide content in ores or all kinds of constituents in a food matrix can be done along the same lines and are subject to current development activities [3]. The hyperspectral imaging (HSI) technology in the NIR regime is about to develop in the food processing industry from a sensor technology used mainly for classification tasks (e.g. removal of foreign bodies from an input stream) to a method for spatially resolved quantitative analysis of chemical food parameters (sugar, starch, proteins etc.). The inline inference of for instance dry matter values can help in order to save energy for the frying process and control/adjust the product quality for different products and customers on short time scales. The latter expect specific lower limits on the dry matter levels for their product.

2 Data Taking and Analysis

Hyperspectral imaging data in the NIR regime (1050-1690 nm) was acquired using a HELIOS NIR G1 HSI camera with a scanning rate of 330 Hz full frame translating into $\approx$ 81000 processed data points per second.[1] The inline inference of spatially resolved dry matter values in French fries and potatoes was investigated with this inspection technology. The outline of this work was first to perform a proof of principle test with a prototype setup in a French fry factory and then in a second step the transfer of the full functionality onto a commercializable monitoring machine.

2.1 Inline Determination of Dry Matter

As was already shown in [4] & [3] the quantitative inference of dry matter levels in potato tuber slices is feasible using NIR hyperspectral imaging in conjunction with a factor analytical ansatz such as partial least

[1] A more thorough description of the HELIOS camera and hyperspectral imaging in general can be found in [4] & [3]

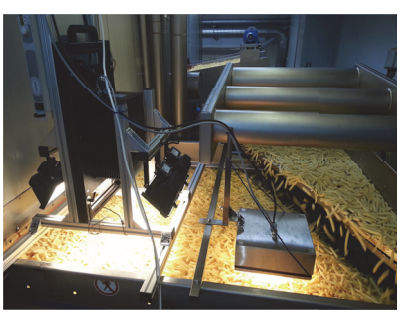

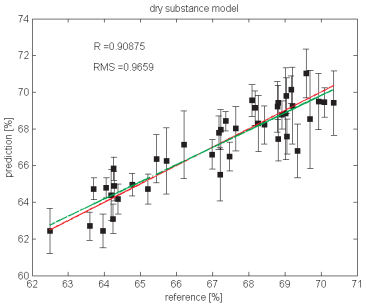

Figure 22.1: (left) Inline test setup for dry matter measurements of French fries using HELIOS NIR G1. Figure taken from [3]. (right) Correlation between reference analysis and model prediction. The red line indicates perfect correlation whereas the green line depicts a fit to the data.

squares regression (PLSR) [5]. While this could be shown for a laboratory based test setup the next project step included the validation of this method during an inline test run in a French fry factory and the ultimate transfer to a working machine fit for commercialization [6]. The inline method validation was carried out by mounting a HELIOS NIR G1 camera right after the freezer[2] unit on top of the product stream (see fig.22.1). The product was illuminated by 4 halogen lights mounted at an inclination of roughly 60° with respect to the camera optical axis. Such the camera was positioned head on to the inspection line allowing for an optimal trade-off between diffuse reflection, i.e. reduced specular reflection and overall image intensity. Overall roughly 3 min of data, corresponding to 15 million spectra, were taken over a full day in single shots of 2 seconds duration each. The target value range was spanned by deliberately varying the product dry matter, i.e. manipulating the frying time of the frying unit. For each data acquisition shot a reference analysis was performed on a sample of about 5 kg of French fries drawn from the product stream at the moment of data taking. Each sample was analyzed for its average dry matter content by means of a *SMART Turbo Solids Analyzer* [7]. The dataset was pre-prosessed using the spec-

[2] At this point of the production line the French fries feature a stable temperature of about 5°.

tral first derivative and split into two subsets one for implementing a chemometric calibration based on PLSR with 5 latent variables and one (by selecting every second data) for internal validation. The correlation plot between reference values and model prediction is shown in the right plot of fig. 22.1. As can be seen from the Pearson correlation $R \approx 0.9$ and the root mean square error of calibration $RMSEC < 1\,\%$ the suggested model is within statistical margins fully compatible with the reference analysis method. The figures for the validation set showed a somewhat reduced but stable prediction behaviour at levels of $R = 0.86$ and $SEP = 1.3\,\%$ for original spectra and $R = 0.74$ and $SEP = 1.9\,\%$ for the normalized spectra.

While R and $RMSEC$ are in particular sensitive to the calibration precision, i.e. repeatability of the measurement, it is more important for an inline calibration to focus on the accuracy of a model, i.e. the degree of closeness of the measurement to the true value, especially if the dataset comprises high statistical, Gaussian scatter that will be easily marginalized under the impression of the enormous inline data statistics. One has to note that the almost perfect alignment between the (green) linear fit to the correlation plot fig. 22.1 and the (red) line denoting a correlation coefficient of one is in fact a better measure for accuracy of the HSI method than any figure of merit prone to noise (see also [8]). While the model precision is based on only 2 seconds of data taking per measurement point, the accuracy of the method will surpass any laboratory based method by averaging out fluctuations that otherwise propagate into the low sampling rate results of classical at line methods. The method's accuracy is thus to first order only limited by the intrinsic sampling error of the reference method.

2.2 Dry Matter Monitoring Machine

With the inline test meeting the accuracy requirements for a field application the ultimate goal of this work was the transfer of the described HSI dry matter measurement to the technically more challenging environment of a real monitoring machine. Such a machine in contrast to the described test setup suffers e.g. from suboptimal local resolution (due to commercially triggered maximization of the working width) and other optical limitations (reduced focal length of the fore lens and thus enhanced lens aberrations etc.). Thus a proof of principle as described

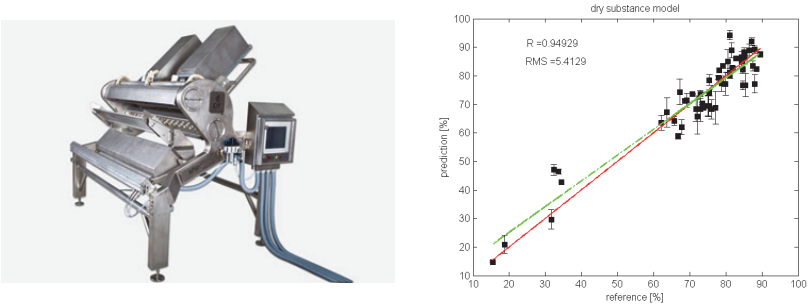

Figure 22.2: (left) HSI monitoring machine *Sherlock Observer* from INSORT. (right) Correlation plot dry matter prediction vs. reference values for *Sherlock Observer*. The red line indicates perfect correlation whereas the green line depicts a fit to the data.

above does not at all guarantee feasibility for field applications. Therefore the dry matter measurement method using a HELIOS NIR camera was implemented on a monitoring machine of the type *Sherlock Observer* from INSORT GmbH (see fig. 22.2 (left) and [6]). The implementation on the machine was performed using raw potato slices to arrive at similar optical conditions, i.e. surface reflectance etc., than for e.g. French fries. The various slices were measured on the *Sherlock Observer* featuring a working width of 300 mm. Reference analysis was carried out along the same lines as for the factory test with a *SMART Turbo Solids Analyzer* using only 10x10x10 mm cubes from the central parts of the corresponding slices. Accordingly, only spatially resolved spectra from the same center region from the HSI image were used for the PLSR multivariate analysis. The sample preparation included the generation of two different populations. Population I spanned an extended value range from below 20% to over 90% moisture in the tubers. In order to generate very dry potato probes a desiccation chamber for dehydrating the samples was used. Population II comprised only natural sampling, thus featuring a confined range in moisture levels. Figure 22.3 shows the validated correlation of the model prediction based on splitting the data into a training and a test set for the population I model (left) as well as the model performance for the confined population II (right). Both models

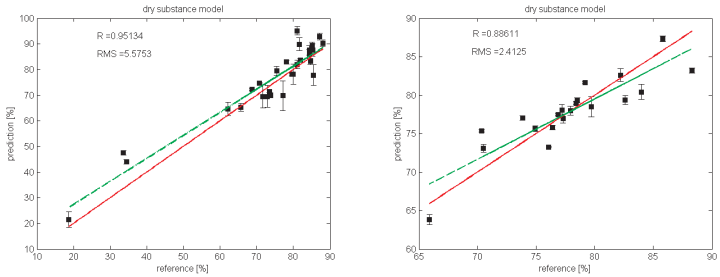

Figure 22.3: (left) Validated correlation between model prediction and reference analysis of potato moisture levels over the extended dry matter level range (population I). (right) Model correlation for confined dry matter levels (population II). The red lines indicate perfect correlation whereas the green lines depict a fit to the data, respectively.

show a fairly high correlation with the true values from the reference analysis, i.e. $R = 0.95$ and $R = 0.88$ for population I and II, respectively. However, the RMS model error is enhanced for the population I, i.e. $RMSEC = 5.4\%$, in comparison to acceptable $RMSEC = 2.4\%$ for population II. In general the RMS is higher for both models as compared to the inline tests results (fig. 22.1). Presumably, this is related to an enhanced sampling error using only a limited number of spectra from spatially confined cubic probes as compared to the much broader inline data acquisition with hundreds of thousands of spectra per measurement which allow averaging out intrinsic sample scatter. It has to be noted that in this study the natural scatter of dry matter values across a 1x1 cm spatial region of interest on a potato slice was at best of the order of 2% and could be as high as $\sim 10\%$ if moisture inhomogeneities such as water channels were part of the inspection region. This can also be seen in fig. 22.4 showing the spatially resolved moisture levels of a potato slice as measured with the *Sherlock Observer*. Peculiar moisture inhomogeneities in the fruit cross section as well as the fact that potato tubers show a dry matter gradient from the centre to the outer rims are obviously traced by the NIR HSI online measurement.

Validation runs were done by measuring several 1 ccm raw potato cubes with the machine in comparison to the SMART device. Table 22.1 shows the outcome of these tests in terms of several statistical figures

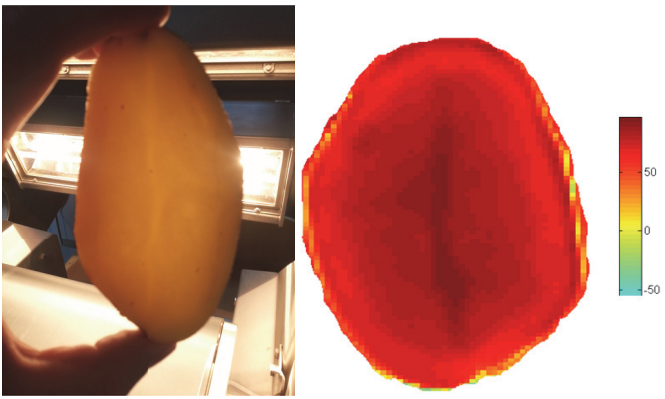

Figure 22.4: (left) Potato slice including water channels as seen with the naked eye. (right) Same slice viewed as color coded moisture map (in % water content) as seen with *Sherlock Observer* (crf. [6]).

of merit. According to this the two models show a stable behaviour in the validation in comparison to the calibration with respect to the magnitude of model deviations (RMSEC and SEP, respectively). However, both calibrations lead to a prediction bias of the order of 3%. While such a bias if purely Gaussian and statistical in nature can always be corrected for by e.g. a linear correction of the multivariate parameters and has thus no impact for a working machine, it hints to the fact that chemometric calibrations in quantitative applications can be sensitive to changes in process parameters other than the interesting target variables. Presumably the bias encountered here goes back to alterations of the optical setup and feeder mechanics of the *Sherlock Observer* in-between calibration and validation runs. It has to be noted that a comparison of the RPD values between the two models with respect to the poor $RPD = 0.7$ for model I has to be taken with care since the calibration set I had a very sparse coverage and the validation set was limited in sample numbers. As shown in [9] dataset distributions deviating from normality can introduce a bias to the RPD value. With a $SEP = 2\%$ calibration II seems suitable for an inline application in the production line. The fact that model I features a somewhat poorer $SEP = 5\%$ with a systematic bias towards drier samples, the sparse midrange dry matter

Table 22.1: Statistics of validation runs for population I and II calibration. Shown are the model bias, the standard error of prediction (SEP), standard deviation of prediction (SDP), standard deviation of reference (SDR) and the ratio between standard error of prediction and standard deviation of the reference (RPD), respectively.

	Model I	Model II
BIAS [%]	-3.5	-3.0
SEP [%]	5.3	2.1
SDP [%]	4.5	3.0
SDR [%]	3.7	4.2
RPD	0.7	2.0

value data coverage (right plot in fig. 22.2) and the observation that samples pre-treated in the desiccation chamber show deviations from the usual spectral potato signature presumably due to changes in the fruit matrix (e.g. gelatinization effects) would suggest that it is favourable to only use natural potato probes as done for model II and stick to a more confined value range as typically present in production lines (e.g. $10 - 35\%$ dry matter). In general any calibration model will need thorough recalibration and maintenance over the whole life cycle of the production process due to changes in related parameters ultimately also impacting the HSI NIR spectra. [10].

3 Conclusions

NIR-HSI is by now an established technology in different industries such as food, mining, recycling and pharmaceuticals. It has been developing from a mere inspection technology to a fast, reliable and spatially resolved quantitative analysis method suitable as PAT tool. Results in applying these innovative sensor systems for the inline measurement of dry matter levels in potato processing suggest its suitability for industrial use with a precision in the %-regime being presumably only limited by the sampling statistics of the training set. With the technology being fit for commercialization the first machines operating with according functionalities (dry matter detection, inference of residual peel amounts) are presently being deployed in the field [6].

Acknowledgments

I would like to thank the staff of INSORT GmbH for their great assistance and support with the measurement setup. Valuable discussions with E. Leitner (TU-Graz) and W. Märzinger (i-RED Infrarot Systeme GmbH) were highly appreciated.

This work was in parts carried out within the project *Forschung-Technologie-Innovation (FTI) - Inline Food Analyser* and was supported by the Austrian research council FFG under the project number 834298.

References

1. K. H. Esbensen, P. Geladib, and A. Larsenc, "The goal for my on-line nir is to be an automated copy of the lab technician," *NIR news*, vol. 25, no. 8, pp. 30–32, 2014.
2. http://www.evk.biz/en/products/helios-hyperspectral-imaging-camera-system.html.
3. M. Kerschhaggl, "Hyperspectral imagery for real-time quantitative inline analysis," *Sensor-Based Sorting 2014, GDMB Verlag GmbH*, vol. 135, 2014.
4. M. Kerschhaggl, W. Märzinger, E. Leitner, N. Haar, M. Zangl, M. Jeindl, and P. Kerschhaggl, *Inline HSI food inspection and concentration measurements of pharmaceuticals – a report from an industrial environment*. Karlsruhe: KIT Scientific Publishing, Karlsruhe, 2013.
5. S. Wold, M. Sjöström, and L. Eriksson, "Pls-regression: a basic tool of chemometrics," *Chemometrics and Intelligent Laboratory Systems*, vol. 58, no. 2, pp. 109–130, 2001.
6. http://potatopro.com/news/2014/insort-sherlock-analyst-sets-new-standards-process-monitoring-potato-processing.
7. http://www.cem.com/smart-turbo.htmlg.
8. P. P. Mortensen, "Myth: A partial least squares calibration model can never be more precise than the reference method," *NIR news*, vol. 25, no. 3, pp. 20–22, 2014.
9. K. H. Esbensen, P. Geladi, and A. Larsen, "The rpd myth..." *NIR news*, vol. 25, no. 5, pp. 24–28, 2014.
10. M. B. Mercader and A. R. Puigdomènech, "Near infrared multivariate model maintenance: the cornerstone of success," *NIR news*, vol. 25, no. 7, pp. 7–9, 2014.

Tailoring spectroscopic performance for high end material characterization by customizing grating based spectroscopic equipment

Harald Kroker[1] und Brice Villier[2]

[1] HORIBA Jobin Yvon GmbH,
Hauptstr. 1, 82008 Unterhaching
[2] HORIBA Jobin Yvon S.A.S. ,
Avenue de la Vauve - Passage Jobin Yvon CS 45002 - 91120 Palaiseau - France

Abstract Typical spectroscopic equipment in research labs has varying levels of complexity, covering different applications. When going to industrial instrument design for material characterization, the demands become highly specific: Parameters like stray light performance, resolution, coverage, sensitivity, speed, size, robustness and cost need to be weighted against each other. Especially for large quantities, custom design is one way to target a key market with a unique instrument. This might involve design of a grating, tailoring to the optical configuration, proper detector choice and integration into the instrument. For higher level instrumentation, customization might be mandatory to enabling difficult application. Our approach will be illustrated by showing examples for different categories of spectroscopic equipment, to demonstrate the advantage of customization in fields like material characterization.

1 Introduction: Tailoring of Spectroscopic Equipment

There are very different types of spectroscopic equipment used in R&D or labs for material characterization, starting from simple mini spectrometers or photometers up to complex multi-million € research facilities. To show what tailoring and customization might enable, it makes sense to look into three different categories of instruments separately:

- Workhorse
  This type of instrument is designed for a highly specific application, which are used for routine analysis of the same kind. It is operated by several users with little or no training. The goal is routine use in a highly efficient and simple way. For this instruments, it is important to ”hide” technical details, and concentrate only on simple output results and their validity, e.g. ”red or green” flag, even if the underlying technique might be complex. Typical examples are photometers, microplate readers, fluorimeters and Raman spectrometers.

- Advanced analytical tools
  These enable a broader range of application. They are capable to solve some of the unexpected, new and exiting or more difficult analytical questions. Usually, these equipment is offered in a more modular, open way, e.g. with configurations optimized to the customer’s demands. Upgrade options are important aspects for the selection of the right tool. To be able to achieve best results, more experienced and educated users are important who have to judge on the limits of the methods. (e.g. high end fluorimeters, advanced micro-Raman spectrometers, spectroscopic ellipsometers (SE))

- Unique research tool
  This equipment makes use of state of the art techniques. Latest developments were incorporated to push the limits for detection and analytical capabilities. This type of instruments need full understanding of the techniques used. Checking for ”features”, errors and limits is a major part of data acquisition and analysis carried out by the user.

For new, demanding applications, it might happen, that the market doesn’t offer well fitting solutions, or only very complex and expensive tools that are not really tailored to this new application.

We work on extending the capabilities of instruments in all of the three categories described above. This will be explained in some examples, split up into the three categories introduced above.

2 How to Help Making a Workhorse

2.1 Considerations for Workhorse Design

Common points for this type of equipment are:

- simple operation
- robust performance
- high number quantities within a clearly defined target market
- moderate customer price
- ”hidden” technique
- clear indication of the validity of result

To get a competitive instrument, these points need to be addressed. For typical spectroscopic techniques like photometry, absorption, fluorescence, Raman, NIR, emission, LIBBS or others, the demands differ a lot. Which means specifications and design parameters for the actual analytical method need to be carefully controlled, to reach a convincing performance level.

For a good instrument design, the crucial spectroscopic parameters which will determine the instrument’s success (e.g. stray light, spectral resolution and range, sensitivity, speed, instrument size, environmental stability, and last but not least, cost) need to be identified, weighted for their relevance and carefully handled. Component selection has the ultimate goal to reduce the performance and cost to the necessary level. These instruments are usually built at significant number quantities, which means customization is a valuable method to control manufacturing costs.

Horiba as a grating manufacturer is active in this field as an OEM partner giving the opportunity to start customization at very basic components, like the grating, spectrometer and related optics hardware.

For this, we work very closely together with the equipment manufacturer, to find the optimum solution. One important point is to look for the value each partner can add to the project, and by this, define the best interface between the partners. Two examples can be presented to show how tailoring of spectroscopic equipment will lead to workhorse performance.

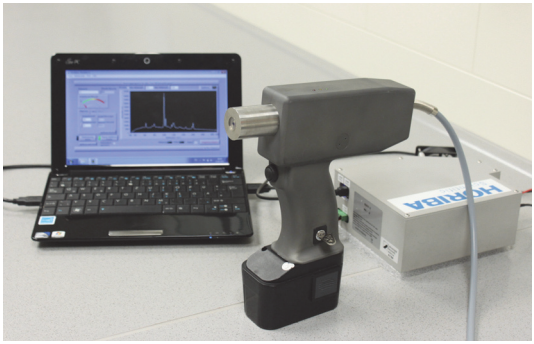

Figure 23.1: Mobile Raman setup, with "pistol" containing the Raman probe and the laser, the spectrometer and the control computer. (Picture courtesy of H.Schmidt)

2.2 Meat Qualification Using a Portable Raman Device

An optical method for analyzing raw meat non-invasively was developed to control different parameters that govern the quality of meat [1]. The device is able to measure parameters like freshness, meat type, pH, drip loss, shear force and others. These parameters can be attributed to detailed molecular components and their change with time after exsanguination [2]. Raman spectroscopy is known to provide a "fingerprint" of the molecular composition and structure of materials. It was selected as the appropriate analytical method, because it provides better correlation to classical, invasive reference methods than other optical techniques like fluorescence or VIS-NIR reflectance spectroscopy.

To achieve optimum results, it was mandatory to fine tune some key instrument parameters:

- Laser wavelength:
  It has to be reasonably short to get good detector sensitivity and high Raman efficiency, which is $\sim \lambda^{-4}$, but long enough to avoid excess fluorescent background.

- Trade off between spectral resolution and coverage:
  spectral lines need to be resolved, while sufficient range on the detector needs to be provided to measure all key lines.

- High throughput and sensitivity:
  Integration time needs to be kept moderate, to avoid deep cooling of the detector.
- Mobility and robustness:
  The goal is a mobile instrument which is used in harsh environment (cooling rooms of abattoirs, at 100% humidity).

Taking this into account, Horiba provided a customized spectrometer system tailored to these demands. (See fig. 23.1) Recent publications are describing the method and results like aging of meat [1], pH of pork [3] or multiple parameters [2].

For getting results on the individual parameters, key features in the spectrum need to be separated and analyzed in detail. Here we show some steps necessary for estimating the pH values in meat (more details can be found in [3]):

- Getting Raman and reference data (puncture electrode) on different meat samples, 0.5h and 10h post mortem.
- Baseline correction (fluorescence background) by fitting a 5th order polynomial to the Raman spectra, followed by spectral smoothing.
- Intensity normalization.
- Generation of difference spectra, to investigate evolution with time of the Raman spectra.

Finally, the Raman-derived pH results were correlated with the reference measurement by different methods. Even the simplest method using the intensity ratio of only two spectral features gives strong correlation (R^2 = 0.71). More robust predictions were achieved by applying more advanced regression methods. MLR (multiple linear regression), using the 11 peaks gives R^2 of 0.78), while non linear methods (PLSR, partial least-square regression), which make use of the entire spectra, give an R^2 = 0.95 and correlate very well even at low pH level. The apparent offset between Raman data and reference data is attributed to a dislocation of the actual measuring positions, reflecting a biological variance in the muscle.

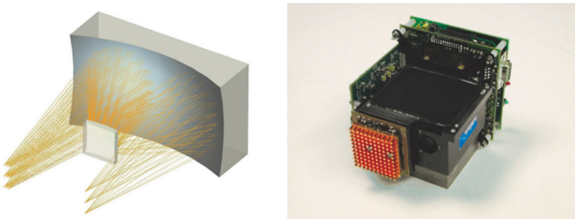

Figure 23.2: Optical design of an all-reflective hyperspectral imager, and an example for a compact VIS imager including CCD

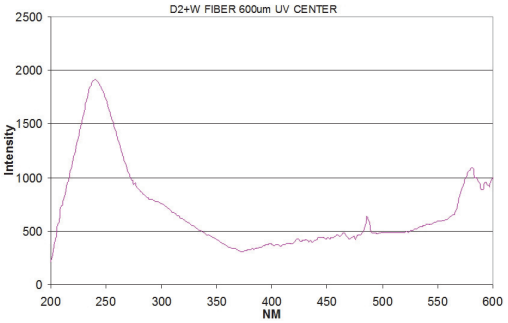

Figure 23.3: UV-VIS spectral output from combined D2 and halogen source

2.3 Hyperspectral Imager for UV Wavelengths

Hyperspectral imaging has his major roots in remote sensing, which is why it is carried out mainly in the atmospheric windows from VIS to MIR. This technique is becoming more important for material characterization in industrial environments, like waste sorting, food inspection and others, but is usually restricted to reflectivity measurements in the VIS-NIR range. Other techniques like fluorescence or Raman [4] are explored as next generation hyperspectral imaging, but don't seem to be very common up to know.

An example for a different spectral range is presented here:

We developed major hardware components for a UV hyperspectral imaging system: the imaging spectrograph and a dedicated relay optics system tailored to the special requirements of the UV wavelength.

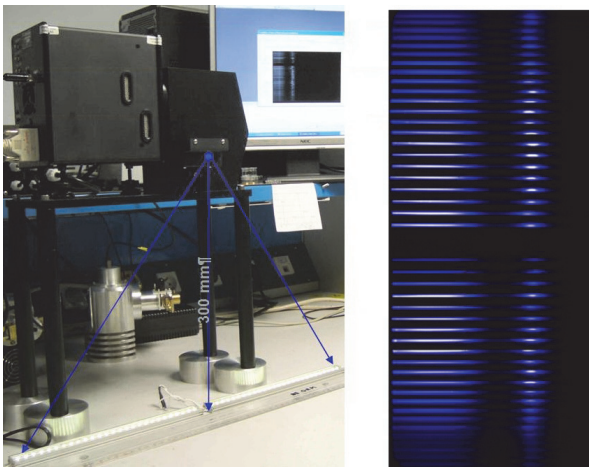

Figure 23.4: Hyperspectral Imager for the UV. Left: Test setup with two LED arrays of 30cm length each. Right: Resolved raw spectra of individual LEDs

The UV CCD with 512x512p, was defined by the customer. The design goal was to record the UV reflectance spectra of samples running on a conveyor belt. The samples were illuminated by an UV line source of $500 \times 2.5mm$ at a free distance of 300mm (see fig. 23.4).

The main instrument challenges were:

- Spectral range: 200-500nm
- High sensitivity and throughput of the spectrometer: A F/3 design was achieved by using a convex holographic grating.
- Efficient relay optics with anamorphic magnification (1:50 and 1:25). Our 3 - mirror design matched performance specs very well.

Even though this spectrometer is designed for the UV, it will of course work for any other wavelength range with an appropriate grating.

3 How to Give More Flexibility to Advanced Instruments

Advanced research instruments were operated by highly skilled users, which often hold a PhD degree. This is the market of high level re-

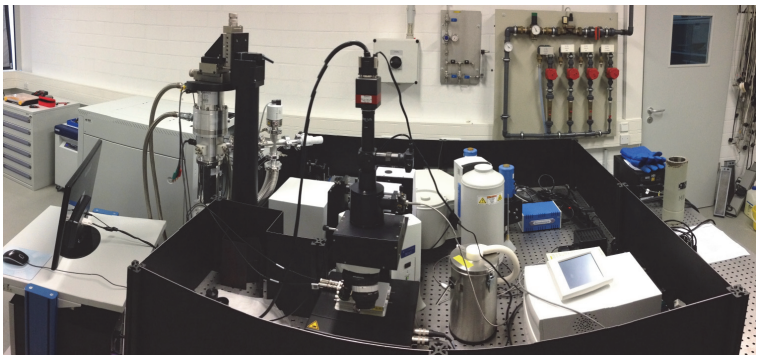

Figure 23.5: Overview on the IR-PL-EL instrument

tail instruments, that are offered by various vendors, including Horiba. But in material research, it is often hard to predict the future demands of the application, when new materials or combinations are developed. An important asset is to be able to enhance capabilities later, and is a major distinction to the workhorse instruments. Manufacturers take this into account and give some opportunity to upgrade the instrument by adding modules or advancing certain capabilities. This can be a further laser for a Raman tool, a life-time module upgrade in fluorescence, or a dedicated sw library to enhance data analysis functions. But tailoring goes one step further: the equipment's architecture is either open enough for customer extensions, or customized extensions, which means, either the researcher himself can include the needed capability, or the vendor does it.

An example is given here for a IR-Photo- and Electroluminescence instrumentation project, where it became quite clear from the beginning, that a retail instrument couldn't provide all the required measurement modes. The instrument was built by using modules and parts out of different categories:

- Horiba standard spectroscopic components: iHR320 spectrograph; NIR array detector; IR single channel detectors (1-5µm)
- Special Horiba accessories: macro-PL interface; lens free microscope with free beam mirror coupling to spectrograph

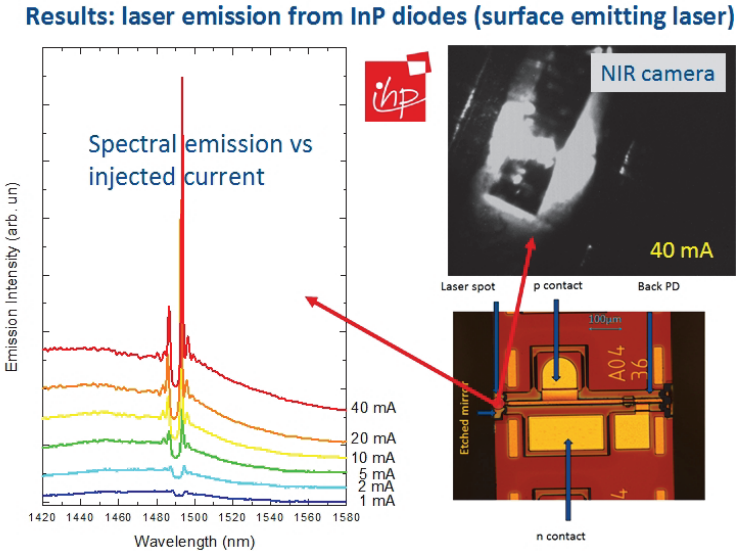

Figure 23.6: EL result for an InP surface emitting laser device

- Components from specially selected vendors: 10K macro cryostat; 77K micro cryostat; high power lasers; NIR-vision-camera; NIR/IR-objectives

- Customized components and design: confocal adaptation; extended IR range optics

Even though the tailoring was significant, only very moderate R&D effort was necessary, because most components had been developed already for other projects in the past, which means tailoring instrumentation by using "available" equipment and working experience can enable commercial solutions which were not available otherwise.

Some first results were shown in fig.23.6: The NIR emission from an vertical emitting laser is resolved both spectroscopically with the iHR320 and spatially with the NIR camera. The threshold current for lasing operation can be determined by looking at these signatures.

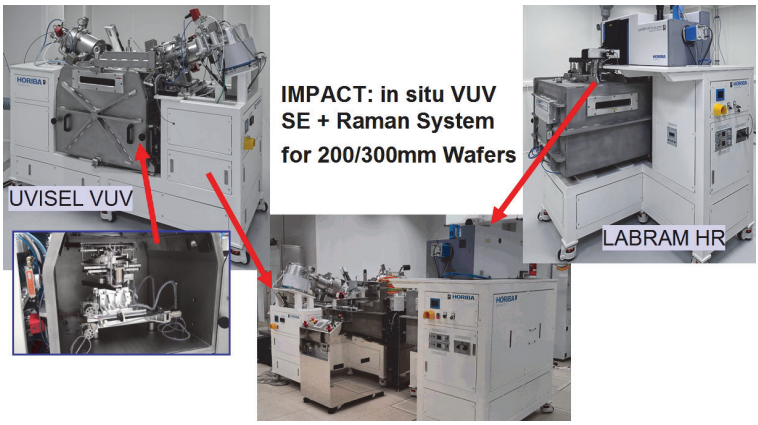

Figure 23.7: IMPACT hardware: main modules and assembly at customer site

4 How to Help Achieving Top End Instrumentation

For this category of instrumentation customization goes one major step further: we involve a dedicated R&D project team ("TIM") within our company to build unique instrumentation. Typical resources for this are:

- Standard and not-standard retail products from Horiba or other vendors
- Components/interfaces from customers: e.g. vacuum chambers, synchrotons, ...
- Customized add-ons from Horiba's R&D project team: optics, mechanics, vacuum parts, electronics, sw, ...

A recent result is shown in fig. 23.7. This is an instrument that is built for the use at a high level research institute. The goal was to be able to measure different properties on large Si wafers without breaking the vacuum where the wafers are processed. Two main instruments were integrated into a cluster tool: An in-situ VUV spectroscopic ellipsometer (SE), and a micro Raman spectrometer. Even though we built VUV SE

working down to 150nm before using Horiba's VUV monochromators, this cannot be considered being a retail instrument. And it was further tailored to the needs of this special environment, which demanded significant R&D manpower.

For the Raman spectrometer, the main constituents of our retail instrument LabRam were used, but adapted for special demands like vacuum use. Further, a common vacuum environment including xyz tables and wafer handling was included, together with a sw interface to the customer's driving sw.

References

1. H. Schmidt, K. Sowoidnich, M. Maiwald, B. Sumpf, and H. Kronfeldt, "Hand-held raman sensor head for in-situ characterization of meat quality applying a microsystem 671 nm diode laser," in *Advanced environmental, chemical, and biological sensing technologies VI, 7312, proceedings of SPIE*, 2009.
2. R. Scheier, A. Bauer, and H. Schmidt, "Early postmortem prediction of meat quality traits of porcine semimembranosus muscles using a portable raman system," in *Food and Bioprocess Technology, 9 (2014), 2732-2741*, 2014.
3. R. Scheier and H. Schmidt, "Measurement of the ph value in pork meat early postmortem by raman spectroscopy," in *Applied Physics B, 111, 289–297*, 2013.
4. M. DeBiasio, T. Arnold, G. McGunnigle, R. Leitner, D. Balthasar, and V. Rehrmann, "Detection of fire protection and mineral glasses in industrial recycling using raman mapping spectroscopy," in *Proc. SPIE 8032, Next-Generation Spectroscopic Technologies IV, 80320H*, May 2011.

IM Chapter IEEE GERMANY SECTION [KCM] Karlsruhe Center for Material Signatures KIT Karlsruhe Institute of Technology Fraunhofer IOSB

INTERNATIONAL CONFERENCE ON OPTICAL CHARACTERIZATION OF MATERIALS

Each material has its own specific spectral signature independent if it is food, plastics, or minerals. New trends and developments in material characterization have been discussed as well as latest highlights to identify spectral footprints and their realizations in industry.

CONFERENCE TOPICS:

- Food Inspection
- Plastic Recycling
- Waste Recycling
- Mineral Characterization
- Industrial Solutions
- Spectral Data Processing

The International Conference on Optical Characterization of Materials (OCM-2015) was organized by the Karlsruhe Center for Material Signatures (KCM) in cooperation with the German Chapter of the Instrumentation & Measurement Society of IEEE.

KCM is an association of institutes of the Karlsruhe Institute for Technology (KIT) and the business unit Automated Visual Inspection of the Fraunhofer Institute of Optronics, System Technologies and Image Exploitation (Fraunhofer IOSB).

ISBN 978-3-7315-0318-7
9 783731 503187 >